

N° d'ordre:

Année 2015

**UNIVERSITÉ LILLE 1 - SCIENCES ET TECHNOLOGIES**  
**ÉCOLE DOCTORALE SCIENCES DE LA MATIÈRE DU RAYONNEMENT ET DE**  
**L'ENVIRONNEMENT**

# THÈSE

*pour obtenir le grade de*  
**DOCTEUR DE L'UNIVERSITÉ LILLE 1**

**Spécialité: Molécules et Matière condensée**

*Soutenance publique le 13 novembre 2015 par*

**Ignacio BLAZQUEZ ALCOVER**

**Towards new materials by  
hierarchical topotactic syntheses.**

**Thèse dirigée par :**

Ms.Sylvie DAVIERO-MINAUD and Mr. Olivier MENTRÉ

**Composition de la commission d'examen:**

**Rapporteurs :**

Nathalie VIART, Professeur, IPCMS – DCMI, Strasbourg

Alain DEMOURGUES, Directeur de recherche CNRS, ICMCB, Bordeaux

**Examineurs :**

Christian MASQUELIER, Professeur, LRCS, Amiens

Pascal ROUSSEL, Directeur de Recherche CNRS, UCCS, Lille



## REMERCIEMENTS

*Ce travail de thèse a été effectué au sein de l'Equipe de Chimie du Solide de l'UCCS dirigée par Madame la Professeure Sylvie Daviero-Minaud et le Docteur Olivier Mentré. Ils sont été une sorte de mes « parents scientifiques ». Je tiens à remercier tout l'équipe de l'UCCS par son gentil accueil. Je voudrais remercier aussi à ma famille en Madrid pour son amour et soutien et aussi à la nouvelle famille que j'ai fait au cours de ces années à Lille (amis, colocs, colegues...). Pour finir un grand merci aux filLeS qui m'ont supporté pendant les dures nuits de travaille.*

*Merci infiniment à vous.*

# SUMMARY

<b>Introduction to topotactic transformations</b>	3
<b>Bibliography</b>	11

## Chapter I.

### Anionic mobility and exfoliation in oxybromide cobaltites.

<b>Abstract.</b>	15
<b>1. Introduction.</b>	16
1.1. Anion exchange.	16
1.2. Exfoliation.	17
1.3. 14-H Ba <sub>7</sub> Co <sub>6</sub> BrO <sub>17</sub> and 18R-Ba <sub>6</sub> Co <sub>5</sub> BrO <sub>14</sub> : Structure and properties.	20
<b>2. Experimental processes and characterization techniques.</b>	22
2.1. Powder synthesis.	22
2.2. Ionic and molecule insertion process.	23
2.3. Characterization techniques.	23
<b>3. Anion exchange in aqueous solution treatments.</b>	24
3.1. Treatment in pure water.	26
3.2. Nitrates treatment.	31
3.3. Conclusion.	37
<b>4. Organic molecule insertion.</b>	38
4.1. Soaked powders characterization.	39
4.2. Exfoliation of 14-H Ba <sub>7</sub> Co <sub>6</sub> BrO <sub>17</sub> .	45
4.2.1. Systematic colloidal suspension characterization.	46
4.2.2. Butanol case: Full colloidal suspension characterization.	48
4.2.3. Cobalt oxidation state evolution by XANES.	54
4.3. Conclusion.	60
<b>Bibliography</b>	61

## Chapter II.

### Iron exsolution and cationic mobility in $\text{BaFe}_2(\text{PO}_4)_2$ and $\text{BaFe}_{2-y}\text{M}_y(\text{PO}_4)_2$

<b>Abstract.</b>	65
<b>1. Introduction.</b>	66
<b>2. State of the art <math>\text{BaFe}_2(\text{PO}_4)_2</math>.</b>	69
2.1. Magnetic properties of $\text{BaFe}_2(\text{PO}_4)_2$ .	69
2.2. Fe exsolution at moderate temperatures.	72
2.3. Further progress in $\text{BaFe}_2(\text{PO}_4)_2$ .	72
<b>3. The logic of <math>\text{Fe}/\text{V}_{\text{Fe}}</math> ordering in reversible Iron exsolution under soft oxidizing/reducing atmosphere at moderate temperatures.</b>	74
3.1. Experimental: Synthesis and characterization techniques.	74
3.2. New insights in $\text{BaFe}_2(\text{PO}_4)_2$ iron exsolution.	75
3.3. Microstructural aspects:	78
• $\text{BaFe}_2(\text{PO}_4)_2$ polycrystals.	78
• Production of $\text{Fe}_2\text{O}_3$ nanoparticles.	80
3.4. Crystal chemistry of the Fe-depleted layers.	82
3.4.1. Intermediate exsolution ratio: Crystal structure of $\text{BaFe}_{1.5}(\text{PO}_4)_2$ .	84
3.4.2. Ultimate exsolution: Crystal structure of $\text{BaFe}_{1.33}(\text{PO}_4)_2$ .	85
3.4.3. Iron oxidation state in $\text{BaFe}_{1.33}(\text{PO}_4)_2$ .	87
3.4.4. Generalization of $\text{Fe} / \text{V}_{\text{Fe}}$ ordering versus $x$ .	88
• Small $x$ values ( $x=2/7$ , $x=1/3$ )	88
• Intermediate $x$ values ( $x=1/2$ )	89
• High $x$ values ( $x=2/3$ )	90
• Forbidden situations	90
• Distribution of the vacancies into 1D motifs and predictive tools	91
• Imbrication of the 1D-chains into 2D-lattices	94
3.4.5. Prediction of the structure of $\text{BaFe}_{1.4}(\text{PO}_4)_2$ ( $x=3/5$ )	97

<b>4. BaFe<sub>2-y</sub>M<sub>y</sub>(PO<sub>4</sub>)<sub>2</sub> (M = Co<sup>2+</sup>, Ni<sup>2+</sup>) solid solutions with selective and reversible iron exsolution</b>	99
4.1. Experimental: Synthesis and characterization techniques	100
4.2. Microstructure and Fe/M composition.	101
4.2.1. As prepared BaFe <sub>2-y</sub> M <sub>y</sub> (PO <sub>4</sub> ) <sub>2</sub> .	101
4.2.2. BaFe <sub>2-y</sub> M <sub>y</sub> (PO <sub>4</sub> ) <sub>2</sub> after thermal treatment.	103
4.2.3. Reversibility in iron exsolution.	107
4.3. Selective iron exsolution in BaFe <sub>2-y</sub> M <sub>y</sub> (PO <sub>4</sub> ) <sub>2</sub> solid solutions.	108
4.3.1. Metal oxidation states before and after exsolution by XANES	108
4.3.2. Contrast between observed and ideal exsolution process	109
4.3.2.1. Co/Fe case	110
• TGA analysis.	110
• <sup>57</sup> Fe Mössbauer spectroscopy.	110
4.3.2.2. Ni/Fe case	112
• TGA analysis	112
• <sup>57</sup> Fe Mössbauer spectroscopy	113
4.3.3. Full Fe/M reorganization in depleted phase; a single crystal study.	115
<b>5. Synchrotron “in situ” diffraction.</b>	120
<b>6. Magnetic characterization</b>	125
6.1. BaFe <sub>2-x</sub> (PO <sub>4</sub> ) <sub>2</sub>	125
6.2. Exsolved BaFe <sub>2-x</sub> M <sub>x</sub> (PO <sub>4</sub> ) <sub>2</sub> (M= Co <sup>2+</sup> , Ni <sup>2+</sup> )	127
6.2.1. Fe/Ni system	127
6.2.2. Fe/Co system	128
<b>7. Conclusion</b>	130
<b>8. Li insertion in iron deficient phases.</b>	132
8.1. Li-ion batteries.	132
8.1.1. Sample preparation.	134
8.1.2. Electrochemical measures.	135
8.2. Synthesis and characterization techniques.	135
8.2.1. Powder synthesis.	135

8.2.2. Characterization techniques.	136
8.3. Lithiated phase characterization.	136
8.3.1. Inductively coupled plasma atomic emission spectroscopy.	136
8.3.2. Solid state $^7\text{Li}$ NMR.	137
8.3.3. Structure of the lithiated phase.	140
8.3.3.1. Polycrystalline sample.	140
8.3.3.2. Single crystal structure.	141
8.4. Electrochemical experiences.	143
8.4.1. $\text{BaFe}_{1.33}(\text{PO}_4)_2$ as cathode in a Li battery.	143
8.4.2. Electrochemical oxidation of $\text{BaFe}_{1.33}(\text{PO}_4)_2$ .	145
8.4.3. $\text{BaFe}_{1.33}\text{Li}_{0.425}(\text{PO}_4)_2$ as cathode in a Li battery.	146
8.5. Conclusion	147
<b>Bibliography.</b>	149

## Chapter III.

New  $\text{Fe}^{2+}$  phases with interesting topotactic transformations.

<b>Abstract.</b>	153
<b>1. <math>\text{Fe}_{13.5}(\text{AsO}_4)_8(\text{OH})_6</math> and its imbricated charged structures after thermal treatment.</b>	154
1.1. Synthesis and characterization techniques	154
1.2. Structural: characterization	156
1.2.1. Crystal structure and Fe valence of $\text{Fe}_{13.5}(\text{AsO}_4)_8(\text{OH})_6$	156
1.2.2. Topotactic Transformation	160
1.3. Evidence for two imbricated charged sublattices	162
1.3.1. Transmission electron microscopy characterization.	162
1.3.2. Single crystal analysis.	164
1.4. Conclusion.	170

<b>2. Structure and magnetism about the new <math>\alpha</math>-BaFe<sub>2</sub>(PO<sub>4</sub>)<sub>2</sub>.</b>	171
2.1. Powder synthesis.	171
2.2. Structural characterization.	172
2.3. Magnetic characterization.	174
<b>3. RbFeAsO<sub>4</sub>(OH).</b>	175
3.1. Synthesis.	176
3.2. Structure determination.	176
<b>Bibliography.</b>	179
<b>General conclusion.</b>	180

## ANNEXES.

<b>Annexe 1. Characterization techniques.</b>	186
<b>1. X-ray diffraction (XRD).</b>	186
1.1. Funfamental principles of XRD.	186
1.2. Single crystal XRD.	187
1.3. Powder XRD.	191
• Powder structural refinement: Rietveld method.	193
<b>2. X-ray absorption.</b>	195
2.1. SOLEIL synchrotron: DiffAbs beamline.	195
2.2. X-ray absorption spectroscopy (XAS).	196
• Diffraction anomalous near edge structure (DANES).	199
<b>3. Scanning electron microscopy (SEM).</b>	200
<b>Bibliography.</b>	202
<b>Annexe 2. Single crystal data tables.</b>	203
<b>Annexe 3 Atomic coordonates and displacement tables.</b>	212

Introduction to topotactic transformations in  
inorganic solids.

## Introduction

---

Nowadays, the continued growth in the demand of new materials for advanced technology represents an important quest for chemists. Inorganic chemistry considers some basic concepts as the role of d-electrons in transition metals, coordination geometries, Jahn-Teller distortions, crystal field theory, acidity/basicity, electron transfer reactions, stabilization of oxidation states or cation-anion redox competition. All these concepts are very useful and find rewarding applications in practical material science. New synthesis methods try to give an answer to the new challenges proposed for the 21<sup>st</sup> century. One of these is the production and storage of “clean” energy [1], others are the requirements by the electronic industry with respect to the new materials for spintronics [2], multiferroics [3], or devices for optoelectronic applications where transparent conductors are needed for LEDs, solar cells and flat panels displays. [4]

The challenges proposed cannot be achieved exclusively by classic synthesis methods like solid-solid reactions at high temperature, sol-gel processes or even solvothermal reactions. All of these synthesis methods are limited to obtaining corresponding thermodynamically stable phases. At that point, new synthesis methods are envisaged in order to obtain new metastable phases, and topotactic transformations could be considered one of them.

The term of topochemistry was first used almost 100 years ago by V. Kohlschütter [5] to describe reactions where the occurring reactions and the obtained product are in strong correlation with the initial solids structure and shape. This concept has been developed for over 50 years [6], with a necessity to give a general definition of “topotactic reactions”. The IUPAC Gold Book defines a topotactic transition as “a transition in which the crystal lattice of the product phase shows one or more crystallographically equivalent, orientational relationships to the crystal lattice of the parent phase”, but in the solid state chemistry this definition can be completed by the definition given by Günter and Oswald in 1975 [7]: “A chemical reaction of a solid is called topotactic, if the product is formed in one or several crystallographically equivalent orientations relative to the parent crystal, if there has been an exchange of components with the surroundings, and if the reaction can proceed throughout the entire volume of the parent crystal”. Then, the expression “topotactic reaction” is associated to structural or compositional changes of initial reactants, leading to the formation of new compounds that retain structural similarities with the original ones. Thus, we can speak of “child” compounds in relation to “parents” precursors.

## Introduction

---

These transformations can range from simple ionic exchange or ionic insertion, to more complex paths such as metathesis reactions, wherein the elementary structural-blocks are not only retained but also rearranged.[8-10]

Since the 50s researches about this type of transformations have not stopped growing. These kinds of reactions represent a very broad area of study, and because of the complexity of the mechanisms involved, a variety of characterization techniques (XRD, microscopy, spectroscopy ...) and the combination of different scientific fields (synthetic chemistry, crystallography, physics ...) are necessary to understand how the reactions occurs.

As examples of topotactic transformations, which have been extensively studied to obtain novel compounds for technological applications, we can cite different structural changes of iron oxides and hydroxides[11-13] (magnetic applications, memories...) or the different transformations at low temperature of thin layers of superconducting  $\text{YBa}_2\text{Cu}_3\text{O}_7$  under the action of water vapor[14]. These types of transformations have gained great importance in the last decade due to several advantages:

- First of all, topotactic transformations are typically conducted by “soft” chemistry, which means lower energy requirements than conventional processes.

- Secondly, these transformations allow to obtain metastable products which cannot be obtained by conventional chemical reactions pathways, which preferentially lead to stable equilibrium phases. As shown by many examples in literature, these obtained new metastable phases have different physical properties from those of the starting compounds. The significant improvement of capacity as cathode for Li-air batteries of manganese oxide after exfoliation and restacking of the compound[15], or the transition by halogenation from semiconductor  $\text{Sr}_2\text{CuO}_3$  to superconducting  $\text{Sr}_2\text{CuO}_2\text{F}_{2+d}$ [16] are striking examples of these changes in the properties.

A classification of topotactic transformations can be made according to changes made during the reaction, from the simplest to the most complex:

## Introduction

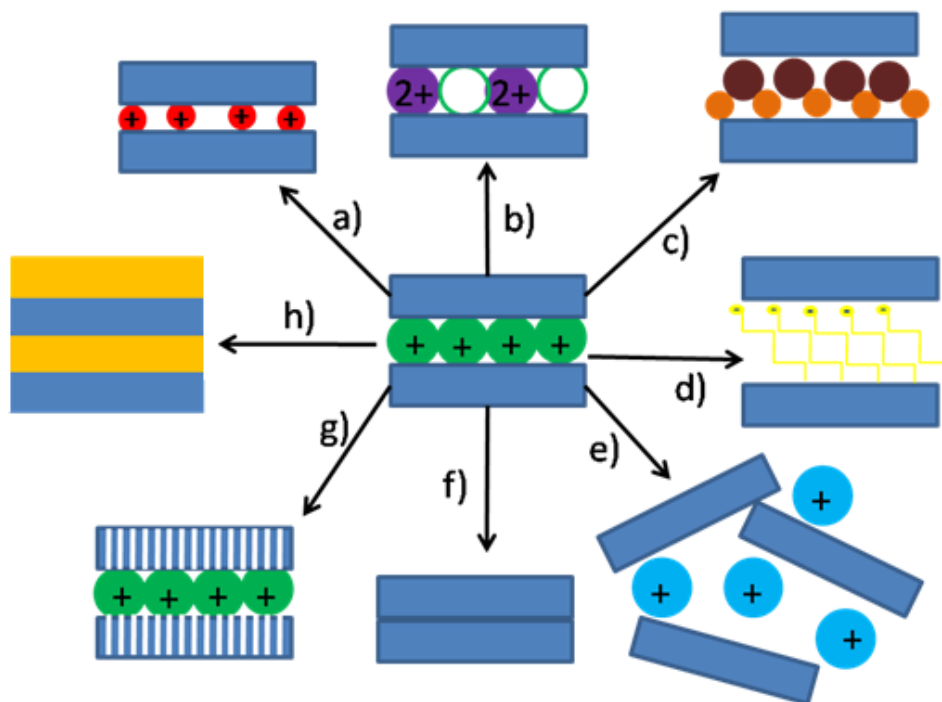


*Figure 1. Various examples of topotactic reactions: a) cationic substitution, b) cationic substitution with creation of vacant sites, c) metathesis reactions, d) "grafting" (substitution with organic molecules), e) exfoliation f) reduction and condensation, g) ion Extrusion, h) nanosheets deposition. (according to Mallouk et al.)*

- The simplest topotactic reactions are those which represent structural modifications without any compositional changes as it can be seen for  $\text{Li}_2\text{ZnSiO}_4$  for example. This silicate presents different polytypes and wherein the cationic storage will vary from one to another by replacement of lithium and zinc atoms in different sites according to the experimental conditions. [17, 18]

- Atomic insertion and / or des-insertion reactions are somewhat more complex. In these reactions the starting compounds will lose, win or exchange some of the cations or anions of the structure, which often modify oxidation states of atoms remaining unchanged in the structure.

There is a large amount of literature about this type of transformations that will cover various structures types: those where the ion mobility is favored (3D Tunnel structures, honeycombs ...; 2D layers ...) and denser structures such as cubic perovskites. A typical example concerning ions exchange associated with the mobility of cations, leading to metastable phases, is the case of Dion-Jacobson phases (2D). Here, the treatment with nitrate molten salts allows to replace bulky cations like  $\text{K}^+$ ,  $\text{Cs}^+$  or  $\text{Rb}^+$ , with smaller ones such as  $\text{Li}^+$ ,  $\text{Na}^+$  or even with molecular cations like  $\text{NH}_4^+$ . These phases with smaller alkali cations

## Introduction

---

between the blocks cannot be obtained by conventional solid-solid reaction, since three-dimensional perovskite are generally more stable at high temperatures synthesis conditions.

The cationic exchange can also be done by divalent cations as alkaline rare earth cations. These latest will occupy half of initial monovalent cationic sites, as it is shown with the partial substitution of  $\text{Rb}^+$  by  $\text{Ca}^{2+}$  or  $\text{Sr}^{2+}$  in the  $\text{RbCa}_2\text{Nb}_3\text{O}_{10}$  phase[19]. Another example is the “two-step” ion exchange route of alkaline cations by  $\text{Ca}^{2+}$ [20]. This substitution generates new vacancy sites which will be refilled in the second step [20, 21], generating new mixed-valence compounds with perovskite-related structures. These divalent cations exchanges, produced by soft chemistry, can also be done by transition metals as the new layered oxides  $\text{M}^{\text{II}}\text{La}_2\text{Ti}_3\text{O}_{10}$  (M= Co, Cu and Zn) obtained by ionic exchange in melting salts from the parent  $\text{Na}_2\text{La}_2\text{Ti}_3\text{O}_{10}$  or the  $\text{M}_{0.5}\text{LaNb}_2\text{O}_7$  (M = Fe, Ni) obtained in sealed and evacuated Pyrex tube at  $350^\circ\text{C}$  from  $\text{RbLaNb}_2\text{O}_7$ . Both of the examples are shown in [22] and [23].

Another very famous example of cationic mobility with high technological interest, concerns the series of different compounds used for Li-ion batteries. Generally, these materials consist in metal transition oxides, highlighting the  $\text{LiCoO}_2$  phase, which was the first material used for these kinds of batteries[24]. A continuous and increasing research in order to improve the electrochemical properties has allowed researchers to pay close attention to phases, such as the different iron phosphates compounds, which present a very interesting intercalation / de-intercalation properties of the  $\text{Li}^+$  in its network[25-32].

On the other hand, we can also find examples where it will be the anionic framework that will be modified. If in cation-exchangeable compounds the cohesion is mainly due to electrostatic interactions without covalent bonds between host and guest networks, allowing a large number of cationic exchange reactions, in contrast, in compounds with potentially exchangeable anions, these latest are usually strongly bound to metal ions in the crystal framework, making anionic exchange reactions more difficult.

However, the elaboration of novel compounds and materials with mixed anions and chemical bonding types is getting an increasing interest. The expected alteration of the properties of the parent compounds is of great academic interest and may also lead to specific applications as superconductivity, as seen for  $\text{LaO}_{1-x}\text{F}_x\text{FeAs}$  and  $\text{SmO}_{1-x}\text{F}_x\text{FeAs}$  which shown superconductivity behavior till 43K and 55K respectively [33, 34]. They are good examples of cation and anion mixed networks. In addition, these systems based in mixed anions and mixed cations can favor segregation obeying to anion-cation affinities, leading to new intergrowth

## Introduction

---

structures. The resulting structural units could subsequently exhibit different chemical natures and hold their own properties.

A good example of mixed anion compounds obtained by topotactic transformation is the case of the oxynitrides, which have been highlighted as a fascinating class of materials, since it was first reported thirty years ago by Marchand and co-workers[35, 36]. These compounds have attractive properties among semiconductors sensible to the visible light, becoming good candidates as photocatalyst, UV absorbers, or optical materials for colored pigments [37-39]. Oxynitrides are generally obtained by oxide precursors anneal in flowing ammonia, leading to the final products such as the different solid solution of  $\text{CaTaO}_2\text{N}$  and  $\text{LaTaON}_2$  which exhibit color ranging from yellow to red [40]. The systematic color evolution, related to the band-gap evolution in the perovskite-related oxynitride solid solutions, can be explained by a combination between the symmetry changes in the crystal and the different electronegativity of the B cation in the perovskite network. Lower symmetry in the crystal structure will generally involve smaller angles than  $180^\circ$  in B-O-B bonds, which correspond to sharper conduction bands, increasing the gap. On the other hand, a lower electronegativity of the B cation leads to an energy increment of the conduction band, turning to a larger band-gap as well. These studies were made for pure oxides[41] and verified later for nitrogen substituted oxynitrides[42].

The photocatalytic activity is strongly related to a broad optical absorption-band and the efficient separation and transport of the photogenerated electrons [43]. In general, oxynitrides have a lower band-gap than the corresponding oxides precursors, which present an advantage for photocatalytic hydrogen production from water splitting. For instance, nitrogen substituted  $\text{TiO}_{2-x}\text{N}_x$  has its edge absorption at longer wavelengths than the titanate oxide precursor, which improves the photocatalytic activity under visible light irradiation.

That type of modifications, changing the oxidation state in the anionic network by ionic exchange, lead to a better control of the electronic properties of the synthesized phases.

Topotactic halogenation reactions in metal transition oxides are another remarkable example. This is the case for  $\text{La}_2\text{CuO}_4\text{F}$ , made by topotactic fluorination at low temperature from the 2-D phase  $\text{La}_2\text{CuO}_4$ [44]. The initial compound presents semiconducting properties, however, after fluorination,  $\text{La}_2\text{CuO}_4\text{F}$  presents superconductivity until  $T_c=40\text{K}$  and a strong magnetic susceptibility at 6K under a magnetic field of 1 Oe [44]. This method has also been used in the field of thin films for electronics applications [45], enabling a good control of the electronic properties of the films after reaction.

## Introduction

---

Several fluorination routes have been studied and several possibilities of fluorination can exist: i) the fluorine insertion can be done with one oxygen atom substituted by a fluorine atom (reduction)[46], ii) insertion of two fluorine ions for each oxygen exchanged (charges conservation)[47], iii) a fluorine ion is insert in an interstitial site (oxidation)[48]. The choice of the followed route will be depend on the reactants chosen during the reaction. As example, the use of  $F_2$  gas leads preferentially to fluorine insertion (oxidation), while using  $NH_4F$  as fluorine precursor leads to oxygen substitution, and the use of metals fluorine as  $MF_2$  leads to a mix of the two cases above. However, all the three different reaction paths, lead to very interesting electronic and structural changes, as example of the superconductivity until  $T_c=111K$  of the  $Sr_2Ca_{(n-1)}Cu_nO_{(2n+\delta)}F_2$  ( $n=3$ ) phase [49].

Halogenations are not the unique examples of anionic network modifications. Oxygen de-intercalation by topotactic reduction has also been deeply researched. Oxygen topotactic reduction can guide to materials with improved properties compared to the initial compounds as observed in the case of the ionic conductivity of  $BaTiO_3$  which greatly increase after hydruration [52] or the magnetic properties of  $Sr_3Fe_2MoO_9$  after reduction [53]. Typically, oxides reduction reactions, are performed under  $H_2$  atmosphere, or in evacuated tube using oxygen-getters metals at temperatures beyond  $500^\circ C$ . Nevertheless, these kinds of reactions can happen at lower temperatures, in the range of  $200^\circ C-400^\circ C$  [50, 51], and lead to metastable products which cannot be obtained by classic synthesis. In 1999 Rosseinsky and co-workers presented their results about novel low-temperature method, able to create a large amount of oxygen vacancy[50]. In this work,  $LaNiO_3$  is topotactically reduced at  $200^\circ C$  using sodium hydride as solid state reductant. The reaction reaches the  $LaNiO_2$  compound, isostructural with the “infinite layered” cuprates, without decomposition of the oxidized precursor.

Changes in the anionic network can also lead to new hybrid materials with outstanding electronic or catalytic properties, thanks to microporous structures. The first exchange of interlamellar anions by organic species (dicarboxylic acid anions) was published by Miyata and Kumura[54]. A variety of layered host structures as clays[55] or layered double hydroxides (LDH)[56, 57] has been combined with organic compounds since then, to get pillared structures, meaning a possible design of novel 3D networks.

In addition to the multiple exchange candidates of monovalent anions ( $NO_3^-$ ,  $HO^-$ , halogens...), and in the same way that in the cationic case, the anionic exchange can also be done by divalent anions such as  $CO_3^{2-}$  or  $SO_4^{2-}$ [54].

## Introduction

---

To finish this classification we will have a look on a third kind of topotactic reaction, more complex than the two precedent cases: the metathesis reactions. These reactions concern essentially materials with a dimensionality, where the reaction products will present a combination or an assembly of the structural blocs belonging to the initial reactants. The phase transformation of Ruddlesen-Poppers,  $A_2[A'_{(n-1)}B_nO_{(3n+1)}]$  or Dion-Jacobson,  $MA_{(n-1)}B_nO_{(3n+1)}$ , phases to Aurivillius phases  $(Bi_2O_2)(A_{n-1}B_nO_{3n+1})$  or  $(MBiO)(A_{n-1}B_nO_{3n+1})$  [10, 58] by exchange of the interlayer cation for a  $[BiO]^+$  layer, or the reaction by substitution of the interlayer cations by other different layers as the  $[MCl]^+$  (M= Cr, Mn, Fe, Co) are representatives examples[59].

Similarly, deposition procedures as “layer by layer” or even “Langmuir-Blodgett” methods allow creating news metastable phases from exfoliation and restacking of different lamellar phases (oxides, hydroxides, chalcogenides...). The different physic-chemical properties of these lamellar hetero-structures will strongly depend of the combination of the properties of the assembled units. That opens the door to a large applications spectrum in such a divers fields as magnetism[60], photocatalysis[61], photoluminescence[62], photovoltaic[63], or even as supercapacitor electrodes [64]. Those transformations can also lead to new materials by combination of organic and inorganic layers, which means an alternative process to the previously presented anionic exchange, to get these new hybrid materials.

As it has been shown before, through the list of possible topotactic reactions, only some compounds are able to follow these topotactic transformations, and they must possess specific structural characteristics. The most adapted materials will be those presenting different combination of interatomic interactions such as ionic bond, covalent bond, Van Der Waal forces or even Hydrogen bonds. These different bond combinations, lead to the coexistence of different structural segments, leading to a one, two or three dimensional framework. The segments obtained after the reactants transformation, will be the elementary bricks to be combine to get the final new compound. Typical examples of compounds which lead to one dimension elementary brick through topotactic transformation are  $KFeS_2$  [65] or  $Tl_2Mo_6Se_6$  [66] with their metal-chalcogenide chains. Compounds available for 2D transformations are layered compounds such as graphite [67], layered oxides ( $LiCoO_2$ ) [68], clays as montmorillonite[69] as well as Ruddlesen- Popper[10, 70, 71] and Dion-Jacobson perovskites[72-74]. To finish,  $\beta-Al_2O_3$  [75] or different zeolites compounds[76] can be cited as examples for materials with 3D transformations capabilities. It is worth to remark that

## Introduction

---

perovskites are excellent candidates for topotactic reactions, presenting a large spectra of succeeded transformations. Ionic exchange or intercalation reactions, intercalation by reduction or nanosheets exfoliation are some examples of reactions achieved so far [77].

The study of topotactic transformation, through the observation and understanding of reactions pathways, will lead to thought to retro-synthesis methods to obtain materials with specific properties. To get there, a wide library of reactions and of interesting materials able to carry out these kinds of reactions is necessary.

The aim of this manuscript is to present the results obtained during the last three years of researches of different topotactic routes applied on compounds synthesized in the laboratory. These compounds were chosen because of their structural particularities or their interesting physical properties as it will be explained and developed hereafter.

This work has been divided in three general points:

- Fully characterization of oxybromide hexagonal perovskites during anion exchange reactions and exfoliation process.
- Structural evolution of  $\text{BaFe}_2(\text{PO}_4)_2$  and the family  $\text{BaFe}_{(2-y)}\text{M}_y(\text{PO}_4)_2$  ( $\text{M}=\text{Co}, \text{Ni}$ ) after iron exsolution by thermal treatment and following Li insertion.
- New  $\text{Fe}^{2+}$  compounds with remarkable topotactic transformations.

## Bibliography

- [1] I. Dincer, C. Acar, *International Journal of Energy Research* **39** (2015) (5) 585.
- [2] C. Felser, G.H. Fecher, B. Balke, *Angewandte Chemie-International Edition* **46** (2007) (5) 668.
- [3] W. Eerenstein, N.D. Mathur, J.F. Scott, *Nature* **442** (2006) (7104) 759.
- [4] H. Kabbour, L. Cario, S. Jobic, B. Corraze, *Journal of Materials Chemistry* **16** (2006) (42) 4165.
- [5] V. Kohlschutter, P. Haenni, *Zeitschrift Fur Anorganische Und Allgemeine Chemie* **105** (1919) (3) 121.
- [6] L.S.D. Glasser, F.P. Glasser, H.F.W. Taylor, *Quarterly Reviews* **16** (1962) (4) 343.
- [7] J.R. Günter, O. Hans-Rudolf, *Bulletin for the Institute of Chemical Research* **53** (1975) (2) 249.
- [8] R. Frankovsky, A. Marchuk, R. Pobel, D. Johrendt, *Solid State Communications* **152** (2012) (8) 632.
- [9] R.E. Schaak, T.E. Mallouk, *Chemistry of Materials* **14** (2002) (4) 1455.
- [10] J. Gopalakrishnan, T. Sivakumar, K. Ramesha, V. Thangadurai, G.N. Subbanna, *Journal of the American Chemical Society* **122** (2000) (26) 6237.
- [11] Y. Cudennec, A. Lecerf, *Solid State Sciences* **7** (2005) (5) 520.
- [12] J.D. Bernal, D.R. Dasgupta, A.L. Mackay, *Nature* **180** (1957) (4587) 645.
- [13] F.R.S. J. D. Bernal, D. R. Dasgupta and A. L. Mackay, *Clay Minerals Bulletin* **4** (1959) (21) 15.
- [14] W. Gunther, R. Schollhorn, H. Siegle, C. Thomsen, *Solid State Ionics* **84** (1996) (1-2) 23.
- [15] S. Ida, A.K. Thapa, Y. Hidaka, Y. Okamoto, M. Matsuka, H. Hagiwara, T. Ishihara, *Journal of Power Sources* **203** (2012) 159.
- [16] Z. Hiroi, M. Takano, M. Azuma, Y. Takeda, *Nature* **364** (1993) (6435) 315.
- [17] A.R. West, F.P. Glasser, *Journal of Materials Science* **5** (1970) (7) 557.
- [18] A.R. West, F.P. Glasser, *Journal of Materials Science* **5** (1970) (8) 676.
- [19] C.H. Mahler, B.L. Cushing, J.N. Lalena, J.B. Wiley, *Materials Research Bulletin* **33** (1998) (11) 1581.
- [20] B.L. Cushing, J.B. Wiley, *Materials Research Bulletin* **34** (1999) (2) 271.
- [21] R.A. McIntyre, A.U. Falster, S.C. Li, W.B. Simmons, C.J. O'Connor, J.B. Wiley, *Journal of the American Chemical Society* **120** (1998) (1) 217.
- [22] L. Viciu, N. Liziard, V. Golub, T.A. Kodenkandath, J.B. Wiley, *Materials Research Bulletin* **39** (2004) (14-15) 2147.
- [23] K.A. Hyeon, S.H. Byeon, *Chemistry of Materials* **11** (1999) (2) 352.
- [24] M. Yoshio, R. J. Rodd, K. Akiya, *Lithium-Ion Batteries*, Springer (2009).
- [25] J. Come, P.L. Taberna, S. Hamelet, C. Masquelier, P. Simon, *Journal of the Electrochemical Society* **158** (2011) (10) A1090.
- [26] R.G. Iyer, C. Delacourt, C. Masquelier, J.M. Tarascon, A. Navrotsky, *Electrochemical and Solid State Letters* **9** (2006) (2) A46.
- [27] G. Ouvrard, M. Zerrouki, P. Soudan, B. Lestriez, C. Masquelier, M. Morcrette, S. Hamelet, S. Belin, A.M. Flank, F. Baudalet, *Journal of Power Sources* **229** (2013) 16.
- [28] C. Delacourt, P. Poizot, D. Bonnin, C. Masquelier, *Journal of the Electrochemical Society* **156** (2009) (7) A595.
- [29] C. Delacourt, C. Wurm, P. Reale, M. Morcrette, C. Masquelier, *Solid State Ionics* **173** (2004) (1-4) 113.
- [30] L. Laffont, C. Delacourt, P. Gibot, M.Y. Wu, P. Kooyman, C. Masquelier, J.M. Tarascon, *Chemistry of Materials* **18** (2006) (23) 5520.
- [31] P. Reale, B. Scrosati, C. Delacourt, C. Wurm, M. Morcrette, C. Masquelier, *Chemistry of Materials* **15** (2003) (26) 5051.
- [32] C. Delacourt, L. Laffont, R. Bouchet, C. Wurm, J.B. Leriche, M. Morcrette, J.M. Tarascon, C. Masquelier, *Journal of the Electrochemical Society* **152** (2005) (5) A913.
- [33] H. Takahashi, K. Igawa, K. Arii, Y. Kamihara, M. Hirano, H. Hosono, *Nature* **453** (2008) (7193) 376.

## Introduction

---

- [34] Z.-A. Ren, W. Lu, J. Yang, W. Yi, X.-L. Shen, Z.-C. Li, G.-C. Che, X.-L. Dong, L.-L. Sun, F. Zhou, Z.-X. Zhao, *Chinese Physics Letters* **25** (2008) (6) 2215.
- [35] R. Marchand, R. Pastuszak, Y. Laurent, G. Roul, *Revue De Chimie Minerale* **19** (1982) (6) 684.
- [36] R. Marchand, F. Pors, Y. Laurent, *Revue Internationale Des Hautes Temperatures Et Des Refractaires* **23** (1986) (1) 11.
- [37] K. Maeda, K. Domen, *Mrs Bulletin* **36** (2011) (1) 25.
- [38] F. Tessier, P. Maillard, F. Chevre, K. Domen, S. Kikkawa, *Journal of the Ceramic Society of Japan* **117** (2009) (1361) 1.
- [39] S.G. Ebbinghaus, H.-P. Abicht, R. Dronskowski, T. Mueller, A. Reller, A. Weidenkaff, *Progress in Solid State Chemistry* **37** (2009) (2-3) 173.
- [40] M. Jansen, H.P. Letschert, *Nature* **404** (2000) (6781) 980.
- [41] H.W. Eng, P.W. Barnes, B.M. Auer, P.M. Woodward, *Journal of Solid State Chemistry* **175** (2003) (1) 94.
- [42] R. Aguiar, D. Lopinovich, A. Weidenkaff, A. Rachel, A. Reller, S.G. Ebbinghaus, *Dyes and Pigments* **76** (2008) (1) 70.
- [43] J. Shi, J. Ye, Q. Li, Z. Zhou, H. Tong, G. Xi, L. Guo, *Chemistry-a European Journal* **18** (2012) (11) 3157.
- [44] B. Chevalier, A. Tressaud, B. Lepine, K. Amine, J.M. Dance, L. Lozano, E. Hickey, J. Etourneau, *Physica C* **167** (1990) (1-2) 97.
- [45] S.T. Lees, I. Gameson, M.O. Jones, P.P. Edwards, C. Greaves, F. Wellhofer, P. Woodall, I. Langford, M. Slaski, *Physica C* **270** (1996) (3-4) 305.
- [46] O. Clemens, A.J. Wright, F.J. Berry, R.I. Smith, P.R. Slater, *Journal of Solid State Chemistry* **198** (2013) 262.
- [47] P.R. Slater, *Journal of Fluorine Chemistry* **117** (2002) (1) 43.
- [48] R.K. Li, C. Greaves, *Physical Review B* **62** (2000) (6) 3811.
- [49] T. Kawashima, Y. Matsui, E. Takayama-Muromachi, *Physica C* **257** (1996) (3-4) 313.
- [50] M.A. Hayward, M.A. Green, M.J. Rosseinsky, J. Sloan, *Journal of the American Chemical Society* **121** (1999) (38) 8843.
- [51] E. Dixon, M.A. Hayward, *Inorganic Chemistry* **49** (2010) (20) 9649.
- [52] Y. Kobayashi, O.J. Hernandez, T. Sakaguchi, T. Yajima, T. Roisnel, Y. Tsujimoto, M. Morita, Y. Noda, Y. Mogami, A. Kitada, M. Ohkura, S. Hosokawa, Z.F. Li, K. Hayashi, Y. Kusano, J.E. Kim, N. Tsuji, A. Fujiwara, Y. Matsushita, K. Yoshimura, K. Takegoshi, M. Inoue, M. Takano, H. Kageyama, *Nature Materials* **11** (2012) (6) 507.
- [53] C.A. Lopez, M.D. Viola, J.C. Pedregosa, J.A. Alonso, M.T. Fernandez-Diaz, *European Journal of Inorganic Chemistry* (2010) (26) 4110.
- [54] S. Miyata, T. Kumura, *Chemistry Letters* (1973) (8) 843.
- [55] In: M.L.O.a.H. Robson, Editor, *Synthesis of microporous materials.*, Van Nostrand Reinhold, New York (1992).
- [56] J.W. Lee, W.C. Choi, J.-D. Kim, *Crystengcomm* **12** (2010) (10) 3249.
- [57] V. Rives, M.A. Ulibarri, *Coordination Chemistry Reviews* **181** (1999) 61.
- [58] T. Sivakumar, J. Gopalakrishnan, *Materials Research Bulletin* **40** (2005) (1) 39.
- [59] L. Viciu, G. Caruntu, N. Royant, J. Koenig, W.L.L. Zhou, T.A. Kodenkandath, J.B. Wiley, *Inorganic Chemistry* **41** (2002) (13) 3385.
- [60] M. Osada, Y. Ebina, K. Fukuda, K. Ono, K. Takada, K. Yamaura, E. Takayama-Muromachi, T. Sasaki, *Physical Review B* **73** (2006) (15).
- [61] T. Shibata, N. Sakai, K. Fukuda, Y. Ebina, T. Sasaki, *Physical Chemistry Chemical Physics* **9** (2007) (19) 2413.
- [62] T.C. Ozawa, K. Fukuda, K. Akatsuka, Y. Ebina, T. Sasaki, K. Kurashima, K. Kosuda, *Journal of Physical Chemistry C* **112** (2008) (44) 17115.
- [63] S. Suresh, A. Pandikumar, S. Murugesan, R. Ramaraj, S.P. Raj, *Solar Energy* **85** (2011) (9) 1787.
- [64] X. Zhang, W.S. Yang, D.G. Evans, *Journal of Power Sources* **184** (2008) (2) 695.

## Introduction

---

- [65] H. Boller, *Monatshefte Fur Chemie* **109** (1978) (4) 975.
- [66] M. Potel, R. Chevrel, M. Sergent, *Acta Crystallographica Section B-Structural Science* **36** (1980) (JUL) 1545.
- [67] W.C. Forsman, T. Dziemianowicz, K. Leong, D. Carl, *Synthetic Metals* **5** (1983) (2) 77.
- [68] K. Mizushima, P.C. Jones, P.J. Wiseman, J.B. Goodenough, *Materials Research Bulletin* **15** (1980) (6) 783.
- [69] D. Gournis, A. Lappas, M.A. Karakassides, D. Toebbens, A. Moukarika, *Physics and Chemistry of Minerals* **35** (2008) (1) 49.
- [70] T. Sivakumar, R. Seshadri, J. Gopalakrishnan, *Journal of the American Chemical Society* **123** (2001) (46) 11496.
- [71] Z.S. Gonen, D. Paluchowski, P. Zavalij, B.W. Eichhorn, J. Gopalakrishnan, *Inorganic Chemistry* **45** (2006) (21) 8736.
- [72] K. Maeda, T.E. Mallouk, *Journal of Materials Chemistry* **19** (2009) (27) 4813.
- [73] M.J. Geselbracht, H.K. White, J.M. Blaine, M.J. Diaz, J.L. Hubbs, N. Adelstein, J.A. Kurzman, *Materials Research Bulletin* **46** (2011) (3) 398.
- [74] M. Matsuda, T. Hioki, K. Okada, S. Nishimoto, M. Miyake, *Journal of Physics and Chemistry of Solids* **67** (2006) (5-6) 1325.
- [75] C.N. Poulieff, R. Kvachkov, I.M. Balkanov, *Materials Research Bulletin* **13** (1978) (4) 323.
- [76] G.C. Shen, A.M. Liu, M. Ichikawa, *Inorganic Chemistry* **37** (1998) (21) 5497.
- [77] K.G.S. Ranmohotti, E. Josepha, J. Choi, J.X. Zhang, J.B. Wiley, *Advanced Materials* **23** (2011) (4) 442.

# **Chapter I.**

Anionic mobility and exfoliation in  
oxybromide cobaltites.

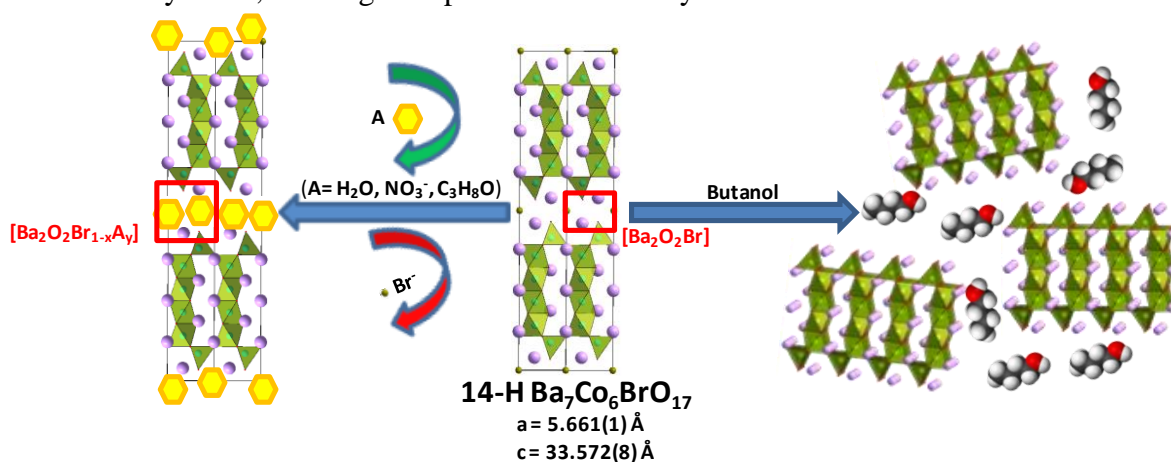
**Abstract.**

In the context of topotactic reactions, where elementary building units are conserved but re-organized into metastable phases [1-3]; the proposition of novel elementary blocks to be assembled is sought, especially in form of highly reactive exfoliated 2D-inorganic nanosheets. If, on one hand, most exfoliations of transition-metal oxides lead to negatively charged nanosheets within colloidal suspension, which can be recombined using a diversity of positive-charged counter-ions (inorganic or organic), on the other hand, only few structural types allow creation of positively charged 2D-units. They mostly belong to LDHs phases or rare-earth hydroxides.

During the first chapter of this manuscript and with the aim to develop new positive 2D-building blocks, we focus on mixed valence  $\text{Co}^{3+/4+}$  oxo-bromides developed in our laboratory, the 14H- $\text{Ba}_7\text{Co}_6\text{BrO}_{17}$  and 18R- $\text{Ba}_6\text{Co}_5\text{BrO}_{14}$ . [4, 5] These compounds are built of ferromagnetic hexagonal-perovskite blocks, 6H- and 5H- respectively, separated by  $[\text{Ba}_2\text{O}_2\text{Br}]$  spacers. Disorder and observation of  $\text{CO}_3^{2-}$  defects in those spacers suggests an easy anion-exchange in favor of the possible bromide ions removal. [4, 6]

In the present chapter, we show in a first set of experiences, that anionic mobility in  $[\text{Ba}_2\text{O}_2\text{Br}]$  layer, allows the anionic exchange by soft chemistry. In that way, the hydration by water molecule insertion in the spacer, and the substitution of bromine by nitrate ions are presented and the products are characterized. In the second part of the chapter, we present the direct exfoliation of these compounds in butanol leading to positive nanoblocks. Zeta potential measurements confirm unambiguously that particles in colloidal suspension are positively charged on their surface.

Full structural characterizations of exfoliated “nanoflakes” were performed by TEM, EDS, Raman and IR spectroscopies, AFM, X-ray absorption spectroscopy (XANES and DANES) and synchrotron X-ray diffraction (in-plane and out of plane) at SOLEIL (Saint Aubin, France). Combination of all these techniques showed the presence of crystalline flat nanoparticles  $\sim 50\text{nm}$  wide, with poor bromine content and with preservation of the local cobalt environment after the exfoliation process, as well as the  $\text{Co}^{3+/4+}$  mixed oxidation degree. Thus, we can conclude that exfoliation process occurs keeping the global structure of the elementary blocs, creating new positive elementary units.



## 1. Introduction.

### 1.1. Anion exchange.

Several anion exchange methods have already mentioned in the text previously, here, we will focus on the state of the art of wet chemistry methods, in mild conditions.

In this context, the main compounds which show a very good ability for anionic exchange are the layered double hydroxides (LDHs). LDHs are also known as anionic clays, most of their structures correspond to that of hydrocalcite, consisting of octahedral-brucite-like  $M(OH)_2$  layers and charge-balancing anions ( $A^{n-}$ ) present in the interleaves. The general formula is  $M^{2+}_{(1-x)}M^{3+}_x(OH)_2 \cdot A^{n-}_{x/n} \cdot mH_2O$  ( $M^{2+}$ :  $Ni^{2+}$ ,  $Zn^{2+}$ ,  $Mg^{2+}$  ...;  $M^{3+}$ :  $Fe^{3+}$ ,  $Al^{3+}$ ,  $Co^{3+}$  ...), where  $A^{n-}$  is an exchangeable interlayer anion[7]. The global charge density of the positively charged metal octahedral layer, of general formula  $[M^{2+}_{(1-x)}M^{3+}_x(OH)_2]^{x+}$ , is determinate by the molar fraction  $x$  ( $0.2 < x < 0.33$ ) of  $M^{3+}$ .

These compounds have been differently used as inorganic anion-exchanger and basic catalyst in the chemical industry[7] or even as phosphate adsorbent in pharmaceutical applications[8].

There is an important research about common anion exchange capacities in the different LDHs. As example, it has already been shown in Mg-Al LDHs, that anion exchange ability increases in the following sequence  $ClO_4^- < NO_3^- < Br^- < Cl^- < F^- < (OH)^- < SO_4^- < CO_3^{2-}$ [9]. Several studies done to explain this series conclude that selectivity for anion exchange is usually related to the guest orientation, its ionic radius and its charge [10-12]. In addition the anion exchange process is not limited to inorganic species, organic compounds as carboxylic acids, amino acids, etc. can also been exchanged in LDHs[13-15].

Similarly to LDHs, rare earth hydroxides have also showed a very efficient anionic exchange at room temperature. [16-18]. In addition, these hydroxides are very attractive from the viewpoint of the unique chemistry of rare-earth compounds. Luminescent property of  $Eu^{3+}$  and  $Tb^{3+}$  hydroxides nanosheets, or the ability to carry a payload of magnetic resonance (MR)-active paramagnetic centers of the  $Gd^{3+}$  based nanosheets are good examples of their interest for physical applications.[19, 20].

### 1.2. Exfoliation.

Thanks to advances in ionic exchange of the last decades, researchers have shown an increasing interest to develop new methods of materials design. Among them, exfoliation and recombination of nanosheets for new materials creation, have had an important role since the sixties until today. This process enable to move towards the concept of retrosynthesis in solid state chemistry, as in the organic chemistry, and open the opportunity to design new materials by combinations of elementary blocks from targeted reactions.

The first evidences of exfoliation process are dated from the beginning of sixties, where clays were used as starting compounds with G. F. Walker work about clays swelling in organic solvents, in 1960.[21] Forty years later, in nineties, this technique has been extended to other lamellar materials with interesting physical properties for technological applications. The most famous are graphenes, which had led to the award of the 2010 chemistry Nobel Prize to Andre Geim and Konstantin Novoselov[22-25]. However, researchers as Takayoshi Sasaki, Thomas E. Mallouk and others try to generalize the exfoliation process with other kind of bidimensional compounds[26, 27], leading to the first works about layered oxide exfoliation and delamination of acid titanates phases.[28-30] These first studies follow the previous work about the good exchange ionic capacities, associated to alkaline cation mobility in those compounds families.[31, 32]

The aim of exfoliation process is to obtain 2D-nanosheets whose thickness is the elementary structural unit. It can goes from one atom thick, like graphene sheets, to few nanometers when the elementary structural unit belong to oxides compounds with larger lattice parameters. The surface length of these particles may achieve one hundred nanometers, meaning a large surface/thickness ratio. Size, morphology or crystallinity of the nanoparticles, in 0 (grains), 1(wires or rods) or 2 (sheets or plates) dimensions, play an important role in the evolution of their electronic, magnetic, optic or even catalytic properties [33-36]. Because of their low thickness, nanosheets can present quantum 2D confinement effects which allow electronic structure modifications, enabling to create new physical phenomena as shown in graphene. This latest presents very interesting electronic properties, because of its bidimensional carbon network of one atom thick, with delocalized electrons on its surface, which allows them to move through the structure at high speed. These properties were used for research of very particular characteristics in quantum mechanics [37, 38].

There is wide spectrum of novel structures which can be achieved combining different bidimensional structural units, this is one of the biggest advantages of these nanosheets. On

the one hand, different compounds with hybrid superstructures can be elaborated by combination with organic molecules, polymers and even inorganic or metallic nanoparticles. On the other hand, depending of nanosheets combination techniques, different nano-architectures can be obtained. These techniques go from lamellar aggregates randomly restacked by addition of counter-ions to the nanosheets suspension to promote the flocculation, to elaboration of organized thin-films thanks to "Layer by layer" or "Langmuir-Bodgett" assembly techniques.

A wide variety of layered compounds with transition metals have been studied for that purpose. This is the case of clays, chalcogenides, LDHs, or layered metallic oxides and phosphates. Electrons and empty levels of *d* orbitals of these metals allow to create different couplings and effects, potentially interesting when confined in the 2D nanosheet network.

Generally bulk materials selected as nanosheets precursors, show good abilities for ionic exchanges and intercalation reactions, which finally lead to soft chemistry delamination in aqueous or organic solvents.

The ionic mobility is the key of success for exfoliation process. In fact, it is based on the decrease of electrostatic interaction forces between the layers until a complete split of the crystals, leaving the elemental nanosheets in suspension. In that way, biggest is the cation inserted between the layers, weaker will be the forces between them. When the layers have no more interactions between them, they make a colloidal suspension with the solvent which stabilizes the sheets charges by electrostatic interactions.

In general, in the layered oxides case, the structural 2D blocks are negatively charged. As examples, some oxides blocks architectures are presented in figure I.1. These are made from  $\text{MO}_6$  ( $\text{M} = \text{Co}, \text{Mn}, \text{Ti}, \text{Nb}, \text{Ta} \dots$ ) octahedra joint by faces or by edges, forming the layers, alkaline cations are placed between them.

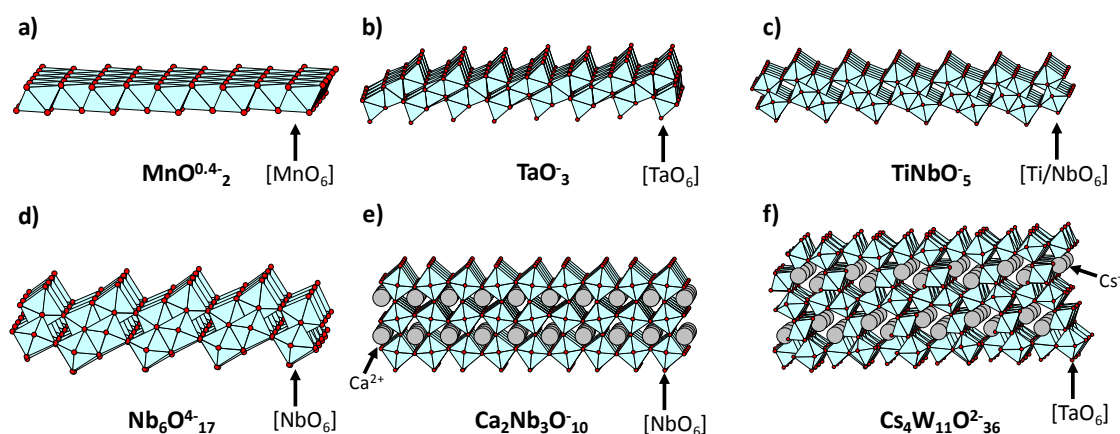


Figure I.1. Typical oxide nanosheets structures.

The protocol for exfoliation of layered oxides is already well established. First, precursors are synthesized, typically by a classical method as solid state reaction at high temperature. In a second step, the synthesized oxides are soaked in an acid solution to get a protonated-hydrated phase where protons will replace alkaline cations. In a third and last step, the interlayer space will be dilated, by substitution of the protons by a voluminous organic molecule as tetrabutylammonium ( $\text{TBA}^+$ ). The interlayer space expansion weakens the electrostatic forces between the blocks, and the application of a mechanic force like stirring or sonication will split the blocks to get a well stabilized suspension of 2D nanosheets.

This exfoliation method has allowed obtaining nanosheets based on different  $d^0$  transition metals ( $\text{Ta}^{3+}$ ,  $\text{Ti}^{4+}$ ,  $\text{Nb}^{5+}$  ...). These metals have semiconductor properties thanks to their large *bandgap*. Electronic properties of titanium oxide have been deeply studied and  $\text{TiO}_2^{\delta-}$  nanosheets present similar electronic properties to classic rutile or anatase bulks. However, quantum effects associated to the size effects, lead to generate anodic photocurrent under UV irradiation, with wavelengths shorter than 320 nm, corresponding to a GAP enlargement of 3.8V, higher than 3.2V value from the bulk phase.[39] In addition, the colloidal suspensions of nanosheets of this phase show Beer-Lambert- behavior for pronounced UV absorption, presenting a large molar extinction coefficient. [40]. This behavior make these nanosheets very promising for photo-catalysis reactions[41]. These photo-catalysis capabilities of nanosheets are not exclusives to titanates, as show several examples of some others restacked nanosheets of different metal oxides [42-44].

Other interesting properties have been attributed to these kinds of compounds, as electrochemical properties. Due to their 2D architecture, nanosheets show notably enhanced host capabilities as active electrodes materials and in this context manganese nanosheets can be cited as example. Layered  $\text{NaMnO}_2$ -derived  $\text{LiMnO}_2$  could substitute  $\text{LiCoO}_2$  as cathode material for Li-ion secondary batteries because of its lower cost and it is eco-friendly. One of the main problem of this phase is the severe capacity fading upon cycling, due to the phase transformation into the spinel form. Nevertheless,  $\text{Li}_{0.36}\text{MnO}_2 \cdot 0.7 \cdot \text{H}_2\text{O}$  obtained by flocculation have a turbostratic structure which avoid the phase transition. In addition, this flocculated compound is also promising for discharge at large current, with a capacity of 79  $\text{mA} \cdot \text{h} \cdot \text{g}^{-1}$  at a current density of 2  $\text{A} \cdot \text{g}^{-1}$  and 151  $\text{mA} \cdot \text{h} \cdot \text{g}^{-1}$  at 50  $\text{A} \cdot \text{g}^{-1}$  .[45]

Finally, the possibility to synthesize new 2D semiconducting nanosheets open the door to the design of more complex nanodevices such as *p-n* junctions[46], or photoconducting cells[43, 47].

As seen before, negatively charged nanosheets are quite easy to obtain, in contrast, positively charged oxide nanosheets are rare because of the limited number of potentially exfoliable structures by anion exchange: LDHs[48] and rare-earth hydroxides[19, 20] are the only examples in the literature and are presented in figure I.2.

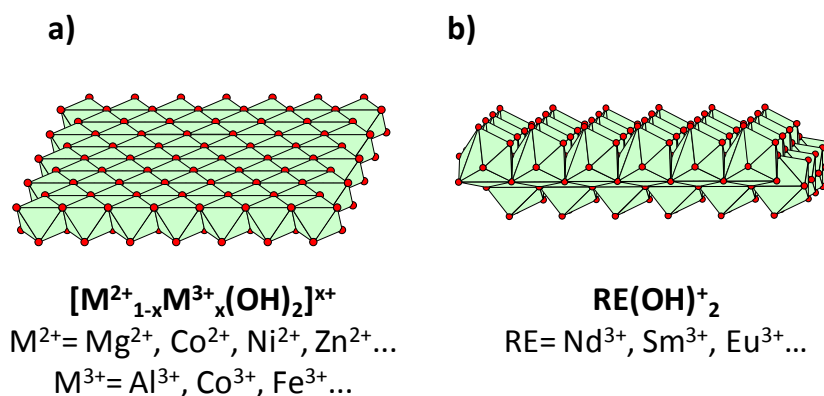


**Figure I.2.** LDHs (a) and Rare-Earth hydroxides (b) representative structures.

The suspensions of positively charged sheets are generally stabilized in organic solvent[49, 50] even if some studies have also been done in aqueous solution.[51, 52] Exfoliated positive charged sheets have been successfully restacked with different counter ions or even with other negative oxide nanosheets by flocculation or layer by layer methods[53], allowing a new design of metastable phases.

To enlarge the number of possible combinations between different 2D structures with positive and negative sheets, it is of great interest to synthesize new positively-charged oxides nanosheets with new compositions and new blocks architectures. For this purpose, we have studied in this work the anionic exchange properties and exfoliation process of two layered oxobromides cobaltites, 14-H  $Ba_7Co_6BrO_{17}$  and 18R- $Ba_6Co_5BrO_{14}$ , both of them synthesized in the laboratory[4].

### 1.3. 14-H $Ba_7Co_6BrO_{17}$ and 18R- $Ba_6Co_5BrO_{14}$ : Structure and properties.

$Ba_{(n+3)}Co_{(n+2)}BrO_{(3n+5)}$  with  $n = 3, 4$  structures are presented in figure I.3 (a,b) these two compounds have a hexagonal perovskite-related structure, built by stacking classic perovskite layers along the c direction, combined with  $Ba_2O_2Br$  layers. [4] The hexagonal perovskites blocks are made of trimeric (18R) or tetrameric (14H) units of face-sharing octahedra ( $Co_3O_{12}$  and  $Co_4O_{15}$  respectively) connected at their extremities to a single isolated tetrahedron. Projection along the  $[110]$  directions of both structures shows the presence of a triangular

network built by the octahedral blocs which are linked between them thanks to the tetrahedron located at the center of each triangle.

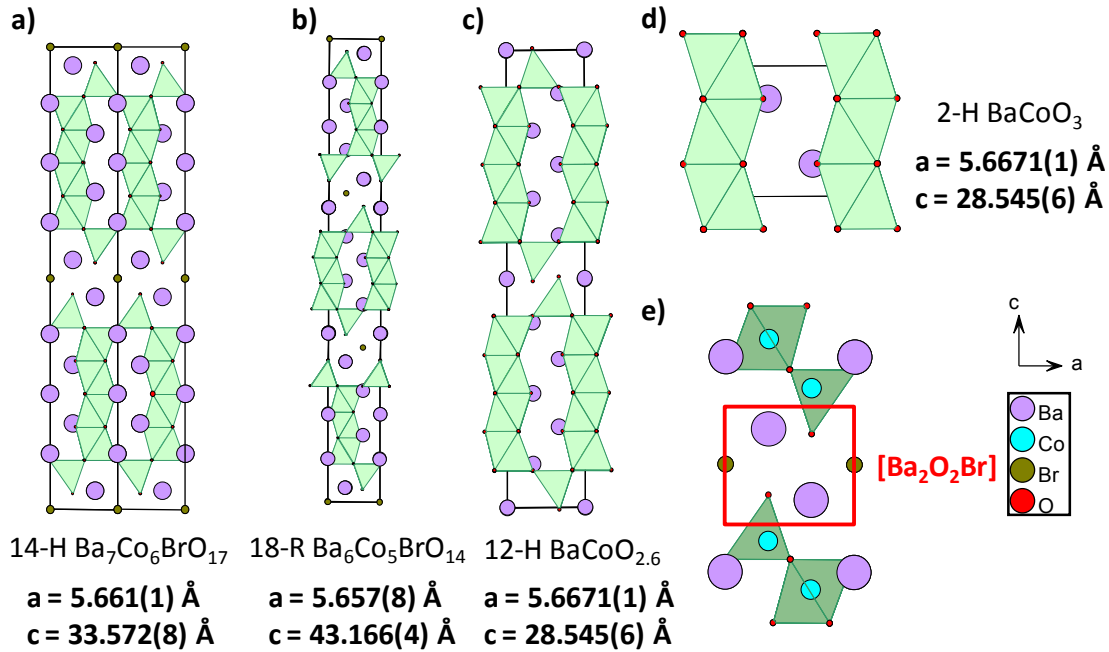


**Figure I.3.** *a-c* structure projection of 14H- $\text{Ba}_7\text{Co}_6\text{BrO}_{17}$  (a), 18R- $\text{Ba}_6\text{Co}_5\text{BrO}_{14}$  (b), 12H- $\text{BaCoO}_{2.6}$  (c), 2H- $\text{BaCoO}_3$  (d) and of the  $[\text{Ba}_2\text{O}_2\text{Br}]$  layer (e).

The 18-R  $\text{Ba}_6\text{Co}_5\text{BrO}_{14}$  can be understood as a version of the 5H-  $\text{Ba}_5\text{Co}_5\text{O}_{14}$ [54] by replacing the  $c'$ - $[\text{BO}_2]$  layer by two  $c'$ - $[\text{BaOBr}]$ , leading to a sequence  $(c'chcc')_3$  which means 5H hexagonal perovskite blocs separated by double  $[\text{BaOBr}]^-$  layers [4], as shown in figure 1 (e). As a result of bromide presence between the blocs, distances between two tetrahedral cobalt are substantially longer ( $6.591(1) \text{ \AA}$ ) than in the 5H phase ( $4.66(1) \text{ \AA}$ ). In the same way,  $\text{Ba}_7\text{Co}_6\text{BrO}_{17}$  is related to 12H- $\text{BaCoO}_{12.6}$  phase[55], presented in figure 3 (c), by creation of a 14-layer stacking sequence  $(c'chhhcc')_2$ . The fact that  $\text{Ba}_7\text{Co}_6\text{BrO}_{17}$  is related to  $\text{Ba}_6\text{Co}_5\text{BrO}_{14}$  by removing one  $h$ - $[\text{BaO}_3]$  and one Co atom could justify the phase transformation observed at high temperatures:



These two phases present mixed 3+ and 4+ cobalt valences, which implies interesting magnetic behavior since the cobaltite blocks are intrinsically ferromagnetic.[5]

Previous studies about these phases and others structurally related, show some remarkable points which make them potential candidates to anion exchange, and even to exfoliation into 2D positively charged blocks, which justify our interest.[56, 57]

Firstly, structure resolution by single crystal X-Ray diffraction and powder Neutron diffraction show a disorder in the anionic network of  $[\text{Ba}_2\text{O}_2\text{Br}]^-$  layers.[4] Secondly, it has already been verified that these kinds of layers present an easy molecule insertion, like water or carbonates, after aging in air.[58]. These two arguments let us to suggest an anionic mobility in the layer, which could lead to a possible bromide exchange.

This last point is very interesting because, as we have seen before, the cationic mobility is at the origin of the successfully exfoliation of different bidimensional perovskites (as Ruddelsden-Popper or Dion-Jacobson) or other oxides, leading to negatively charged nanosheets. So, anionic mobility in our phases should lead to new positive blocks which are going to enrich the limited catalog of positive elementary units provide by LDHs and rare-earth hydroxides.

In order to make real the hypothesis created after the literature reading, we have done a deep study of those phases where, in a first step, we have tried to carry out anionic exchanges, with the aim of verify the anionic mobility and the stability of the hexagonal perovskites blocks. In a second step, thanks to the results obtained previously, the exfoliation process has been carried out in different solvents.

## 2. Experimental processes and characterization techniques.

### 2.1. Powder synthesis.

14-H  $\text{Ba}_7\text{Co}_6\text{BrO}_{17}$  and 18R- $\text{Ba}_6\text{Co}_5\text{BrO}_{14}$  were synthesized by direct solid state reaction following the synthesis process described in reference [57].  $\text{BaCO}_3$  (Alfa Aesar 99.8%),  $\text{Co}_3\text{O}_4$  (Alfa Aesar 99.7%), and  $\text{BaBr}_2$  (Alfa Aesar 99.0%), without further purification, were used as reactants in the 13/14/1 and 33/10/3 stoichiometric proportions respectively. Powders were carefully grinded in mortar and introduce in an alumina crucible. To obtain the pure  $\text{Ba}_7\text{Co}_6\text{BrO}_{17}$  phase, mixed powders were heated at  $900^\circ\text{C}$  for a week, with several intermediate grindings in order to improve the reactivity of the mixture. On the other hand, the synthesis of  $\text{Ba}_6\text{Co}_5\text{BrO}_{14}$  phase is a two steps process involving the  $\text{Ba}_7\text{Co}_6\text{BrO}_{17}$  phase as intermediate. The stoichiometric mixture was heated in a first step at  $900^\circ\text{C}$  for 48h to obtain a mix of  $\text{Ba}_7\text{Co}_6\text{BrO}_{17}$  and  $\text{BaCoO}_3$ , then reheated at  $990^\circ\text{C}$  for 72h with several intermediate grindings and finally quenched at ambient temperature to lead to the pure  $\text{Ba}_6\text{Co}_5\text{BrO}_{14}$  phase.

Both compounds were achieved as pure phase after this solid state synthesis and were systematically checked by powder XRD in order to verify their purity.

### **2.2. Ionic and molecule insertion process.**

For all exchanges tests, different media were chosen in agreement with the literature, and were classified as aqueous anionic solutions (carbonates, nitrates, acetates, sulfates) and organic solvent (DMF, DMSO, dimethylformamide, ethanol, propanol and butanol). Aqueous solutions (deionized water or solutions 1M anionic concentration) have been tested for anionic exchange process, while organic solvents were tested for molecules insertion.

Typically, 0.2 grams of the original oxybromides were soaked in 50 ml of the different solutions during various times, in a close vessel, under stirring and with daily ultrasonic baths. Treatments in organic solutions were carried out at room temperature, whereas aqueous solutions were treated at 50°C in order to improve reactions kinetics.

After different soaking times (from 5 to 15 days) the powders were filtered for solvent separation. In some case, samples had to be centrifuged (4000 r.p.m. during 8 minutes) to separate the supernatant from the powders, because of the diminution of crystallite size after soaking treatment. Then, treated powder samples were carefully washed several times with deionized water and ethanol and dried in an oven at 100°C for one night before carrying characterizations in order to follow the soaking effect on the grains.

The resulting powders were systematically characterized by Scanning Electron Microscopy (SEM) and Energy Dispersive X-Ray Spectroscopy (EDS), Powder X-Ray Diffraction (P-XRD), Raman and Fourier-Transformed Infrared spectroscopy (FTIR). Their thermal evolution after soaking treatment was followed by thermogravimetric analysis (TGA).

### **2.3. Characterization techniques.**

All the powdered samples were characterized by powder XRD at room temperature using a Bruker D8 Advance diffractometer, with a Bragg-Brentano geometry using monochromated  $\text{CuK}\alpha$  radiation in the range  $2\theta=(3-60)^\circ$  with  $0.02^\circ$  step and 1 second/step. The lattice parameters evolution (on the basis of the initial lattice parameters) of the grains after soaking treatment was followed after refinement using the CHECKCELL software[59].

To carry out the SEM experiments, small amount of the powder samples were placed on a carbon tape and introduced in a field-emission gun microscope Hitachi S4700 equipped with an Energy-dispersive X-Ray detector, operating at 20kV electron beam energy. The EDS

measurements results were obtained from average of several different points acquisitions.

The TGA/TDA analyses have been performed on washed and dried powders, and were carried in a Shimadzu DTG-60M from room temperature to 600°C under air at 5°C/min heating rate.

FT-IR spectra were collected with a Perkin Elmer spectrometer supplied with an attenuated total reflectance (ATR) accessory, under pressing in order to get a good optical contact between the crystal and the film. The samples were analyzed by means of diamond crystal prism. The crystal geometry was a 45° triangle with mirrored angle faces. ATR spectra are shown with an absorbance scale corresponding to  $\log(R_{\text{reference}}/R_{\text{sample}})$ , where R is the internal reflectance of the device. The spectra were recorded between 4000 and 400  $\text{cm}^{-1}$  with 4  $\text{cm}^{-1}$  spectral resolution. For each spectrum, 10 scans were averaged. Air was taken as a reference.

Raman spectra were recorded at room temperature with the 647.1 nm excitation line from a Spectra Physics krypton ion laser with less than 2 mW laser power. The beam was focused on the samples using the microscopic configuration and the scattered light was analyzed with an XY800 Raman Dilor spectrometer equipped with an optical multichannel detector (liquid nitrogen-cooled charge coupled device). The spectral resolution was approximately 0.5  $\text{cm}^{-1}$  in the investigated 15-1500  $\text{cm}^{-1}$  wavelength range.

### **3. Anion exchange in aqueous solution treatments.**

The first tests of a possible mobility of the interlayer ions and consequently show a possible anion exchange in our phases, were made in aqueous solutions. Several solutions were prepared with concentration of 1M of different anions, for the oxybromides treatment. For that purpose, barium acetate ( $\text{BaC}_2\text{H}_3\text{O}_2$ ), barium nitrate ( $\text{BaNO}_3$ ), sodium sulfate ( $\text{Na}_2(\text{SO}_4)$ ) and sodium carbonate ( $\text{Na}_2(\text{CO}_3)$ ) were weighed and introduced in a vessel with 50ml of water to form the soaking medium in which 0.2 grams of oxybromides powders were soaked. A control test with solely deionized water was also performed with the same soaking conditions of time and sample quantity.

Figure I.4 presents the resulting XRD patterns of the powders soaked in carbonates, acetates and sulfates solutions after one week treatment. Treatments with carbonates and acetates lead to a complete decomposition of the original phases, even at room temperature, after 1 week of soaking and powder XRDs show mainly the presence of barium carbonate

(after acetates treatment there are still two reflections from the original phase). Same kind of behaviour is observed with sulphate aqueous solution, leading to barium sulphate after treatment. In the same way numerous tests were realized with different voluminous carboxylic acids as phtalic, succinic, adipic or malonic acids and some amino acids (serine; alanine or glycine) as well, in different proportions. In all cases, the presence of  $Ba^{2+}$  makes the oxybromide compounds very sensitive to carbonation, and leads to their decomposition.

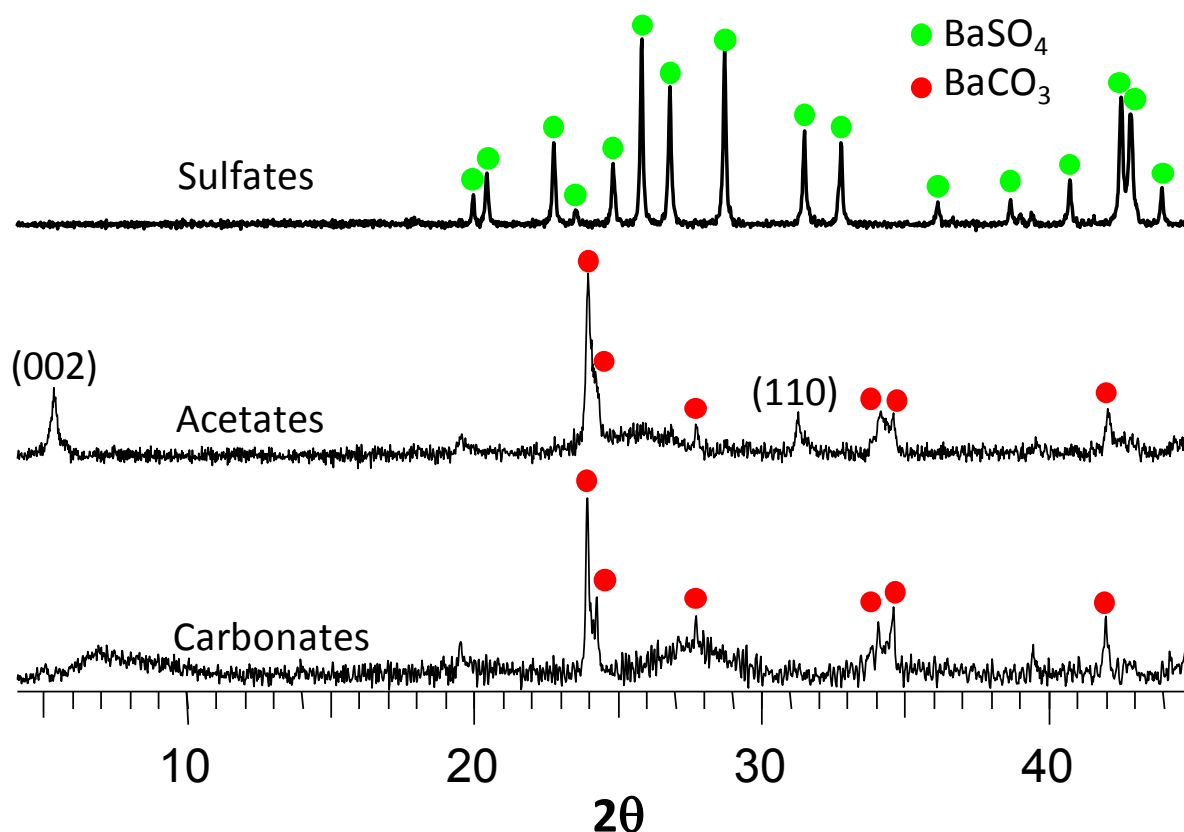


*Figure I.4. Powder-XRD patterns of 14H-  $Ba_7Co_6BrO_{17}$  after 1 week of soaking treatment carbonates, acetates and sulphates.*

This result is explained by the high anionic affinity of  $Ba^{2+}$  for poly-charged anions (carbonates, sulphates) which easily react with the barium ions, thus destroying the original phase.

Then, monovalent anions such as nitrates, with a lower charge than the groups mentioned before and possibly less reactive with  $Ba^{2+}$  ions, can be envisaged as better candidates for the anionic substitution. Unlike the previous cases, powders soaked in nitrate solutions and those soaked in deionized water keep the parental structure but with light lattice parameters modifications, as we will see hereinafter.

Behaviour of 14H and 18R oxyhalides are quite similar, so even if we have made all

the tests on both phases, we finished by concentrate our efforts in the complete characterization of the 14H- $\text{Ba}_7\text{Co}_6\text{BrO}_{17}$ . Thus, in this chapter we will just show the results related to this phase, those of 18R-  $\text{Ba}_6\text{Co}_5\text{BrO}_{14}$  can be consequently extrapolated.

### 3.1. Treatment in pure water.

Because we are working in water solutions, we have checked the effect on the samples of soaking in pure water. After treatment, the powders have been separated from supernatant by centrifugation and dried following the protocol detailed previously. The recovered solution is clear and colourless and the mass of collected solid corresponds to the initial one, even if the grains are significantly smaller. There is no evidence of a possible dissolution process. SEM pictures of the grains after treatment in water show an evident crystal attack and the size reduction, consequence of the mechanical effect of the ultrasonic treatment, as it can be seen on figure I.5.

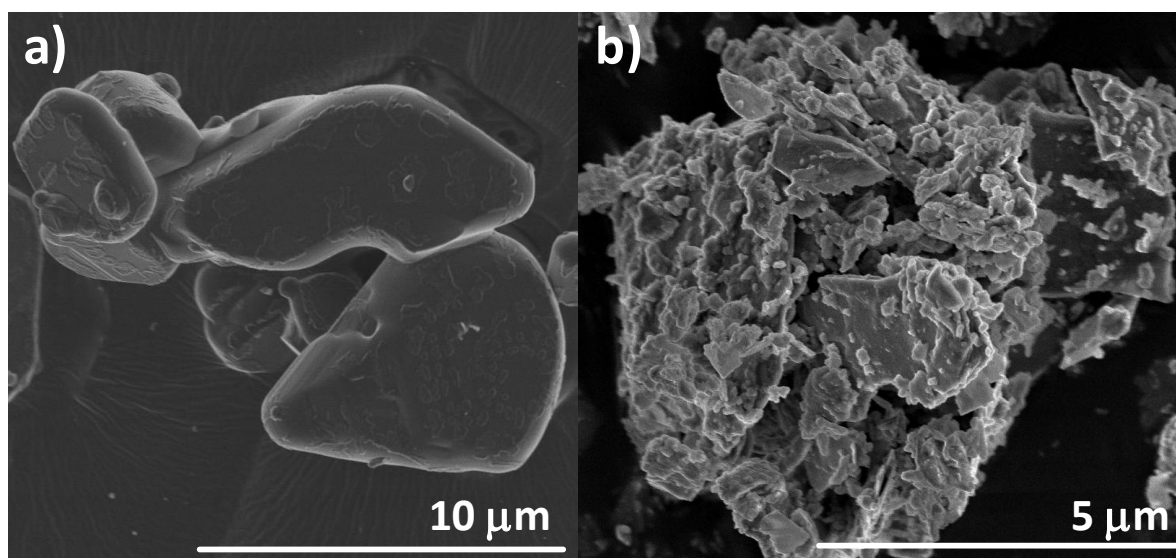


**Figure I.5.** SEM images of 14-H  $\text{Ba}_7\text{Co}_6\text{BrO}_{17}$  as prepared (a), and after 10 days in deionised water treatment.

The EDS analysis performed on several points give a lower content of bromine present in the grains as presented in table I.1. This slight bromine diminution is convenient because if we take in account the neutrality of the water molecule, a process with a high bromine decrease could involve a cobalt oxidation in the perovskite blocks.

**Table I.1.** EDS analysis results before and after soaking treatment in deionised water for 1 month .

<b>14H-Ba<sub>7</sub>Co<sub>6</sub>BrO<sub>17</sub></b>			
	% atomic		
	<b>Ba</b>	<b>Co</b>	<b>Br</b>
<b>Theoretical</b>	50,0(0)	42,8(5)	7,14
<b>Initial compound</b>	49,(9)	42,(9)	7,(2)
<b>Deionized water</b>	49,(8)	45,(3)	6,(5)

Evolution of the Ba<sub>7</sub>Co<sub>6</sub>BrO<sub>17</sub> under water treatment was controlled at several times (5, 10 and 30 days). Figure I.6 shows powder-XRD of the Ba<sub>7</sub>Co<sub>6</sub>BrO<sub>17</sub> phase after soaking 5, 10 days and 1 month treatment in water compared to the original phase. We can observe that treatment time effect is weak since the diffractograms remain superimposable after 10 days of soaking treatment.

Nevertheless, diffractograms show a broadening of the diffraction peaks which can be correlated to a decrease of grain size and a loss of crystallinity. However, we can still observe the (110) peak, slightly affected by the treatment, and the two first (00*l*) reflections, which are shifted toward lower angles values.

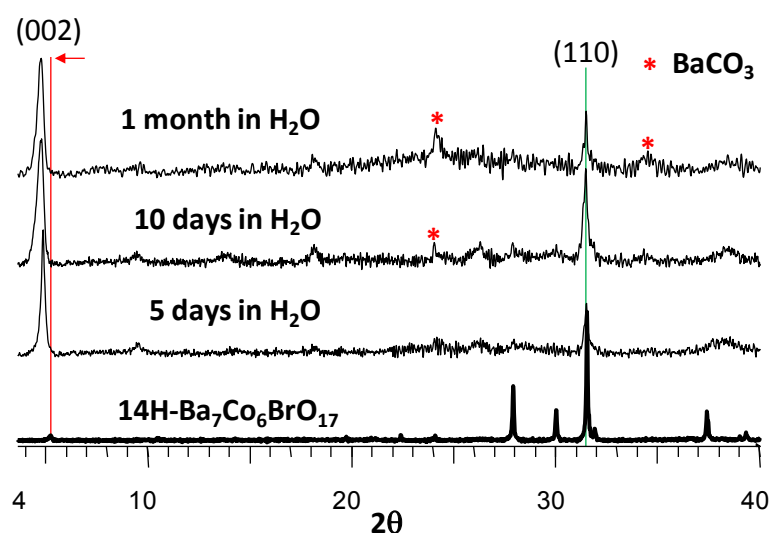


**Figure I.6** Powder XRD comparison of soaked powders after different time treatment in pure water. The barium carbonate impurity appearing after 10 days of treatment is pointed by stars.

The conservation of the (110) reflection indicate the preservation of the “*in plane*” initial block structure. On the other hand, both of the (00*l*) reflections show exaggerated intensity, because of a strong preferential orientation of the grains in the stacking direction.

Peaks position allowed us to perform a unit cell refinement of the different soaked phases with CHECKCELL software [59], in order to follow the lattice parameter evolution, compared to the initial values of the original phase. The shift observed on (00*l*) peaks corresponds to an enlargement of the *c* parameter, which can be potentially induced by a modification of the [Ba<sub>2</sub>O<sub>2</sub>Br]<sup>-</sup> interlayer. After parameters refinement, the *c* parameter evolves from the 33.594 Å of the original phase to 38.515 Å after soaking in water for 10 days, which remains unchanged after longer treatment. This enlargement supposes an increase of about 2.45 Å of the interlayer space. The *c* parameter increase can be correlated to a possible water molecules insertion in the interleaves, even if a carbonation of the phase cannot be excluded, as shows the presence barium carbonate impurity observed after 10 days of treatment. Considering a water diameter size of around 2.7 Å [60] it would suppose the insertion of a layer of water of about one molecules thick per interlayer space.

To follow the molecular insertion process, FTIR and Raman vibrational spectra have been recorded on all dried powders after treatment, and compared to the original compound. Spectra of the original phase and the soaked phases are given in figure I.7 (a). One must mention that potentially, the quantity of inserted molecules is low compared to the overall atomic structure, implying that generated bands by those molecules will be less intense than those corresponding to the original phase.

For the original sample, the IR spectrum shows absorptions bands at 460 and 535 cm<sup>-1</sup>, see figure I.7 (a), which correspond to the metal–oxygen (ν<sub>Co–O</sub>) stretching vibration modes. According to literature[58, 61], sharp band vibration observed at 858 cm<sup>-1</sup> can be attributed to characteristic ν<sub>1(CO<sub>3</sub>)</sub> bonding, and the two bands observed at 1415 cm<sup>-1</sup> and 1460 cm<sup>-1</sup> correspond to the split of the degenerate antisymmetric mode existing in free CO<sub>3</sub><sup>2-</sup> (D<sub>3h</sub> symmetry [62]), due to its punctual symmetry lowering in the solid. This suggests that significant amount of CO<sub>3</sub><sup>2-</sup> anions is already present in the starting bulk material, confirming the easy carbonation of the [Ba<sub>2</sub>O<sub>2</sub>Br]<sup>-</sup> layers, even if surface carbonates are probable but in a weaker amount.

For powders after water treatment, also shown in figure I.7 (a), small large band is observed in the (3500-3000) cm<sup>-1</sup> domain corresponding to free water molecules, having low interactions with the lattice and without strong geometric restrictions. This shows the presence of slight quantity of water molecules adsorbed on the grains surface. However, the presence

of a broad band around  $1000\text{ cm}^{-1}$ , corresponding to the footprint of rotation-vibration bands of hindered water [63] confirms the existence of water molecules in strong interaction with the structure and not only adsorbed on the surface.

The assignation of peaks in Raman spectra to a specific mode is not straightforward, and in our case valuable information is obtained by comparison between observed bands and available data in the literature. As show on Figure I.7 (b), Raman spectrum of original  $\text{Ba}_7\text{Co}_6\text{BrO}_{17}$  presents a set of at least five vibrational modes between  $230$  and  $700\text{ cm}^{-1}$ , one intense at  $610\text{ cm}^{-1}$  and four weaker signals at  $490$ ,  $400$ ,  $300$  and  $210\text{ cm}^{-1}$ . If we base on similar assignments in the literature for cobalt in hexagonal perovskite [64], the more intense band observed at  $610\text{ cm}^{-1}$  could arise from the symmetric stretching of the cobalt–oxygen octahedra.

This band is kept in the powder samples after soaking treatments in water. The very small evolutions observed after soaking process confirm that the global cobalt environment is slightly affected. However, after water treatment, an additional peak is seen at  $670\text{ cm}^{-1}$  and the one at  $610\text{ cm}^{-1}$  greatly decreases. This could correspond to a shift of this last one, related to the water molecules insertion, inducing some local lattice distortions.

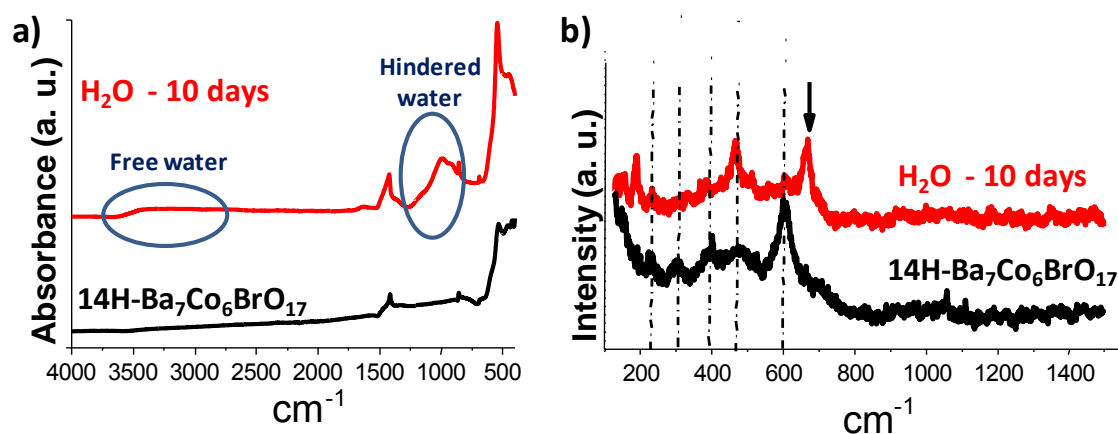


**Figure I.7.** Compared FTIR (a) and Raman (b) spectra between original 14H- $\text{Ba}_7\text{Co}_6\text{BrO}_{17}$  and powder soaked in water for 10 days.

Thermogravimetric analyses (TGA) of the original  $\text{Ba}_7\text{Co}_6\text{BrO}_{17}$  and the samples after aqueous treatments are presented in figure I.8. The original cobaltite shows a weight loss around  $400^\circ\text{C}$  of about 2% which can be related to the decomposition of the carbonates groups present in the interlayer. After water treatment, the weight loss of the sample is regular till  $200^\circ\text{C}$  showing the presence of adsorbed water on surface, slightly seen by IR spectroscopy. Then the evolution presents a plateau and a first step between  $300$  and  $500^\circ\text{C}$ ,

which could be attributed to lattice carbonates and water loss, corresponding to a total loss of about 4%. A second step is observed at 520°C which correspond to the phase decomposition confirmed by XRD of the sample after TGA. The global weight loss is of about a 12.5%. If between 250 and 500°C we consider interlayer inserted water only, that would correspond to 4% of weight loss. But taking into account the 2% weight loss in the original phase caused by originally inserted carbonates, and considering it unchanged after water treatment because there are no changes in the intensities of carbonate bands in IR spectra; the weight loss relied directly with the interlayer water it is around 2%

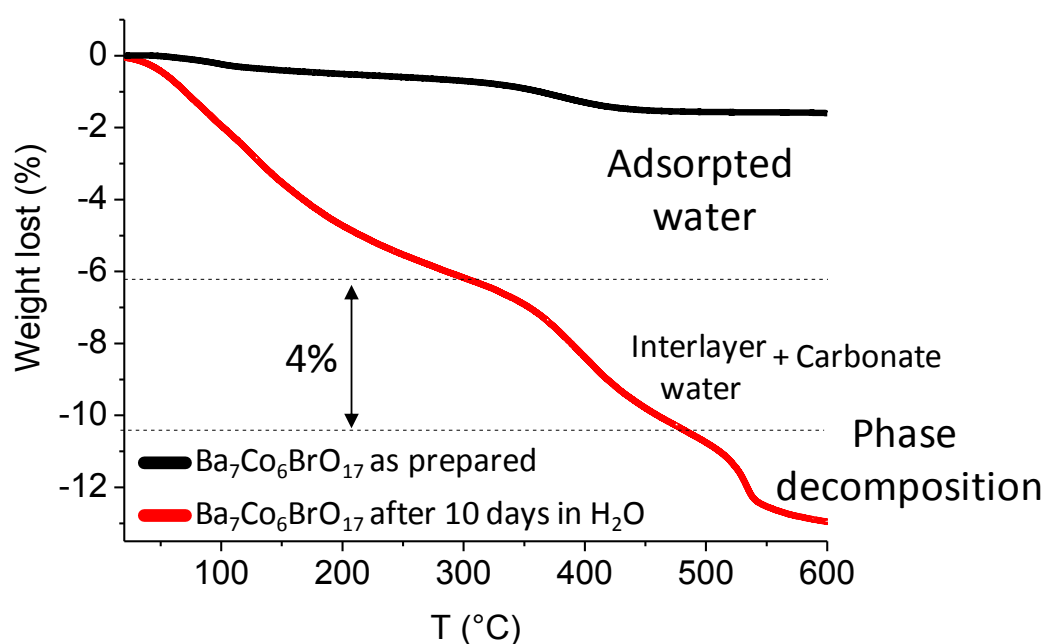


**Figure I.8.** TGA of original powder (black) and powder after 10 days in water (red).

An easy calculus can be done allowing us to establish an approximate number of water molecules inserted by unit cell, considering  $Ba_7Co_6Br_{1-x}O_{17} \cdot yH_2O$  and deducing the remaining bromide content from EDS analyses. For this purpose, we just considered the weight loss corresponding to the interlayer water. The approximate calculus would lead to an insertion of  $\sim 2$  water molecules per  $[Ba_2O_2Br_{1-x}]$  interlayer.

This approximate calculus match well with the result obtained by XRD where the difference interlayer distance calculated by the (00*l*) reflections shift corresponded to a layer of one water molecule width. Tacking in account that *a* parameter of the original unit cell ( $a=5.661(1)$  Å) is slightly affected after treatment and only *c* parameter is modified, we can assume the hypothesis of two water molecules inserted in series by interlayer.

### 3.2. Nitrates treatment.

After nitrate treatment, as in water soaking case, there is no evidence of a dissolution process. The SEM images of the phase, before and after powder soaking, are shown in figure I.9. The initial well-shaped faces are damaged after soaking and a clear delaminating effect with creation of lamellar sheets is evidenced, conforms to ion exchange process

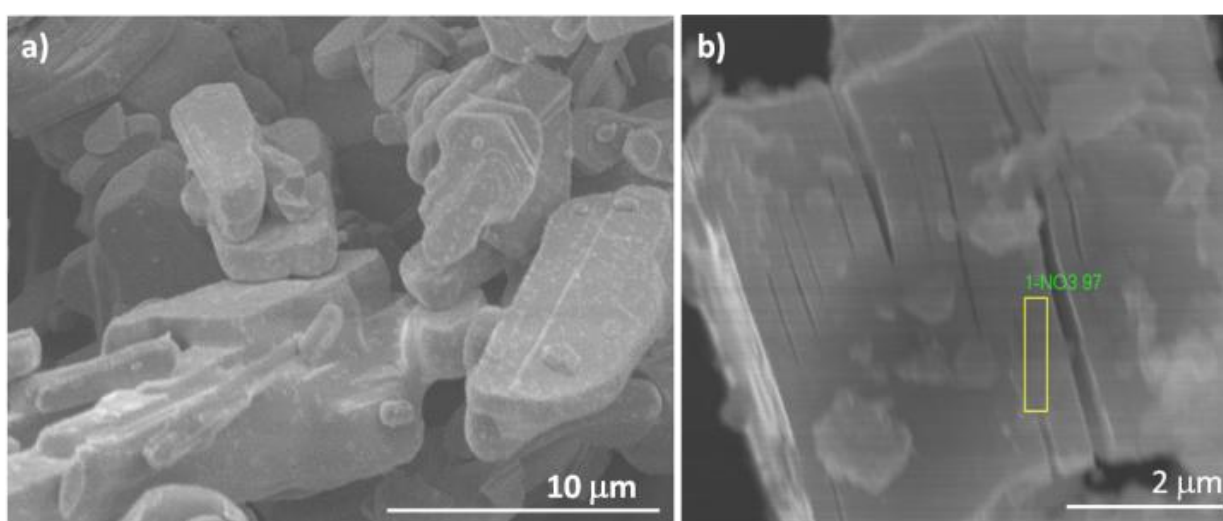


**Figure I.9.** SEM images of (a) the original phase 14-H Ba<sub>7</sub>Co<sub>6</sub>BrO<sub>17</sub> and (b) after nitrates solution treatment.

In addition, EDS analyses on crystals show a significant decrease of the bromine content compared to the original composition. In table I.2, are given the average atomic proportion measured from several crystals which confirms bromide ions removal out the structure, allowing to envisage an exchange process.

**Table I.2.** EDS analysis results before and after soaking treatment in nitrate solution for 2 weeks.

<b>14H-Ba<sub>7</sub>Co<sub>6</sub>BrO<sub>17</sub></b>			
	<b>% atomic</b>		
	<b>Ba</b>	<b>Co</b>	<b>Br</b>
<b>Theoretical</b>	50,0(0)	42,8(5)	7,1(4)
<b>Initial compound</b>	49,(9)	42,(9)	7,(2)
<b>Nitrates</b>	49,(7)	49,(6)	0,(7)

In the nitrates treatment case, the time-dependent evolution is more important than in the water case, as it can be seen on XRD of the phase after soaking for one and two weeks in nitrates solution, see figure I.10. After one week we can observe on XRD the apparition of a second phase, noted with red asterisks above the peaks on figure I.10. It corresponds to the 12-H BaCoO<sub>2.6</sub> phase whose structure possesses similar individual perovskite blocks than Ba<sub>7</sub>Co<sub>6</sub>BrO<sub>17</sub>, but without the [Ba<sub>2</sub>O<sub>2</sub>Br]<sup>-</sup> interlayer, see figure I.3 (e). This phase can be considered as a reaction product after removal of the central bromide layers in Ba<sub>7</sub>Co<sub>6</sub>BrO<sub>17</sub>. It highlights the possibility of significant removal of Br<sup>-</sup> anions and recombination between the blocks. However, this phase is slightly presents after a longer treatment time (2 weeks) and could be considered as a by-product, being an intermediate phase in the exchange process. Similar evolution is not observed starting from the 18R-Ba<sub>6</sub>Co<sub>5</sub>BrO<sub>14</sub> compound for which the related 5-H BaCoO<sub>3-δ</sub> could be expected.

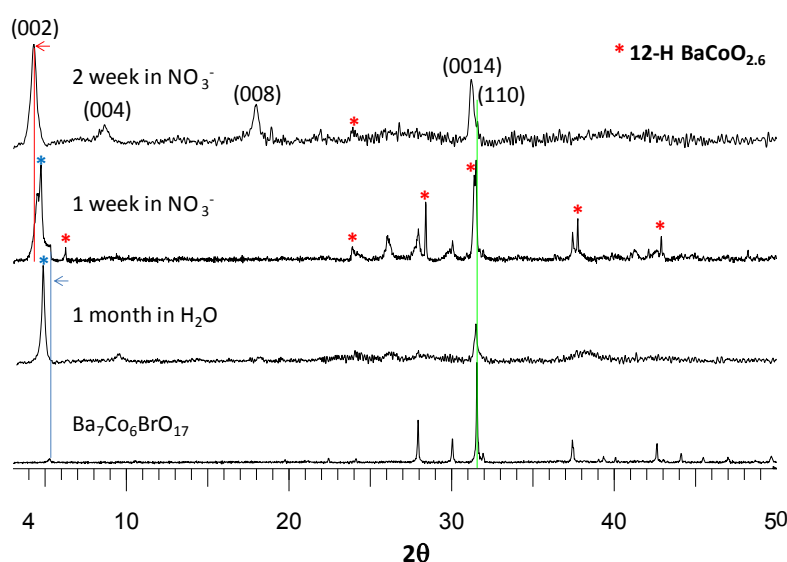


**Figure I.10.** Experimental P-XRD patterns of Ba<sub>7</sub>Co<sub>6</sub>BrO<sub>17</sub> as prepared, powder after soaking 1 month in H<sub>2</sub>O, 1 week in 1M nitrate solution and 2 weeks in 1M nitrate solution.

Additionally, for the shortest time of treatment (one week), the 002 peak is not only shifted but are also split in two, involving a biphasic swelled phase. We can note the position of the most intense peak, marked with a blue asterisk in figure I.10. It corresponds to the 002 peak position observed after soaking in water, meaning that parameter of one phase coincide with the  $c$  parameter of 38.515 Å obtained in the case of the water treated phase. Nevertheless, after two weeks the (00l) peaks of the powder are completely shifted towards lower angles, corresponding to one phase only, with a  $c$  parameter of 41.627 Å after refinement.

Thus, we can reasonably emit hypothesis of an exchange process in 2 stages, involving a biphasic process while anionic exchange occurs. Working in aqueous medium, a possible hydration of the interleaves can be considered as a first step, before the nitrates molecules enter in the structure.

Considering the unit cell of the original phase, the swelled phases after water and nitrates treatment present an interlayer space of 5.16 and 6.71 Å respectively, against the 2.69 Å in the initial phase. One must notice that the interlayer increment of about 150% is the same for the two oxo-bromides, showing a similar behavior. Table I.3 summarizes the different refined lattice parameters after soaking.

**Table I.3.** Refined lattice parameters of 14-H  $Ba_7Co_6BrO_{17}$  corresponding interlayer distances and EDS analysis results after two weeks of nitrates treatment.

<b>Ba<sub>7</sub>Co<sub>6</sub>BrO<sub>17</sub></b>					
	Lattice parameters		Interlayer distance		
	<b>c (Å)</b>	<b>d (Å)</b>	% atomic		
			<b>Ba</b>	<b>Co</b>	<b>Br</b>
<b>Theoretical</b>	33.567(2)	2.67(8)	50.00	42.85	7.14
<b>Experimental</b>	33.59(4)	2.6(9)	49.(9)	42.(9)	7.(2)
<b>Nitrates</b>	41.62(7)	6.7(1)	49.(7)	49.(6)	0.(7)

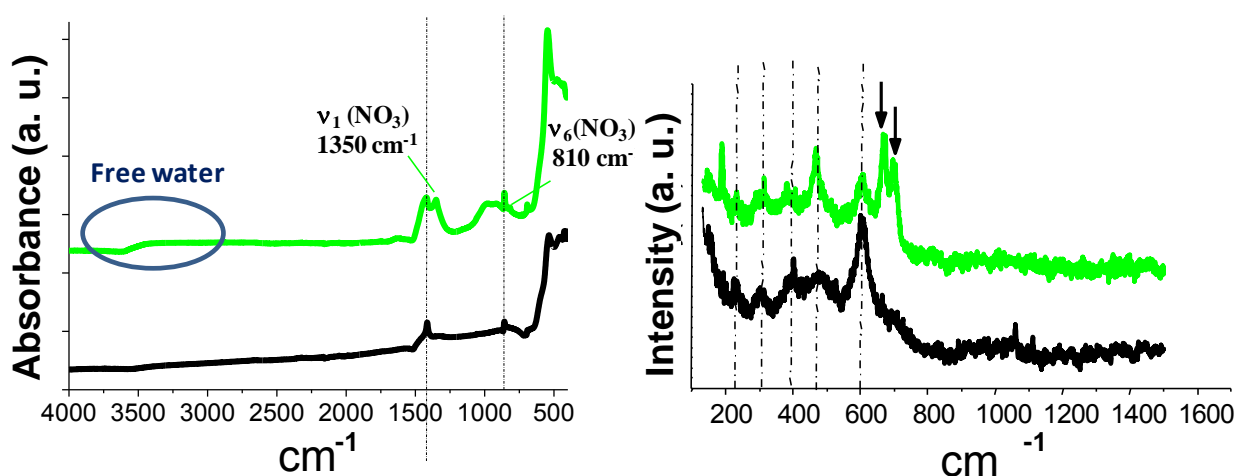
  

<b>Ba<sub>6</sub>Co<sub>5</sub>BrO<sub>14</sub></b>					
	Lattice parameters		Interlayer distance		
	<b>c (Å)</b>	<b>d (Å)</b>	% atomic		
			<b>Ba</b>	<b>Co</b>	<b>Br</b>
<b>Theoretical</b>	43.166(6)	2.68(5)	50.00	41.67	8.33
<b>Experimental</b>	43.28(3)	2.7(2)	50.(5)	41.(0)	8.(5)
<b>Nitrates</b>	55.62(4)	6.8(4)	51.(9)	46.(6)	1.(5)

After nitrate treatment, FTIR spectra of the soaked powders were recorded and are shown in figure I.11. The characteristic antisymmetric stretching vibration  $\nu_4$ , symmetric stretching vibration  $\nu_1$  and the fundamental bending vibration  $\nu_6$  of nitrates are presents at 1480, 1350 and 810  $\text{cm}^{-1}$  respectively.

Similarly to the carbonate, the  $\nu_4$  and  $\nu_1$  vibrations correspond to a split of the degenerate antisymmetric stretching vibration E, of the free  $\text{NO}_3^-$  nitrate ion, characteristic of a bi- and mono-dentate  $\text{NO}_3$  group [65, 66] and suggest strong interactions with the crystal lattice.

With respect to Raman spectroscopy, we observe the same peak shift from 610 to 670  $\text{cm}^{-1}$ , than in the water case, relied to some induced local lattice distortions. One more band appears at 700  $\text{cm}^{-1}$ , which could be attributed to the  $\nu_3$  bending vibration of the nitrate group, active in Raman [67].



**Figure I.11.** a) FT-IR and b) Raman spectra of the original phase (black), and after 2 weeks in nitrate solution (green).

TGA results presented in figure I.12 show a global weight loss of 17.2%, of 5% higher than the one observed after water treatment. In this case, as in the previous one, the curve shows a first slope from ambient temperature to 350°C which correspond to surface adsorbed water and goes to a weight loss up to a 6% . From 350°C to 450°C a marked weight loss is observed until weight stabilization around 500°C. Taking account the information obtained by XRD, IR spectroscopy and EDS analysis, it is reasonable to imagine an interlayer where the bromine is replaced by the nitrates anions but also by water molecules. Considering similar quantities of carbonate present in the sample (verify by FTIR) as in the phase before treatment, and the same number of water molecules inserted as after water soaking, the quantity of weight loss due to nitrates molecules is of about a 7%. This percentage leads to an

insertion of 2 nitrate anion inserted in the interlayer. Taking in account that nitrate molecule has a diameter of approximately 3.3 Å [68], the TGA results are in agreement with the  $c$  parameter enlargement found by XRD if we imagine 2 nitrates ions inserted, arranged in series in the interlayer space.

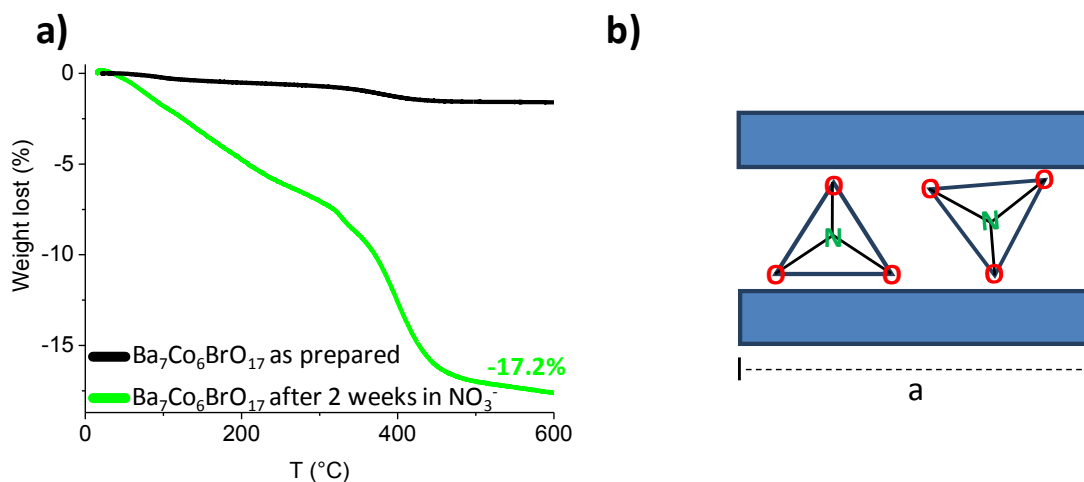


**Figure I.12.** TGA analysis of  $Ba_7Co_6BrO_{17}$  after 2 weeks soaked in 1M nitrate solution (a). Inter-block nitrate insertion (b).

• XANES study of the powders after nitrates treatment:

The mixed oxidation state in cobaltite blocks could allow the insertion of two nitrate ions replacing a bromine anion with a partial oxidation of the cobalt if the charge substitution is not complete. To follow a possible oxidation of the cobalt after treatment, XANES spectrum has been recorded in reflection mode at the Co-K edge on DIFFABS beamline at synchrotron SOLEIL and it is presented in figure I.13 (a). The fine structures of both edges are very similar; which is confirmed by the superimposition of the second derivative curves, see figure I.13 (b). Spectra of the phase before and after soaking show same pre-edge (a) assigned to transitions from the core 1s level to unoccupied 3d state of the cobalt, characteristic of cobalt in tetrahedral environment and in distorted octahedral.[69-71] The white lines positions, characteristic of the oxidation degree of the metal, are in both case at the same position in energy scale implying no changes of the cobalt valence after treatment.

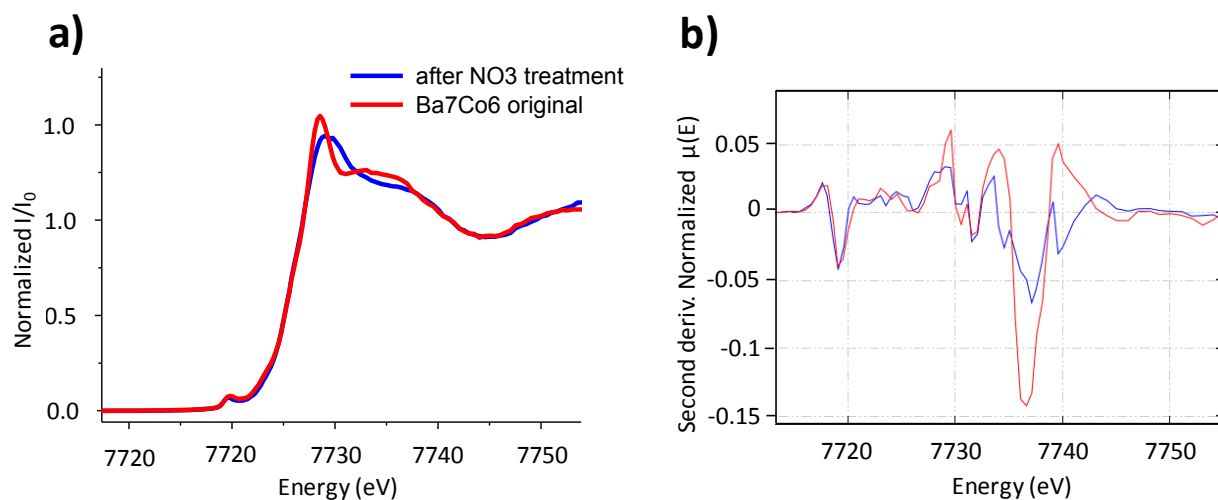


**Figure I.13.** XANES spectra of  $Ba_7Co_6BrO_{17}$  as prepared (red) and after 2 weeks soaked in nitrates solution.

The ionic exchange occurring during the soaking process doesn't seem to affect directly the cobalt environment. However the enlargement and the lowering of intensity of the white line on the XANES spectra after nitrate treatment lets to envisage a partial amorphization of the phase because of the damages on crystals and the beginning of phase decomposition. A linear combination fitting has been made with Athena software, using as reference the original phase before treatment mixed with  $Co_3O_4$  as impurity. This fit was done using normalized  $\mu(E)$ , constraining the standards to be 100 percent of the final phase and with fixed  $E_0$  values to their original values, see figure I. 14. It give a percentage of 35% of  $Co_3O_4$  and 65% of original phase, showing a slight degradation of crystals, with the presence of a disorganized phase containing cobalt and not seen by XRD.

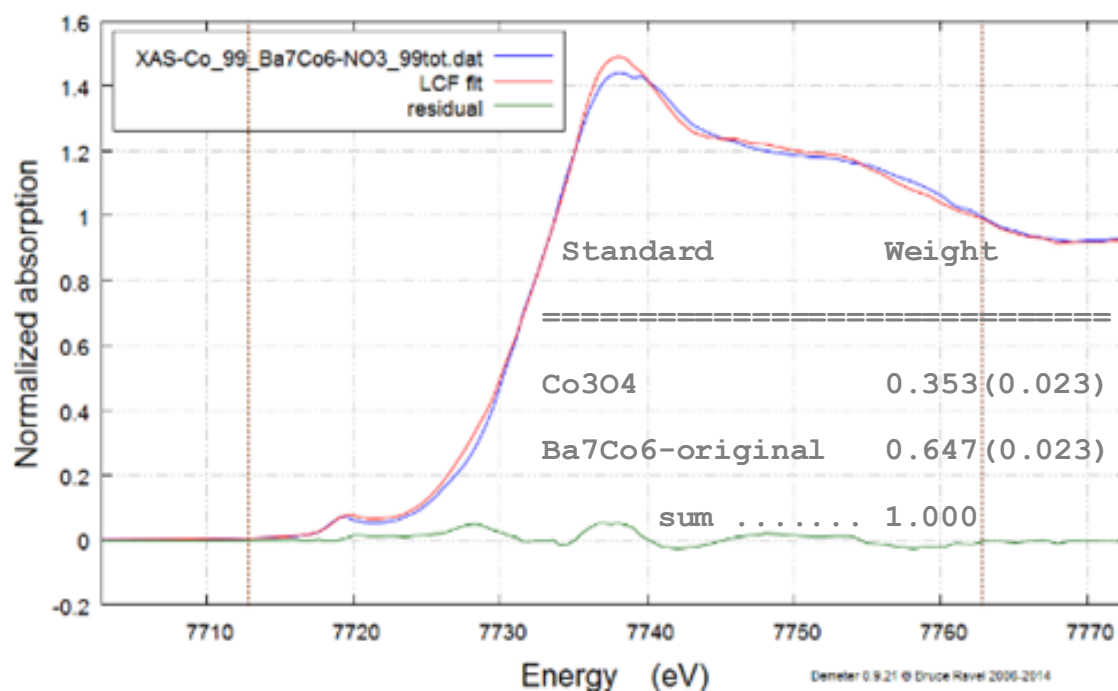


**Figure I.14.** Linear fit of the nanoflakes deposited on silicon substrate, using  $Ba_7Co_6BrO_{17}$  and  $Co_3O_4$  as references

### 3.3. Conclusion.

The results obtained after soaking treatment in deionized water, as well as in the nitrates soaking treatment, demonstrate the capacity of the structure to enlarge its interlayer. However, MEB images after soaking treatment show crystals degradation, with a subsequent loss of crystallinity, confirmed by XANES spectroscopy. In all cases, XRD, FTIR, Raman, and TGA results present reliable values which allow us to establish some hypothesis about the insertion process.

Results obtained after water treatment are consistent with the insertion of a couple of water molecules placed in series in interlayer space with a slight bromine content diminution.

After two weeks of nitrates soaking treatment, analysis show the possible exchange of the bromide ions in  $[Ba_2O_2Br]$  layer of the 14-H  $Ba_7Co_6BrO_{17}$  and 18R- $Ba_6Co_5BrO_{14}$ , for larger oxo-anions, like nitrate ions. Weight loss determined by TGA show a possible nitrate anion insertion which may imply oxidation states changes in cobaltite blocks.

However, their interactions with the network is high because, as suggested by IR spectroscopy, they are inserted rather as ligands than as free ions, limiting further exchanges against larger molecules. So, in order to continue the study of the structural compound behavior under soaking treatment, organic solvents (alcohols, formamide, DMF and DMSO)

have been tested for organic molecules insertion in order to enlarge the interlayer with molecules having less interaction with the lattice.

### **4. Organic molecule insertion and phase exfoliation.**

For exfoliation process, the main difference between the effect of aqueous solutions and the organic solvent used will be the electrostatic interactions generated in towards the interlayer space. As we just said before, the anionic exchange has been successfully realized by substitution of  $\text{Br}^-$  by the  $\text{NO}_3^-$  demonstrating the ionic mobility in the  $[\text{Ba}_2\text{O}_2\text{Br}]$  double layer, however, the new created bonds are too strong and don't allow to make further transformations which could lead to the complete delamination of the hexagonal perovskite blocks. Because of this, we carried out different tests to assess viability to insert a neutral organic molecule in the interlayer. The target is to obtain a similar enlargement of the  $c$  parameter than in the ionic exchange case, but without establishing strong bonding between the blocks, which might lead to a possible “flakes” exfoliation. The molecule insertion will leads to the enlargement of the inter-blocks distance towards a critical point where the attractive forces between the blocks will be completely broken, allowing to create, theoretically, a suspension of  $[\text{Ba}_7\text{Co}_6\text{O}_{17}]^+$  nanoflakes. Nevertheless not all organic molecules will have the capability to reach this critic point without decomposition of the cobaltite blocks.

Taking into account literature about organic molecules insertion in inorganic matrix or LDHs positive nanosheets exfoliation [72-76], organic solvents like Formamide, Dimethylformamide (DMF) or Dimethyl sulfoxide (DMSO) and alcohols as ethanol, propanol or butanol have been tested.

All these solvents present some common characteristics. They are polar solvents, with at least one functional group with high electron density. In general, the polar group wearing an electronic lone pair will try to be inserted in the interleave space and electrostatically will interact with the layers surface. Despite of this polarity all of them are neutrally charged, this will help to introduce the molecules in the interlayer space without establishing strong interactions with the network.

Similarly to the aqueous treatment, the powders were soaked in different organic solvents under stirring for a week at room temperature, centrifuged with intermediate ultrasonic treatment, dried in oven at  $80^\circ\text{C}$  and analysed. In that case we will start by

characterization of the soaked powder as we did just before. When turbidity is observed on solutions after centrifugation, a characterization of this colloidal suspension is done by Dynamic Light Scattering (DLS) and Zeta potential measurements. Transmission electronic microscopy (TEM) and Atomic Force Microscopy (AFM) was performed as well for the most promising results.

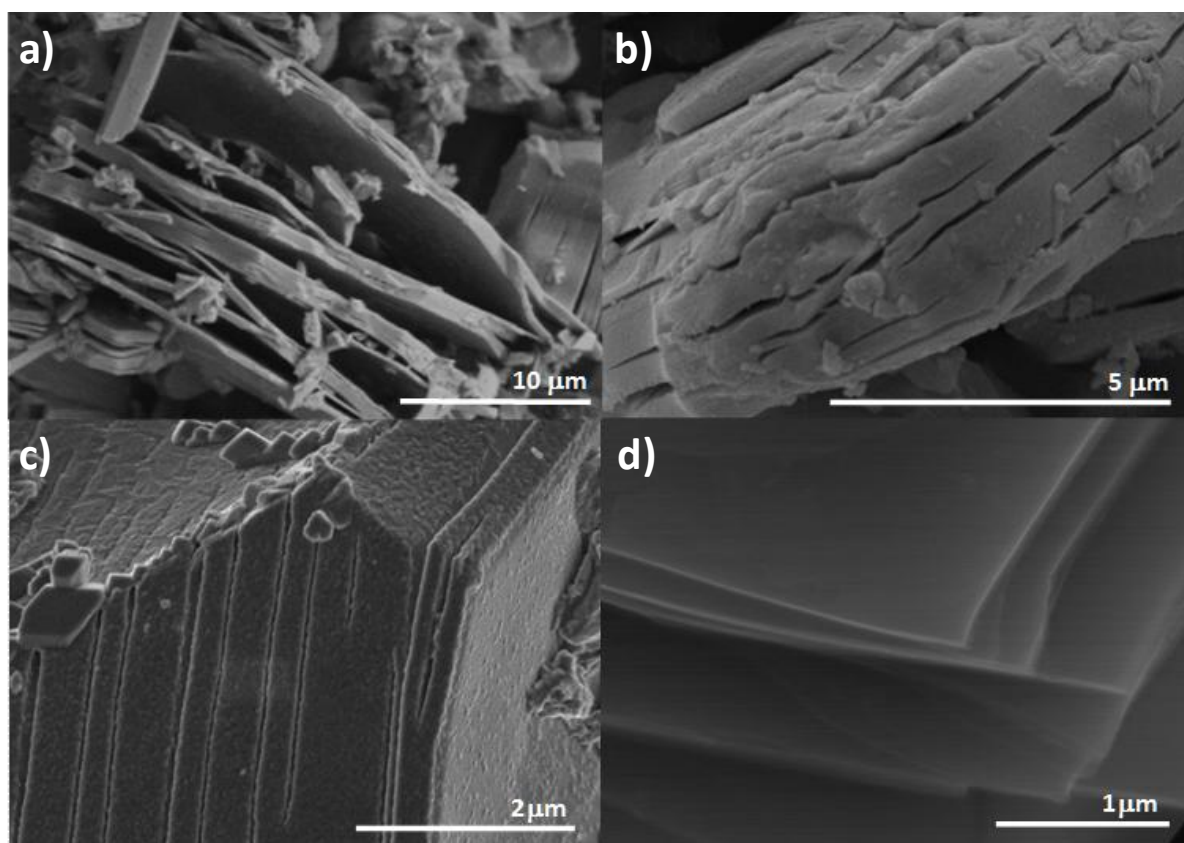
After a week treatment in the different organic solvents, the powders are highly attacked, the crystallite size decrease strongly, requiring a centrifugation for solvent separations.

### **4.1. Soaked powders characterization.**

In the case of formamide used as solvent, after a week treatment there is clear evidences of powder solubilisation. The solution obtained after centrifugation is clean of nanoparticles (no Tyndall effect) and strongly coloured, with almost no solid phase at the bottom of the centrifugation tube.

For ethanol and propanol samples, solutions are completely clear after the centrifugation, however, the solutions after DMF, DMSO or butanol treatment remains a bit cloudy, this latest being the most stable over time. This turbidity gave us the first hint about the possibility of “one step” exfoliation of the oxy-bromide phases, as we will see later.

The SEM images of the grains, before and after soaking, are shown figure I.15. Before soaking treatment, crystals present well-shaped faces, as presented previously in figure I.5 (a) and I.9 (a). After soaking we can clearly observe the effect of the delaminating process on crystal morphology, since crystals seem to open themselves like book pages and surface morphology presents corn-flake like crystallites, revealing their lamellar structure. It is also remarkable the different attack severities of the crystals, depending on the solvent functional groups. Crystals soaked in DMSO presents higher attack violence, see figure I.15 (a), which carries a more advanced degradation by carbonation as XRD will confirm. After DMF and propanol treatment the crystal aspect remains better conserved (figure I.15 b, c). In the propanol case, as in nitrates case, liquid phase is completely clean and transparent after centrifugation, while in the DMF case the solution present turbidity associated with a Tyndall effect. Butanol soaked powders present the cleanest and finest delamination effect, making the butanol the best candidate as solvent to obtain nanoflake suspensions of cobaltites by exfoliation process.



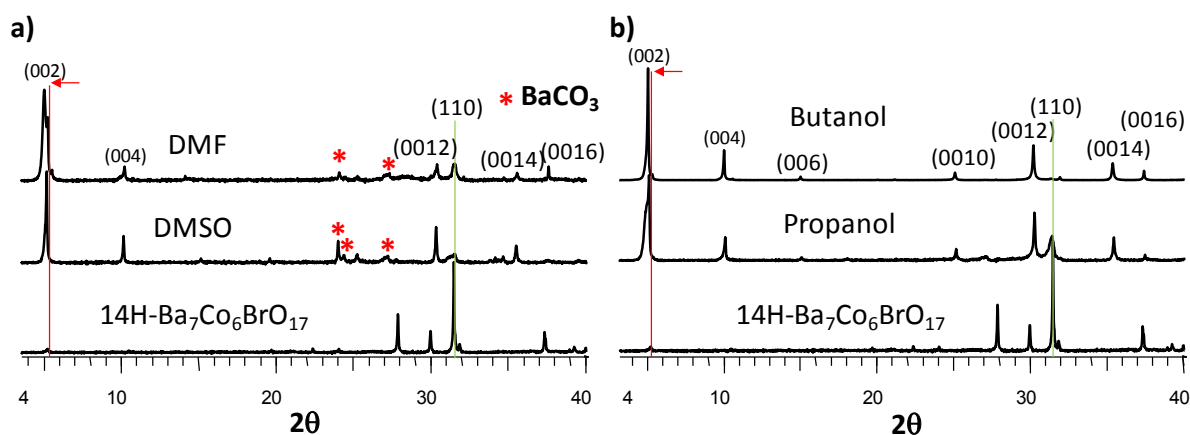
**Figure I.15.** SEM images of  $Ba_7Co_6BrO_{17}$  powders after different organic solvents soaking, a) DMF, b) DMSO, c) propanol, d) butanol.

Table I.4 gives the average values obtained from EDS analyses of several crystals, after soaking treatment in the different organic solvents. The results show a clear decrease of the bromine content in the soaked crystals, with respect to the original oxybromides ones, even if the bromine removal is not homogenous and depends of the organic solvent used. Nevertheless bromine removal is less efficient than in nitrates case. This fact can be related with the role of the different charge balance or with partial reaction completeness because of the reaction kinetics.

*Table 4. EDS analyses of soaked powders after 1 week treatment in different organic solvents.*

<b>Ba<sub>7</sub>Co<sub>6</sub>BrO<sub>17</sub></b>			
	atomic %		
	Ba	Co	Br
<b>Theoretical</b>	50.00	42.85	7.14
<b>Experimental</b>	49.89	42.91	7.21
<b>DMSO</b>	49.79	48.29	1.92
<b>DMF</b>	50.34	45.28	4.36
<b>Propanol</b>	50.48	44.14	4.61
<b>Butanol</b>	51.58	44.03	4.35

XRD patterns of Ba<sub>7</sub>Co<sub>6</sub>BrO<sub>17</sub> after the different treatments are presented and compared with the original phase in Figure I.16. In fact, figure I.16 (a) shows the patterns after DMSO and DMF treatment, whereas figure I.16 (b) shows the evolution after alcohols treatment.



**Figure I.16.** Powder XRD patterns of soaked powders compared to the original phase after DMF and DMSO (a) and propanol and butanol (b) treatments.

Both of DMF and DMSO solvents produce a similar effect in the original cobaltite phase. A broadening of diffraction peaks indicate a decrease in crystallite size, and the exacerbated relative intensities of the (00l) peaks, denote a clear preferential orientation along this direction, higher than in aqueous solution treatments. As consequence, all the peaks indexed are identified as (00l) reflections, except the (110) reflection which correspond to the most intense peak of the original phase and remains in the same position. All the (00l)

reflections shift toward lower angles which correspond to an enlargement of the  $c$  parameter.

A partial phase decomposition is observed in both DMF and DMSO samples with the apparition of  $\text{BaCO}_3$  peaks at  $2\theta$  between  $24^\circ$  and  $26^\circ$ , being in higher proportion in the DMSO case, which can be correlated to the stronger crystals degradation as previously observed by SEM.

In the case of ethanol no noticeable changes were observed on powder XRD and IR after soaking treatment. However, a clear evolution is observed after treatment in propanol or butanol as we can see in figure I. 16 (b). Here again, powder XRD diffractograms show a shift of the  $00l$  reflections to lower  $2\theta$  values, associated to an expansion of  $c$  parameter in the propanol case up to  $35.46\text{\AA}$  for 14-H  $\text{Ba}_7\text{Co}_6\text{BrO}_{17}$  and to  $35.48$  in butanol case as presented in table I.5.

**Table I.5.** Refined lattice parameters of 14-H  $\text{Ba}_7\text{Co}_6\text{BrO}_{17}$ , interlayer distances and distance increment after one week treatment in different organic solvents.

$\text{Ba}_7\text{Co}_6\text{BrO}_{17}$			
	Lattice parameters	Interlayer distance	Distance increment
	$c$ ( $\text{\AA}$ )	$d$ ( $\text{\AA}$ )	(%)
Experimental	33.59	2.70	0.00
DMF	35.47	3.63	34.44
DMSO	35.44	3.62	34.07
Propanol	35.46	3.63	34.44
Butanol	35.48	3.64	34.81

In all cases, the parental structure is kept with similar changes than those observed after the nitrate or water treatments. Nevertheless, little amounts of barium carbonate are created which indicate slight phase degradation.

IR spectra of the powders after 1 week soaking in organic solvents is compared in figure I.17. All of them present the expected vibration modes of the phase before treatment and the apparition of little bands for different wavelength values. In this way powders soaked for one week in DMSO shows the slight apparition of new bands at  $1080\text{ cm}^{-1}$  characteristic of the stretching  $\text{S}=\text{O}$  bond [77], nevertheless the broad band around  $3000\text{ cm}^{-1}$  and the very little intensities of the bands at  $1080\text{ cm}^{-1}$  give a doubt about a real molecule insertion. In the sample after DMF treatment, two new bands appear between  $1150\text{ cm}^{-1}$  and  $1200\text{ cm}^{-1}$  corresponding to the  $\nu_{\text{as}}$  and  $\omega$  ( $\text{CH}_3$ )-N vibrations and a third band is appeared at  $1400\text{ cm}^{-1}$  and it is assigned to  $\nu_{\text{s}}$ . [74, 78]

All the powders after alcohol treatment present similar behaviour, even if in the

propanol case the intensities of the new peaks are very low. We can observe the apparition of a peak around  $1350\text{ cm}^{-1}$  characteristic of  $-\text{CH}_3$  deformations and two little bands around  $1215\text{ cm}^{-1}$  and  $1150\text{ cm}^{-1}$  which might correspond to alcohols C-O bond elongation.[79]

Complementarily, Raman spectroscopy confirms that global cobalt environment after treatment is still very close from the original compound.

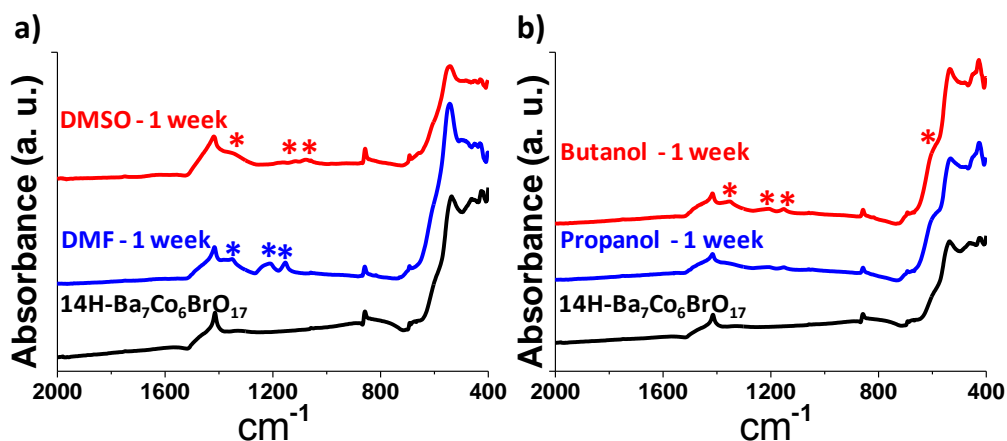


**Figure I.17.** TGA of the powders soaked in DMSO and DMF (a), and in alcohols (b).

Figure I.18 shows the XRD of the residue after TGA analysis of the sample after one week in butanol soaking. All the peaks of the diffractogram have been indexed, showing a mixture of three phases which are structurally related (figure I.3). The first identified phase is the 14-H  $\text{Ba}_7\text{Co}_6\text{BrO}_{17}$ , but with the original  $c$  lattice parameter instead of the swelled one presented before reheat. The recovering of the original oxybromide after calcination, indicates an incomplete bromide removal. The second identified phase corresponds to the 12H- $\text{BaCoO}_{2.6}$  already presented as a possible intermediate phase in the nitrate exchange reaction. This compound may correspond to the fraction of sample where the bromide has been removed. Finally, some peaks are indexed in a third phase, 2H- $\text{BaCoO}_3$ , made of infinite columns of face sharing  $\text{CoO}_6$  octahedra. This phase could be explained as a restacking of the hexagonal blocks resulting of the solvent attack.

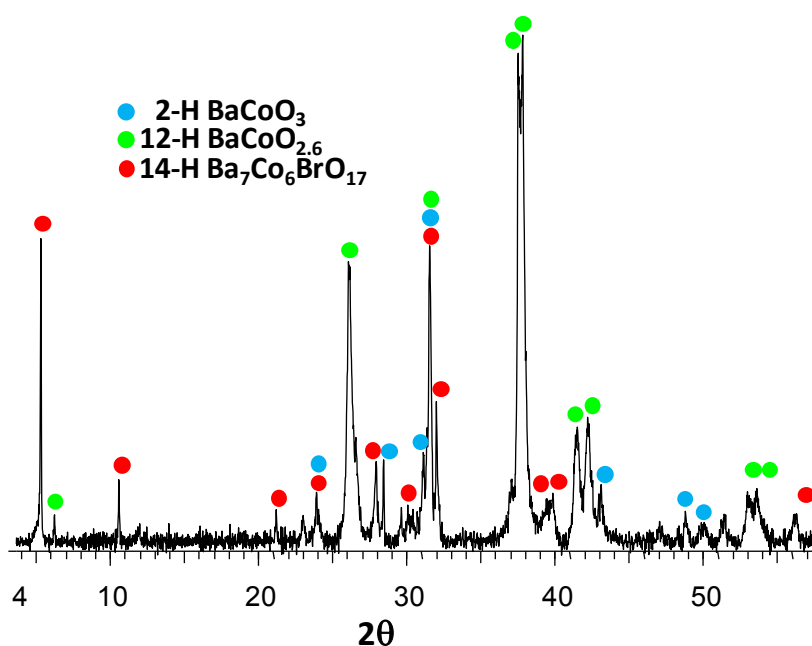


**Figure I.18.** XRD pattern of the residue after TGA of the powder soaked for 1 week in butanol.

All of these results are in agreement with an organic molecule insertion in the inter cobaltite layer space. Comparing to the aqueous solution treatments, powders after soaking in organic solvents, show a smaller enlargement of the  $c$  parameter, going from 35.44 Å in the DMSO case to 35.48 Å in the butanol case. Apparently this minor parameter variation does not prevent a clear delamination attack as seen on SEM images, or molecule insertion as shown with the vibrations band apparitions in FTIR spectra. In addition, process with organic solvents seems to be more efficient from the point of view of the exfoliation process. As predicted, polar molecules without a net charge are able to enter in the  $[\text{Ba}_2\text{O}_2\text{Br}]$  interlayer without establishing strong interactions with the structure. This insertion leads to a weakening of Ba-Br bonding interactions because of the spatial impediments of the molecules. Except for formamide, where a complete dissolution of the phase is observed, the interactions between the  $\text{Ba}^{2+}$  and the carbonate ions seem to be decreased in organic solvents, since the IR band of the carbonates are less visible compared to process done in presence of water. However, the exfoliation process causes a strong degradation of the grains and we must consider that part of the phase is decomposed because of a strong attack by the solvent. Thus, some barium atoms from the interlayer space can be released and maybe few cobalt atoms, even if for these latest, analyzes do not suggest the presence of cobalt oxide. In that case, when the powders are recovered in air the decomposed part of the phase reacts quickly and carbonation process occurs.

## 4.2. Exfoliation of 14-H Ba<sub>7</sub>Co<sub>6</sub>BrO<sub>17</sub>.

Three of the tested solvents (DMSO, DMF and butanol) present evidence of a "one step" exfoliation process. First hints were found after separation from the organic solvents and recovering of the soaked powders for further characterizations. In some cases, the liquid phase recovered after centrifugation presents an evident Tyndall effect, as we can observe in figure I.19. This effect corresponding to light scattered by particles in a fine suspension, can be considered as the first visual characterization of solutions containing nanoparticles since it occurs when particles size is between 1 and 1000 nm. We can remark a decreasing nanoparticles concentration in the supernatant colloidal suspension, going from the most concentrated butanol sample to the less concentrated one after DMF treatment, with same time of soaking and centrifugation (4000 rpm., 8 minutes). This supernatant suspension remains stable for more than 24h but with different evolutions over time depending of the solvent.

In butanol, the solid part slowly drop down at the bottom of the vessel after 24h, leaving an almost clear and clean liquid phase, 1 week after centrifugation. This "two phases" state can be reverted by sonication of the solution, coming back to a stable suspension.

On the other hand, DMSO and DMF colloid suspensions are less stable and lead to a slow solubilisation of the nanoparticles over time, shown after one week by an alteration of the solution color and by the loss of Tyndall effect, without any solid deposition at the vessel bottom.

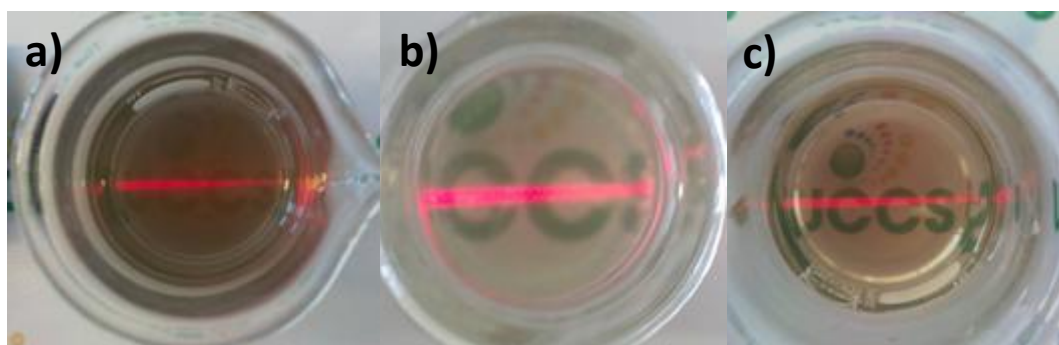


**Figure I.19.** Tyndall effect of colloidal suspension after centrifugation of powder soaked treated for a week in butanol (a), DMSO (b), and DMF (c).

Zeta potential measurements and Dynamic Light Scattering (DLS) were systematically carried on the three colloidal suspensions after centrifugation, for particles average size and charge determination. However, due to the low stability of DMF and DMSO colloids, deeper characterizations were performed only on well-stabilized butanol colloidal suspensions. These

further characterizations will allow a better knowledge of crystallinity, thickness and composition of these particles. For this purpose, transmission electron microscopy (TEM) with micro-EDS analysis has been performed, to check the particles crystallinity and composition, to determine bromide content in the crystals fragments. Atomic force microscopy (AFM) was carried on particles deposited under silicon wafer by solvent evaporation, to determine the particles thickness.

### **4.2.1. Systematic colloidal suspension characterization.**

The first approach was to determine the average size of particles in suspension in the solvent. For this purpose we have used the Dynamic Light Scattering (DLS) technique, broadly used to measure particles size distribution in a fluid. This technique is based on the Doppler Shift caused by spherical particles in Brownian motion, when a monochromatic light hits the particle moving in the solution, inducing a change of wavelength of the incoming light. This change will depend on the particle size.

This technique can be used routinely for characterization of particles sizes; it is non-destructive with a short measurement time and almost fully automated. The DLS technique measures particles diffusion coefficient, which can be used to infer their size by the Stokes-Einstein relation. This approach is well suited for spherical objects, but it is less reliable for non-spherical objects, which could be a problem for nanosheets characterization because of their flat geometry. However, recent work has revealed a good correlation between the particle size distribution outputted by DLS, corresponding to the hydrodynamic radius determined assuming a spherical geometry, and the nanosheets length [80]. Nevertheless, we verified on some samples that sizes measured by TEM correspond to those measured by DLS. Thus particles in suspension present a homogenous particle size distribution between 50-200 nm for the three organic solvents as we can observe in figure I.20.

We also used this technique to check effect of centrifugation speed and time, on the selection of particles size in suspension.

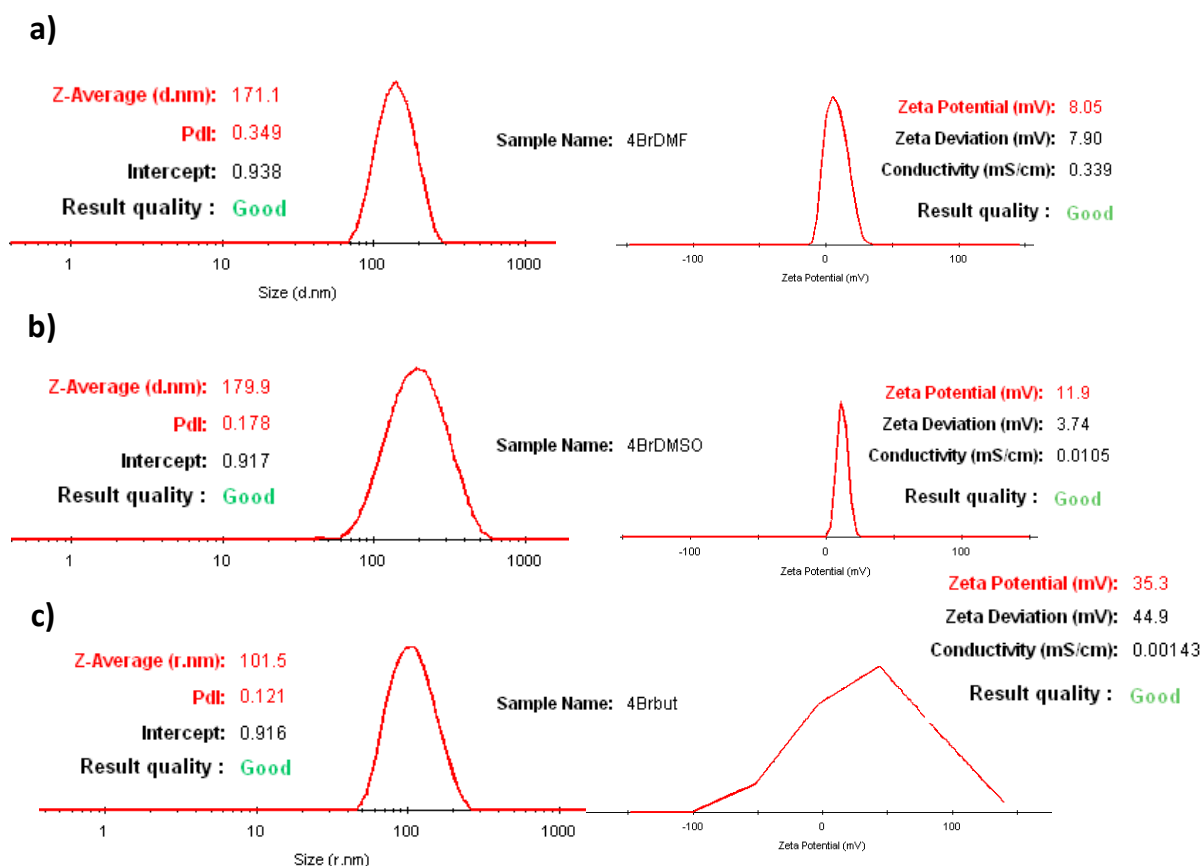


**Figure I.20.** DLS and Zeta potential measurements of DMF (a), DMSO (b) and butanol (c) colloidal suspensions after centrifugation (4000 r.p.m., 8 min).

Zeta potential can be considered from a theoretical point of view as the electric potential located at the interface between the fluid molecules adsorbed to the particle surface and the solvent itself. In other words, zeta potential can be defined as the potential difference between the dispersion medium (solvent) and the solvent molecules attached to the dispersed particle. This parameter is a good indicator of the suspension stability. Since the magnitude of the Zeta potential value indicates the electrostatic repulsion forces between the different particles similarly charged in the suspension; high Zeta potential values will lead to a good stability whereas, for low values, attractive forces can be stronger than the repulsive ones, breaking the suspension stability and leading to a flocculate.

Zeta potential is determined by the measure of velocity of particles in an electric field. Figure I.20 presents the Zeta measurements results of the three colloidal suspensions (DMSO, DMF and butanol) after centrifugation. All of them present positive values of Zeta potential, confirming the global positive charge of the particles, as expected after an exfoliation process where the break point would be the bromide interlayer. DMF and DMSO samples show a similar behavior whereas butanol sample presents higher charge heterogeneity, which can be due to the lower polarizing property of the butanol molecules.

UV-Visible spectra of the colloidal suspensions were systematically recorded to check the nature of the particles. The spectra have been collected on a Perkin-Elmer 650 spectrophotometer. All of them show an absorbance band around 350-400 nm, characteristic of octahedral  $\text{Co}^{3+}$ -O interactions[81], as it can be seen on figure I.21 where is presented the UV-Vis spectra of the suspensions in butanol as example.

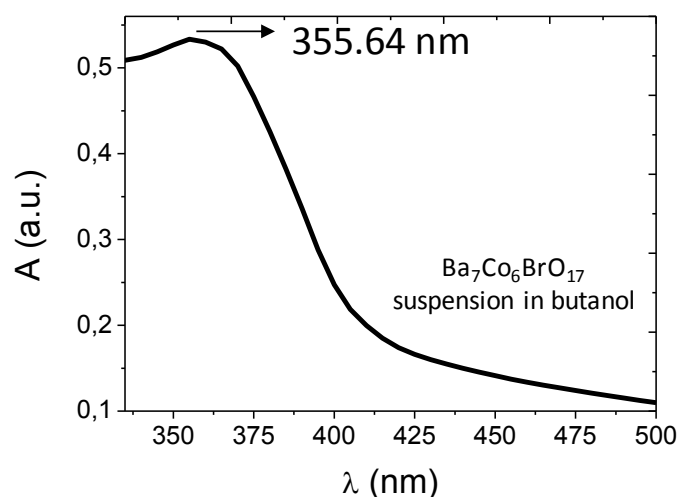


*Figure I.21. UV-Vis spectra of nanoflakes suspension in butanol.*

### 4.2.2. Butanol case: Full colloidal suspension characterization.

As we said earlier, only stable butanol colloid were characterized more deeply. For that purpose we have performed TEM and AFM on the nanoparticles obtained after the exfoliation process, and laid on a substrate by solvent evaporation.

TEM images were collected on a Jeol400EX with a point resolution of 1.7Å. A drop of the colloidal suspension was dispersed and evaporated on a holey carbon film deposited on a copper grid. The computed HREM images were calculated using JEMS program. As we can observe in figure I.22 estimated length values obtained by DLS are in good agreement with those calculated from TEM images. Low contrast between the particle and the membrane it is a clear indicator of the very small particle thickness.

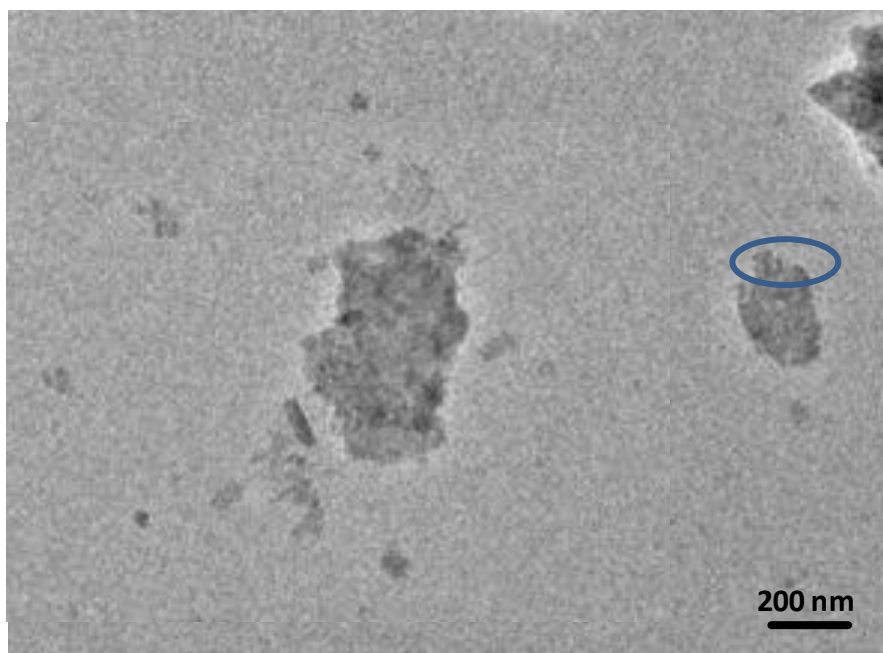


**Figure I.22.** Transmission electron microscopy of nanoflakes in butanol suspension after centrifugation of powder soaked over a week.

A zoom of the particle marked with a blue circle in the figure I.22 is presented figure I.23. Orange line shows the border between the particle and the membrane, the lack of contrast between them, suggest very thin particles. However, inside the particle we can see the characteristic interference lines of crystallized materials. The separating distance between these lines of  $2.9\text{\AA}$ , matches perfectly with the stacking distance of the  $[\text{BaO}_3]$  layer in perovskites. In addition EDS microanalysis on this particle, shows a good ratio Ba/Co but no bromide inside.

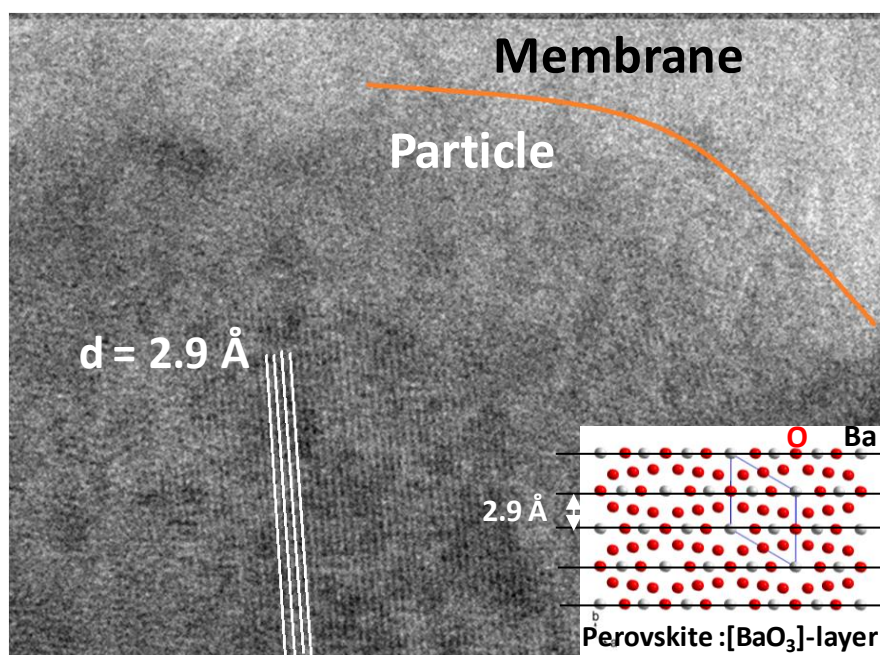


**Figure I.23.** TEM image of a nanoflake showing the crystallized domains with the characteristic distance of 2.9Å of the [BaO<sub>3</sub>] layer in perovskites. The low contrast between particle and membrane indicate a very small thickness.

Microscopy results obtained so far, allow us to have a qualitative knowledge about the surface/thickness ratio of the particles, confirming their flat geometry. Nevertheless, to quantify the particle thickness we have performed atomic force microscopy (AFM) on the sample prepared by evaporation of a colloid drop on a flat silicon wafer.

The corresponding AFM image is presented figure I.24. Similarly to TEM image, particles of about 150 nm width are observed. A linear scan along the marked direction, through two particles, was used to determine their thickness. Both, show a homogeneous thickness of about 8-10 nm, corresponding to 2.5-3 unit cells respectively. Even if exfoliation process does not lead to sheets of “one block” size, we are able to obtain particles, that we will call nanoflakes, with a surface/thickness ratio >10.

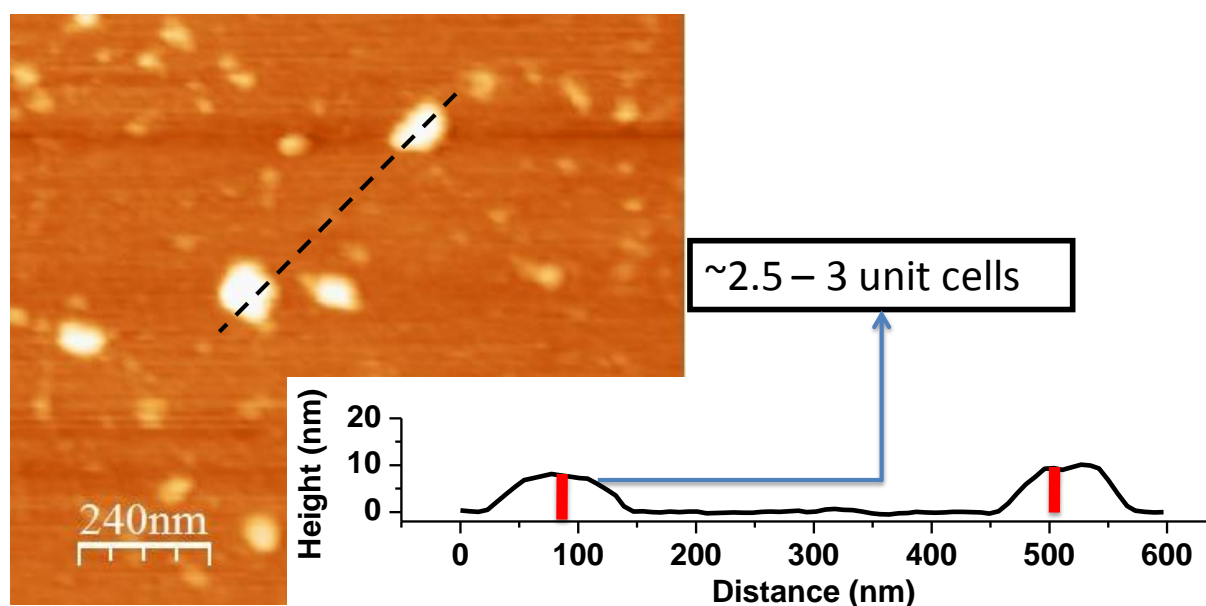


**Figure I.24.** AFM image of butanol suspension after solvent evaporation. Dotted line represents the zone where thickness was analyzed.

After the full morphological characterization performed, the next step will be firstly to verify the conservation of the a-b plane structure in the nanoflakes, and secondly, to check the oxidation state of the cobalt and compare the possible changes between the original powders, the soaked one and the nanoflakes obtained after centrifugation. To achieve the full characterization of the nanoflakes, we have gone to SOLEIL synchrotron to carry out experiences on DIFFABS beamline, specialized in X-Rays techniques as diffraction, absorption or fluorescence.

The X-ray diffractograms have been recorded in reflection mode with the X-PAD detector on the 8 circles diffractometer at 7.6 keV energy, before the cobalt absorption edge to avoid fluorescence effects. As expected, the Synchrotron radiation X-ray diffraction used in "in-plane" geometry, have enable us the direct characterization of the crystallinity of the bi-dimensional sheets. The in-plane x-ray diffraction is a powerful technique for thin films characterization because it allows the access to the lattice parameters and the crystal structure information of the planes perpendicular to the film surface.

Nanoflakes were prepared in two different samples: the first one is made of recovered and stored nanoflakes, whereas the second one corresponds to nanoflakes deposited by solvent evaporation on flat disorientated single crystal silicon support. This support was used because of its low background.

The first remarkable fact synchrotron powder-XRD patterns, is the apparition of a non-negligible quantity of  $\text{BaCO}_3$  in both samples, not seen clearly on powder XRD collected

on the laboratory diffractometer because the corresponding peaks were lost in the background. Carbonate proportion is higher when the sample was evaporated and recovered as powder, than on the one deposited on silicon. Both diffractometers are presented figure I.25 (a). As we have seen previously, nanoflakes are positively charged. The positive charges must come from cobalt cations as well as the  $\text{Ba}^{2+}$  ions present at the flakes surface. A possible explanation of this carbonation could be that these cations, stabilized in suspension in the organic solvent, are highly reactive when they are in contact with atmospheric  $\text{CO}_2$  to form Barium carbonate. Thus, the smaller quantity of  $\text{BaCO}_3$  observed when the flakes are laid on silicon substrate could be justified by the lower contact with the  $\text{CO}_2$  of the air. This fact would act in favor of the stabilization of the sheets when they are laid on the substrate.

On figure I.25 (b) are presented the XRD patterns of the original powder (black), the nanoflakes after butanol evaporation on the Si substrate recorded in “out of plane” configuration (blue) and in “in plane” configuration (red).

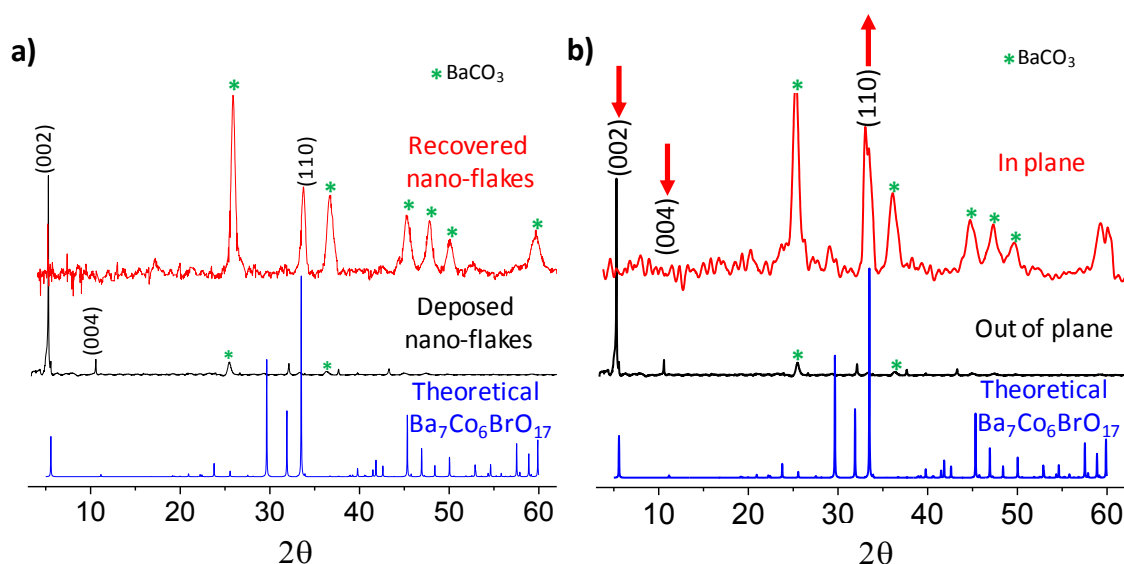


**Figure I.25.** Synchrotron PXRD diffractogram of the recovered nanoflakes as powder (red) and as deposited on Si substrate (black) (a).  $\text{Ba}_7\text{Co}_6\text{BrO}_{17}$  powder pattern (black) compared to “in plane” (red) and “out of plane” (blue) patterns of the nanoflakes deposited on Si substrate (b).

Compared to the original crystalline powder, the X-ray diffractogram of the layers deposited by solvent evaporation, recorded out of the plane, shows a very strong preferential orientation along the  $00l$  direction. However, in “in-plane” configuration this very strong orientation disappears and we can observe the apparition of the strong (110) reflection, which is the most intense of the diffractogram of  $\text{Ba}_7\text{Co}_6\text{BrO}_{17}$ . This reflection shows that the elementary blocks structure is preserved during the exfoliation process even if as expected,

the soaking treatment involve a considerable decrease in the crystallinity. The intensities of peaks belonging to the  $\text{BaCO}_3$  impurity remains constant showing that it is not affected by the sample orientation.

In addition, we have also performed a texture characterization in order to determinate the mosaicity and crystallite size of the nanoflakes deposited on the Si-substrate. For the mosaicity determination, a series of six omega scans (rocking curves) have been carried out and are presented in figure I.26; however three of the reflections measured are common with  $\text{BaCO}_3$  and have to be excluded. For the calculation of the crystallite size we measured the full width at half maximum (FWHM) of the same six reflections, hence in both cases we have focused just on the three same reflections, which corresponds to (00l) peaks for  $l= 2, 4$  and  $10$ .

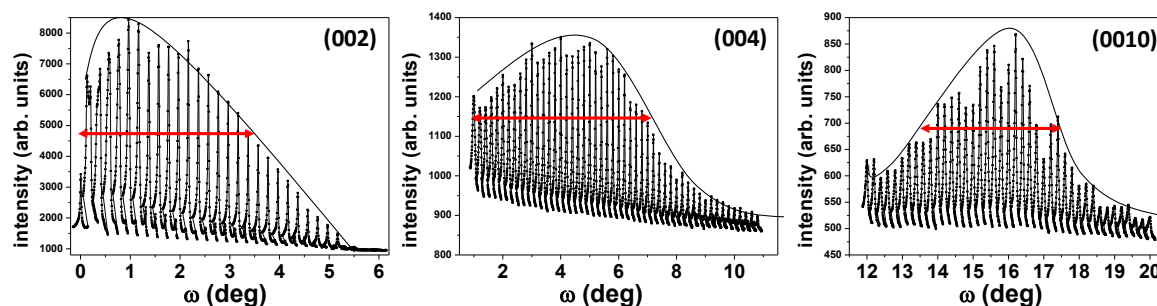


**Figure I.26.** Rocking curves (omega scan) of (002), (004) and (0010) reflections.

From a structural point of view, mosaicity can be seen as the average misorientation of the crystallites, thus, described by a cone with an angle equal to the mosaicity itself (see figure I.27).

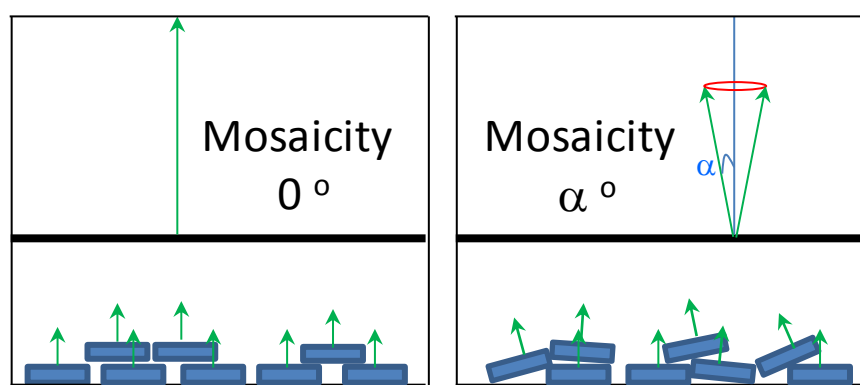


**Figure I.27.** Mosaicity in a polycrystalline sample.

In general, the mosaicity of a sample is the FWHM of the rocking curve, but when this value is not constant for the different peaks, it might be constraints associated to particle size. In that case, mosaicity can be expressed as a convolution type:  $\omega_{\text{peak}} = \text{mos}^2 + B(2\pi/D)^2$ , being

“mos” the mosaicity, B the slope and  $(2\pi/D)^2$  the term associated to the particle size constraints.[82]

Linear fit of the three points leads to a value of about  $3.4^\circ$ , confirming the very strong bi-dimensional feature of the sheets laid on a flat substrate and consequently highly orientated (figure I.28, a).

With respect to the crystallite size determination, Williamson-Hall method [83] was performed, the results are presented figure I.28 (b). A linear fit allows us to determine a value of about 55 nm for crystallites thickness. This value corresponds to the particle thickness because the reflections used for calculation belong only to the (00l) family.

This unexpected result of thickness, 5 times higher than the one determined by AFM, can be explained by the grains size inhomogeneity. An important difference between diffraction and microscopic experiments is the probe size. Whereas techniques such as AFM or TEM measure areas in the order of nanometers the synchrotron beam probe does so in the order of micrometers. So, microscopy techniques allow a very local analysis of the sample, while diffraction experiment gives a more general and average analysis of the sample. Thus, the intensity diffracted by some big particles will mask that of the smaller ones.

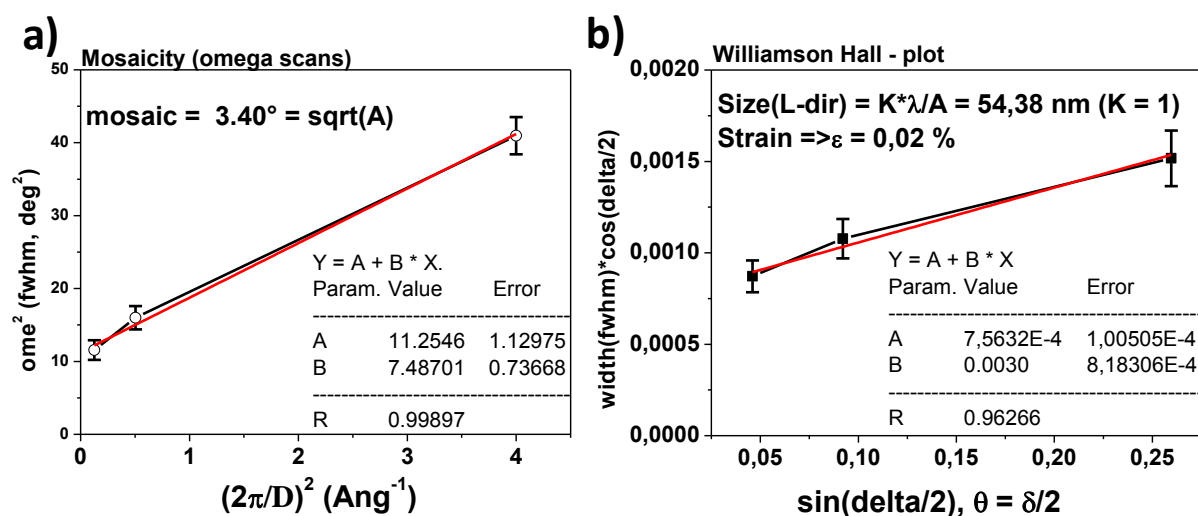


Figure I.28. Mosaicity ( $q^2 = (2\pi/D)^2$ ) (a) and crystallite size (b) determination.

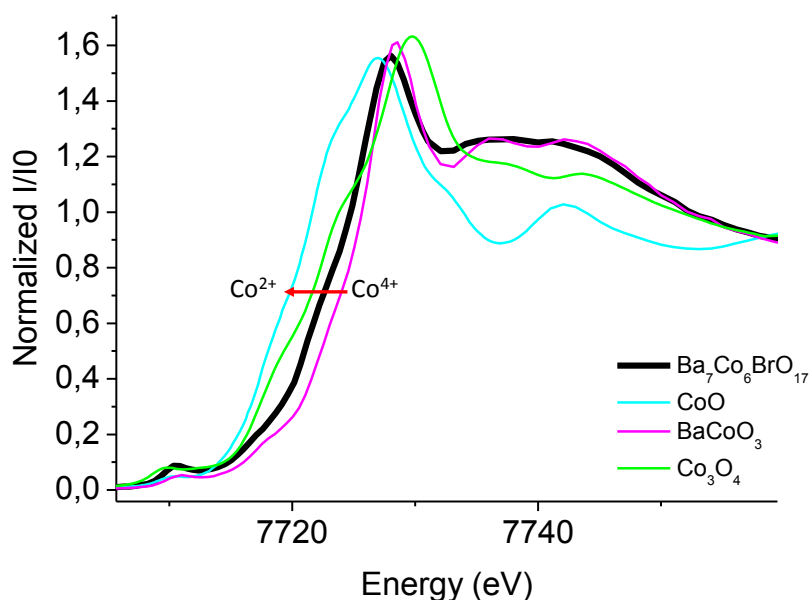
#### 4.2.3. Cobalt oxidation state evolution by XANES.

X-ray absorption near-edge (XANES) and diffraction anomalous near-edge structure (DANES) have been realized as well. Some details about the main principles which govern the two different techniques and the data treatment are detailed in the annex.

All the samples will be recorded in reflection mode at the cobalt and bromine K-edges, with the 4-element SDD silicon drift detector for X-ray fluorescence measurement. On a first step XANES spectra have been collected on all the samples and on second step DANES have been collected on nanosheets laid on the flat silicon substrate and on 14H-Ba<sub>7</sub>Co<sub>6</sub>BrO<sub>17</sub> on powder form. For this last part, the data have been collected at the intense lines (002) and (110) of the X-ray diffractogram, with the objective to perform a selective spectroscopy on the crystalline part of the layer concerning only the nanosheets, without interaction of amorphous impurities which can possibly be present.

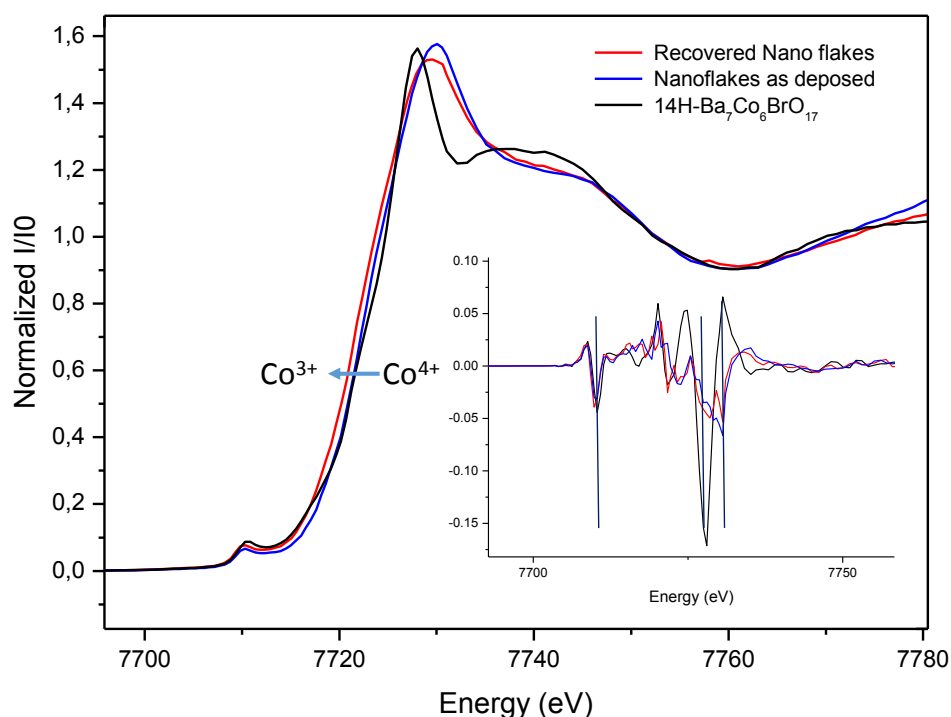
Regarding the data treatment, Co K-edge spectra were processed by the program Athena.[84] All the data were calibrated towards the inflexion point of the Co K-edge energy of Co metal foil ( $E_0=7713\text{eV}$ ).  $E_0$  for each spectrum was determined using the nearest zero-crossing of the second derivative of  $\mu(E)$  in energy and used for « $E_0$ » of the Co K-edge XANES. Then the spectrum was normalized to unit step height in the post-edge using a linear pre-edge subtraction and a quadratic polynomial post-edge line, routine process in Athena.

Figure I.29 shows a comparison of the Ba<sub>7</sub>Co<sub>6</sub>BrO<sub>17</sub> spectrum and the different references used at the cobalt K-edge to evaluate and follow the cobalt valence changes. As expected, the threshold position of the original phase match very well with a mix of Co<sup>3+</sup> and Co<sup>4+</sup>.



**Figure I.29.** XANES spectra comparison of Ba<sub>7</sub>Co<sub>6</sub>BrO<sub>17</sub> as prepared (black) and Co references. Co references were chosen because of their different cobalt oxidation states.

If we compare the original phase with the recovered nanoflakes after solvent evaporation, or the nanoflakes deposited on silicon substrate, an evolution of the threshold is observed towards lower energies (figure I.30). This evolution corresponds to a decrease of the cobalt oxidation degree. In addition, the threshold evolution is accompanied by a widening of the white line, corresponding to the split of the most intense peak on the second derivative curves. This indicates a slight decomposition of the phase after butanol treatment to be associated to the formation of barium carbonate observed by XRD, which leads in parallel to formation of an amorphous phase where the cobalt is present. However, very few changes in the pre-threshold are observed: only a very small shift towards lower energies is seen on the second derivative.

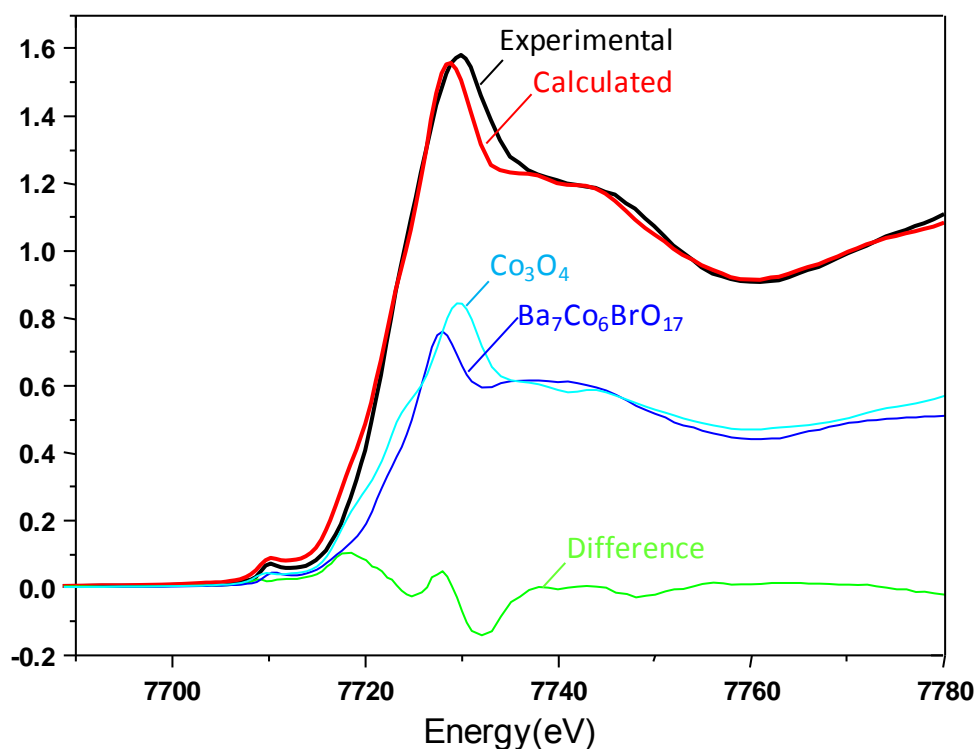


**Figure I.30.** XANES spectra comparison of  $Ba_7Co_6BrO_{17}$  as prepared (black), recuperated powder after nanoflakes deposition (red) and nanoflakes as deposited in a Si substrate (blue).

A more careful analysis of the spectra obtained of the nanoflakes recovered after solvent evaporation and the nanoflakes measured as deposited on Si substrate has been performed with a linear fit using as reference the original phase before treatment, mixed with  $Co_3O_4$  as impurity. It was made with Athena Software, using normalized  $\mu(E)$  and

constraining the standards to be 100 percent of the final phase with fixed  $E_0$  values to their original values.

Figure I.31 presents the XANES spectra of the nanoflakes on Si substrate compared to the result of the linear fit. It gives a percentage of about 50% of  $\text{Co}_3\text{O}_4$  and 50% of original phase. However, the fitting result is not good as shows the residual curve (in green), difference between the experimental spectra and the calculate one. It just gives an estimation of the presence of an amorphous impurity containing cobalt, not seen by XRD.

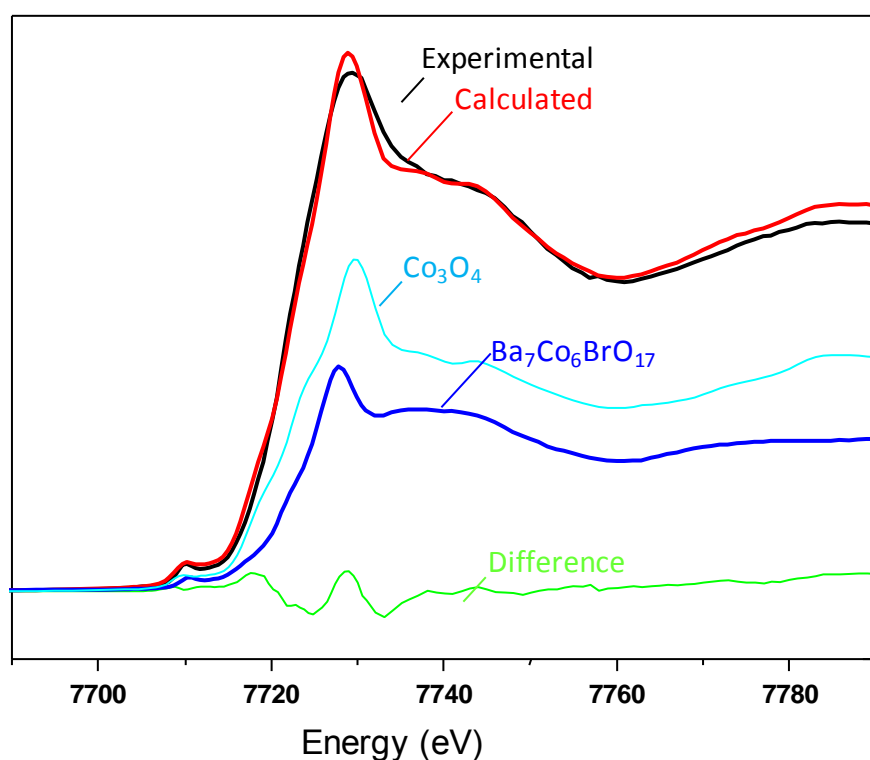


Standard	Weight	
=====		R-factor = 0.0075053
$\text{Co}_3\text{O}_4$	0.520 (0.055)	Chi-square = 0.19249
$\text{Ba}_7\text{Co}_6\text{BrO}_{17}$	0.480 (0.055)	Reduced chi-square = 0.0025666
sum .....	1.000	

**Figure I.31.** Linear fit of the nanoflakes deposited on silicon substrate, using  $\text{Ba}_7\text{Co}_6\text{BrO}_{17}$  and  $\text{Co}_3\text{O}_4$  as references.

Same analysis has been done on recovered nanoflakes after solvent evaporation. The linear fit has been done as previously and the result is given figure I.32 (red curve). It gives a percentage of 60% of  $\text{Co}_3\text{O}_4$  and 40% of original phase. As precedently, the fitting result is not very good, as shows the residual curve (in green), but one must notice that the decomposition is more important than in the case of the flakes deposited on substrate. It seems that the interactions with the substrate stabilize the particles and prevent their

decomposition.



Standard	Weight	
-----		R-factor = 0.0051819
Co <sub>3</sub> O <sub>4</sub>	0.607 (0.044)	Chi-square = 0.12956
Ba <sub>7</sub> Co <sub>6</sub> BrO <sub>17</sub>	0.393 (0.044)	Reduced chi-square = 0.0017048
sum .....	1.000	

**Figure I.32.** Linear fit of the recovered nanoflakes after solvent evaporation using Ba<sub>7</sub>Co<sub>6</sub>BrO<sub>17</sub> and Co<sub>3</sub>O<sub>4</sub> as references.

To summarize, we have been able to study the cobalt oxidation state changes of the products obtained after exfoliation process. The edge shift towards smaller energies, indication of a cobalt reduction in the sheets, is very small and even if the fit is made using Co<sub>3</sub>O<sub>4</sub> as impurity, we cannot consider it being really present since the fitting result is not satisfactory. However, the enlargement of the white line can correspond to an amorphous phase, showing a decomposition of the phase when the nanoflakes are recovered after solvent evaporation. This leads to BaCO<sub>3</sub>, present on powder XRD, and to amorphous cobalt phase not seen by XRD but clearly presents after the XANES spectra analysis.

In view of these results and for deepening our study we carried out on a second time DANES (diffraction anomalous fine structure near edge region) on the nanosheets laid on the flat silicon substrate and on the original 14H-Ba<sub>7</sub>Co<sub>6</sub>BrO<sub>17</sub> on powder form. The data are collected when the detector is on a reflection peak position. This technique, detailed in the

experimental techniques annex, offers the possibility of a selective spectroscopy. It allows to collect information about the electronic structure of the studied element, comparable to XANES information, but on the crystalline part of the sample without interaction of amorphous impurities which can possibly be present. Then it allows us to separate the signal of the organized nanosheets from the amorphous phase whose presence was detected in XANES. In our case the data have been collected at the intense 002 and 110 peaks of the X-ray diffractogram for the crystalline sample, but for the nanosheets the 110 line is not enough intense for a good data collection and exploitation, the DANES signal being too small. Figure I.33 present the DANES spectra recorded at the 002 peak of the layer compared to the parent compound. Both spectra are very similar, which is confirmed by the superimposition of the second derivative curves (inset figure I.33). We can conclude that electronic structure and local environment of the cobalt are preserved in the sheets, confirming the blocks preservation after the exfoliation process. This point is crucial, more especially for the tetrahedral Co that, at first sight, could have been affected by the removal of the bromine sheets but still being present, as shows the presence of the band in the pre-edge.

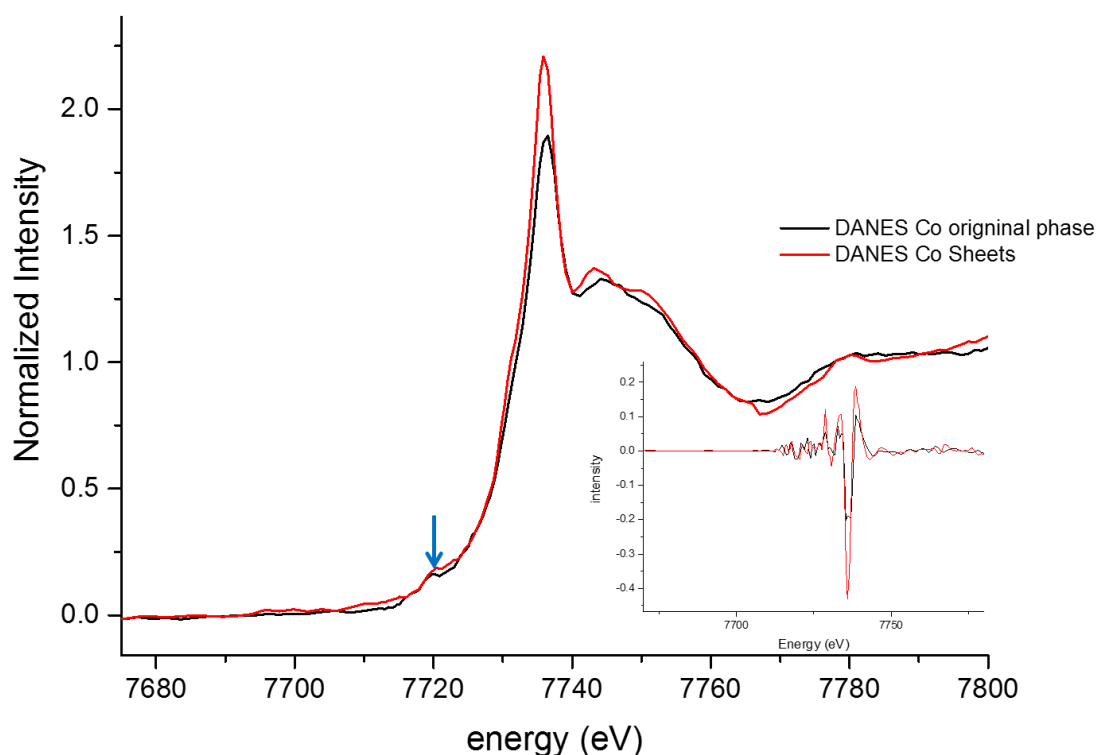


**Figure I.33.** DANES spectra of the nanosheets on silicon substrate compare to the original  $Ba_7Co_6BrO_{17}$  one.

The combination of X-ray absorption spectroscopy and synchrotron X-ray diffraction has allowed us to show that the exfoliation process occurs, keeping the global elementary blocs structure, even if a small part of the compound is decomposed. The deposited layer on flat silicon substrate is of good crystallinity and highly orientated. The absorption spectra shows that oxidation degree and environment of cobalt are preserved after exfoliation process, allowing an overall positive charge of nanosheet.

### **4.3. Conclusion.**

During this part of my work, I have been able to establish a reaction pathway to obtain oxide nano-flakes by exfoliation process. We have obtained nano-particles with a surface/width ratio higher than 100, so they can be considered as bi-dimensional nanoflakes. These new 2D blocks, may serve as elementary brick to build new materials with tailored properties depending of their combination. These new nanoflakes are positively charged at their surface, which is rare in those kinds of 2D oxides, as explained in the introduction of this chapter. This positive charge will allow them to interact with negatively-charged oxide nanosheets, leading to a huge number of possible combinations. Nevertheless we have also to admit some problems and limitations. The AFM measures indicated homogeneous values corresponding to 5-6 layers together. Even if we can just establish hypothesis, it seems to have some kind of stability limit to keep the original structure. So when the particles get smaller than these 5 or 6 assembled blocks, they decompose. Barium is quickly carbonated and amorphous oxide cobalt residue is generated. In addition, the use of an organic solvent such a butanol, immiscible in water, complicates the next step of recombination with others nanosheets suspended in water solutions.

### Bibliography

- [1] A. Clearfield, *Chemical Reviews* **88** (1988) (1) 125.
- [2] K.G.S. Ranmohotti, E. Josepha, J. Choi, J.X. Zhang, J.B. Wiley, *Advanced Materials* **23** (2011) (4) 442.
- [3] M.A. Hayward, *Semiconductor Science and Technology* **29** (2014) (6).
- [4] M. Kauffmann, P. Roussel, *Acta Crystallographica Section B-Structural Science* **63** (2007) 589.
- [5] O. Mentre, M. Kauffmann, G. Ehora, S. Daviero-Minaud, F. Abraham, P. Roussel, *Solid State Sciences* **10** (2008) (4) 471.
- [6] (!!! INVALID CITATION !!!).
- [7] E.L. Crepaldi, J.B. Valim, *Quimica Nova* **21** (1998) (3) 300.
- [8] A. Ookubo, K. Ooi, F. Tani, H. Hayashi, *Langmuir* **10** (1994) (2) 407.
- [9] S. Miyata, *Clays and Clay Minerals* **31** (1983) (4) 305.
- [10] A.M. Fogg, A.L. Rohl, G.M. Parkinson, D. O'Hare, *Chemistry of Materials* **11** (1999) (5) 1194.
- [11] M. del Arco, S. Gutierrez, C. Martin, V. Rives, J. Rocha, *Journal of Solid State Chemistry* **151** (2000) (2) 272.
- [12] S.-L. Wang, P.-C. Wang, *Colloids and Surfaces a-Physicochemical and Engineering Aspects* **292** (2007) (2-3) 131.
- [13] S. Carlino, *Solid State Ionics* **98** (1997) (1-2) 73.
- [14] J.W. Lee, W.C. Choi, J.-D. Kim, *Crystengcomm* **12** (2010) (10) 3249.
- [15] F. Silverio, M.J. dos Reis, J. Tronto, J.B. Valim, *Applied Surface Science* **253** (2007) (13) 5756.
- [16] S.A. Hindocha, L.J. McIntyre, A.M. Fogg, *Journal of Solid State Chemistry* **182** (2009) (5) 1070.
- [17] L.J. McIntyre, T.J. Prior, A.M. Fogg, *Chemistry of Materials* **22** (2010) (8) 2635.
- [18] L. Poudret, T.J. Prior, L.J. McIntyre, A.M. Fogg, *Chemistry of Materials* **20** (2008) (24) 7447.
- [19] B.-I. Lee, K.S. Lee, J.H. Lee, I.S. Lee, S.-H. Byeon, *Dalton Transactions* (2009) (14) 2490.
- [20] L. Hu, R. Ma, T.C. Ozawa, T. Sasaki, *Chemistry-an Asian Journal* **5** (2010) (2) 248.
- [21] G.F. Walker, *Nature* **187** (1960) (4734) 312.
- [22] A.K. Geim, K.S. Novoselov, *Nature Materials* **6** (2007) (3) 183.
- [23] M.I. Katsnelson, K.S. Novoselov, *Solid State Communications* **143** (2007) (1-2) 3.
- [24] J.C. Meyer, A.K. Geim, M.I. Katsnelson, K.S. Novoselov, D. Obergfell, S. Roth, C. Girit, A. Zettl, *Solid State Communications* **143** (2007) (1-2) 101.
- [25] K.S. Novoselov, A.K. Geim, S.V. Morozov, D. Jiang, Y. Zhang, S.V. Dubonos, I.V. Grigorieva, A.A. Firsov, *Science* **306** (2004) (5696) 666.
- [26] P.J. Ollivier, N.I. Kovtyukhova, S.W. Keller, T.E. Mallouk, *Chemical Communications* (1998) (15) 1563.
- [27] D.M. Kaschak, S.A. Johnson, D.E. Hooks, H.N. Kim, M.D. Ward, T.E. Mallouk, *Journal of the American Chemical Society* **120** (1998) (42) 10887.
- [28] T. Sasaki, M. Watanabe, H. Hashizume, H. Yamada, H. Nakazawa, *Journal of the American Chemical Society* **118** (1996) (35) 8329.
- [29] T. Sasaki, M. Watanabe, *Journal of the American Chemical Society* **120** (1998) (19) 4682.
- [30] T. Sasaki, *Supramolecular Science* **5** (1998) (3-4) 367.
- [31] T. Sasaki, M. Watanabe, Y. Komatsu, Y. Fujiki, *Inorganic Chemistry* **24** (1985) (14) 2265.
- [32] T. Sasaki, M. Watanabe, Y. Komatsu, Y. Fujiki, *Bulletin of the Chemical Society of Japan* **58** (1985) (12) 3500.
- [33] V.I. Rupasov, V.I. Klimov, *Physical Review B* **76** (2007) (12) 6.
- [34] L.S. Li, J.T. Hu, W.D. Yang, A.P. Alivisatos, *Nano Letters* **1** (2001) (7) 349.
- [35] N.I. Kovtyukhova, T.E. Mallouk, *Chemistry-a European Journal* **8** (2002) (19) 4355.
- [36] S. Ida, Y. Okamoto, H. Hagiwara, T. Ishihara, *Catalysts* **3** (2013) (1) 1.
- [37] K.I. Bolotin, F. Ghahari, M.D. Shulman, H.L. Stormer, P. Kim, *Nature* **462** (2009) (7270) 196.
- [38] X. Du, I. Skachko, F. Duerr, A. Luican, E.Y. Andrei, *Nature* **462** (2009) (7270) 192.
- [39] N. Sakai, Y. Ebina, K. Takada, T. Sasaki, *Journal of the American Chemical Society* **126** (2004) (18) 5851.

- [40] T. Sasaki, M. Watanabe, *Journal of Physical Chemistry B* **101** (1997) (49) 10159.
- [41] T.W. Kim, S.G. Hur, S.-J. Hwang, H. Park, W. Choi, J.-H. Choy, *Advanced Functional Materials* **17** (2007) (2) 307.
- [42] Y. Ebina, T. Sasaki, M. Harada, M. Watanabe, *Chemistry of Materials* **14** (2002) (10) 4390.
- [43] K. Maeda, M. Eguchi, W.J. Youngblood, T.E. Mallouk, *Chemistry of Materials* **21** (2009) (15) 3611.
- [44] K. Maeda, M. Eguchi, S.-H.A. Lee, W.J. Youngblood, H. Hata, T.E. Mallouk, *Journal of Physical Chemistry C* **113** (2009) (18) 7962.
- [45] S. Suzuki, S. Takahashi, K. sato, M. Miyayama, *Electroceramics in Japan IX* **320** (2006) 223.
- [46] H. Sato, K. Okamoto, K. Tamura, H. Yamada, K. Saruwatari, T. Kogure, A. Yamagishi, *Applied Physics Express* **1** (2008) (3) 3.
- [47] T. Yui, Y. Kobayashi, Y. Yamada, T. Tsuchino, K. Yano, T. Kajino, Y. Fukushima, T. Torimoto, H. Inoue, K. Takagi, *Physical Chemistry Chemical Physics* **8** (2006) (39) 4585.
- [48] O.H.D. Wang Qiang, *Chemical Reviews* **112** (2012) 4124.
- [49] C. Nethravathi, G. Harichandran, C. Shivakumara, N. Ravishankar, M. Rajamathi, *Journal of Colloid and Interface Science* **288** (2005) (2) 629.
- [50] M. Adachi-Pagano, C. Forano, J.P. Besse, *Chemical Communications* (2000) (1) 91.
- [51] D.G. Costa, A.B. Rocha, W.F. Souza, S.S.X. Chiaro, A.A. Leitao, *Applied Clay Science* **56** (2012) 16.
- [52] E. Gardner, K.M. Huntoon, T.J. Pinnavaia, *Advanced Materials* **13** (2001) (16) 1263.
- [53] L.D. Hongjuan Li, Gang Zhua, Liping Kanga, ZongHuai, Liu, *Materials Science and Engineering B* **177** (2012) 8.
- [54] M. Parras, A. Varela, H. Seehofer, J.M. GonzalezCalbet, *Journal of Solid State Chemistry* **120** (1995) (2) 327.
- [55] A.J. Jacobson, J.L. Hutchison, *Journal of Solid State Chemistry* **35** (1980) (3) 334.
- [56] M. Luciana, Oxo-halogénures de cobalt: Compréhension de l'influence des substitutions cationiques et anioniques., Thesis (2012).
- [57] M. Kauffmann, Structure, dimensionalité et magnétisme de nouvelle halogéno-cobaltites., Thesis (2007).
- [58] E. Quarez, M. Huve, F. Abraham, O. Mentre, *Solid State Sciences* **5** (2003) (7) 951.
- [59] L. J., B. B., CHECKCELL, *LMGP-Suite Suite of Programs for the Interpretation of X-ray 16 Experiments*, ENSP/Laboratoire des Matériaux et du Génie Physique BP46.38042, Saint Martin d'Hères, France (2000).
- [60] M. Chaplin, Water structure and science., [http://www1.lsbu.ac.uk/water/water\\_structure\\_science.html](http://www1.lsbu.ac.uk/water/water_structure_science.html).
- [61] Y. Breard, C. Michel, M. Hervieu, N. Nguyen, A. Ducouret, V. Hardy, A. Maignan, B. Raveau, F. Bouree, G. Andre, *Chemistry of Materials* **16** (2004) (15) 2895.
- [62] M. Taibi, S. Ammar, N. Jouini, F. Fiévet, *Journal of Physics and Chemistry of Solids* **67** (2006) (5-6) 932.
- [63] R. Ylmen, U. Jaglid, I. Panas, *Journal of the American Ceramic Society* **97** (2014) (11) 3669.
- [64] M. Liegeois-Duyckaerts, *Spectrochimica Acta Part A: Molecular Spectroscopy* **41** (1985) (4) 523.
- [65] N. Zotov, K. Petrov, M. Dimitrova-Pankova, *Journal of Physics and Chemistry of Solids* **51** (1990) (10) 1199.
- [66] C.C. Addison, N. Logan, S.C. Wallwork, C.D. Garner, *Quarterly Reviews, Chemical Society* **25** (1971) (2) 289.
- [67] R.L. Frost, K.L. Erickson, T.J. Klopogge, *Spectrochimica Acta Part a-Molecular and Biomolecular Spectroscopy* **61** (2005) (13-14) 2919.
- [68] S. Tezuka, R. Chitrakar, A. Sonoda, K. Ooi, T. Tomida, *Green Chemistry* **6** (2004) (2) 104.
- [69] P. Behrens, *Molecular Sieves - Science and Technology*, Springer (2004), p.427-466.
- [70] D.P. Koningsberger, R., In: J. Winefordner, Editor, *Chemical Analysis*, New York (1988).
- [71] A. Bianconi, *Physical Review B* **26** (1982) (6) 2741.
-

- [72] G. Abellan, E. Coronado, C. Marti-Gastaldo, E. Pinilla-Cienfuegos, A. Ribera, *Journal of Materials Chemistry* **20** (2010) (35) 7451.
- [73] S. Zhang, Q. Liu, H. Cheng, F. Zeng, *Applied Surface Science* **331** (2015) 234.
- [74] S. Olejnik, A.M. Posner, J.P. Quirk, *Clays and Clay Minerals* **19** (1971) (2) 83.
- [75] Y. Kamiya, S. Ueki, N. Hiyoshi, N. Yamamoto, T. Okuhara, *Catalysis Today* **78** (2003) (1-4) 281.
- [76] L. Benes, J. Votinsky, J. Kalousova, J. Klikorka, *Inorganica Chimica Acta* **114** (1986) (1) 47.
- [77] J.A. Mbey, F. Thomas, C.J.N. Sabouang, Liboum, D. Njopwouo, *Applied Clay Science* **83-84** (2013) 327.
- [78] L. Yi, G. Hu, *Rsc Advances* **3** (2013) (45) 23461.
- [79] Nice University,  
[http://www.unice.fr/cdiec/animations/spectroscopie/infra\\_rouge/infra\\_rouge.htm](http://www.unice.fr/cdiec/animations/spectroscopie/infra_rouge/infra_rouge.htm).
- [80] M. Lotya, A. Rakovich, J.F. Donegan, J.N. Coleman, *Nanotechnology* **24** (2013) (26).
- [81] A. Fernandez-Osorio, A. Vazquez-Olmos, R. Sato-Berru, R. Escudero, *Reviews on Advanced Materials Science* **22** (2009) (1-2) 60.
- [82] B.E. Warren, *X-Ray Diffraction*, Addison-Wesley Publishing Co (1969).
- [83] G.K. Williamson, W.H. Hall, *Acta Metallurgica* **1** (1953) (1) 22.
- [84] B. Ravel, M. Newville, *Journal of Synchrotron Radiation* **12** (2005) 537.

## **Chapter II.**

Iron exsolution and cationic mobility in  
 $\text{BaFe}_2(\text{PO}_4)_2$  and  $\text{BaFe}_{2-y}\text{M}_y(\text{PO}_4)_2$



### 1. Introduction.

Transition metal oxides have been deeply studied since longtime ago due of the huge variety of physical properties together with a good stability compared to alloys, intermetallics, sulfides etc .... From the electronic viewpoint, these properties are dependent of the different coupling strength between electronics states of atoms in the solids into localized states, more or less separated bands, continuum ... etc. Of course, the properties are related to the topology and geometry of the metal-oxygen network. As a result, any kind of structural transformations realized in the network will lead to more or less drastic changes of the physical properties. Dealing with oxides, the major route concerns the modification of the anionic lattice by aliovalent substitution on the cationic sites changing the oxygen content, or on the anionic sites (e.g. oxofluorides[6]). Very exciting routes of topochemical transformations of the anionic lattice have been cited previously in the introductory chapter, such as the ultimate reduction of oxides using hydrides  $\text{CaH}_2$ ,  $\text{LiH}$ ,  $\text{NaH}$  leading for instance to  $\text{SrFeO}_2$  from  $\text{SrFeO}_3$  reduction.[7] Eventually the incorporation of H- hydrides in mixed oxo-hydrides lead to even more fascinating phases such as  $\text{BaTi}(\text{O}, \text{H})_3$ .[8]

Besides the well-known playground of cationic substitution at constant ratio, the material-change after cationic incorporation or exsolution is also very rich. The most typical cases implies alkali des(intercalation) at the origin of mobile  $\text{Li}^+$  ion science. In well adapted structure, the diffusion of alkali ions can be rather easy because of their sizes and poor electronegative nature. On the opposite, the exsolution of metal transition M from solids is a rare phenomenon, because it involves well adapted diffusion paths for  $\text{M}^{n+}$  cations which strongly interact with the anionic array. In most cases, this process happens in reducing conditions and ideally leads to the precipitation of non-percolating metallic nanoparticles anchored at the surface of the modified compound. The different cases show interesting utilities in various fields.

For example, electrochemical reversible Cu exsolution from  $\text{Cu}_x\text{V}_2\text{O}_5$  was proposed as a new direction for developing an alternative class of higher energy density Li storage electrodes[9, 10]. “In situ” characterization of  $\text{Cu}_x\text{V}_2\text{O}_5$  used as cathode material in Li ion batteries shows how Cu cations go out from the network to form  $\text{Cu}^0$  dendrites during Li insertion (discharge).

In the reforming catalysis field, it is well known that exsolved catalysts are less sensitive to coking due to the finely-dispersed metal grains such as nickel[11, 12]. When the

exsolution process is reversible, it allows developing intelligent regenerative catalysts with improved durability. Pd nanoparticles with hampered growth upon cyclic redox cycles is a good example[13].

In magnetism or conductivity fields these kinds of process also play an important role. The activation energy of Ni exsolution in layered Ni selenides[14] gives chemical insight behind the controversial relationships of vacancy-order and the emergence of magnetism or superconductivity in iron selenides[15].

More rarely we can find compounds that exhibit a spontaneous extrusion of cations in oxidizing conditions under thermal stimuli. It generally concerns  $\text{Fe}^{2+}$  oxides due to very favorable  $\text{Fe}^{2+}/\text{Fe}^{3+}$  redox properties, as reported for the olivine  $\text{LiFePO}_4$  and  $\text{Fe}_2\text{SiO}_4$  with Fe-exsolution into  $\text{Fe}_2\text{O}_3$  nano-clusters[16-18]. In both of cases these iron exsolution will lead, by topotactic transformations, to new phases with various stoichiometries and structures, hence, with different physical properties (ionic conductivity, magnetism...) from the original ones.

The study of these new compounds is also very interesting from the point of view of mineralogy and crystallography. Essentially in my work, I investigated in compounds from the laboratory, structural features related to Fe exsolution similarly to what was initiated in these olivine-derivatives. For instance, the investigation around the different super structures in Lahuinite is a representative example. This iron silicate, whose composition is  $\text{Fe}^{2+}_{0.8}\text{Fe}^{3+}_{0.8}\text{SiO}_4$ , has a distorted olivine-like structure with iron vacancies. Deep crystallographic studies have shown complex structural transformations. This mineral can be synthesized after the oxidation in air of the Fayalite ( $\text{Fe}_2\text{SiO}_4$ ). Structure resolution by single crystal XRD showed that lahuinite commonly occurs with a pseudo-twins along the (001)plane [19] [20]. Finally, supplementary reflections in  $c^*$  axis were identified, associated to a superstructure with double or triple  $c$  parameter due to ordering between  $\text{Fe}^{2+}$ ,  $\text{Fe}^{3+}$  and the vacancies. Finally it is possible to establish a relationship between this order and non-stoichiometry in olivine structure[21]. In general, this rare behavior seems to be encouraged by ferrous  $\text{Fe}^{2+}$  ions, reminiscent of the exsolution of Fe-rich inclusions out of minerals or meteorite rocks[22, 23].

In a similar way, the famous  $\text{LiFePO}_4$  phase shows similar behavior. It is used as positive electrode (cathode) in Li-ion batteries because of its high reversibility in lithiation process, its relative low prices comparing with other cathodes materials, and its environmental harmlessness. This compound was announced to a substantial iron exsolution in presence of  $\text{H}_2\text{O}$  molecules which are often present as impurities in  $\text{LiPF}_6$  electrolyte at high

temperatures[24]. Lately, Guyomard group has demonstrate that structural changes in  $\text{LiFePO}_4$  can be associated to a partial oxidation of iron or to a de-lithiation after long air or humidity atmosphere exposition[25, 26]. An extensive study of the behavior of  $\text{LiFePO}_4$  nanopowders after air thermal treatment has also carried out at the LRCS [17]. These nanopowders show at the beginning various point defects as cations vacancies or exchanged Li and Fe sites. The disorder in crystallographic Lithium sites has a drastic effect in its electrochemical behavior, which allows a reversible Li insertion-deinsertion mechanism at 298K by complete solid state solution. This mechanism presents a notable advantage with respected to limitations imposed by structural changes in the others commercial cathode materials as  $\text{LiCoO}_2$ [27]. Those changes will lead capacity losses along the Li insertion-deinsertion cycles. This same work demonstrates the existence of an oxidation reaction of olivine from 200C with the consequent  $\text{Fe}_2\text{O}_3$  nanoclusters formation, which will grow until appearance of crystallized domains. Different oxidized olivine phases have an electrochemical behavior strongly linked to the thermal treatment, with news reversible pathways on Li insertion-deinsertion and unusual work voltage for the different networks.

Indeed, such systems could be also very innovating, due to the environment friendly nature and wide range of applications of  $\text{Fe}_2\text{O}_3$  nanoparticles. The reported applications cover gas sensing, photocatalysis, water splitting, water purification, solar energy conversion and pigmentation[28-32] but cluster size is cruelly driving the activity, which leads to the development of several techniques for their production (co-precipitation[32] which is generally preferred due to its simplicity, while thermal decomposition gives a greatest control size[33]). In this context, the finding of compounds able to exsolute reversibly a large amount of  $\alpha\text{-Fe}_2\text{O}_3$  nano-crystals is relevant for proposition of renewable functional materials, so-called intelligent catalyts.[34] At this point, my work has focused on the very easy reversible exsolution of iron out of  $\text{BaFe}_2(\text{PO}_4)_2$  related phases. Our results highlight unprecedented easy diffusion of metal ions, and other very important phenomena. Before the description of this study, it is important to give a state of art of the  $\text{BaM}_2(\text{XO}_4)_2$  phases, important for their low-Dimension magnetic properties, and particularly to recall the main features of  $\text{BaFe}_2(\text{PO}_4)_2$  prepared at the laboratory during the PhD thesis of R. David, just before my arrival.[35]

## 2. State of the art $\text{BaFe}_2(\text{PO}_4)_2$ .

### 2.1. Magnetic properties of $\text{BaFe}_2(\text{PO}_4)_2$ .

$\text{BaM}_2(\text{XO}_4)_2$  compounds, with  $M = \text{Co}^{2+}, \text{Ni}^{2+}, \text{Fe}^{2+} \dots$  and  $X = \text{As}^{5+}, \text{P}^{5+}, \text{V}^{5+}$ , are formed by stacking of honeycomb layers made of edge-sharing  $M^{2+}\text{O}_6$  octahedra. All oxygen corners are common with  $[\text{XO}_4]^{3-}$  tetrahedral oxo-anions pointing through the interleave space, occupied by the  $\text{Ba}^{2+}$  ions. It leads to inter-layer separations of approximately  $8\text{\AA}$  in favor of unusual quasi 2D-magnetic behaviors at low temperature, depending on the chemical nature of the  $M^{2+}$  ions.

This honeycomb lattice presents three different intralayer spin exchange path, see figure II.1. The superexchange (SE) path  $J_1$  consists of two M-O-M bridges with a M-O-M angle of about  $90^\circ$ , while the super-superexchange (SSE) paths  $J_2$  and  $J_3$  involve M-O...O-M bridges. For instance, The cobaltite  $\text{BaCo}_2(\text{AsO}_4)_2$  is a quasi-2D XY system in which the  $\text{Co}^{2+}$  frustrated magnetic moments are mainly confined in the basal planes responsible for magnetization steps below  $T_N \sim 5.3\text{ K}$ . [36] The same topology with  $\text{Ni}^{2+}$  ions in  $\text{BaNi}_2(\text{VO}_4)_2$  leads to a quasi-2D antiferromagnet that orders below  $T_N \sim 50\text{ K}$  and undergoes a Kosterlitz–Thouless transition at  $T_{KT} \sim 43\text{ K}$  compatible with a weakly anisotropic 2D Heisenberg character. [37, 38]

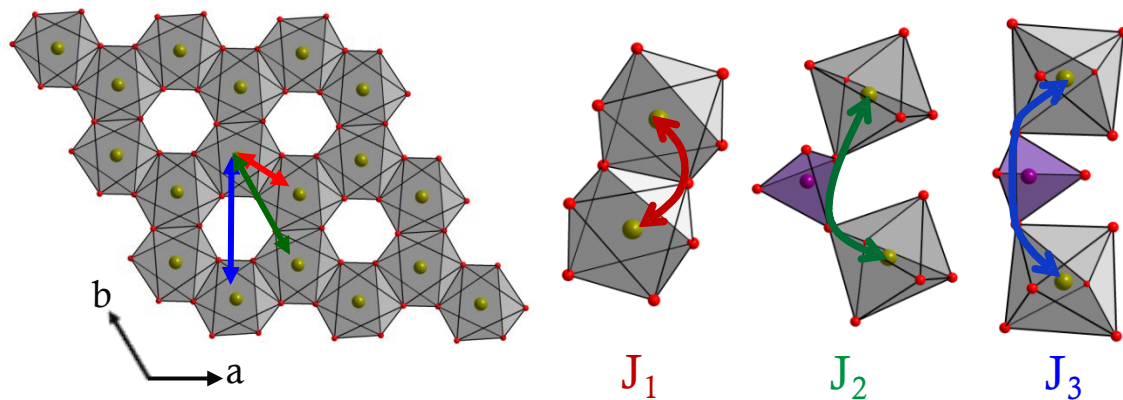


**Figure II.1.** Different intralayer spin exchange paths ( $J_1$ ,  $J_2$  and  $J_3$ ) in honeycomb framework.

For  $M=\text{Fe}^{2+}$ , was expected that the  $90^\circ$  SE  $J_1$  path is ferromagnetic (FM) and predominant for high-spin (HS)  $\text{Fe}^{2+}$  ( $d^6$ ,  $S=2$ ) but antiferromagnetic (AFM) for HS  $\text{Fe}^{3+}$  ( $d^5$ ,  $S=5/2$ ) cations, according to dominant direct  $t_{2g}$ - $t_{2g}$  overlaps.[39] Due to this prediction,  $\text{BaFe}_2(\text{PO}_4)_2$  has been recently synthesized in our laboratory during the research of low dimensionality magnetic oxides.[35] This new phase presents very interesting properties. The layered  $\text{BaFe}_2(\text{PO}_4)_2$  has been presented as the example of the first oxide 2D Ising oxide ferromagnet, with uniaxial ferromagnetism between  $\text{Fe}^{2+}$  ( $S=2$ ) spins below  $T_c=65.5$  K[1].

In addition, this compound presents a very interesting behavior at low temperature showing a very rare re-entrant structural transition. The Re-entrant structural phase transitions consist in a sequence of two phase transition for which the first and third phases have the same symmetry and are effectively identical.

$\text{BaFe}_2(\text{PO}_4)_2$  shows a re-entrant rhombohedral  $\xrightarrow{140K}$  triclinic  $\xrightarrow{70K}$  rhombohedral transition, driven by the competition between Jahn-Teller instability and stabilization of the system by the magnetic ordering. Unpaired electron in a degenerate orbital in the electronic configuration of high spin (HS)  $\text{Fe}^{2+}$  ( $d^6$ ) suppose a condition for the Ising behavior.[40] Such  $\text{FeO}_6$  octahedra showing uniaxial magnetism are expected to be susceptible to Jahn-Teller (JT) instability.[41-43] Indeed such a distortion, seen by powder neutron diffraction [2], arrive below 140 K with the splitting of degenerated  $t_{2g}$  levels and leads to the loss of the trigonal rotation and six different Fe-O distances as shown in figure II.2.

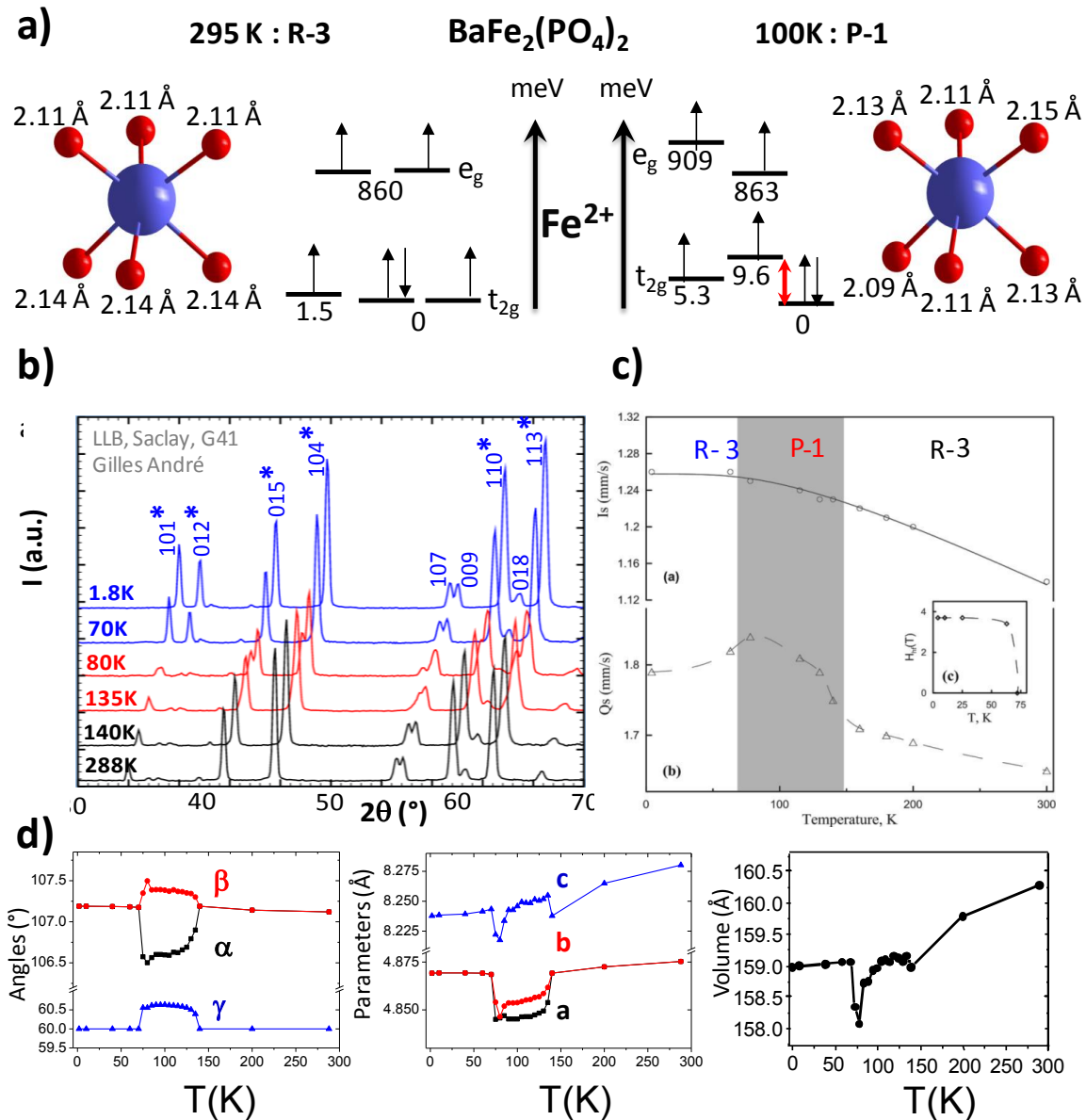


**Figure II.2.** Energetic levels representation of  $\text{Fe}^{2+}$   $d$  orbitals and corresponding iron octahedral structure at room and low temperature (a). Powder neutron diffraction of  $\text{BaFe}_2(\text{PO}_4)_2$  at different temperatures (b) Variation of  $Q_s$  and  $I_s$  Mössbauer parameters versus temperature (c). Unit cell parameters evolution of  $\text{BaFe}_2(\text{PO}_4)_2$  with temperature.

At lower temperature, around 70K, the unit cell suffers an abrupt dilatation and comes back to the initial rhombohedral symmetry. In this low T domain the energy gain for stabilization of the FM order is substantial while its uniaxial FM nature requests the rhombohedral symmetry back.[2]

## 2.2. Fe exsolution at moderate temperatures.

At high temperature, this compound was also shown to display interesting behavior, related in this case to cationic mobility. A reversible Fe-exsolution was demonstrated after heating the phase in air. In this preliminary work [3] performed during the PhD thesis of Rénaud David, the formation of nano-textured  $\alpha$ -Fe<sub>2</sub>O<sub>3</sub> grains after Fe-exsolution in BaFe<sub>2-x</sub>(PO<sub>4</sub>)<sub>2</sub> was discussed from the viewpoint of its complete reversibility and long-Fe diffusion paths able to stabilize fully ordered Fe-depleted at the single crystal scale. Two fully ordered depleted lattices have been reported from crystal XRD data corresponding to:

i)  $x = 2/7$  (i.e.  $\frac{1}{7}$ <sup>th</sup> of Fe vacancies) after aging crystals for long time (+/- 12 months) in grease at room temperature under air.

ii)  $x = 1/3$  (i.e.  $\frac{1}{6}$ <sup>th</sup> of Fe vacancies) after heating single crystals of BaFe<sub>2</sub>(PO<sub>4</sub>)<sub>2</sub> at 550°C for about 5 hours in air.

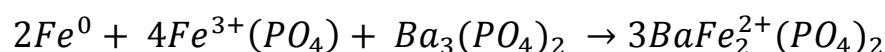
One of the most remarkable fact in this transformation, it is the full reversibility of the reaction all along the exsolution process. It allows supposing the existence of well establish “in plane” cationic mobility pathways, making possible the iron migration from inside to outside the crystal structure and vice-versa.

All along this chapter, we will go forward in the study of BaFe<sub>2</sub>(PO<sub>4</sub>)<sub>2</sub> exsolution process, in order to establish a logic model that would allow us to propose a mechanism and pathways followed by exsolved iron during the thermal treatment. In addition, the selective iron exsolution in BaFe<sub>2-y</sub>M<sub>y</sub>(PO<sub>4</sub>)<sub>2</sub> (M= Co<sup>2+</sup> and Ni<sup>2+</sup>) solid solutions has also been studied, as well as the chemical and electrochemical Li<sup>+</sup> insertion in iron deficient phases.

## 2.3. Further progress in BaFe<sub>2</sub>(PO<sub>4</sub>)<sub>2</sub>.

During my work, I managed the synthesis and extra experiments on BaFe<sub>2</sub>(PO<sub>4</sub>)<sub>2</sub>. For instance the re-entrant transition was re-examined using synchrotron data, and inelastic magnetic scattering was also investigated at the LLB. These results are under investigations and will not be presented in this manuscript. However, dealing with the preparation of this compound – so far exclusively prepared in solvothermal conditions – we have found a solid state route for preparation of the rhombohedral (R) BaFe<sub>2</sub>(PO<sub>4</sub>)<sub>2</sub> phase.

In order to prepare this phase we have formed a new trigonal (T) polytype of BaFe<sub>2</sub>(PO<sub>4</sub>)<sub>2</sub> in evacuated silica tube at 910 °C according to the reaction :



This novel phase will be discussed in the chapter 3. Due to the presence  $\text{Fe}^{2+}$  species in  $\text{T-BaFe}_2(\text{PO}_4)_2$  and by analogy to the behavior of the R-phase, we have studied its thermal stability during heating under air and  $\text{N}_2/\text{H}_2(3\%)$  atmospheres. The HT-XRD patterns are shown on the figure II.3.

The thermal treatment for the in situ XRD consisted in a first step, to heat until  $550^\circ\text{C}$  under air atmosphere, then a thermal plateau is maintained 12h at  $550^\circ\text{C}$  to follow the oxidation of the phase. In a second step, the temperature was kept at  $550^\circ\text{C}$  but the oven atmosphere was purged and changed from air to a mixture  $\text{N}_2/\text{H}_2(3\%)$ , to be in reducing conditions. Sample is maintained for 12h at the same temperature ( $550^\circ\text{C}$ ) in this atmosphere and finally cooled down to room temperature.

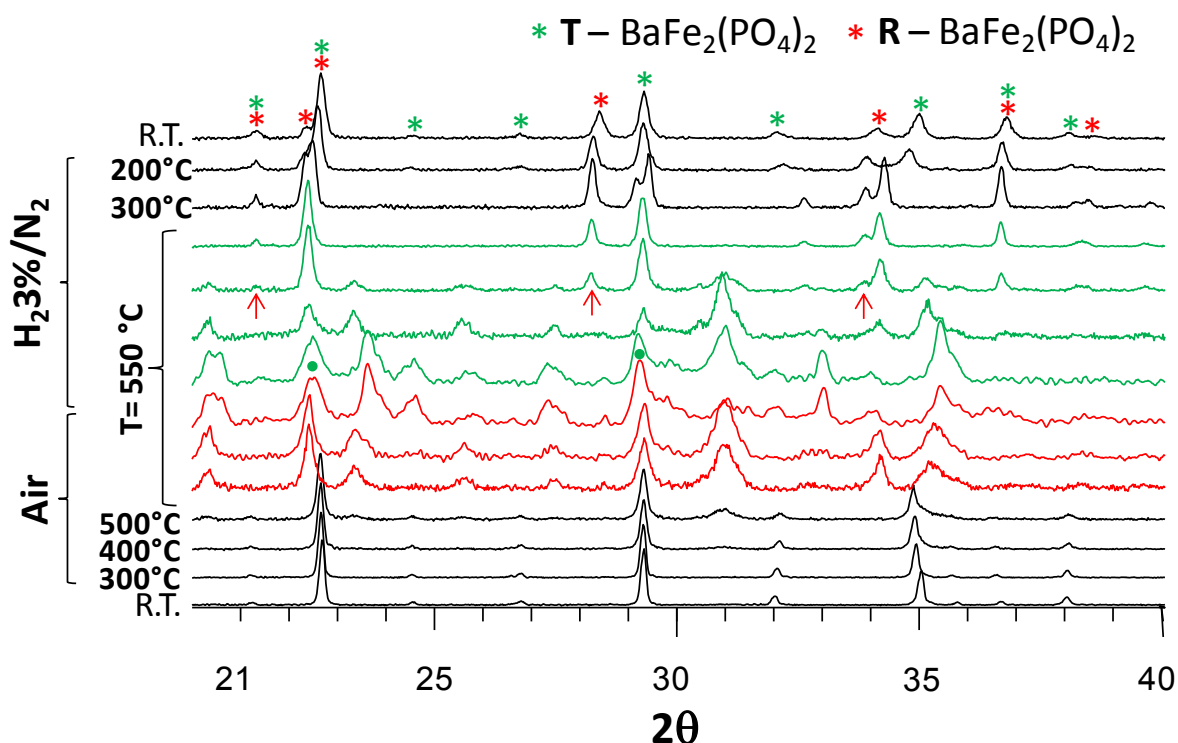


**Figure II.3.** HT-XRD of trigonal  $\text{BaFe}_2(\text{PO}_4)_2$  under air and  $\text{N}_2/\text{H}_2$  (3%) at  $550^\circ\text{C}$ .

The  $\text{T-BaFe}_2(\text{PO}_4)_2$  starts to decompose at  $500^\circ\text{C}$ , however we can observe that at the end of the first plateau (in red figure 3), it remains a little proportion of the phase (indicated with green dots). We can also observe the apparition of new peaks at the end of this first part of the thermal treatment at  $550^\circ\text{C}$ . Unfortunately, the temperature effect makes difficult the identification of these new intermediate phases, we can just say that some peaks could correspond to  $\text{Fe}(\text{PO}_4)$  with slight parameters differences because of the thermal dilatation. The others could be assigned to different Barium/iron mixed oxides.

After this phase transformation at 550°C, the second part of the treatment begun with the atmosphere changed into 3%H<sub>2</sub> N<sub>2</sub> to verify the reversibility of the process. At the beginning, diffractograms show a gradual transformation of the peaks after some hours in the reducing atmosphere, then we can remark the apparition of the peaks corresponding to R-BaFe<sub>2</sub>(PO<sub>4</sub>)<sub>2</sub>, marked with red arrows on figure II.3.

This result is brand new, and further tests will be necessary to succeed in the elaboration of the rhombohedral phase directly from the initial trigonal one with a 100% yield.

### **3. The logic of Fe/VFe ordering in reversible Iron exsolution under soft oxidizing/reducing atmosphere at moderate temperatures.**

#### **3.1. Experimental: Synthesis and characterization techniques.**

The pristine BaFe<sub>2</sub>(PO<sub>4</sub>)<sub>2</sub> was synthesized by hydrothermal method, using microwave heating at 220°C as described previously[2]. Here hydrazine is used as reducing medium for stabilization of the Fe<sup>2+</sup> valence. Powders are formed of tiny light green platelet-like single crystals of the phase as main product and BaHPO<sub>4</sub> second phase. The polycrystalline impurity phase could be fully removed after several hot-water and ethanol rinsing under sonication.

To obtain the intermediate composition BaFe<sub>1.5</sub>(PO<sub>4</sub>)<sub>2</sub>, crystals of the original phase were heated at 550°C in air for 6 hours. For BaFe<sub>1.33</sub>(PO<sub>4</sub>)<sub>2</sub>, the original sample was heated at 600°C for 12h in air. Both of them were cooled down by switching off the oven and washed several times in ethanol by sonication. For the BaFe<sub>1.33</sub>(PO<sub>4</sub>)<sub>2</sub> sample, the complete treatment was carried out once again, in order to make sure the arrival to the most stable compound. Finally at 600°C the XRD pattern stops changing after a two hour treatment which denote fastly reached equilibrium. The aim of sonication under ethanol is to eliminate nano-sized α-Fe<sub>2</sub>O<sub>3</sub> grains, created at the surface of the crystal. The sample was finally dried at 80°C overnight. The light green colored initial phase becomes dark red, signal of the iron oxidation.

Single crystal diffraction of the different phases were collected using a Duo Bruker Kappa APEX 2 diffractometer with Mo Kα radiation (λ=0.7107Å, graphite monochromator) equipped with a detector of CCD (Coupled Charge Device) type. The ω-scan angle was fixed to 0.5° and the D<sub>x</sub> parameter was fixed at 35mm. Diffraction intensities were extracted and

corrected for Lorentz and Polarization using the Bruker program Saint Plus 6.02.[44] The unit-cell parameters were refined from the full data set. Multiscan absorption correction was performed for both compounds using SADABS.[45] Crystal structures were solved by the charge flipping method using the Superflip program[46], Jana 2006 program was used for structure refinements.[47]

Transmission electron microscopy studies and EDS analysis were performed on a FEI Tecnai G2 20. The material was crushed and dropped in the form of aqueous or alcohol suspensions on carbon-supported copper grids followed by evaporation under ambient conditions. The computer simulated HREM images were calculated using the JEMS program.[48]

$^{57}\text{Fe}$  Mössbauer Spectroscopy was performed in a transmission mode using a constant acceleration spectrometer (MS1104, Rostov-na-Donu, Russia) coupled with a nitrogen cryostat. A  $^{57}\text{Co/Rh}$   $\gamma$ -ray source, maintained at room temperature, was used for the measurements. The spectrometers were calibrated with standard  $\alpha$ -Fe or sodium nitroprusside absorbers. All isomer shift values (IS) are referred to  $\alpha$ -Fe. The spectra evaluation was carried out using “UnivemMS” and custom least square fitting software.

### 3.2. New insights in $\text{BaFe}_2(\text{PO}_4)_2$ iron exsolution.

We have re-performed TGA and High Temperature-XRD of the pristine single-phase material and using slow temperature ramps,  $2^\circ\text{C}/\text{min}$ . As mentioned in the section 3.1,  $\text{BaHPO}_4$ , second phase after  $\text{BaFe}_2(\text{PO}_4)_2$  synthesis, was fully removed using several washing stages. When temperature increases, the color change from the initial greenish powder, to black ( $x=0.4$  stoichiometry stabilized after a  $450^\circ\text{C}$  heating stage<sup>12</sup>), and then to dark-reddish ( $x=2/3$  stoichiometry, prepared after a  $650^\circ\text{C}$  heating stage) is shown figure II.4(a). The  $\text{Fe}_2\text{O}_3$  nanometric-size phase presence will be further discussed but can be immediately identified after sonication in ethanol (Fig II.4b) of depleted phases. The red colloidal suspension of nanometric  $\text{Fe}_2\text{O}_3$  grains is stable for +/- 24 hours, before progressive precipitation.

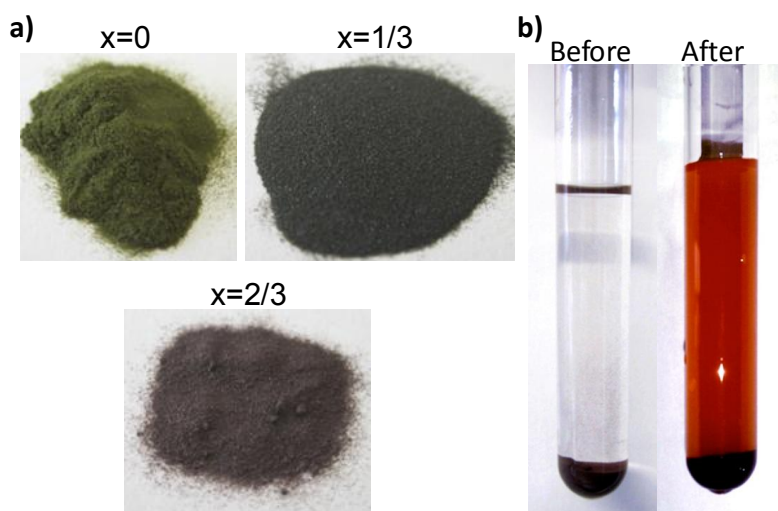


**Figure II.4.** a) Aspect of the powder samples of  $BaFe_{(2-x)}(PO_4)_2$  for  $x=0$ ,  $x=0.4$  and  $x=2/3$ . b) Evidence of  $Fe_2O_3$  colloidal suspension in ethanol before and after  $BaFe_{1.33}(PO_4)_2 + Fe_2O_3$  sonication.

The TGA mass gain starts at  $180^\circ C$  (Fig. II.5) and is ascribed to a rather slow exchange process until  $\sim 440^\circ C$ . In this thermal domain, the XRD patterns show the presence of a unique phase possibly indexed in the parent rhombohedral unit cell. This “low temperature” regime corresponds to the maximal  $x \sim 0.23$  exsolution rate according to the oxidative reaction:

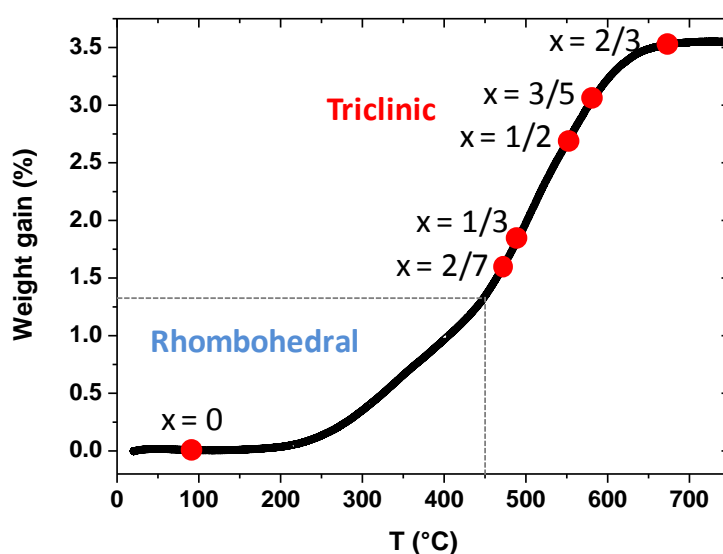


**Figure II.5.** TGA plot of  $BaFe_2(PO_4)_2$  with particular points (red dots) corresponding to ordered single crystals.

$\text{Fe}_2\text{O}_3$  is not yet observed by XRD at this stage, most plausibly due to incoherent nano-sized domains likely coating the surface or intergrown in the crystalline phase, but observed by electron microscopy and Mössbauer spectroscopy. Above  $440^\circ\text{C}$  the evolution of the mass uptake against temperature is more activated. In this range a triclinic distortion caused by significant iron exsolution is observed by the splitting of the XRD peaks. As shown in the prior work [3] from single crystal study and high resolution powder XRD data, the lattice variations versus  $x$ , do not allow refining accurate lattice parameters. Prior unit cell refinements using a common triclinic cell at all temperature (i.e. those from the  $x=1/3$  single crystal model) led to a poor evolution of the triclinic parameters as the temperature increases, possibly due to the compensation between the thermal dilatation and the lattice contraction by Fe-exsolution.[3] Using the equation (1), it is remarkable that the TGA plot suggests a maximal  $x \sim 2/3$  (i.e.  $1/3^{\text{rd}}$  of Fe vacancies) which corresponds to the TGA plateau above  $650^\circ\text{C}$ . Above  $700^\circ\text{C}$ , the Fe-deficient compound transforms into the cubic  $\text{Ba}_{1.5}\text{Fe}^{3+}_2(\text{PO}_4)_3$  of Langbeinite type[49], as discussed in ref [3]. Strikingly even the largest exsolution ratio ( $x = 2/3$ ) proves to be fully reversible during thermal treatment under dilute hydrogen gas-flow as shown on figure II.6. The isothermal ( $T=600^\circ\text{C}$ ) evolution of XRD patterns, presented in figure II.6, shows that the return back to the rhombohedral phase is completed after 5 hours. Concerning the exsolution itself, the TGA plot above  $440^\circ\text{C}$  shows a continuous delivery of  $\text{Fe}_2\text{O}_3$  particles. For instance it is remarkable that no TGA anomaly were detected for  $x$  values =  $2/7$  and  $1/3$  (shown in red, figure II.5) although both compositions correspond to fully ordered  $\text{Fe}/V_{\text{Fe}}$  lattices refined from single crystal diffraction data.[3] It suggests that a variety of fully or not ordered lattices probably paves the  $\text{BaFe}_{2-x}(\text{PO}_4)_2$  phase diagram. In fact, all red dots of the figure II. 5 correspond to prior or novel compositions that we have isolated in single crystals. Their structural analysis has been rationalized during my PhD work.

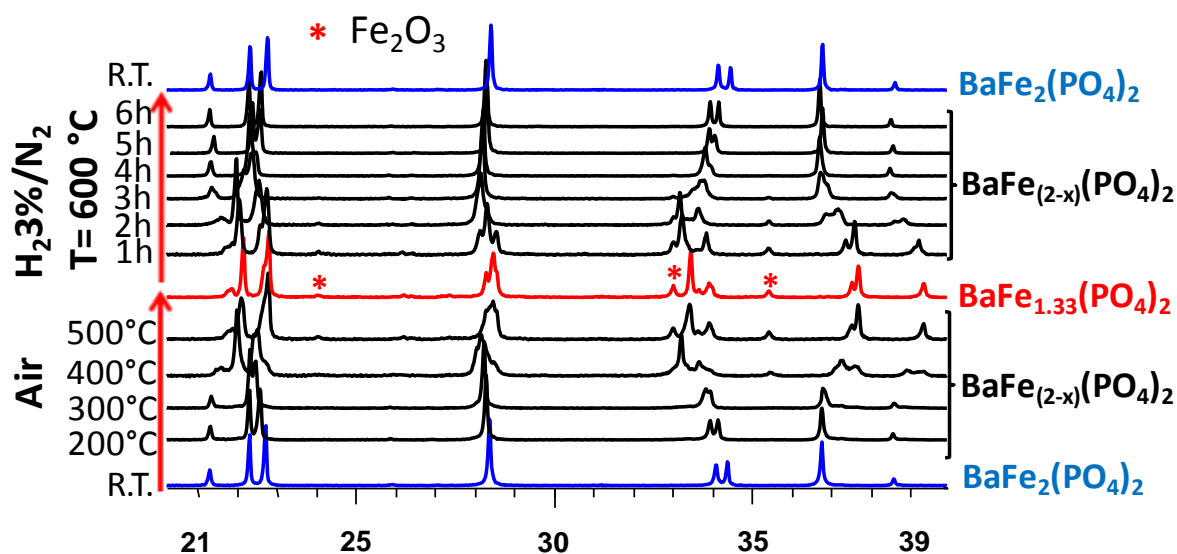


**Figure II.6.** HT-XRD under air (increase) and isotherm at 600°C under  $H_2(3\%)/Ar$  atmosphere of  $BaFe_2(PO_4)_2$ .

### 3.3. Microstructural aspects.

#### 3.3.1. $BaFe_{2-x}(PO_4)_2$ polycrystals.

The evidence of possible exsolution of 1/3rd of the initial Fe content ( $x=2/3$ ) is a brand new result compared to previous reports dealing with  $x = 0.4$  at maximum.[3] The  $BaFe_{1.33}(PO_4)_2$  polycrystalline samples can be prepared after heating at 600°C for 24h. The  $[1\bar{1}0]$  zone axis of the rhombohedral subcell electron diffraction pattern simulated from the single crystal structure details below evidences supercell spots in good agreement with those observed experimentally (Fig. II.7a,b) which comfort the validity of our refined model. They are due to the  $Fe/V_{Fe}$  ordering and to local distortion (e.g. Ba shifts) ordered in the supercell.

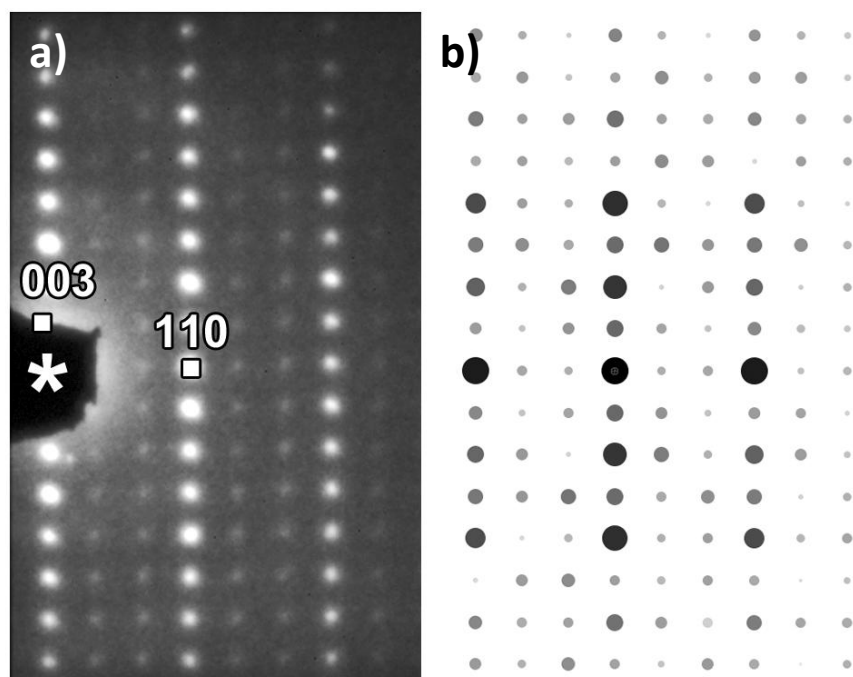


**Figure II.7.** Electron microscopy study for polycrystalline  $\text{BaFe}_{1.33}(\text{PO}_4)_2$ , *a,b*) Experimental and simulated ED pattern of  $[1\bar{1}0]_R$  zone axis with evidences of weak predicted supercell spots. Reflections are indexed in the rhombohedral subcell. The 110 and 003 spots correspond respectively to the 303 and  $0\bar{1}\bar{1}$  spots of the triclinic supercell.

The refined lattice parameters using synchrotron radiation XRD data ( $\lambda = 0.41967 \text{ \AA}$ ) gives  $a = 8.233(4) \text{ \AA}$ ,  $b = 9.622(6) \text{ \AA}$ ,  $c = 12.742(3) \text{ \AA}$ ,  $\alpha = 78.169(4)^\circ$ ,  $\beta = 77.555(0)^\circ$ ,  $\gamma = 73.448(4)^\circ$ ,  $\chi^2 = 1.904$ , in good agreement with the single crystal data (annex), as we can observe on figure II.8(a). Although a particular attention was paid to a fine grinding and sieving during the sample preparation, good profiles have been only obtained using two similar crystallographic phases with different microstructures due to the crystalline anisotropy (platelet crystallites) of the as-prepared prepared pristine phase which is expected to be preserved after Fe exsolution. Typically, coherent domains around  $0.2 \mu\text{m}$  are found in the most isotropic fraction of the sample. The  $\alpha\text{-Fe}_2\text{O}_3$  phase was also considered in the refinement. For  $x = 2/3$ , the powder diffractogram data significantly differs from those collected for  $\text{BaFe}_{1.6}(\text{PO}_4)_2$ , i.e.  $x = 0.4$ , ( a sample studied during the thesis of R nald David, see ref.[3] for details of the preparation). In this latter case, though clear similitudes between the experimental and calculated patterns using the  $x = 1/3$  structural model parameters (figure II.8b) the contribution of one or more additional phase(s) was detected (most probably the  $\text{BaFe}_{1.5}(\text{PO}_4)_2$  stoichiometry discussed below and no far in the exsolution-phase-diagram). Exaggerated overlaps and complex microstructure effects did not allow to achieve a good

pattern matching. At least, it is relevant that tuning the thermal conditions allows preparing distinct  $x$  compositions in large sample amounts.

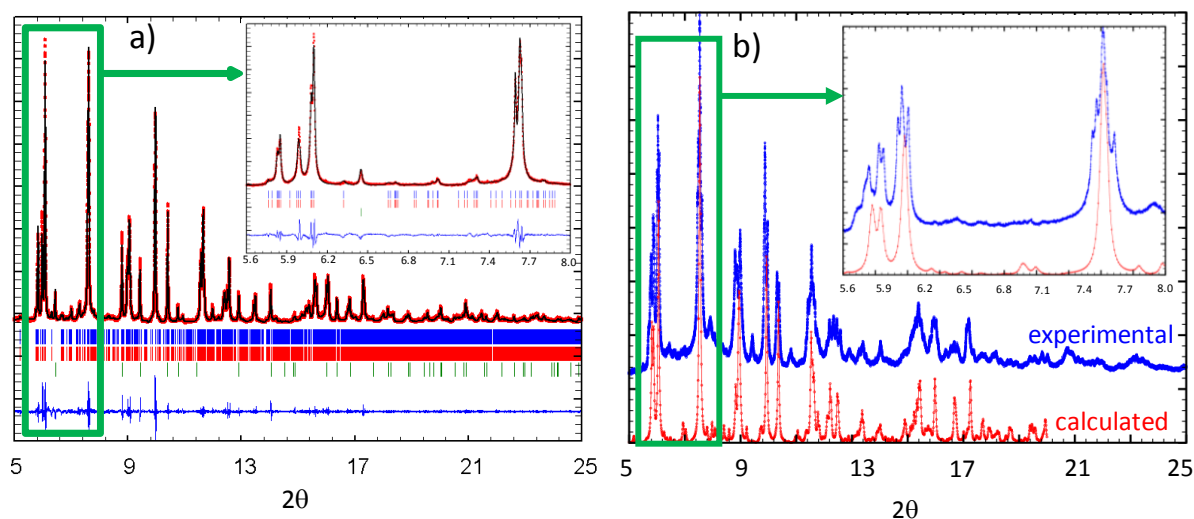


**Figure II.8.** a) XRD full pattern matching for  $x=2/3$  using two  $BaFe_{1.33}(PO_4)_2$  phases with different microstructures and  $\alpha\text{-Fe}_2O_3$ . b) XRD pattern for the composition corresponding to  $x=0.6$  (sample from ref.<sup>12</sup>) proving the major  $BaFe_{1.66}(PO_4)_2$  presence with together with other  $x$  stoichiometries. Data have been collected using synchrotron radiation (11BM Argonne source,  $\lambda = 0.42 \text{ \AA}$ ).

### 3.3.2. Production of $Fe_2O_3$ nanoparticles.

According to equation (1), the maximal oxidation until  $x = 2/3$  consists of the transformation of  $\sim 12$  wt % of initial mass into  $Fe_2O_3$  particles, able to be reincorporated in the phase in mild reducing conditions. A direct observation of the  $Fe_2O_3$  grains was performed by transmission electron microscopy (TEM) on a sample of  $BaFe_2(PO_4)_2$  heated at  $600^\circ\text{C}$  for 12 hours, see figure II.9. It shows  $Fe_2O_3$  islets coating  $BaFe_{2-x}(PO_4)_2$  crystals surfaces. Qualitative Energy dispersive spectroscopy analysis confirms that exsolved nanoparticles consist of iron oxide (Fig. II.9b) in contrast to the stoichiometric amount of Ba and P detected in the grains. We measured by TEM analysis a distribution of  $Fe_2O_3$  crystal size with typical particle of  $\sim 50$  nm diameter at the close  $BaFe_{2-x}(PO_4)_2/Fe_2O_3$  contacts. It seems that  $Fe_2O_3$  grains can grow by agglomeration upon heating and some observed grains can reach up to 400 nm (Fig. II.9b). After exsolution at  $600^\circ$  for 12 hours under air we calculated from the  $Fe_2O_3$ .

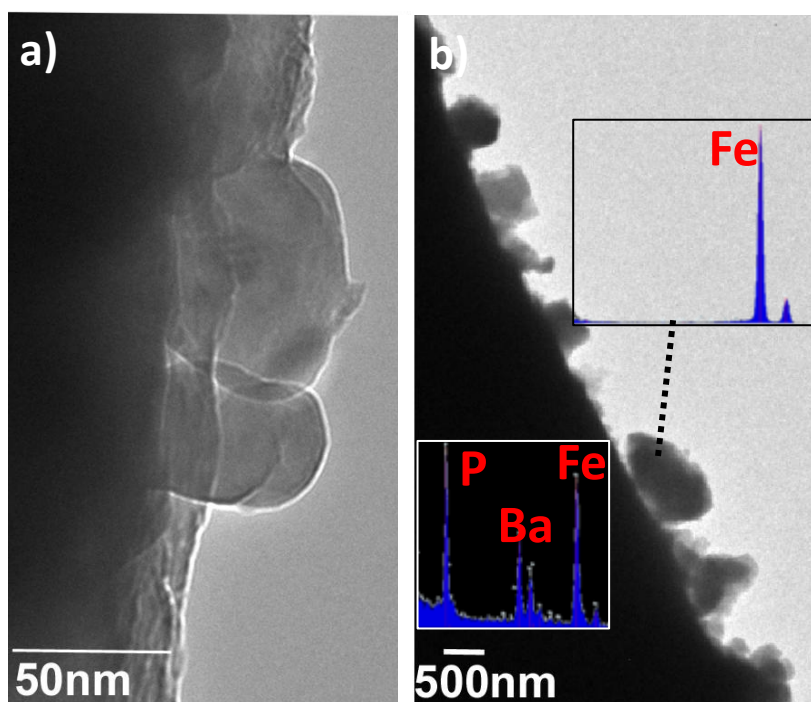


**Figure II.9.** TEM images (a, b) and Energy Dispersive spectra (b) of the  $\text{BaFe}_{2-x}(\text{PO}_4)_2$  surfacial coating by  $\text{Fe}_2\text{O}_3$  at different scales.

XRD profile an average size of coherent diffracting domains of  $\pm 70$  nm using the Scherrer law. The nanometric character of the produced  $\text{Fe}_2\text{O}_3$  was confirmed by Mössbauer spectroscopy. It is known that at 263K, bulk  $\alpha\text{-Fe}_2\text{O}_3$  undergoes a first-order spin reorientation so-called the Morin transition, which appears in Mössbauer spectra as a change in the apparent quadrupole shifts ( $\Delta E_Q$ ) from ac. -0.2 mm/s to +0.4 mm/s. Because of intrinsic finite size effects related to lattice expansion, strains, defects, shape etc; the Morin temperature of small  $\text{Fe}_2\text{O}_3$  particles decreases with decreasing particle size and tends to be below 4K for particles smaller than ac. 8-20 nm[50, 51]. As deduced from Mössbauer spectra collected at 78K (Table II.3), only  $\sim 2/3^{\text{rd}}$  of the produced  $\text{Fe}_2\text{O}_3$  after exsolution of  $\text{BaFe}_2(\text{PO}_4)_2$  underwent the Morin transition, consistently with a significant amount of nanometric clusters. For comparison for  $\text{BaFe}_{1.67}(\text{PO}_4)_2$  obtained at lower temperature, we reported that only  $\sim 1/5^{\text{th}}$  of  $\alpha\text{-Fe}_2\text{O}_3$  underwent the transition at 78K.<sup>12</sup> It suggests a grain growth of the exsolved  $\text{Fe}_2\text{O}_3$  grains as the temperature increases.

### 3.4. Crystal chemistry of the Fe-depleted layers.

It is important that we are dealing in this section with very complex crystal-chemistry for all  $\text{BaFe}_{2-x}(\text{PO}_4)_2$  compounds, as it was already the case during the prior resolution of the  $x = 2/7$  and  $1/3$  compounds from single crystal XRD. In general all the treated compounds crystallize in triclinic supercells of the average rhombohedral  $\text{BaFe}_2(\text{PO}_4)_2$  phase. So defects, pseudo symmetries, twinnings and composite crystals between two close compositions partially damage XRD data, quasi systematically. In addition the superlattice satellites, are as usual very weak compared to the main spots. The figure II.10 shows typical precession frames reconstructed for different  $x$  values. They are presented in the parent  $\text{BaFe}_2(\text{PO}_4)_2$  cell orientation for comparison.

The 2D-Honeycomb  $\infty\{\text{Fe}_2\text{O}_6\}$  layer with trigonal symmetry (space group R-3) of the pristine  $\text{BaFe}_2(\text{PO}_4)_2$  is shown on the figure II. 10(a). In this figure  $w$  denote the honeycomb windows, linked to the  $\text{PO}_4$  groups pointing towards the interleaves. From previous XRD analysis [3] one can say that after creation of  $\frac{1}{7}$ <sup>th</sup> of vacancies ( $x=2/7$ ) the symmetry is lowered from trigonal to triclinic (S.G. P-1). The  $\text{Fe}^{2+}$  ions are confined in strongly distorted  $\text{FeO}_6$  sites while mixed  $\text{Fe}^{2/3+}$  ions are distributed in regular  $\text{FeO}_6$  octahedra, as shown by both bond valence sum (BVS) calculations and Mössbauer spectroscopy.[3] The corresponding fully ordered Fe-depleted  $\infty\{\text{Fe}_{12/7}\text{O}_6\}$  layer is shown on the figure II. 10(b) and is composed of  $5/7$ <sup>th</sup> of regular  $\text{FeO}_6$  octahedra,  $1/7$ <sup>th</sup> of strongly distorted and  $1/7$ <sup>th</sup> of vacancies. The refined formula indicates a mean  $\text{Fe}^{2.33+}$  valence state.

Here again from previous data, after creation of  $\frac{1}{6}$ <sup>th</sup> of vacancies ( $x=1/3$ , S.G. P-1) , the resulting  $\infty\{\text{Fe}_{5/3}\text{O}_6\}$  contains  $4/6$ <sup>th</sup> of regular  $\text{Fe}^{2/3+}$  octahedra,  $1/6$ <sup>th</sup> of strongly distorted  $\text{Fe}^{2+}$  sites and  $1/6$ <sup>th</sup> of vacancies , Figure II.10(c). Note that for both  $x=2/7$  and  $x=1/3$ , the distorted  $\text{Fe}^{2+}\text{O}_6$  are elongated along one unique direction in each layer. In these two crystal structures, unit cells contain two independent Fe-depleted layers such as presented in figure II.10(b,c), which are tilted by about  $120^\circ$  from each other. From the viewpoint of crystallography, it is atypical that the complementary  $240^\circ$  tilted motif does not exist (except via twin interfaces), collapsing the structural trigonality, though the trigonal parent symmetry of  $\text{BaFe}_2(\text{PO}_4)_2$ . [3]

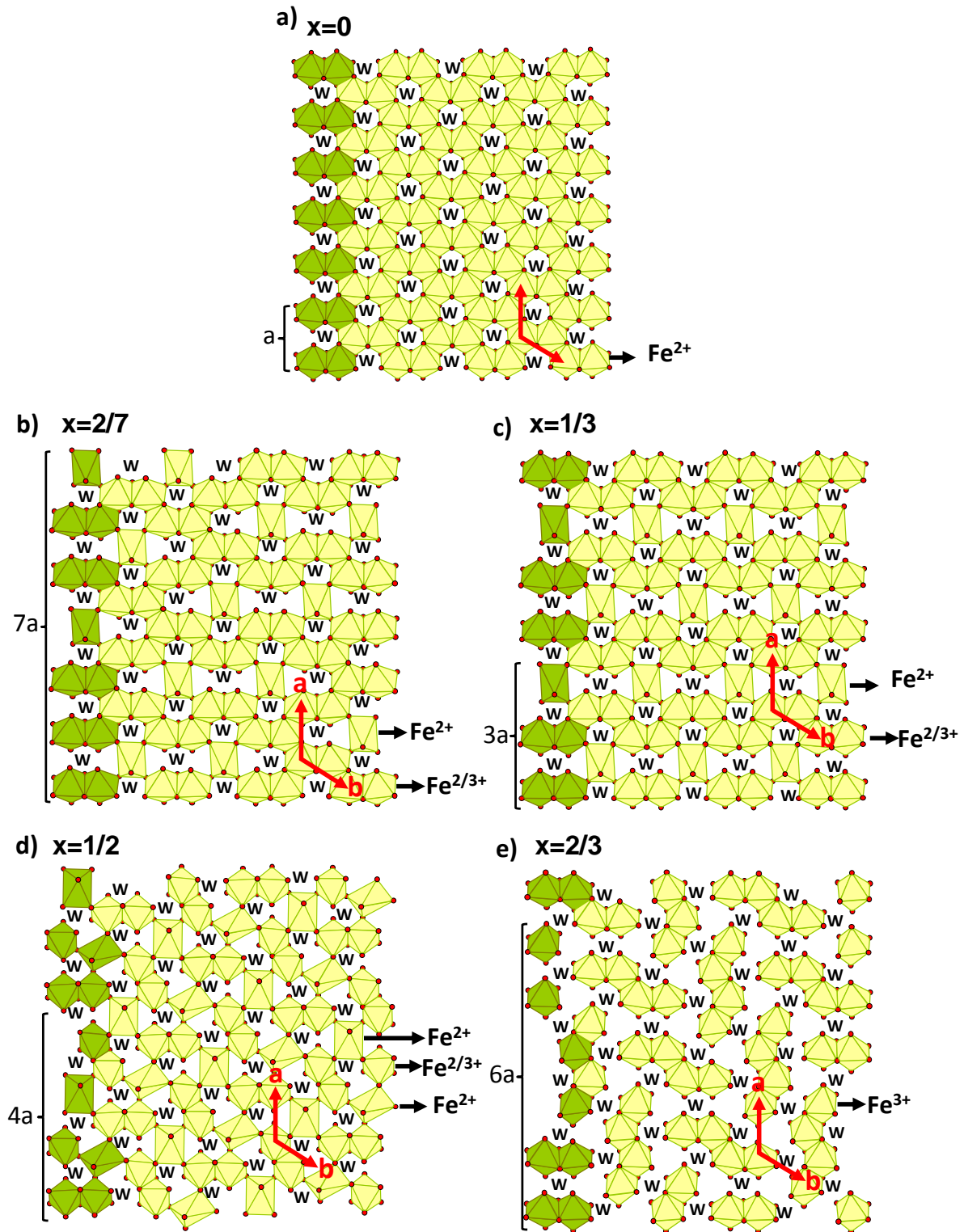


**Figure II.10.** Projection in the parent trigonal  $(ab)$  plane (red axes) of the Fe-depleted 2D-lattices as a function of  $x$  (a to e) for  $\text{BaFe}_{2-x}(\text{PO}_4)_2$  phases. The distribution of  $\text{Fe}^{2+} / \text{Fe}^{2+/3+} / \text{Fe}^{3+}$  is given. For each figures the green column represent the 1D-motif paving the layers. W stand for the windows of the original Honeycomb layers (a) linked to external  $\text{PO}_4$  groups.

### 3.4.1. Intermediate exsolution ratio: Crystal Structure of BaFe<sub>1.5</sub>(PO<sub>4</sub>)<sub>2</sub>.

Single crystals corresponding to x=1/2 stoichiometry i.e. (1/4<sup>th</sup> of Fe vacancies) were found in an inhomogeneous mixture obtained after heating single crystals of the pristine phase at 650°C for two hours, i.e. before completed exsolution. A preliminary refinement was achieved in the parent rhombohedral subcell with parameters a = 4.774(4) Å c = 24.237(4) Å. The subcell allows quantifying the proportion of regular and distorted Fe<sup>2+</sup>O<sub>6</sub> expected in distinct positions 6c (0, 0, z~1/3) and 9e (1/2, 0, 0) respectively, leading to a relatively high R<sub>obs</sub>= 12.78%, with final formula BaFe<sub>1.52</sub>(PO<sub>4</sub>)<sub>2</sub> and 1.1 : 0.42 ratio between regular Fe<sup>3+</sup>O<sub>6</sub> octahedra (6c ; 0,0, z~1/3) and distorted Fe<sup>2+</sup>O<sub>6</sub> octahedra (9e ; 1/2,0,0). Taking into account the supercell reflections due to the Fe/V<sub>Fe</sub> ordering, it was possible to fully index the collected reflections in the triclinic unit cell related to the rhombohedral one by:

$$\begin{matrix} a_{Tricl} \\ a_{Tricl} \\ a_{Tricl} \end{matrix} = \begin{bmatrix} 4 & 0 & 0 \\ -1 & 1 & 0 \\ 1/3 & 2/3 & 1/3 \end{bmatrix} \begin{matrix} a_{Rhomb} \\ b_{Rhomb} \\ c_{Rhomb} \end{matrix}$$

In the crystal we found three twinned domains related by ~120° and ~240° around c\* domains, as verified using the program CellNow.[52] Similar twin laws were also observed in our previous work dealing with x= 2/7 and 1/6.[3] It is due to the subgroup relations between the parent rhombohedral and final triclinic symmetries but conserves the regular spacing between the individual layers in the full crystal. A fully ordered model was refined (a = 19.101(2) Å, b = 8.271(8) Å, c = 8.5254 Å, α = 99.55(9)°, β = 89.7181°, γ = 149.942°, R = 13.79% ) leading to the final formula BaFe<sup>+2.66</sup><sub>1.5</sub>(PO<sub>4</sub>)<sub>2</sub> (x=0.5) with a distribution of empty and fully occupied Fe positions (CSD-number 429450). The ∞{Fe<sub>3/2</sub>O<sub>6</sub>} Fe-depleted layers are shown in the figure II.10(d) and will be discussed latter. The relatively high R in both the subcell and the supercell denote the poor quality of the crystal with inclusion of domains with different stoichiometry. For instance we observed in the reconstructed precessions frames weak reflections belonging to minor domains of BaFe<sub>1.66</sub>(PO<sub>4</sub>)<sub>2</sub>. The fully ordered repartition between elongated Fe<sup>2+</sup>O<sub>6</sub> and regular Fe<sup>3+</sup>O<sub>6</sub> leads to the expected valence Fe<sup>+2.66</sup> within a charge ordered system. It is in good agreement with BVS calculated from Fe-O distances; the interatomic distances, together with the iron BVS values are presented in Table II.1. Details about the single crystal data collection and the structure refinement are reported in annex.

**Table II.1.** Interatomic distances and corresponding iron Bond Valence Sum ( $\Sigma s_{ij}$ ) values, calculated using parameters associated to  $Fe^{+2}$  from reference [51], for  $BaFe_{1.5}(PO_4)_2$ .

Distances d (Å)							
<i>BaFe<sub>1.5</sub>(PO<sub>4</sub>)<sub>2</sub></i>							
<i>Fe ions</i>							
<b>Fe1-O2</b>	2.00(3)	<b>Fe2-O3</b>	1.92(2)	<b>Fe3-O6</b>	2.35(9)x2	<b>Fe4-O3</b>	2.39(7)x
<b>Fe1-O2</b>	2.16(3)	<b>Fe2-O8</b>	2.02(8)				2
<b>Fe1-O6</b>	1.88(9)	<b>Fe2-O8</b>	2.08(1)	<b>Fe3-O15</b>	2.30(7)x2	<b>Fe4-O10</b>	1.80(0)x
<b>Fe1-O7</b>	1.99(6)	<b>Fe2-O9</b>	1.94(8)				2
<b>Fe1-O11</b>	2.02(9)	<b>Fe2-O13</b>	2.01(9)	<b>Fe3-O16</b>	1.91(3)x2	<b>Fe3-O11</b>	2.35(4)x
<b>Fe1-O12</b>	1.94(1)	<b>Fe2-O15</b>	2.00(4)				2
$\Sigma s_{ij}$	3.1(2)	$\Sigma s_{ij}$	3.06(2)	$\Sigma s_{ij}$	2.03(1)	$\Sigma s_{ij}$	2.17(1)
<i>P ions</i>							
<b>P1-O5</b>	1.59(1)	<b>P2-O3</b>	1.55(0)	<b>P3-O4</b>	1.54(5)	<b>P4-O1</b>	1.52(2)
<b>P1-O8</b>	1.58(0)	<b>P2-O7</b>	1.51(4)	<b>P3-O6</b>	1.67(4)	<b>P4-O2</b>	1.58(2)
<b>P1-O12</b>	1.60(9)	<b>P2-O11</b>	1.66(4)	<b>P3-O9</b>	1.57(5)	<b>P4-O10</b>	1.60(9)
<b>P1-O16</b>	1.58(5)	<b>P2-O14</b>	1.58(5)	<b>P3-O15</b>	1.64(7)	<b>P4-O13</b>	1.57(5)
<i>1. Ba ions</i>							
<b>Ba1-O1</b>	2.71(8)x2	<b>Ba3-O4</b>	2.76(0)	<b>Ba3-O14</b>	2.86(1)		
		<b>Ba3-O5</b>	2.59(7)	<b>Ba3-O14</b>	2.81(2)		
<b>Ba2-O1</b>	2.63(9)x2	<b>Ba3-O10</b>	2.86(1)				

### 3.4.2. Ultimate exsolution: Crystal structure of $BaFe_{1.33}(PO_4)_2$ .

Single crystals corresponding to  $x=0.66$  ( $\frac{1}{3}$ <sup>rd</sup> of Fe vacancies) were analyzed by XRD. Similarly to the two previous cases, precession frames calculated from the collected data set show existence of main spots that correspond to the rhombohedral subcell, together with weaker satellite spots due to the Fe/vacancy ordering and local rearrangements. Once again, It can be fully indexed in the triclinic unit cell with parameters  $a=8.241(3)$  Å,  $b=9.642(6)$  Å,  $c=12.699(9)$  Å,  $\alpha=78.197(1)^\circ$ ,  $\beta=77.508(5)^\circ$ ,  $\gamma=73.469(5)^\circ$  using three twin domains tilted of  $\sim 120^\circ$  and  $\sim 240^\circ$  around [011] in the reciprocal base, as verified using the program CellNow.[52] The relationship between the triclinic supercell and the rhombohedral subcell is given this time by:

$$\begin{matrix} a_{Tricl} \\ a_{Tricl} \\ a_{Tricl} \end{matrix} = \begin{bmatrix} -1 & -2 & 0 \\ -4/3 & -2/3 & -1/3 \\ 5/3 & -1/3 & -1/3 \end{bmatrix} \begin{matrix} a_{Rhomb} \\ b_{Rhomb} \\ c_{Rhomb} \end{matrix} .$$

In a first stage the crystal structure was refined in the R-3 subcell ( $a = 4.760(4)$  Å,  $c = 23.793(6)$  Å,  $R_{obs} = 4.00\%$ ) using the  $BaFe_2(PO_4)_2$  model. We found the  $BaFe_{1.35}(PO_4)_2$  formula with empty distorted octahedral  $Fe^{2+}$  positions. It comforts the iron valence close to +3, and the absence of elongated  $Fe^{2+}O_6$  polyhedra in 9e sites.

In a second stage, the supercell crystal structure was refined using the full collected dataset in the P-1 space group. Several models can be determined from both charge flipping

and direct methods among which only one shows fully ordered empty and vacant Fe positions together with the lower  $R_{\text{obs}} = 5.96\%$ . It leads to the formula  $\text{BaFe}_{1.33}(\text{PO}_4)_2$  (CSD-number 429449). The unit cell contains one independent  $\infty\{\text{Fe}_{4/3}\text{O}_6\}$  layer separated by  $\sim 8\text{\AA}$ . The refined 2D-lattice is shown in the figure II.10(e). Concerning the octahedral array, it consists of a complex arrangement between  $2/3^{\text{rd}}$  of regular  $\text{FeO}_6$  octahedra and  $1/3^{\text{rd}}$  of vacancies, leaving isolated edge sharing octahedral tetramers. All oxygen corners are shared by  $\text{PO}_4$  groups. The 2D-layers significantly differ from those refined for low x values. We note that even after heating crystals of the pristine phase at  $450^\circ\text{C}$  under oxygen pressure, the crystals found have same lattice parameters and XRD precessions frames.

Interatomic distances and Fe BVS values are listed in the Table X. BVS [53] for the four  $\text{Fe}^{3+}$  ions (sites 1-4) are +2.86, +3.04, +3.10 and +3.02 respectively. It corresponds well to the full trivalent states in this ultimately Fe-depleted phase. Details about the single crystal data collection and the structure refinement are reported in annex. The atomic coordinates together with the anisotropic displacements are reported in annex.

**Table II.2.** Interatomic distances and corresponding iron Bond Valence Sum ( $\Sigma s_{ij}$ ) values, calculated using parameters associated to  $\text{Fe}^{+2}$  from reference[53], for  $\text{BaFe}_{1.33}(\text{PO}_4)_2$ .

Distances d (Å)							
<i>BaFe</i> <sub>1.33</sub> ( <i>PO</i> ) <sub>2</sub>							
<i>Fe ions</i>							
<b>Fe1-O5</b>	2.00(3)	<b>Fe2-O9</b>	1.94(2)	<b>Fe3-O3</b>	1.93(2)	<b>Fe4-O4</b>	1.92(4)
<b>Fe1-O6</b>	2.16(3)	<b>Fe2-O11</b>	2.09(3)	<b>Fe3-O6</b>	2.23(3)	<b>Fe4-O11</b>	2.00(2)
<b>Fe1-O8</b>	1.94(3)	<b>Fe2-O17</b>	1.90(2)	<b>Fe3-O7</b>	1.95(3)	<b>Fe4-O12</b>	2.00(3)
<b>Fe1-O10</b>	2.03(2)	<b>Fe2-O19</b>	2.08(2)	<b>Fe3-O7</b>	2.17(2)	<b>Fe4-O12</b>	2.15(3)
<b>Fe1-O13</b>	2.06(2)	<b>Fe2-O20</b>	2.09(3)	<b>Fe3-O13</b>	1.98(3)	<b>Fe4-O19</b>	2.13(2)
<b>Fe1-O24</b>	2.05(3)	<b>Fe2-O22</b>	2.01(4)	<b>Fe3-O18</b>	1.90(2)	<b>Fe4-O23</b>	1.94(3)
$\Sigma s_{ij}$	2.85(8)	$\Sigma s_{ij}$	3.03(9)	$\Sigma s_{ij}$	3.09(9)	$\Sigma s_{ij}$	3.02(1)
<i>P ions</i>							
<b>P1-O3</b>	1.53(3)	<b>P2-O11</b>	1.60(3)	<b>P3-O2</b>	1.48(3)	<b>P4-O1</b>	1.58(3)
<b>P1-O13</b>	1.64(3)	<b>P2-O21</b>	1.52(3)	<b>P3-O4</b>	1.54(4)	<b>P4-O6</b>	1.48(3)
<b>P1-O16</b>	1.47(3)	<b>P2-O22</b>	1.55(3)	<b>P3-O8</b>	1.50(2)	<b>P4-O9</b>	1.58(3)
<b>P1-O24</b>	1.55(3)	<b>P2-O23</b>	1.47(3)	<b>P3-O19</b>	1.58(2)	<b>P4-O18</b>	1.57(3)
<b>P5-O5</b>	1.54(3)	<b>P6-O7</b>	1.61(2)				
<b>P5-O12</b>	1.58(3)	<b>P6-O10</b>	1.53(3)				
<b>P5-O14</b>	1.50(2)	<b>P6-O15</b>	1.49(3)				
<b>P5-O20</b>	1.48(3)	<b>P6-O17</b>	1.56(3)				
<i>Ba ions</i>							
<b>Ba1-O14</b>	2.80(2)x2	<b>Ba2-O2</b>	2.79(3)x2	<b>Ba3-O1</b>	2.84(3)	<b>Ba4-O1</b>	2.71(3)
<b>Ba1-O21</b>	2.74(3)x2	<b>Ba2-O15</b>	2.86(3)x2	<b>Ba3-O2</b>	2.77(3)	<b>Ba4-O15</b>	2.72(3)
				<b>Ba3-O14</b>	2.83(2)	<b>Ba4-O16</b>	2.75(2)
				<b>Ba3-O14</b>	2.82(2)	<b>Ba4-O21</b>	2.79(3)

**3.4.3. Iron oxidation state in BaFe<sub>1.33</sub>(PO<sub>4</sub>)<sub>2</sub>.**

The ambient temperature Mössbauer spectra of the three available polycrystalline samples: x=0 [2], x=0.4 [3] and x =2/3 are compared in figure II.11. For x=2/3, it was measured without post Fe<sub>2</sub>O<sub>3</sub> sonication and washing. It consists of a paramagnetic component ascribed to BaFe<sub>1.33</sub>(PO<sub>4</sub>)<sub>2</sub> phase and a magnetically split component of α-Fe<sub>2</sub>O<sub>3</sub>, Fig II.11(c). The paramagnetic part was fitted with two doublets of equal contributions (Table II.3). According to their isomer shifts (ISs), both belong to Fe<sup>3+</sup> cations in octahedral oxygen coordination. It proves the single Fe<sup>3+</sup> valence state of iron in as-prepared BaFe<sub>1.33</sub>(PO<sub>4</sub>)<sub>2</sub> following our thermal treatment. The D2 doublet with slightly higher IS was ascribed to Fe<sup>3+</sup> cations in larger central Fe(3,4) sites (<dFe(3, 4)-O> = (2.06, 2.03)Å) in the octahedral tetramers, while the D1 doublet correspond to smaller terminal Fe(1,2)O<sub>6</sub> sites (<dFe(1, 2)-O> = 2.016Å). For comparison, figure II.11(a, b) show the Mössbauer spectra of the pristine BaFe<sub>2</sub>(PO<sub>4</sub>)<sub>2</sub> with solely Fe<sup>2+</sup> ions, and the mixed valent Fe<sup>2+</sup>/Fe<sup>3+</sup> BaFe<sub>1.6</sub>(PO<sub>4</sub>)<sub>2</sub> from reference[3]. The spectral atomic contribution of ~36% (at 78K) of the Fe<sub>2</sub>O<sub>3</sub> sextets is close to its amount determined from the reaction (1), viz. 33.3%, proving the chemical composition as BaFe<sub>1.33</sub>(PO<sub>4</sub>)<sub>2</sub>.

**Table II.3.** <sup>57</sup>Fe Mössbauer Hyperfine Parameters of BaFe<sub>1.33</sub>(PO<sub>4</sub>)<sub>2</sub> in absence of Fe<sub>2</sub>O<sub>3</sub> washing. (IS, isomer shift relative to α-Fe at ambient temperature; ΔE<sub>Q</sub>, apparent quadrupole shift; H<sub>Hf</sub>, magnetic hyperfine field; G, line width; A, relative spectral area)

T, K	Component	IS, mm/s ± 0.01	ΔE <sub>Q</sub> , mm/s ± 0.01	H <sub>Hf</sub> , T ± 0.1	A % ± 1	G, mm/s ± 0.01	Assignment
<b>300K</b>	S1	0.37	-0.14	51.8	38	0.34	Fe <sub>2</sub> O <sub>3</sub>
	D2	0.40	1.19	-	31	0.28	Fe <sup>3+</sup> (1)
	D3	0.42	0.81	-	31	0.27	Fe <sup>3+</sup> (2)
<b>78K</b>	S1	0.49	0.32	54.0	24	0.28	Fe <sub>2</sub> O <sub>3</sub> (i) in Morin tr.
	S2	0.49	0.02	53.7	12	0.30	Fe <sub>2</sub> O <sub>3</sub> (ii) no Morin tr.
	D3	0.52	1.18	-	32	0.26	Fe <sup>3+</sup> (1)
	D4	0.54	0.81	-	32	0.26	Fe <sup>3+</sup> (2)

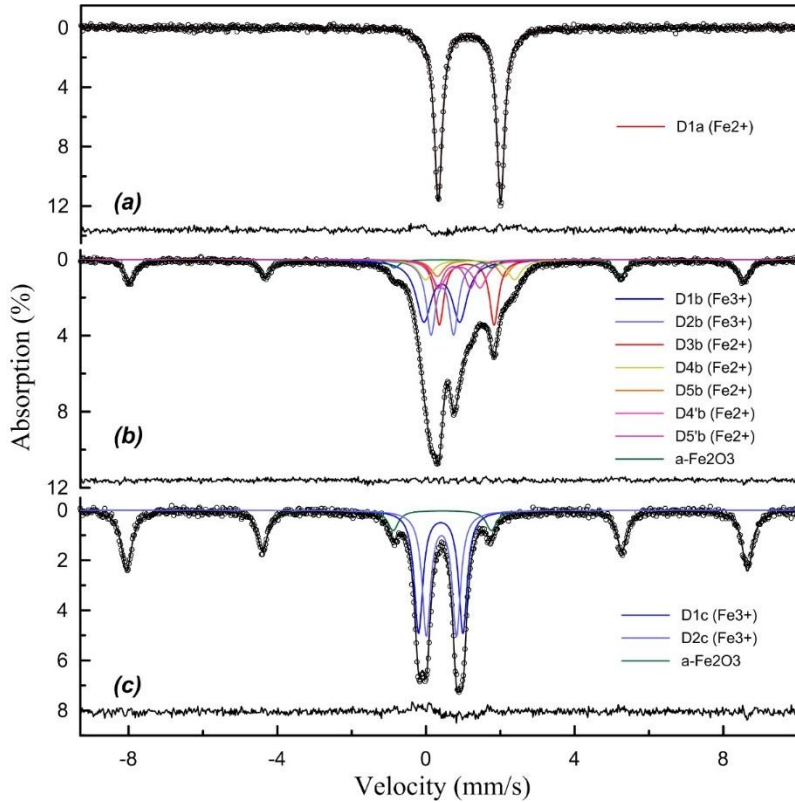


**Figure II.11.** Mössbauer spectra for a)  $BaFe_2(PO_4)_2$ , b)  $BaFe_{1.66}(PO_4)_2$  and c)  $BaFe_{1.33}(PO_4)_2$  with labelled fitted components.

#### 3.4.4. Generalization of $Fe/V_{Fe}$ ordering versus $x$ .

One motivation of my PhD work concerns the understanding of structural relationships at various exsolution ratio, most plausibly ruling the metal exsolution mechanism. The fine examination of all refined crystal structures allows highlighting particular features common to the full series. For this, we found a great interest to consider 1D columns containing edge-sharing Fe/Fe dimers growing along the trigonal a-axis of the pristine compound and their modifications in the exsolved phases, as shown in green in figures II.12, 13 and 14. So, what happens to dimers after Fe-exsolution ?

- *Small  $x$  values ( $x=2/7$ ,  $x=1/3$ ):*

After Fe-exsolution, the creation of vacancies in one column involves the coalescence of one dimer into one distorted/elongated  $Fe^{2+}O_6$  site and two empty half spaces. Here one considers that two half-vacancies are equivalent to one  $V_{Fe}$  vacancy for a common nomenclature in the full  $x$ -range. The process can be written  $Fe^{2+}/Fe^{2+} \rightarrow Fe^{2+}_{dist}/V_{Fe}$ , as sketched in the figure II.12. Typical  $Fe^{2+}$ -O distances are listed in Table II.1. The charge

balance is achieved by introduction of mixed  $\text{Fe}^{2/3+}$  valence in the surrounding regular octahedral sites. We note that the BVS calculated for oxygen of the distorted  $\text{FeO}_6$  corners is close to -2, which comfort their stability, at least when connected to regular octahedra. This configuration shows a redistribution Fe charges and coordinations to lower columbic repulsion verified in the full series.

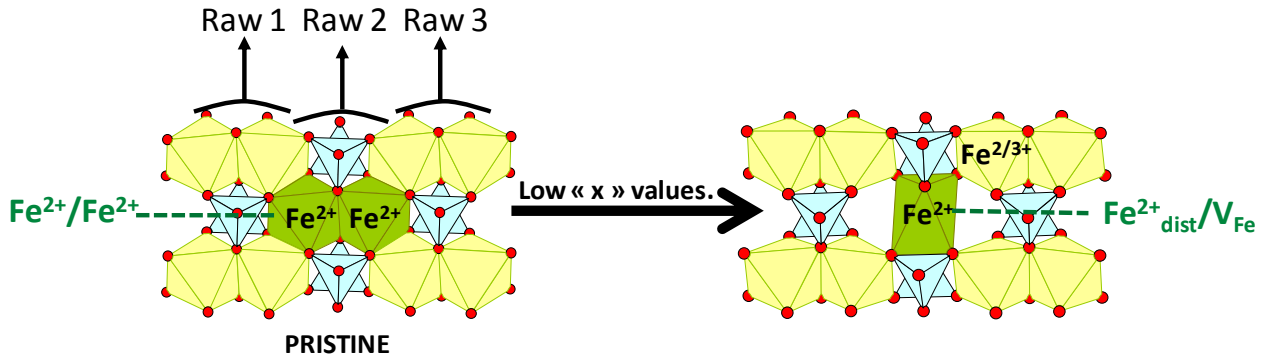


**Figure II.12.** Vacancies creation after condensation of octahedral dimers within parallel 1D columns for low  $x$  values. For one  $V_{\text{Fe}}$  created one dimer/one column are involved.

- Intermediate  $x$  values ( $x=1/2$ ):

In addition to the  $V_{\text{Fe}}$  vacancies discussed above, supplementary vacancies involve two adjacent columns. Starting from two distinct dimers, it leads to the creation of two external regular  $\text{Fe}^{3+}\text{O}_6$  octahedra, one elongated but tilted  $\text{Fe}^{2+}\text{O}_6$  (common to two columns) and one  $V_{\text{Fe}}$ , see fig. II.13. All surrounding regular  $\text{FeO}_6$  sites contain  $\text{Fe}^{3+}$ . In terms of individual columns useful latter, the common distorted  $\text{Fe}^{2+}\text{O}_6$  site can be considered as belonging to one single column while the next one displays a vacancy at this site ( $2 \text{Fe}^{2+}/\text{Fe}^{2+} \rightarrow \text{Fe}^{2+}_{\text{dist}}/\text{Fe}^{2/3+} + \text{Fe}^{2/3+}/V_{\text{Fe}}$ ).

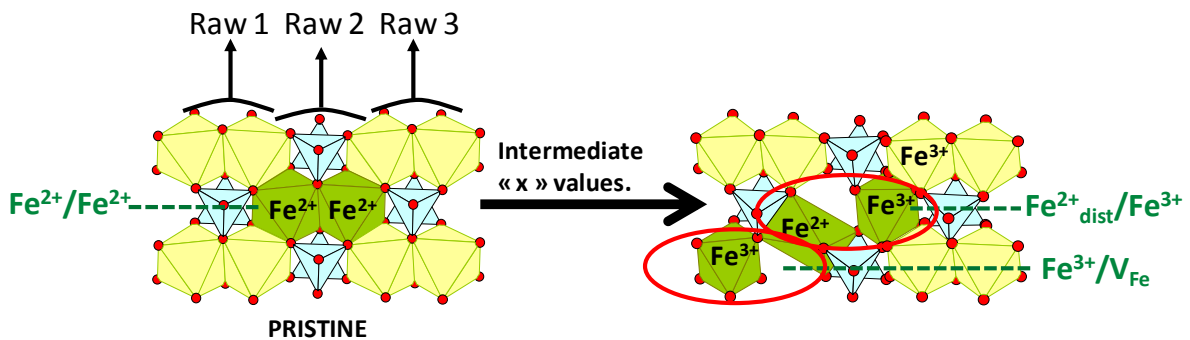


**Figure II.13.** Vacancies creation after monomerization of octahedral dimers within parallel 1D column for intermediate  $x$  values. In this case one  $V_{\text{Fe}}$  involves two dimers/two columns.

- *High x values ( $x=2/3$ ):*

The creation of one vacancy in a dimer leaves one terminal regular  $\text{Fe}^{3+}\text{O}_6$  site ( $\text{Fe}^{2+}/\text{Fe}^{2+} \rightarrow \text{V}_{\text{Fe}}/\text{Fe}^{3+}$ ), see fig II.14. Here again as deduced from the  $\text{BaFe}_{1.33}(\text{PO}_4)_2$  structure, all surrounding sites are occupied by  $\text{Fe}^{3+}$  ions.

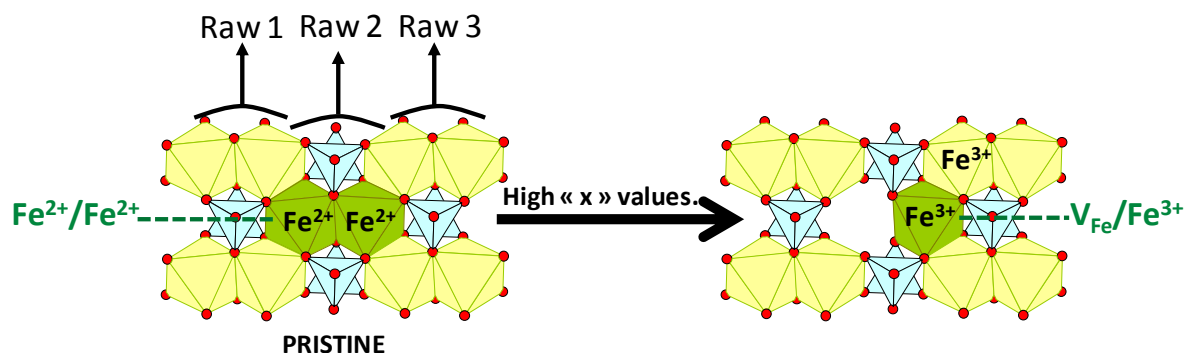


**Figure II.14.** Vacancies creation after condensation of octahedral dimers within parallel 1D column for high  $x$  values. Here, as in the low  $x$  values case, one  $\text{V}_{\text{Fe}}$  involves one dimers/one columns.

- *Forbidden Situations:*

Here we have established forbidden configurations between Fe ions and  $\text{V}_{\text{Fe}}$  that could be very important (in terms of avoiding them) in the context of a good understanding of each crystal structures and for predictive approach as it is the case of  $\text{BaFe}_{1.4}(\text{PO}_4)_2$  phase that will be developed in 3.4.5.

The observation of the  $x=2/7$ ,  $1/3$  and  $1/2$  crystal structures together with BVS calculations suggest that three hypothetical dispositions are unfavorable after condensation of Fe/Fe dimers sites. Three identified “forbidden” situations are represented in the figure II.15 and will be used for further rationalization of the adopted crystal structures.

Case 1) Two consecutive  $\text{Fe}^{2+}\text{O}_6$  inside one single column are aligned at both sides of one phosphate bridge, fig. II.15(a)A. In such situation, local constraints are expected too strong because locally each  $\text{Fe}^{2+}\text{O}_6$  extends the external P-P distance from 4.58 to 5.01 Å. Such dilatation should not be tolerated two consecutive times in one column without serious mismatches between adjacent columns.

Case 2) Two adjacent  $\text{Fe}^{2+}\text{O}_6$  are disposed on two adjacent columns, with parallel elongations axes, as shown on the figure II.15(a)B. Here, the BVS for the oxygen atoms sharing one  $\text{PO}_4$  and one  $\text{Fe}^{2+}\text{O}_6$  octahedra is estimated to 1.36 Å (contributions from one O-P bond + one long O- $\text{Fe}^{2+}$  bonds), out of the stable values for  $\text{O}^{2-}$ .

Case 3) For high exsolution rate ( $x = 2/3$  crystal structure), one unfavorable situation is assumed to be “forbidden”. It is shown on the figure II.15(b) and concerns the close contact between two large vacancies. In this hypothetical case the BVS for terminal oxygen corners inside the voids are estimated to the unrealistic  $\sim 1.15$  value (one O-P bond only).

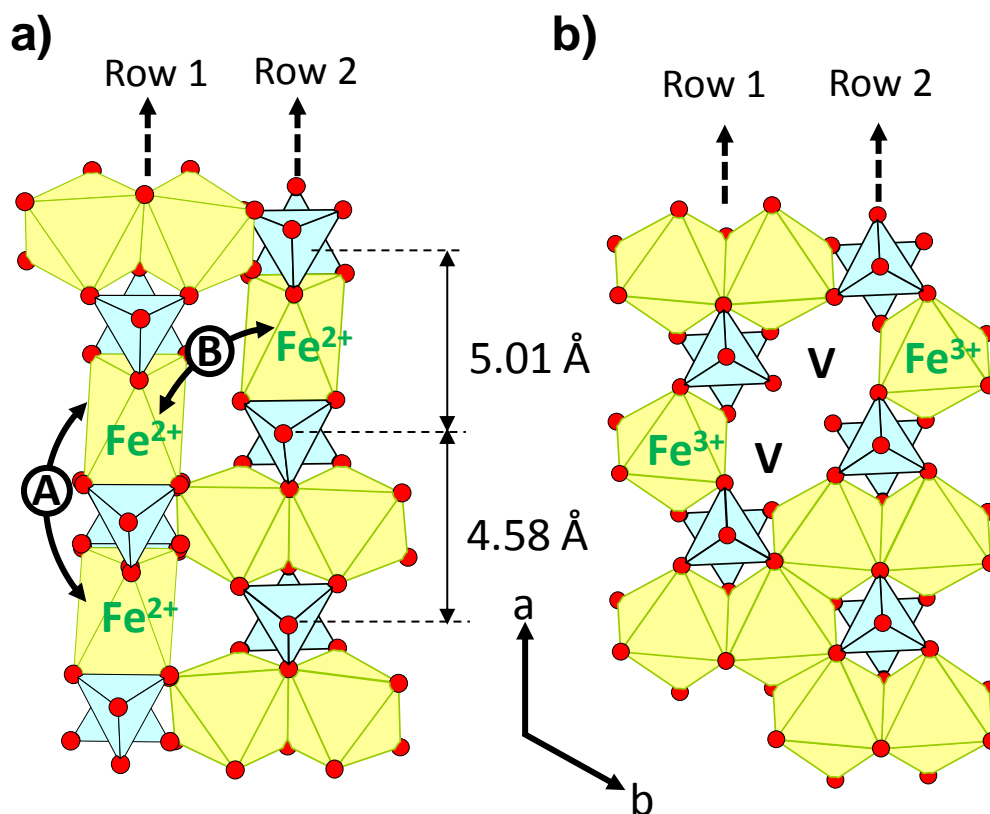


**Figure II.15.** Forbidden Topologies after exsolution : a) unrealistic A and B dispositions between two distorted  $Fe^{2+}O_6$  octahedra. b) unrealistic disposition between  $Fe^{3+}O_6$  and  $V_{Fe}$ .

- *Distribution of the vacancies into 1D motifs and predictive tools:*

We have seen above in this section that in the four depleted observed structures, each vacancy results from the condensation of one Fe/Fe dimer into one Fe/ $V_{Fe}$  pair. This can be generalized to any  $x$  values, since most of the “forbidden configurations” shown above correspond to the co-presence of two neighboring  $V_{Fe}$ . Counting the effect of the condensation of dimers in  $BaFe_{2-x}(PO_4)_2$  phases, the exsolution of  $n$   $Fe^{2+}$  ions (organized along 1D-columns) creates  $2n$  monomers. After analyzing the four available structures, we found that full Fe/ $V_{Fe}$  structural sequences and periods are  $x$ -dependent and always confined in the Fe-depleted 1D motifs greened up as was presented in figure II.10. It can be rationalized, as follows:

For  $x = 2/7$  ( $1/7^{\text{th}}$  of  $V_{\text{Fe}}$ , i.e.  $2/7^{\text{th}}$  of monomers created) the expected 1D-ordering period is  $7a_{\text{rhomb}}$ . For reasons given above, the existence of two next  $\text{Fe}^{2+}_{\text{dist}}$  along the chains is forbidden. It follows that one can identify the sequence of Fe/Fe and  $\text{Fe}^{2+}_{\text{dist}}/V_{\text{Fe}}$  using the Farey tree by analogy to the determination of the sequence of trigonal prisms (Pr) and octahedra (Oct) in the  $A_{1+x}(A'_x B_{1-x})O_3$  hexagonal perovskite family.[54, 55] In essence, these compounds are formed of 1D chains ( $q$  polyhedra period) with complex order between  $p$  Pr and  $q-p$  Oct connected by face-sharing. Similarly to the  $\text{Fe}^{2+}_{\text{dist}}$  sites in the title compounds, two consecutive Pr are not allowed such that the full Oct/Pr sequence can be derived using the “Farey tree reduction” for all  $p/q$  fractions. Applying the same reduction for  $2/7^{\text{th}}$  of disconnected  $\text{Fe}^{2+}_{\text{dist}}$  and  $5/7^{\text{th}}$  of remaining dimers within the  $7a_{\text{rhomb}}$  period, we find :  $2/7 = 1/3 \oplus 1/4$ . It suggests that the full column period is formed of two fragments (3-dimers long and 4-dimers long respectively) with one  $\text{Fe}^{2+}_{\text{dist}}$  in each. It leads to the ideal sequence  $-(\text{Fe}^{2+}_{\text{dist}}/V_{\text{Fe}}-\text{Fe}/\text{Fe}-\text{Fe}/\text{Fe})-(\text{Fe}^{2+}_{\text{dist}}/V_{\text{Fe}}-\text{Fe}/\text{Fe}-\text{Fe}/\text{Fe}-\text{Fe}/\text{Fe})-$  along the column axis, that matches perfectly with the experimental crystal structure, see fig 10 (b).

For  $x = 1/3$  ( $1/6^{\text{th}}$  of  $V_{\text{Fe}}$  i.e.  $1/3^{\text{rd}}$  of monomers), using the same reasoning one could predict along the 1D columns with period  $3a_{\text{rhomb}}$ , the ideal sequence  $-(\text{Fe}^{2+}_{\text{dist}}/V_{\text{Fe}}-\text{Fe}/\text{Fe}-\text{Fe}/\text{Fe})-$ , as experimentally observed, see fig. II.10(c). Note that  $1/3$  is a fully reduced fraction of the Farey suite.

For  $x = 1/2$  ( $1/4^{\text{th}}$  of  $V_{\text{Fe}}$  i.e.  $1/2^{\text{nd}}$  of monomers) one expect a supercell based on  $2a_{\text{rhomb}}$  on the basis of the previous observations for  $x = 2/7, 1/3$ . One plausible periodic motif is drawn on the figure II.16(a). It corresponds to the  $-(\text{Fe}^{2+}_{\text{dist}}/V_{\text{Fe}}-\text{Fe}/\text{Fe})-$  sequence. This topology is indeed impossible since the stacking between chains in the  $(a,b)$  plane would systematically create the large forbidden large vacancies of figure II.15(a)B. Then the shortest available 1D period is  $4a_{\text{rhomb}}$  in which two  $\text{Fe}_{\text{dist}}/V_{\text{Fe}}$  pairs order, as experimentally verified. The compound is stabilized by a distribution of axial/tilted distorted  $\text{Fe}^{2+}\text{O}_6$  octahedra and vacancies along (see fig. II.16b), they are hardly predictable but in good agreement with the period deduced from the  $x$  value. In terms of involved pairs, it corresponds to a situation intermediate between  $(\text{Fe}^{2+}_{\text{dist}}/V_{\text{Fe}})$  found for low  $x$  values and  $(\text{Fe}^{3+}_{\text{regul}}/V_{\text{Fe}})$  found for  $x = 2/3$ , see below.

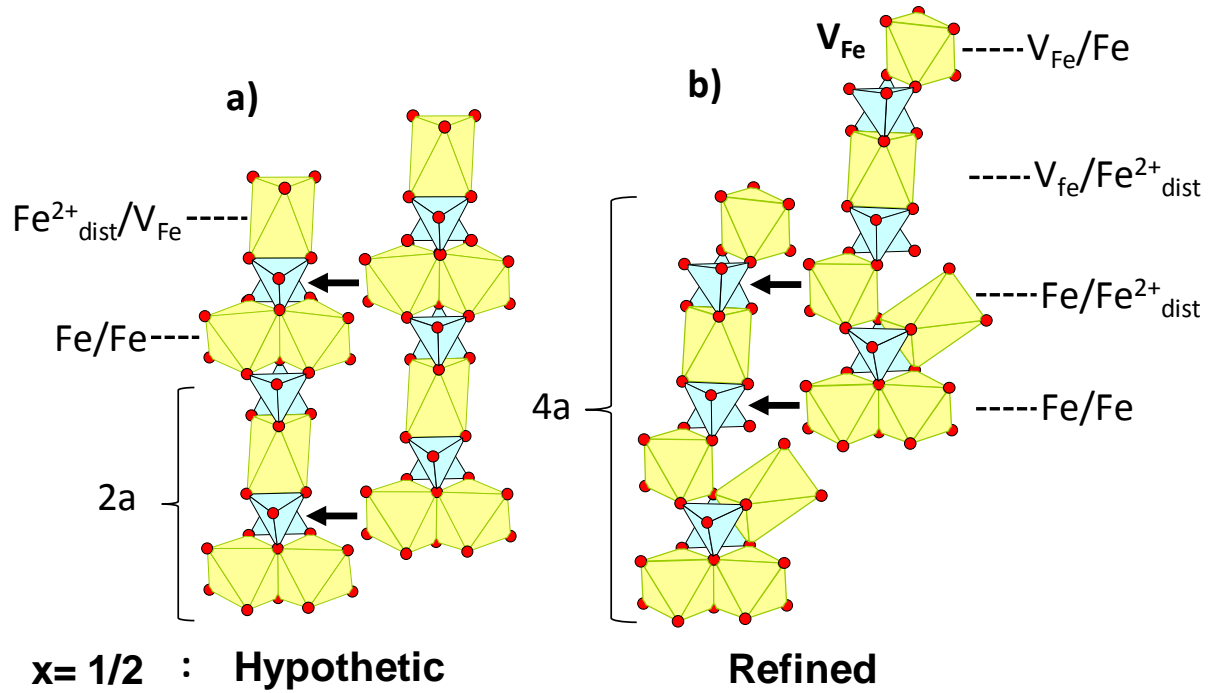


**Figure II.16.**  $BaFe_{1.5}(PO_4)_2$  case ( $x=1/2$ ): a) Unrealistic plugging between two columns with  $-(Fe/Fe-Fe_{dist}/V_{Fe})$ - periods due to the creation of two forbidden large vacancies. b) Experimental model with  $-(Fe/Fe-Fe/Fe_{dist}-Fe_{dist}/V_{Fe}-V_{Fe}/Fe)$ - period.

For  $x=2/3$ , ( $1/3^{rd}$  of  $V_{Fe}$  i.e.  $2/3^{rd}$  of monomers) the situation now involves creation of regular trivalent ions only inside  $Fe/V_{Fe}$  and  $Fe/Fe$  pairs. The good adaptability between these units makes more complex the predictive approach due to the double possibilities for  $V_{Fe}$  to stand at the right or left part of the half occupied dimer. At least the  $x$  values suggest any  $3n \times a_{\text{rhomb}}$  periods. The two  $-hFe/V_{Fe}-Fe/V_{Fe}-Fe/Fe-$  and  $-(Fe/V_{Fe}-V_{Fe}/Fe-Fe/Fe)-$  1D motifs shown figure II.17(a, b) are plausible but distinguish the most plausible appears difficult. Experimentally, the system chooses a third ordering with a longer period. It is built on the  $4/6^{th}$  ratio of monomers (i.e.  $=2/3^{rd}$ ) along the  $6a_{\text{rhomb}}$  period with sequence  $-(Fe/V_{Fe}-Fe/V_{Fe}-V_{Fe}/Fe-V_{Fe}/Fe-Fe/Fe-Fe/Fe)-$ , see figure II.17(c). Though the multiple possibilities of ordering between  $V_{Fe}/Fe$  and  $Fe/Fe$  pairs, the observed one is expected more stable in terms of 2D-charge repartition. Concerning the predictive aspect, once more the existence of elementary 1D motifs with period related to the  $x$  ratio of monomers persists in this compound.

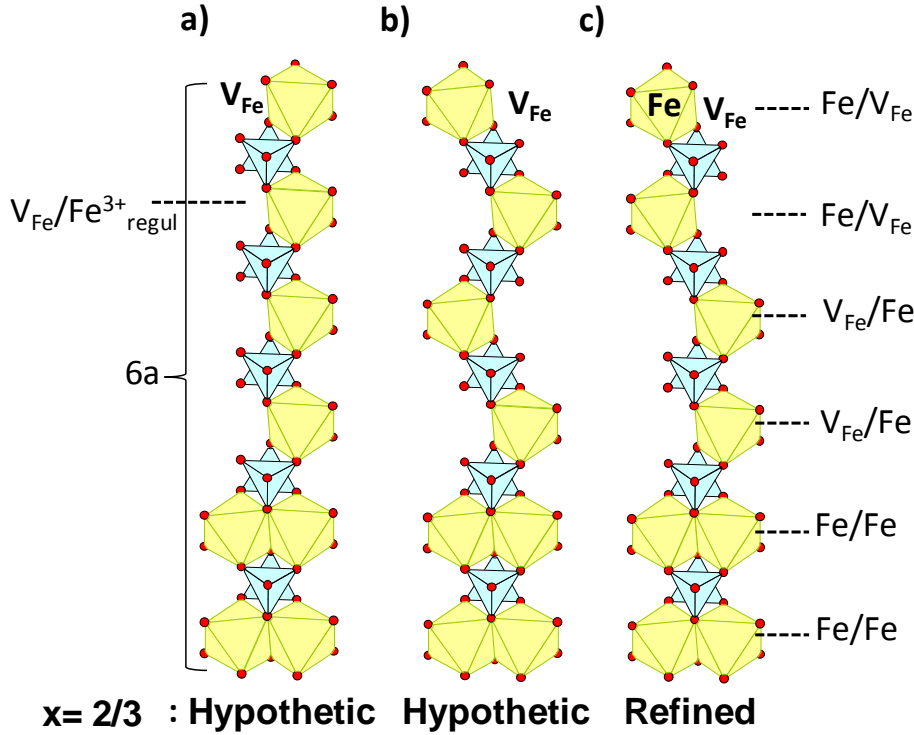


**Figure II.17.**  $BaFe_{1.33}(PO_4)_2$  case ( $x=2/3$ ): a,b) two hypothetical  $Fe/V_{Fe}$  sequences versus c) the experimental one.

- *Imbrication of the 1D-chains into 2D-lattices:*

Now focusing on the 2D-lattices after exsolution, it is remarkable that the 1D-period (shown above to depend on the  $x$  depletion rate) can be easily deduced from the indexation of single crystal XRD supercell satellite peaks. The figure II.18 shows the projection of the collected reflections in the elementary reciprocal trigonal cell ( $a^*, b^*$ ). It allows determining the supercell  $q$ -vector. Here, only in-plane components were considered, the principle ruling the shifts between next depleted layers along  $c$  being out of the scope of this discussion. We find for  $x=2/7, 1/3, 1/2$  and  $2/3$   $q=1/7a^* + 1/7b^*$ ,  $1/3a^*+1/3b^*$ ,  $1/4a^*+1/4b^*$  and  $1/6a^*+1/6c^*$ , respectively, in perfect agreement with periodicities along the 1D-units discussed above. For  $x=1/2$ , we observe the contamination by  $q = 1/3 a^* + 1/3b^*$  satellites that correspond to intergrown domains of  $BaFe_{1.66}(PO_4)_2$ , as mentioned in the section dedicated to its structure refinement. One also notes the systematic presence of extra-spots of the twinned domains by  $120^\circ$  and  $140^\circ$  rotation around the parent trigonal axis whose overlappings have been taken into account in the structural refinements. Concerning the arrangement between the chains in the  $(a, b)$  layers, the systematic equalities between the  $q_{a^*}$  and  $q_{b^*}$  components involves a constant shift between all columnar motifs in the layers.

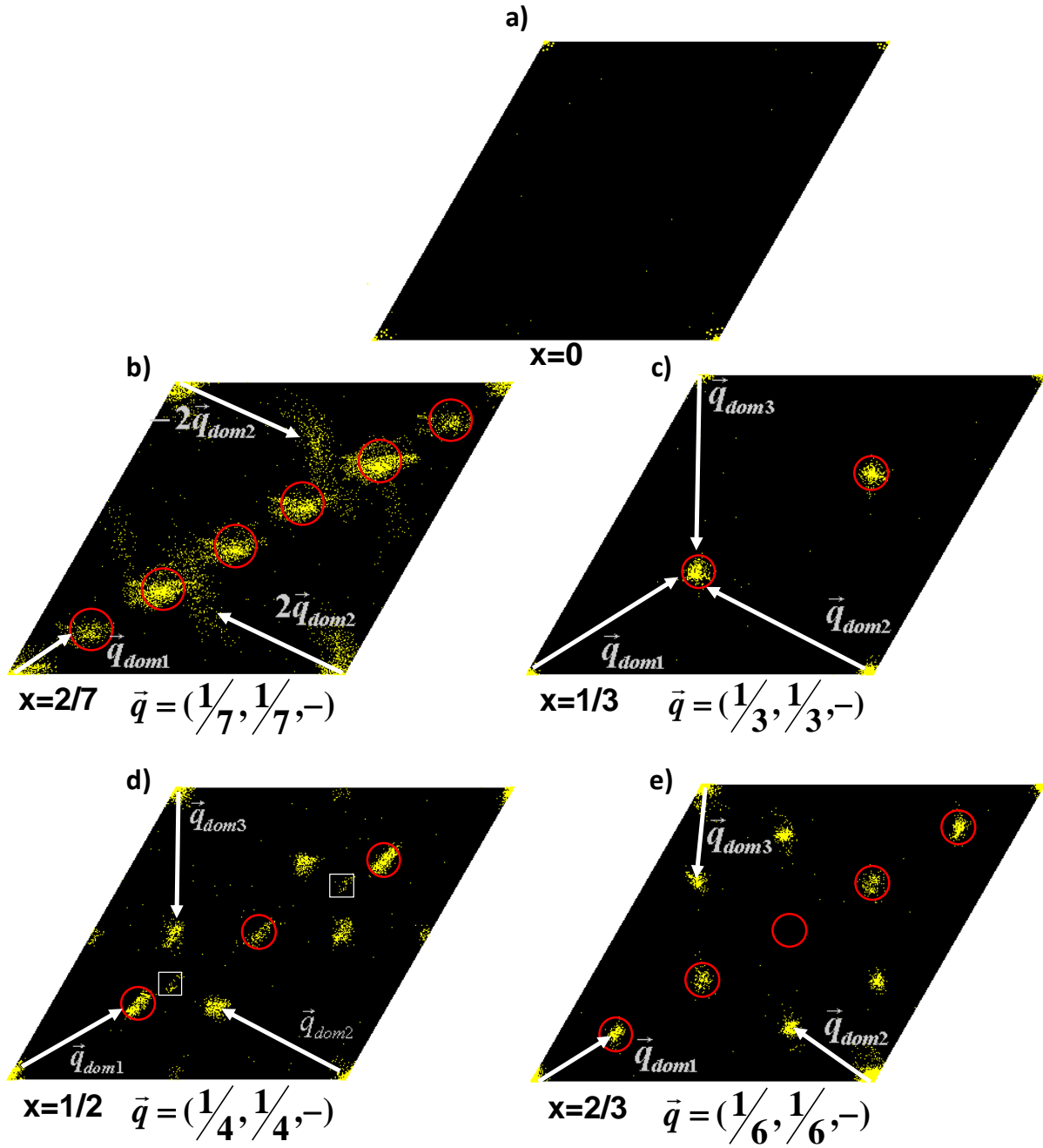


**Figure II.18.** Projection in the elementary reciprocal ( $a^*$ ,  $b^*$ ) plane of collected reflections with evidence of the  $\vec{q}$  modulation vectors and  $120^\circ/240^\circ$  tilted superstructure satellites reflections for different  $x$  values.

The geometrical principle responsible for the  $a^*$  and  $b^*$  equal  $\vec{q}$  component is sketched in the figure II.19 for an hexagonal cell with a  $3\vec{a}_h$  supercell period (i.e.  $q_{a^*} = 1/3$ ), shifted uniformly in the  $(a, b)$  plane by the translation vector  $\vec{T}$  shown in red. Given the  $(3\vec{a}_h, \vec{T})$  cell surligned in yellow, the shortest translational vector along the  $b_h$  axis is  $3\vec{b}_h = -3\vec{a}_h + \vec{T}$ . It follows that in such a topology of one kind of uniformly shifted chains,  $|q_{a^*}| = |q_{b^*}| = 3/a_h = 3/b_h$  by symmetry.

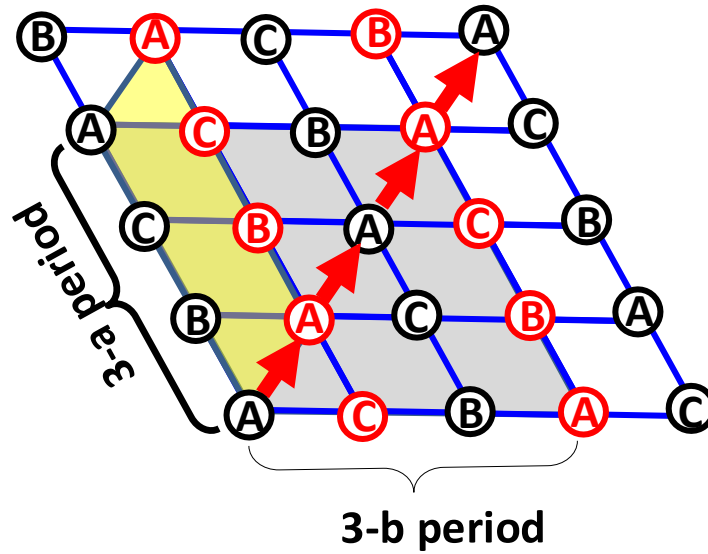


**Figure II.19.** Sketch of the equality between the  $a^*$  and  $b^*$   $\vec{q}$  components for 3a-periodic (ABC) chains, shifted by a unique  $\vec{T}$  vector (in red). It creates a 3b period (ACB). The yellow area corresponds to the smallest in-plane unit cell.

This result is of importance and implies that the full in-plane structure can be deduced or anticipated from the knowledge of 1D-motif along the a-axis and the  $\vec{T}$  shift, which are sufficient pre-requests to build the layers in the full x-range. This assessment was verified after examination of the 2D layers for each composition as shown on the figure II.20. In each case the full 2D-lattice can be paved using from 1D infinite columns translated by  $\vec{T}$ .

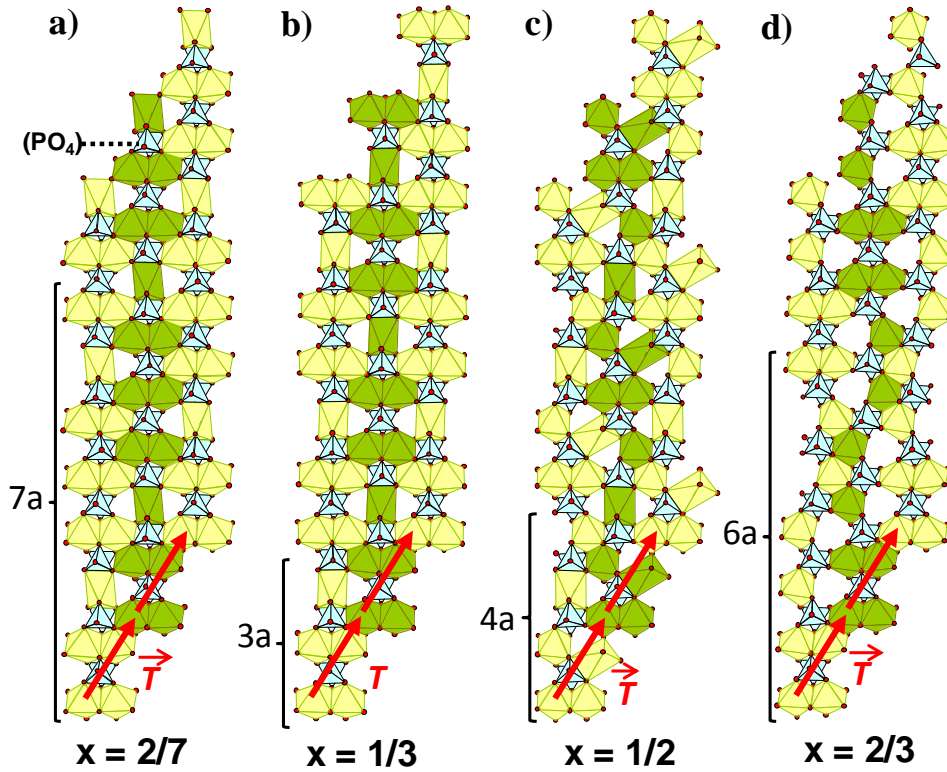


**Figure II.20.** a-d) 2D-pavement by in-plane shifting of the elementary 1D-motifs columns (see figure 2) using the translation vector  $\vec{T}$  for the four refined structures. The two colors differentiate adjacent 1D motif for clarity. For each compounds we find

$$\vec{T} = 2a_{Rhomb\sigma} + b_{rhomb\sigma}.$$

In the four compounds, we find  $\vec{T} = 2\vec{a}_{Rhomb\sigma} + \vec{b}_{rhomb\sigma}$ , see figure II.20, though this common value should not be generalized but depends case by case of the most stable distribution of vacancies. This finding grandly simplifies the understanding of all concerned lattices and prediction of new terms, because the only knowledge the 1D-motif and the shift  $\vec{T}$  between.

### 3.4.5. Prediction of the structure of $\text{BaFe}_{1.4}(\text{PO}_4)_2$ ( $x=3/5$ ).

A batch of single crystal of  $\text{Ba}(\text{Fe}_2(\text{PO}_4)_2)$  was heated at 500 °C for 6h, leading to the selection a an inhomogeneous mixture of one specimen with novel structural characteristics. Unfortunately, the single crystal fell down and was lost during the data collection. Also from the small fraction of collected reciprocal space, its quality is estimated as relatively bad. However, using the incomplete set of diffracted reflections, we have tried to deduce the model although it was not possible to perform a full and fine structure determination, due to the expected complexity of the structure. The figure II.21 shows basic reconstructed layers, which show the poor completeness of the crystal structure.

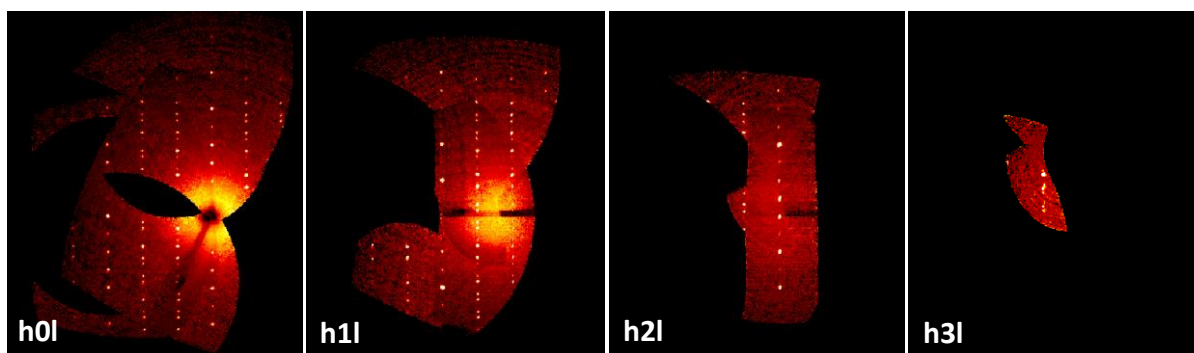


*Figure II.21. Precessions images of collected crystal denote poor completeness*

At least, the projection in the elementary reciprocal ( $a^*$ ,  $b^*$ ) plane of the collected reflections it is shown (see figure II.22a) highlights a new  $\vec{q}$  modulation vector ( $\vec{q} = 1/5a^* + 1/5b^*$ ), which means a new phase with a novel exsolution rate. As discussed above, it means that the full ordering information is contained in a 1D- column with a  $5a_h$  period. That is the maximum we can say at this stage about the superstructure, although several attempts to solve the structure with our poor dataset.

Nevertheless, the dataset allows the refinement of the rhombohedral subcell structure, such as systematically performed in a first stage for other compositions discussed previously.

This refinement was made in order to get the first hints about the compound stoichiometry after integration of the fundamental reflections only and to clearly count the proportion of regular  $\text{FeO}_6$  ( $6c$  ;  $0,0, z \sim 1/3$ ) , distorted  $\text{FeO}_6$  ( $9e$  ;  $1/2,0,0$ ) and  $V_{\text{Fe}}$  as detailed in the  $\text{BaFe}_{1.5}(\text{PO}_4)_2$  and  $\text{BaFe}_{1.33}(\text{PO}_4)_2$  cases.

For the unknown compound, the refinement yields the final  $R_{\text{obs}}=11.55\%$ , with a final formula after occupancy sites refinement of  $\text{BaFe}_{1.41}(\text{PO}_4)_2$ . In that case the high  $R_{\text{obs}}$  can be explained by the low quantity of reflections collected. The sites occupancies refinement lead to around a 60% of regular octahedral occupiers and a 10% of distorted ones per formula.

This stoichiometry gives  $x \sim 3/5$  (i.e.  $3/10^{\text{th}}$  of vacancies and  $3/5^{\text{th}}$  of condensed dimers), fully compatible with the experimental  $\vec{q} = 1/5a^* + 1/5b^*$ . Using all the deduced parameters, and avoiding the forbidden situations (see figure II.15), we have established a predicted unit cell which fulfills all these requirements, with a fivefold period and a shift vector of  $\vec{T} = 4\vec{a}_{\text{Rhombo}} + \vec{b}_{\text{Rhombo}}$ . This solution is the unique possible one and includes both regular  $V_{\text{Fe}}$  and distorted  $\text{Fe}^{2+}\text{O}_6$  sites. If our hypothesis is exact the  $\text{Fe}^{+2.86}$  mean valence deduced from the  $\text{BaFe}_{1.4}(\text{PO}_4)_2$  formulation, is exactly reproduced for distorted  $\text{Fe}^{2+}\text{O}_6$  an regular  $\text{Fe}^{3+}\text{O}_6$  only, see the figure II.22(b).

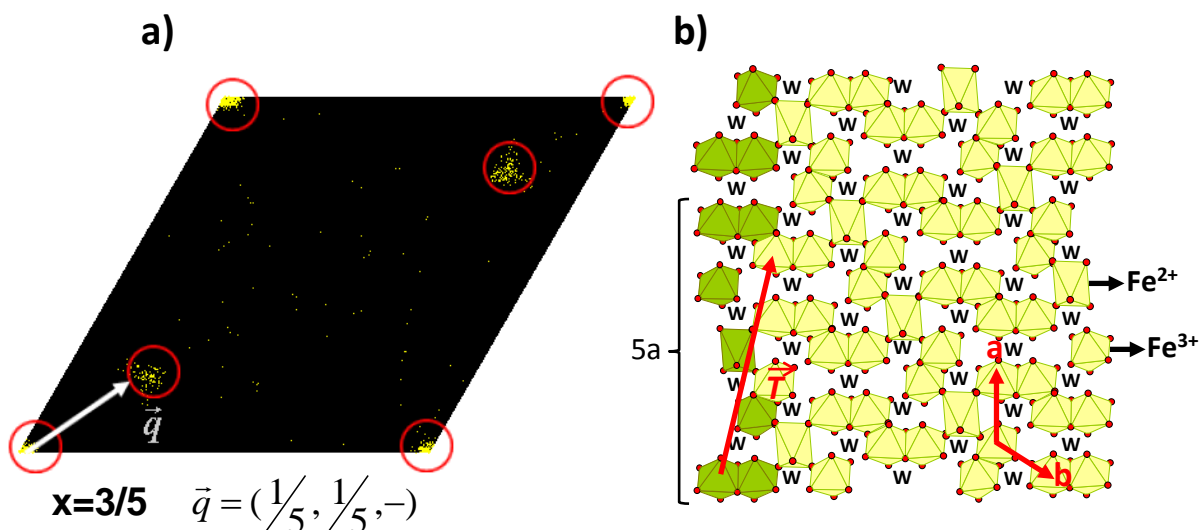


*Figure II.22. Reciprocal ( $a^*$ ,  $b^*$ ) plane of initial rhombohedral unit cell (a) and  $[FeO_6]$  layer of deduced structure for  $x = 3/5$ .*

#### 4. $BaFe_{2-y}M_y(PO_4)_2$ ( $M = Co^{2+}, Ni^{2+}$ ) solid solutions with selective and reversible iron exsolution.

Based on the above explained  $BaFe_2(PO_4)_2$  behavior at moderate temperature, we decided to enlarge our study to the mild oxidation of mixed metal  $Ba(Fe,M)_2(PO_4)_2$  compounds. The preparation of pristine mixed  $Fe^{2+}/M^{2+}$  materials is challenging due to the various synthetic routes required for specific  $M^{2+}$  ions and the complex phase diagrams.  $BaNi_2(PO_4)_2$  can be prepared by a solid state route[56], but  $BaCo_2(PO_4)_2$  is more complex due to a puzzling metamorphism with competition between at least six polymorphs.[57] These phases are stable under oxidizing conditions (at least they are prepared in air), but the stabilization of  $Fe^{2+}$  in  $BaFe_2(PO_4)_2$  requires a hydrothermal route in reducing media (hydrazine solution) while so far, our synthesis attempts by solid state routes led to another form T- $BaFe_2(PO_4)_2$  discussed in 2.3 and in chapter 3, beyond the scope of this chapter. Here we report on  $BaFe_{2-x}M_x(PO_4)_2$  solid solutions ( $M=Co, Ni$ ) prepared under hydrothermal conditions and we discuss the metal exsolution and its reversibility in comparison to the behavior of the parent  $BaFe_2(PO_4)_2$  phase.

#### 4.1. Experimental: Synthesis and characterization techniques.

*Synthesis:* BaFe<sub>(2-x)</sub>M<sub>x</sub>(PO<sub>4</sub>)<sub>2</sub> phases have been prepared for M= Co, Ni and x= 0.5, 1, 1.5. CoCl<sub>2</sub>·6H<sub>2</sub>O (Alfa Aesar, 99.90%), FeCl<sub>2</sub>·4H<sub>2</sub>O (Aldrich, 98.00%), BaCO<sub>3</sub> (Aldrich, 99.00%), H<sub>3</sub>PO<sub>4</sub> (Prolabo, 85.00%) and hydrazine mono hydrate (N<sub>2</sub>H<sub>4</sub>·H<sub>2</sub>O, Alfa Aesar, 98.00%) were used as reactants as received. The hydrazine serves as reducing agent to stabilize Fe<sup>2+</sup> in the solution. The different phases were synthesized by using stoichiometric mixtures of metal chlorides and a microwave assisted solvothermal method heating at 220°C as described previously for the pristine BaFe<sub>2</sub>(PO<sub>4</sub>)<sub>2</sub>[2]. The phases were always obtained as main phase with variable amount of polycrystalline BaHPO<sub>4</sub>. The impurity can be separated and removed after sonication in ethanol. To proceed the exsolution all the samples were heated in air at 600°C for 12 hours and cooled down by switching off the oven.

As-prepared and reheated phases were characterized by several techniques.

*Characterization:* The accurate composition was determined by microprobe analysis. A Cameca SX100 electron probe microanalyser (EPMA) was used to perform elemental analysis. Quantifications of Fe, Co, Ni, Ba and P were carried out at 20 kV and 20 nA with a spot size of 20µm. A LiF crystal was used to detect the Fe, Co and Ni Kα X-rays and a PET crystal to detect the P Kα and the Ba Lα X-rays. Oxygen was calculated by difference to 100 wt % and taken into account for matrix corrections. Standards used for quantification were made of pure Fe<sub>2</sub>O<sub>3</sub>, Co, Ni, apatite (Ca<sub>5</sub>(PO<sub>4</sub>)<sub>3</sub>(OH)) and Ba(SO<sub>4</sub>) powder pressed into small plates. Means and standard deviations were calculated from measurements carried out at five different places at least on each sample.

Powder X-Ray diffraction (PXRD) was performed using a Bruker D8 Advance diffractometer, with a Bragg Brentano geometry and monochromated CuKα radiation. The lattice parameters have been refined by profile matching using FULLPROF. [58]

The exsolved phases were also characterized by Fe<sup>57</sup> Mossbauer spectroscopy in order to verify the Fe valence.

X-Ray Absorption Near Edge Spectroscopy (XANES) was realized in SOLEIL synchrotron facilities. Experiences were carried out in the DIFFABS beamline. The aim of XANES will be to compare the initial and final valences of Co and Ni. The samples were prepared by deposition of well grinded powder sieved at 10 µm in a silicion all the measures were performed in reflection mode at room temperature in air atmosphere. Cobalt and nickel samples, before and after the thermal treatment, were measured at cobalt (7.65-7.90 KeV),

nickel (8.25-8.50 KeV) and iron (7.05-7.30 KeV) K-edges respectively with the 4-element SDD silicon drift detector for X-ray fluorescence measurement.

Thermogravimetric analyses were carried out with the same instrument and in the same conditions announced in 3.1.

Transmission electron microscopy and  $^{57}\text{Fe}$  Mössbauer spectroscopy were performed in the exsolved phases at the same conditions and with the same instruments used for  $\text{BaFe}_{1.33}(\text{PO}_4)_2$  and in the same experimental conditions (see 3.1).

## 4.2. Microstructure and Fe/M composition.

### 4.2.1. As prepared $\text{BaFe}_{2-y}\text{M}_y(\text{PO}_4)_2$ .

After hydrothermal synthesis, the  $\text{BaHPO}_4$  second phase, announced in the experimental section, can be more or less efficiently removed by sonication in ethanol and evacuation of the upper colloid. The degree of separation between the two phases depends on the crystal size of the  $\text{Ba}(\text{Fe},\text{M})_2(\text{PO}_4)_2$  compared to submicronic  $\text{BaHPO}_4$  grains. Representative SEM images of as prepared  $\text{Ba}(\text{Fe},\text{M})_2(\text{PO}_4)_2$  particles are shown on the figure II.23. For the Co series (Fig. II.23a-c), it shows typical crystal size of  $\sim 40\ \mu\text{m}$ , rather independently of the y ratio. However, in the Fe/Ni case (Fig. II.23d-e), the situation is far different. The crystal size decreases drastically with y Ni ratio. It drops rapidly from  $\sim 40\ \mu\text{m}$  ( $y=0.46$ ) to  $<5\ \mu\text{m}$  ( $y=1.45$ ).

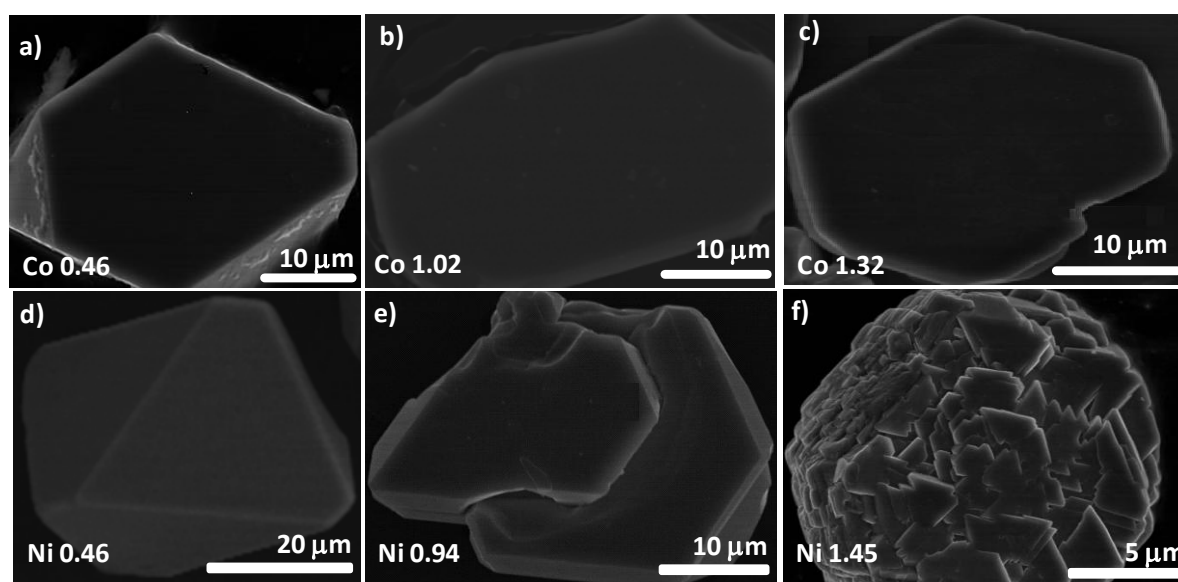


**Figure II.23.** SEM images of  $\text{BaFe}_{2-y}\text{M}_y(\text{PO}_4)_2$  a, b, c for  $M = \text{Co}^{2+}$  and d, e, f for  $M = \text{Ni}^{2+}$  show the different size and morphology depending of composition.

These features have drastic effects on the efficiency of the  $\text{BaHPO}_4$  separation, whose contribution can be observed on XRD patterns for  $y = 0.94$  and  $1.45$ . Apart from  $\text{BaHPO}_4$ , no extra peak was detected by XRD of the as-prepared samples, see figure II.24(a, b) nor by electron diffraction which suggest a statistic Fe/M occupancy in the crystallographic positions.

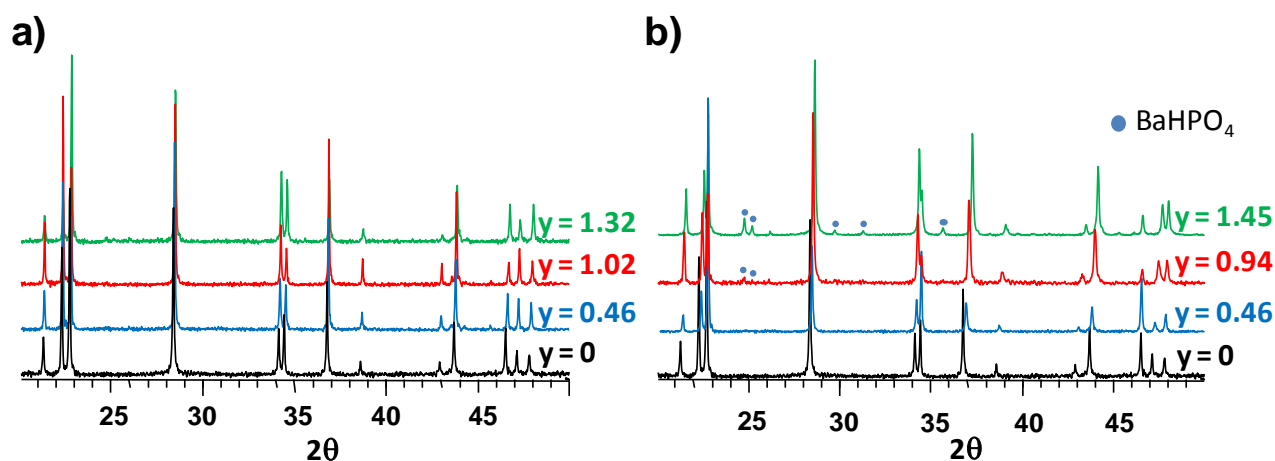


**Figure II.24.** Powder XRD patterns for  $\text{BaFe}_{2-y}\text{Co}_y(\text{PO}_4)_2$  (a) and  $\text{BaFe}_{2-y}\text{Ni}_y(\text{PO}_4)_2$  (b) as prepared.

$\text{BaFe}_{2-y}\text{M}_y(\text{PO}_4)_2$  ( $\text{M}=\text{Co}, \text{Ni}$ ) samples have been prepared using reagents stoichiometries corresponding to  $y = 0, 0.5, 1.0$  and  $1.5$ . However, microprobe analysis shows that the incorporation of the Fe/M incorporation during the hydrothermal treatment is not fully stoichiometric, after averaging on  $\pm 10$  points. Results are given in the Table II. 4. For  $\text{M}=\text{Ni}$  The  $\text{Fe}/(\text{Fe}+\text{M})$  ratio respects the experimental stoichiometries in the full range though slight deviations. For  $\text{M}=\text{Co}$ , we note that the stoichiometry is well respected until  $y = 1$  while for Co-rich sample ( $y=1.5$ ) the composition deviates from the ideal one, i.e. we find  $\text{Fe}/(\text{Fe}+\text{M}) = 34\%$  rather than  $25\%$ . This result is reproducible after examination of two different samples prepared with the same starting ratio. This result indicates different reactivities of  $\text{Fe}^{2+}$  versus  $\text{Co}^{2+}$  ions in our experimental conditions while  $\text{Fe}^{2+}$  and  $\text{Ni}^{2+}$  roughly look similarly reactive.

Taking into account the good accuracy on titrated transition metals by microprobe analysis, we will use in this paper experimental “y” compositions deduced from microprobe as the real ones. Concerning the Ba analysis the deviation from the expected Ba/M is not more than 5 % (e.g. expected value =  $1/2$ , experimental value =  $1.11/2$  for  $\text{BaFe}_{0.55}\text{Ni}_{1.45}(\text{PO}_4)_2$ ). The examination of PXRD patterns of the as-prepared samples show a systematic crystallization in the rhombohedral lattice of the parent  $\text{BaM}_2(\text{XO}_4)_2$  phases. The evolution of the lattice parameters versus  $y$  is plotted in the figure II.25 for the  $\text{M}=\text{Co}$  and  $\text{Ni}$  systems,

respectively. Both the  $a$  and  $c$  parameters decrease versus  $y$  following the differences of ionic radii ( $r_{\text{Fe}^{2+}} = 0.78 \text{ \AA} < r_{\text{Co}^{2+}} = 0.745 \text{ \AA} < r_{\text{Ni}^{2+}} = 0.69 \text{ \AA}$ ). [59] It is noteworthy that so far we have not been able to prepare the targeted phase in presence of manganese

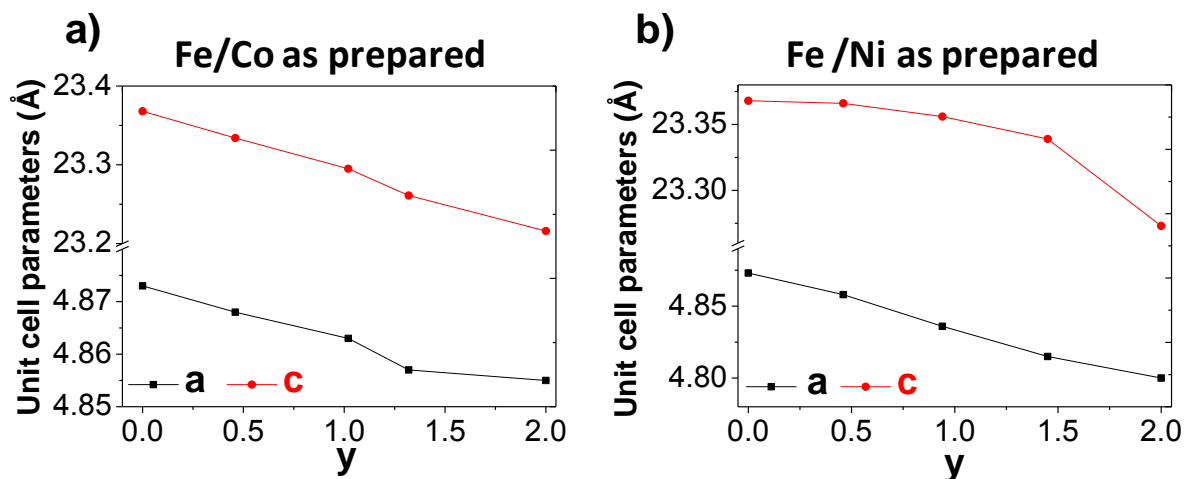


**Figure II.25.** Rhombohedral unit cell parameters as a function of  $y$  for a) as-prepared  $\text{BaFe}_{(2-y)}\text{Co}_y(\text{PO}_4)_2$  b) as-prepared  $\text{BaFe}_{(2-y)}\text{Ni}_y(\text{PO}_4)_2$ .

#### 4.2.2. $\text{BaFe}_{2-y}\text{M}_y(\text{PO}_4)_2$ after thermal treatment.

After heating  $\text{BaFe}_{2-y}\text{M}_y(\text{PO}_4)_2$  ( $\text{M}=\text{Co}, \text{Ni}$ ) compounds at  $600^\circ\text{C}$  for 12h, we observe significant changes of the XRD patterns as shown in figure 26 (a, b). From our prior results on the exsolved  $\text{BaFe}_{2-x}(\text{PO}_4)_2$  phases leading to a variety of triclinic Fe deficient crystal structures depending on the thermal treatment, we expect fine triclinic splitting of the main reflections while weak supercell spots are expected due to  $\text{Fe}/\text{V}_{\text{Fe}}$  [60]. However, even using synchrotron data we have previously shown that the determination of accurate lattice parameters is hampered by the co-presence of several phases with minor compositional  $x$  changes.[60] For mixed exsolved Fe/M phases, using standard diffraction equipment with  $\text{Cu-K}\alpha$  radiation, the XRD patterns can be correctly indexed in the parent rhombohedral unit cells, neglecting broadening sometimes observed at high  $2\theta$  angles. The refined lattice parameters and the corresponding Fe/M microprobe analysis are given in the Table 4. In the full range for both  $\text{M} = \text{Co}^{2+}$  and  $\text{Ni}^{2+}$ , it shows a significant contraction of the  $a$  parameter together with a  $c$ -dilatation compared to as-prepared compounds, see fig II.26 (c ,d) for Co and Ni respectively. As proved for the Fe-only compound ( $y=0$ ), this evolution shows the creation and redistribution of vacancies in the original Honeycomb layers. The increasing of the interleave measured along  $c$  show is most plausibly due to the stacking between non-fully

planar M-depleted layers, reminiscent of the Fe-only  $\text{BaFe}_{2-x}(\text{PO}_4)_2$  compounds at  $y=0$ , see 3.3.[3]

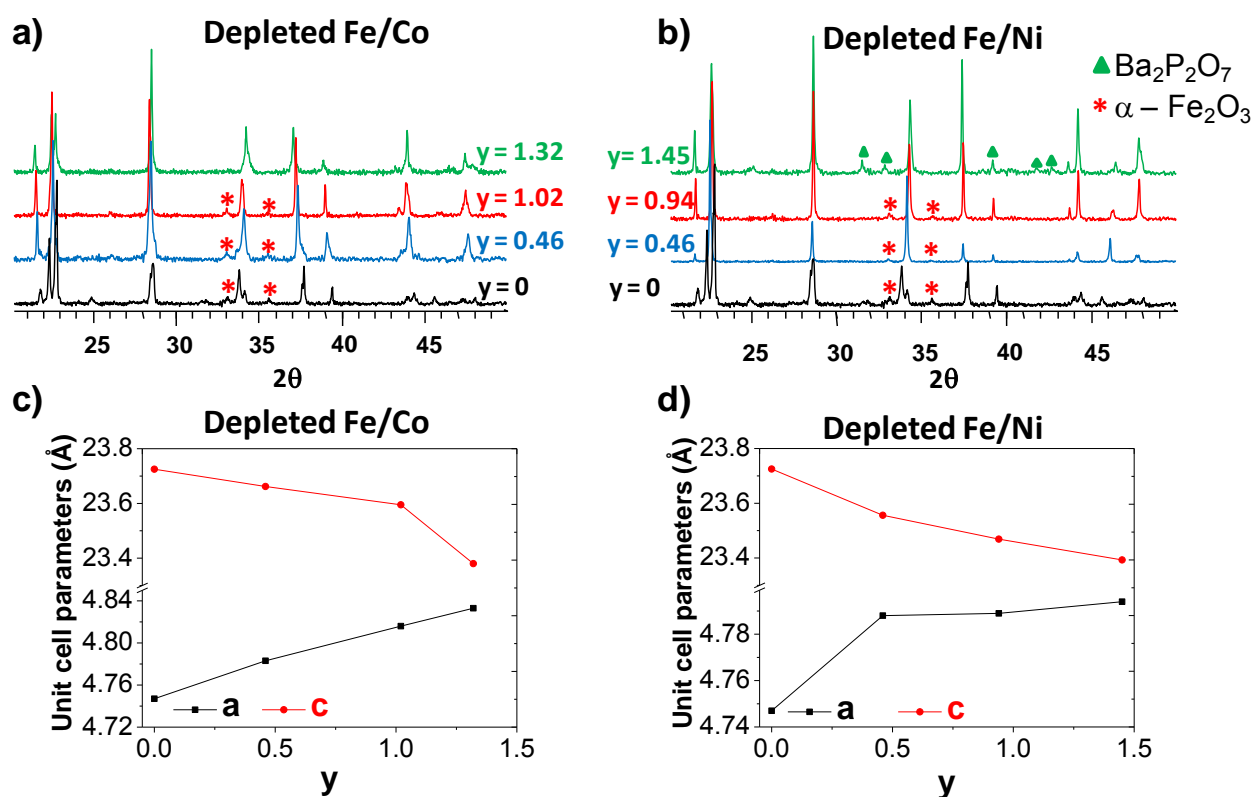
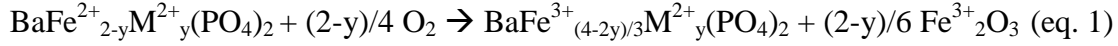


**Figure II.26.** Powder XRD patterns for  $\text{BaFe}_{2-y}\text{Co}_y(\text{PO}_4)\text{O}_2$  (a) and  $\text{BaFe}_{2-y}\text{Ni}_y(\text{PO}_4)\text{O}_2$  (b) as prepared and rhombohedral unit cell parameters as a function of  $y$  for depleted  $\text{BaFe}_{2-y}\text{Co}_y(\text{PO}_4)_2$  (c) and  $\text{BaFe}_{2-y}\text{Ni}_y(\text{PO}_4)_2$  (d).

Here, a symmetry lowering could be suggested but was not verified using standard XRD powder data in which the absence of extra peaks suggests the formation of disordered rhombohedral phases as soon as mixed Fe/M phases are concerned, contrarily to triclinic supercells in  $\text{BaFe}_{2-x}(\text{PO}_4)_2$  phases. This disordered rhombohedral model will be partially refuted dealing with single crystal XRD data, as further discussed. Finally, after exsolution, it is noteworthy that the Fe-rich phases show more dramatic changes of their lattice parameters compared to Co/Ni-rich phases, giving preliminary clues for the preferred exsolution of  $\text{Fe}^{2+}$  ions.

Though not fully understood yet, it is clear that the Fe-exsolution in several  $\text{Fe}^{2+}/\text{oxo}$ -anion systems such as  $\text{BaFe}_2(\text{PO}_4)_2$  but also in the olivine  $\text{Fe}_2\text{SiO}_4$ [16] and  $\text{LiFe}(\text{PO}_4)$  [17], is driven by the  $\text{Fe}^{2+}/\text{Fe}^{3+}$  redox properties. An indirect measure of the relative cationic stability in these systems is given during the charge/discharge cycling of  $\text{LiM}(\text{PO}_4)$  cathodes by the  $\text{Mn}^{3+}/\text{Mn}^{2+}$  (4.1 V),  $\text{Co}^{3+}/\text{Co}^{2+}$  (4.8 V) and  $\text{Ni}^{3+}/\text{Ni}^{2+}$  (5.4V) couples that show increasing

redox potentials, all higher than the  $\text{Fe}^{3+}/\text{Fe}^{2+}$  couple (3.5 V).[61] Indeed, the exsolution of  $\text{Fe}^{2+}$  only in mixed metal  $\text{Li}(\text{Fe},\text{Mn})_{1-x}\text{PO}_4$  phases was recently proved leaving  $\text{Mn}^{2+}$  stable though the complete oxidation of  $\text{Fe}^{2+}$  ions into  $\text{Fe}^{3+}$  and the formation of outer  $\text{Fe}_2\text{O}_3$  grains.[62] Overall, in our mixed metal compounds, the ideal full Fe oxidation reaction can be written:



Note that after exsolution, the ideal expected ratio  $\text{Fe}^{3+}_{\text{phase}}/\text{Fe}^{3+}_{\text{hematite}}$  between the depleted phase and the external  $\text{Fe}_2\text{O}_3$  cluster is equal to 2. Shifts from this value may warn about incomplete oxidation or other competing reactions.

One could also speculate on the partial or full removal of the  $\text{M}^{2+}$  co-cation for oxidation of  $\text{Fe}^{2+}$  into  $\text{Fe}^{3+}$ . The hypothetical chemical reaction for full  $\text{M}^{2+}$  removal is given by the following reactions in the Ni and Co cases respectively, taking into account the stability of NiO in our experimental conditions. In the case of cobalt, the thermodynamic stability of  $\text{Co}_3\text{O}_4$  (i.e.  $\text{CoO}_{1.33}$ ) compared to CoO up to  $\sim 900^\circ\text{C}$  was considered:



We note that eq. 1 and eq.  $2_{\text{Ni}}$  are not discriminating in terms of oxygen mass uptake, i.e.  $(2-y)/4 \text{O}_2$  in both cases.

as prepared				After exsolution. 12h-600°C							
Expected composition	Microprobe composition % Fe/M	a, c (Å)	Impurities	Expected composition %Fe/M	Microprobe composition % Fe/M	a, c (Å)	MB (78K) %Fe <sup>3+</sup> <sub>phase</sub> / % Fe <sup>3+</sup> <sub>Fe2O3</sub>	Paramagnetism		$\theta_{cw}$	Subproduct phases
								Calc.	Exp.		
BaFe <sub>2</sub> (PO <sub>4</sub> ) <sub>2</sub> 100	BaFe <sub>2</sub> 100	4.87(3), 23.36(8)	-	BaFe <sub>1.33</sub> (PO <sub>4</sub> ) <sub>2</sub> 100	BaFe <sub>1.34</sub> 100	4.74(7), 23.72(5)	64/36	6.82	7.01	-35.7	Fe <sub>2</sub> O <sub>3</sub>
BaFe <sub>1.5</sub> Co <sub>0.5</sub> (PO <sub>4</sub> ) <sub>2</sub> 75	BaFe <sub>1.54</sub> Co <sub>0.46</sub> 77	4.86(8), 23.33(4)	-	BaFe <sub>1.03</sub> Co <sub>0.46</sub> (PO <sub>4</sub> ) <sub>2</sub> 67	BaFe <sub>1.44</sub> Co <sub>0.40</sub> 78	4.78(3), 23.66(2)	67/33	6.55	7.74	-11.4	Fe <sub>2</sub> O <sub>3</sub>
BaFeCo(PO <sub>4</sub> ) <sub>2</sub> 50	BaFe <sub>0.98</sub> Co <sub>1.02</sub> 49	4.86(3), 23.29(5)	-	BaFe <sub>0.65</sub> Co <sub>1.02</sub> (PO <sub>4</sub> ) <sub>2</sub> 40	BaFe <sub>0.85</sub> Co <sub>1.00</sub> 46	4.81(6), 23.59(5)	68/32	6.17	7.16	33.7	Fe <sub>2</sub> O <sub>3</sub>
BaFe <sub>0.5</sub> Co <sub>1.5</sub> (PO <sub>4</sub> ) <sub>2</sub> 25	BaFe <sub>0.68</sub> Co <sub>1.32</sub> 34	4.85(7), 23.261	-	BaFe <sub>0.45</sub> Co <sub>1.32</sub> (PO <sub>4</sub> ) <sub>2</sub> 18	BaFe <sub>0.55</sub> Co <sub>1.45</sub> 27	4.83(3), 23.38(0)	75/25	5.96	7.49	41.0	-
BaFe <sub>1.5</sub> Ni <sub>0.5</sub> (PO <sub>4</sub> ) <sub>2</sub> 75	BaFe <sub>1.54</sub> Ni <sub>0.46</sub> 77	4.85(8), 23.36(6)	-	BaFe <sub>1.03</sub> Ni <sub>0.46</sub> (PO <sub>4</sub> ) <sub>2</sub> 67	BaFe <sub>1.21</sub> Ni <sub>0.46</sub> 72	4.78(8), 23.55(6)	64/36	6.30	5.72	-24.4	Fe <sub>2</sub> O <sub>3</sub>
BaFeNi(PO <sub>4</sub> ) <sub>2</sub> 50	BaFe <sub>1.06</sub> Ni <sub>0.94</sub> 53	4.83(6), 23.35(6)	BaHPO4	BaFe <sub>0.71</sub> Ni <sub>0.94</sub> (PO <sub>4</sub> ) <sub>2</sub> 40	BaFe <sub>0.83</sub> Ni <sub>0.85</sub> 49	4.78(9), 23.46(9)	73/27	5.69	7.58	-59.6	Fe <sub>2</sub> O <sub>3</sub>
BaFe <sub>0.5</sub> Ni <sub>1.5</sub> (PO <sub>4</sub> ) <sub>2</sub> 25	BaFe <sub>0.55</sub> Ni <sub>1.45</sub> 28	4.81(5), 23.33(9)	BaHPO4	BaFe <sub>0.37</sub> Ni <sub>1.45</sub> (PO <sub>4</sub> ) <sub>2</sub> 18	BaFe <sub>0.37</sub> Ni <sub>1.22</sub> 23	4.79(4), 23.39(3)	66/34	4.95	5.7	-24.3	Ba2P2O7

**Table II.4.** Expected and experimental compositions, refined unit cell parameters and detected impurities for synthesized solid solutions of BaFe<sub>2-y</sub>M<sub>y</sub>(PO<sub>4</sub>)<sub>2</sub> (as prepared). Expected composition and expected paramagnetic moments  $\mu_{eff}$ , experimental compositions, unit cell parameters, ratios  $Fe^{3+}_{phase}/Fe^{3+}_{Fe2O3}$ , magnetic parameters and subproduct phases for exsolved phases (after exsolution at 12h-600C). are also shown.

### 4.2.3. Reversibility in iron exsolution.

In the same way that for the  $\text{BaFe}_2(\text{PO}_4)_2$  compound, high temperature XRD has been also performed for the  $\text{BaFe}_{1.5}\text{Co}_{0.5}(\text{PO}_4)_2$  in order to verify the reversibility of the redox solid state reaction in the different Fe/M mixed phases. For that purpose, a polycrystalline sample of the phase was followed by “in situ” XRD during all the thermal treatment, see figure II.27.

This treatment consisted on heating the sample at  $600^\circ\text{C}$  for 12 hours in air atmosphere, to follow the oxidation process. Then, oven atmosphere is changed from air to a reducing atmosphere  $\text{N}_2/\text{H}_2$  (3%) mixture and temperature is kept for another 12h, and finally cooled down to room temperature. Above  $400^\circ\text{C}$  deeper changes are observed than those corresponding to thermal parameters variation only. At  $500^\circ\text{C}$  the first traces of  $\text{Fe}_2\text{O}_3$  are identified. When the temperature reaches  $600^\circ\text{C}$  final exsolved phase, with 100% of  $\text{Fe}^{3+}$  (verified by Mössbauer), is reached and remains stable (unchanged XRD isotherm) during the 12 hours.

After this phase transformation at  $600^\circ\text{C}$ , the blowing atmosphere was changed into 3% $\text{H}_2$   $\text{N}_2$  to verify the reversibility of the process. In the same way, the temperature was kept for 12h. When the oven atmosphere was changed we can observe the beginning of the reduction reaction, marked by the  $\alpha\text{-Fe}_2\text{O}_3$  disparition. After 3 hours at  $600^\circ\text{C}$  under the reducing atmosphere, no more signs of iron oxides are observed. A profile refinement of the sample back to room temperature presents no remarkable unit cell parameters differences with respect to the original phase before heating.

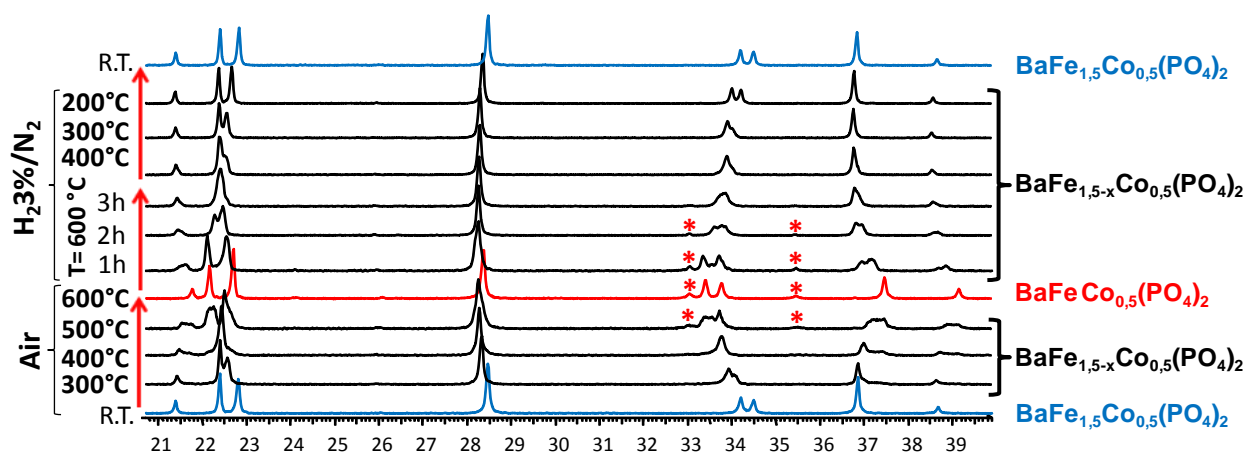


**Figure II.27.** HT-XRD under air under (3%)/Ar atmosphere of  $\text{BaFe}_{1.5}\text{Co}_{0.5}(\text{PO}_4)_2$  showing the reversibility exsolution process.

### 4.3. Selective iron exsolution in $\text{BaFe}_{2-y}\text{M}_y(\text{PO}_4)_2$ solid solutions.

#### 4.3.1. Metal oxidation states before and after exsolution by XANES.

$\text{BaFe}_{-0.5}\text{M}_{-1.5}(\text{PO}_4)_2$  samples were studied as-prepared and after heating in order to compare their spectral evolution before and after the extrusion process. All measurements have been performed using powders in air at room temperature.

Concerning  $\text{Ni}^{2+}$  and  $\text{Co}^{2+}$ , one notes that the edge energies, marked by the white line (w.l.) and those of the pre-edges (a) shown in figure II.28(a, b), are not modified after heating treatment; the extrusion process therefore does not affect the cobalt or nickel redox, at the experimental resolution.

At the iron k-edge, the evolution for before and after clearly shows the edge shift (w.l.) and the pre-edge evolution (a) related to the  $\text{Fe}^{2+} \rightarrow \text{Fe}^{3+}$  oxidation process. It is shown on the figure II.28(c) for the Co-rich phase. The same behavior has been observed for the exsolved Ni rich phase. We can conclude unambiguously that the redox changes induced by the extrusion process in the substituted compounds only concern the iron atoms while  $\text{Ni}^{2+}$  and  $\text{Co}^{2+}$  are not affected (at least a great majority of them).

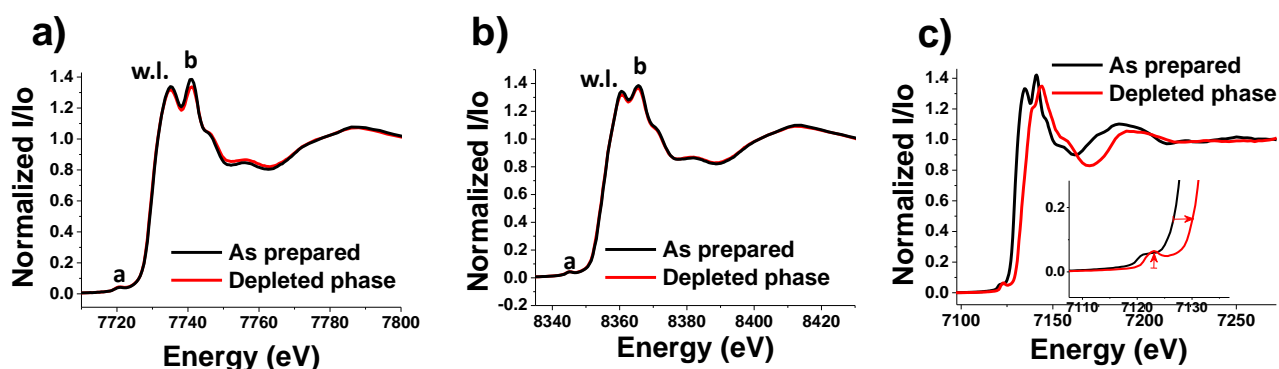


**Figure II.28.** Comparison between the XANES spectra of as-prepared compounds and Fe-depleted-phase after thermal treatment for (a)  $\text{BaFe}_{0.58}\text{Co}_{1.32}(\text{PO}_4)_2$  at the Co K edge (b)  $\text{BaFe}_{0.55}\text{Ni}_{1.45}(\text{PO}_4)_2$  at the Ni K edge (c)  $\text{BaFe}_{0.58}\text{Co}_{1.32}(\text{PO}_4)_2$  at the Fe K edge.

On the other hand, spectra comparison between the different Fe/Co ratios is presented in figure II.29. Even if oxidation state is not modified in any case, differences in between the relative intensities of the white line and the after-edge band (b) are observed. These differences can be explained by their direct environment in the structure, which will change depending on the M concentration as shows the evolution of the after-edge structure (b). After iron exsolution, this evolution is stronger for high iron content, i.e. the direct Co environment

is much more modified than for the low Fe contents ones, these latest being almost unchanged.

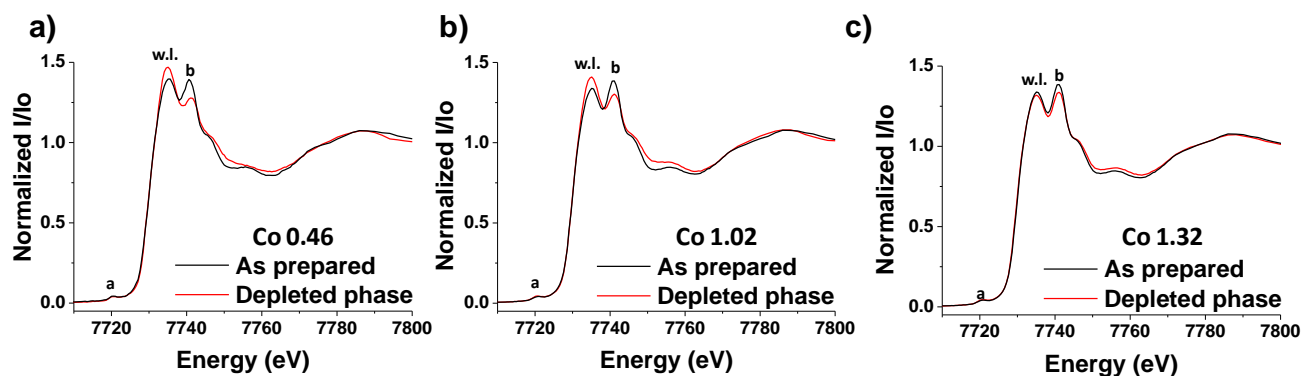


**Figure II.29.** Comparison between the XANES spectra of as-prepared compounds and Fe-depleted-phase after thermal treatment of different Fe/Co ratio at the Co K edge.

#### 4.3.2. Contrast between observed and ideal exsolution process.

In following, the TGA mass uptake ( $\Delta M$ ) was correlated to our Mössbauer spectroscopy results. The TGA plots versus “y” are compared to ideal  $\Delta M_{\text{calc}}$  calculated using equation (1) for both the Fe/Co and Fe/Ni systems, see figure II.30. Apart for iron poor compositions, all compounds show a mass uptake above  $\sim 250^\circ\text{C}$ , with a more activated regime above  $450\text{--}500^\circ\text{C}$ , as already observed during exsolution of  $\text{BaFe}_2(\text{PO}_4)_2$ . [3, 60] Above  $\sim 600^\circ\text{C}$  the observed plateau after the maximal uptake corresponds to full oxidation of  $\text{Fe}^{2+}$  into  $\text{Fe}^{3+}$ , as confirmed by Mössbauer spectroscopy, Table II.5 and II.6.

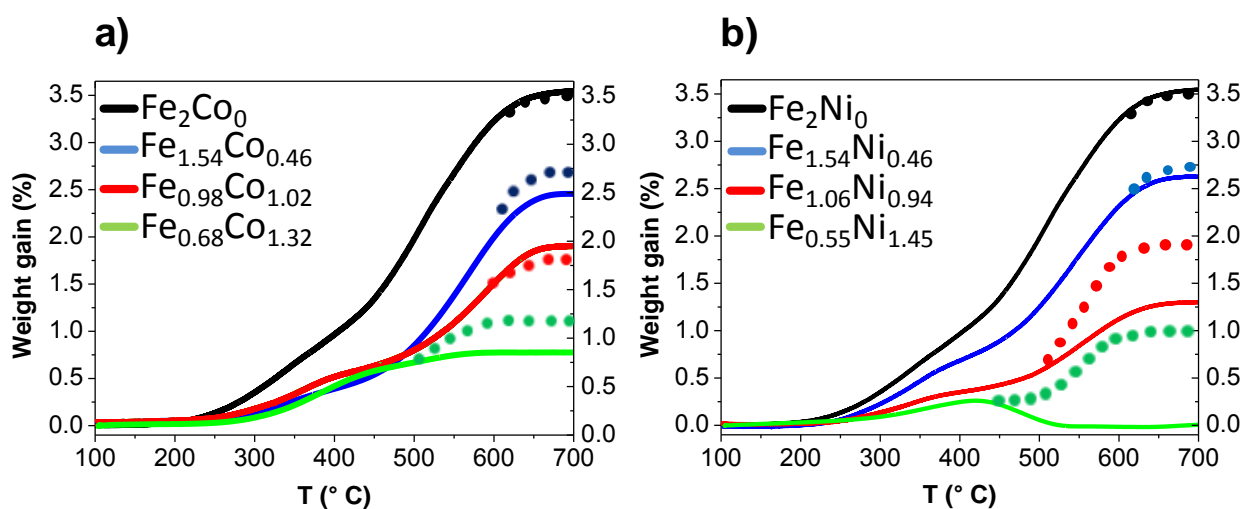


**Figure II.30.** Weight gain after Thermogravimetric analysis (TGA) for a)  $\text{BaFe}_{(2-y)}\text{Co}_y(\text{PO}_4)_2$  and b)  $\text{BaFe}_{(2-y)}\text{Ni}_y(\text{PO}_4)_2$ .

4.3.2.1. Co /Fe case.

- TGA analysis:

TGA For the mixed Co/Fe compounds, the TGA mass uptake matches rather well  $\Delta M_{\text{calc}}$  in the full y range though slight discrepancies for  $y=0.46$  and  $y=1.32$  (Fig. II.24a). The Mössbauer spectra shows only  $\text{Fe}^{3+}$  ions after heating, see Table 5. At this point, taking into account equations (1) and (2<sub>Co</sub>), deviations of the TGA from  $\Delta M_{\text{calc}}$  could denote deviations of the real Co/Fe ratio from the microprobe results, due to the averaging of several experimental points. For instance the 2.44 % (for  $y=0.46$ ) and 0.79% (for  $y=1.32$ ) mass uptake gives ideal 0.62 and 1.56 stoichiometries not far but different from those deduced from the analysis, i.e. 0.46 and 1.32.

- $^{57}\text{Fe}$  Mossbauer spectroscopy:

In the figure 31 are presented the three different Mössbauer spectroscopy spectra of the different Fe/Co ratio compounds. Dealing with these spectra for Fe-rich compounds ( $y=0.48$  and 1.02) the  $\text{Fe}^{3+}_{\text{phase}}/\text{Fe}^{3+}_{\text{hematite}}$  atomic ratio ( $\sim 2$ ) is in good agreement with equation (1). For these two samples, A broad distribution of nanometric size can be deduced from the proportion of  $\text{Fe}_2\text{O}_3$  that underwent the Morin transition at 78 K, see Table II.5. The presence or not of this latter spin-flip reorientation gives good clues about the nanosize of  $\text{Fe}_2\text{O}_3$  clusters, as developed in ref [60]. Because of intrinsic finite size effects related to lattice expansion, strains, defects, shape etc, the Morin temperature of small  $\text{Fe}_2\text{O}_3$  particles decreases with decreasing particle size and tend to be below 4K for particles smaller than ac. 8-20 nm.[50, 51]

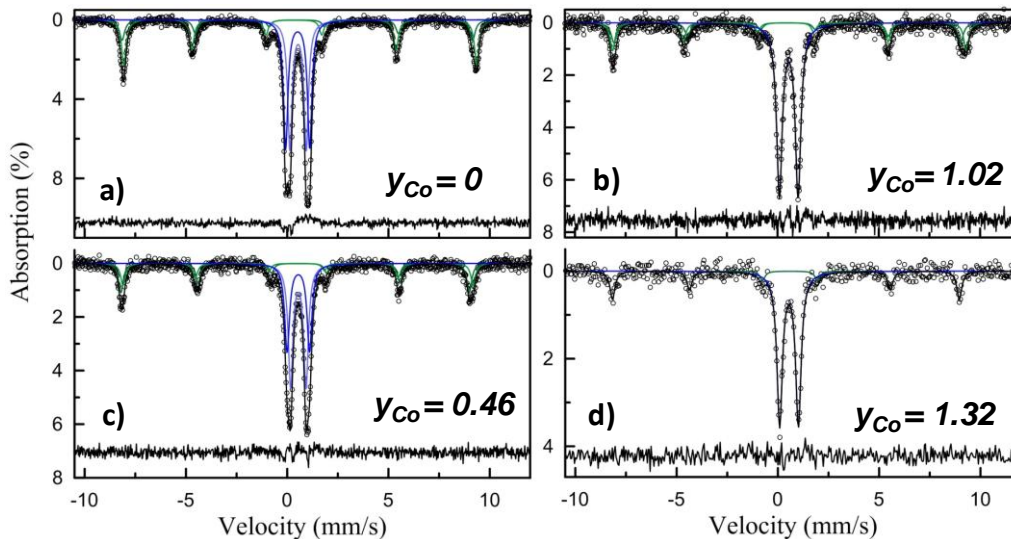


Figure II.31. Mössbauer spectra at 78 K and at 298 K of depleted  $\text{BaFe}_{(2-y)}\text{Co}_y(\text{PO}_4)_2$

**Table II.5.**  $^{57}\text{Fe}$  Mössbauer Hyperfine Parameters of the oxidized  $\text{BaFe}_{1.33}(\text{PO}_4)_2$  and  $\text{BaFe}_{1-y}\text{M}_y(\text{PO}_4)_2$  compounds. (IS, isomer shift relative to  $\alpha\text{-Fe}$  at ambient temperature;  $\Delta E_Q$ , apparent quadrupole shift;  $H_{\text{Hf}}$ , magnetic hyperfine field; G, line width; A, relative spectral area).

<b>BaFe<sub>2-y</sub>Co<sub>y</sub>(PO<sub>4</sub>)<sub>2</sub></b>								
<b>As prepared and after heat</b>								
<b>T, K</b>	<b>ideal composition</b>	<b>Component</b>	<b>IS, mm/s</b> ± 0.01	<b><math>\Delta E_Q</math>, mm/s</b> ± 0.01	<b>H<sub>Hf</sub>, T</b> ± 0.1	<b>A</b> %	<b>G,</b> mm/s	<b>assignment</b>
300	$\text{BaFe}_{1.33}(\text{PO}_4)_2$	F2S1	0.37	-0.14	51.8	38	0.34	$\text{Fe}_2\text{O}_3$
		F2D2	0.40	1.19	-	31	0.28	$\text{Fe}^{3+}$ (1)
		F2D3	0.42	0.81	-	31	0.27	$\text{Fe}^{3+}$ (2)
78	$\text{BaFe}_{1.33}(\text{PO}_4)_2$	F2S2	0.49	0.02	53.7	12	0.30	$\text{Fe}_2\text{O}_3(\text{i-im})$
		F2S2	0.49	0.32	54.0	24	0.28	$\text{Fe}_2\text{O}_3(\text{ii-m})$
		F2D4	0.52	1.18	-	32	0.26	$\text{Fe}^{3+}$ (1)
		F2D5	0.54	0.81	-	32	0.26	$\text{Fe}^{3+}$ (2)
300	$\text{BaFe}_{1.03}\text{Co}_{0.46}(\text{PO}_4)_2$	C05S1	0.35	-0.19	51.7	35	0.32	$\text{Fe}_2\text{O}_3$
		C05D1	0.39	1.13	-	27	0.30	$\text{Fe}^{3+}$ (1)
		C05D2	0.40	0.76	-	38	0.30	$\text{Fe}^{3+}$ (2)
78	$\text{BaFe}_{1.03}\text{Co}_{0.46}(\text{PO}_4)_2$	C05S2	0.48	-0.20	53.5	19	0.28	$\text{Fe}_2\text{O}_3(\text{i-nm})$
		C05S3	0.50	0.07	53.8	14	0.28	$\text{Fe}_2\text{O}_3(\text{ii-im})$
		C05D3	0.54	1.11	-	29	0.29	$\text{Fe}^{3+}$ (1)
		C05D4	0.54	0.76	-	38	0.28	$\text{Fe}^{3+}$ (2)
300	$\text{BaFe}_{0.65}\text{Co}_{1.02}(\text{PO}_4)_2$	C1S1	0.37	-0.18	51.6	34	0.29	$\text{Fe}_2\text{O}_3$
		C1D1	0.43	0.93	-	66	0.33	$\text{Fe}^{3+}$ (1)
78	$\text{BaFe}_{0.65}\text{Co}_{1.02}(\text{PO}_4)_2$	C1S2	0.49	-0.03	53.3	16	0.33	$\text{Fe}_2\text{O}_3(\text{i-nm})$
		C1S3	0.49	0.18	54.4	19	0.29	$\text{Fe}_2\text{O}_3(\text{ii-m})$
		C1D2	0.55	0.93	-	66	0.34	$\text{Fe}^{3+}$ (1)
300	$\text{BaFe}_{0.45}\text{Co}_{1.32}(\text{PO}_4)_2$	C15S1	0.37	-0.21	51.5	28	0.33	$\text{Fe}_2\text{O}_3$
		C15D1	0.43	0.93	-	72	0.34	$\text{Fe}^{3+}$ (1)
78	$\text{BaFe}_{0.45}\text{Co}_{1.32}(\text{PO}_4)_2$	C15S2	0.49	-0.20	53.2	25	0.29	$\text{Fe}_2\text{O}_3(\text{i-nm})$
		C15D2	0.54	0.93	-	75	0.32	$\text{Fe}^{3+}$ (1)

For  $y_{\text{Co}} = 1.32$ , in first approximation one find  $\text{Fe}^{3+}_{\text{phase}}/\text{Fe}^{3+}_{\text{hematite}} = 3$  at 78 K above the expected 2 ratio. In addition, no Morin transition was detected at 78K proving nano-sized domains. It is probable that for such Co-rich composition the  $\text{Fe}^{2+}$  diffusion paths are blocked by the more static  $\text{Co}^{2+}$  ions. At this point, the processes depicted by equations 1 and 2<sub>Co</sub> could be in competition as evidenced by TEM and EDX analyzes of unwashed depleted  $y_{\text{Co}} = 1.32$  after TGA: the majority of the crystallites show a Fe/Co close to 0.4/1.4 as expected after Fe-exsolution into  $\text{BaFe}^{3+}_{0.45}\text{Co}^{2+}_{1.3}(\text{PO}_4)_2$  with an increased concentration of Fe ions at their edges, as shown in figure II.32(a). Contrarily to our previous results on  $\text{BaFe}_{1.33}(\text{PO}_4)_2$ , we did not find clear evidences of  $\text{Fe}_2\text{O}_3$  clusters by EDX since Ba and P are found in the

coating particles which may be due to the analyzed area sized such that the core is probed as well. These results support the creation of intimately intergrown nanosized  $\text{Fe}_2\text{O}_3$  grains. At this point it is reasonable that part of  $\text{Fe}_2\text{O}_3$  is in super paramagnetic state even at 78K, which means undistinguished by Mössbauer spectroscopy from those of the depleted phase, in agreement with the  $\text{Fe}_2\text{O}_3$  deficiency mentioned above. More rarely can we find Co-rich particles crystallites coated by Co-rich nanograins with absence of P and Ba elements (eq.  $2\text{Co}_0$ ), assigned to Fe doped  $\text{Co}_3\text{O}_4$  clusters, figure II.32(b). It shows a certain degree of inhomogeneity in the sample, but above all shows that for Co very rich compositions, the cobalt depletion via equation  $2\text{Co}_0$  is possible. However this phenomenon should be very rare taking into account the minor occurrence of such crystallites in our TEM analysis and our Co-K edge XANES results.

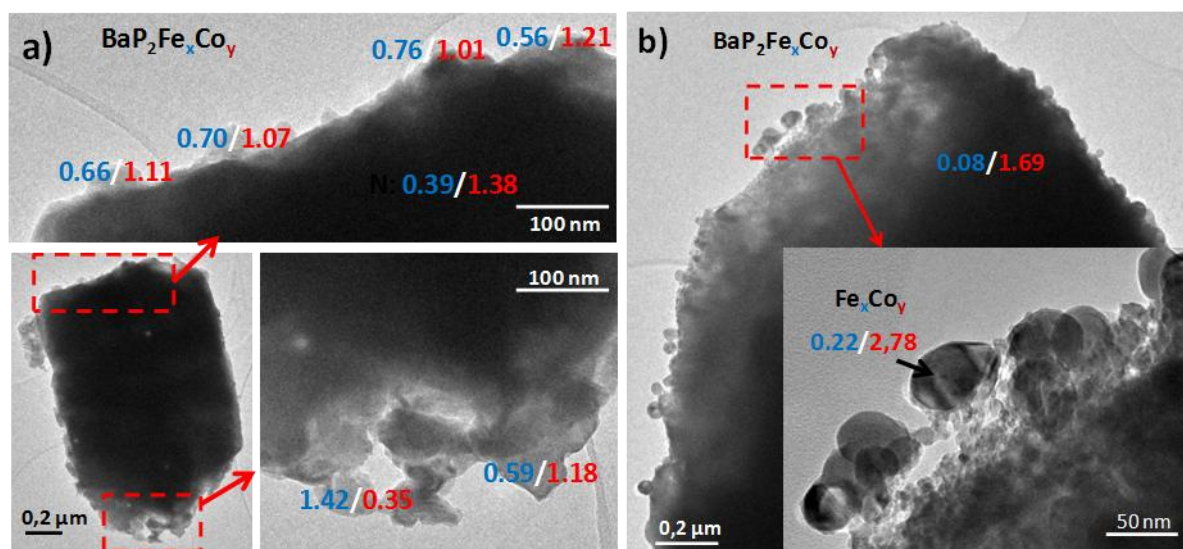


**Figure II.32.** Coupled TEM images and EDX analysis for two different crystals (a) and (b) of  $\text{BaFe}_{0.45}\text{Co}_{1.32}(\text{PO}_4)_2$ . The Fe/Co ratio (indicated respectively in blue and red) shows a homogeneous expected composition core and Fe surfacial enrichment due to intergrown  $\text{Fe}_2\text{O}_3$  (a) and cobalt excess in the core with Fe doped cobalt oxide at the surface (b).

#### 4.3.2.2. Fe/Ni case.

- **TGA analysis:**

Concerning the  $\text{BaFe}_{2-y}\text{Ni}_y(\text{PO}_4)_2$  solid solution, important discrepancies between TGA plots and  $\Delta M_{\text{calc}}$  are observed as soon as  $y = 0.94$ , see figure II.29(b). Especially, for  $y = 1.45$  the mass uptake turns into a mass loss above  $450^\circ\text{C}$ . Besides, the possible deviation from the announced stoichiometry from microprobe analysis, the dehydration of the  $\text{BaHPO}_4$  [63] second phase (see section 4.2), remaining in the sample after sonication, is responsible for this weight loss. It occurs according to the chemical reaction:



It was verified by XRD analysis before, fig II.24(b), and after thermal treatment showing appearance of  $\text{Ba}_2\text{P}_2\text{O}_7$  diffraction peaks after heating for the Ni rich phase, see figure II.26(d).

- $^{57}\text{Fe}$  Mossbauer spectroscopy:

Concerning the Mössbauer spectroscopy, shown in figure II.33 and table II.6, the  $\text{Fe}_2\text{O}_3$  content ( $\sim 1/3^{\text{rd}}$ ) matches perfectly the equation 1, but as soon as  $y = 0.94$ , an apparent  $\text{Fe}_2\text{O}_3$  deficiency is observed at 78 K ( $\sim 28\%$  instead of 33%). For  $y = 1.45$  even no more magnetically ordered  $\text{Fe}_2\text{O}_3$  is detected, but two paramagnetic  $\text{Fe}^{3+}$  components with a 62:38 ratio. Once again the high concentration of  $\text{Ni}^{2+}$  ions hampers the Fe diffusion, but in an even more drastic way.

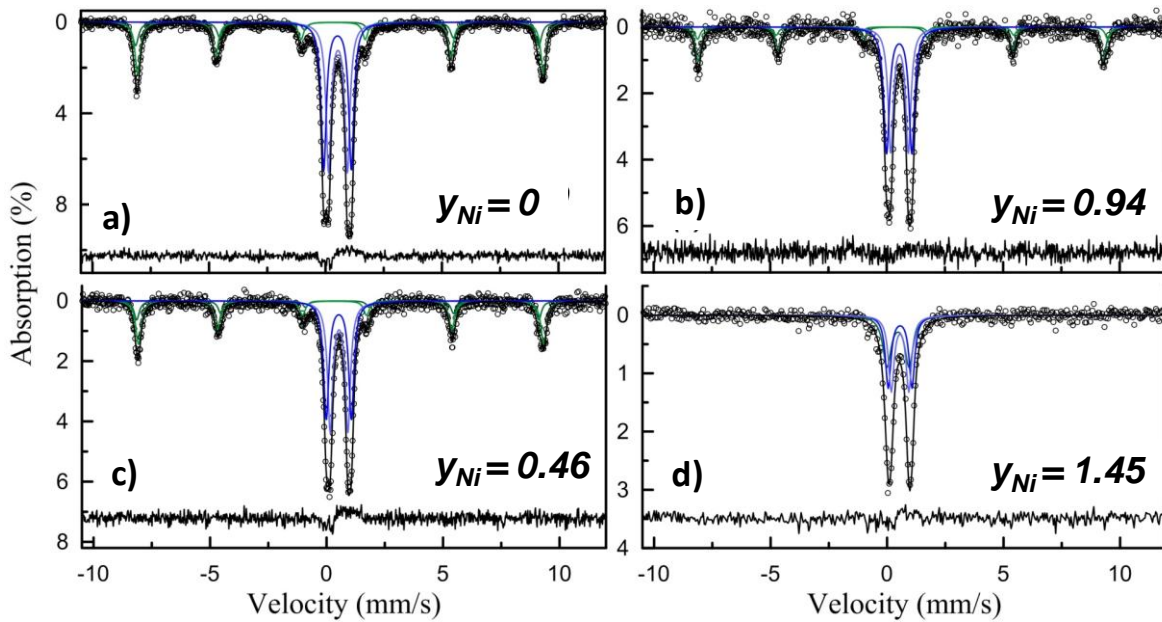
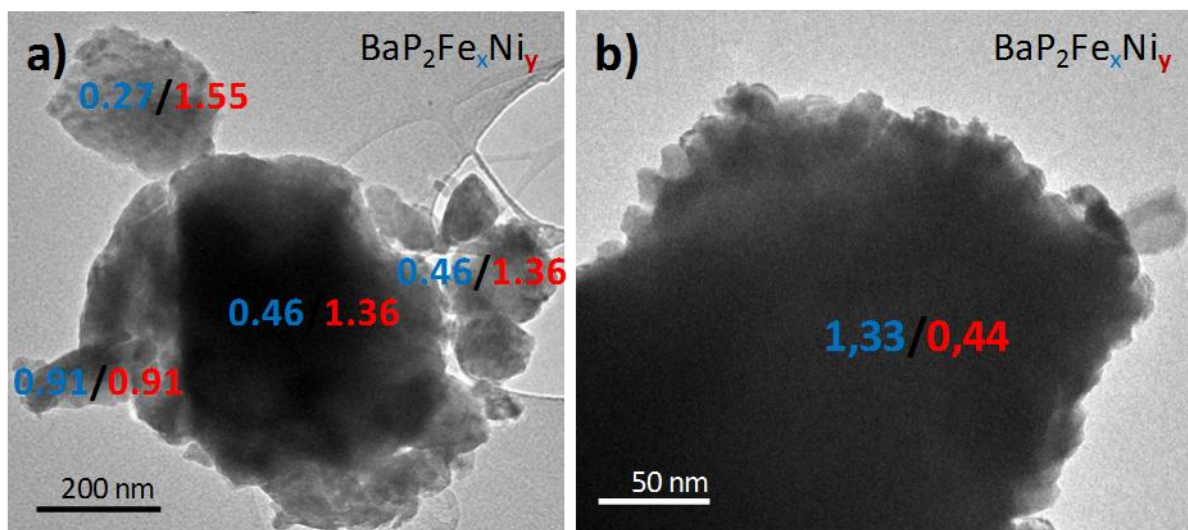


Figure II.33. Mössbauer spectra at 78 K and at 298 K of depleted  $\text{BaFe}_{(2-y)}\text{Co}_y(\text{PO}_4)_2$

**Table II.6.**  $^{57}\text{Fe}$  Mössbauer Hyperfine Parameters of the oxidized  $\text{BaFe}_{1-y}\text{Ni}_y(\text{PO}_4)_2$  compounds. (IS, isomer shift relative to  $\alpha\text{-Fe}$  at ambient temperature;  $\Delta E_Q$ , apparent quadrupole shift;  $H_{\text{HF}}$ , magnetic hyperfine field; G, line width; A, relative spectral area).

<b>BaFe<sub>2-y</sub>Ni<sub>y</sub>(PO<sub>4</sub>)<sub>2</sub></b>								
<b>As prepared and after heat</b>								
<b>T, K</b>	<b>ideal composition</b>	<b>Component</b>	<b>IS, mm/s</b> $\pm 0.01$	<b><math>\Delta E_Q</math>, mm/s</b> $\pm 0.01$	<b><math>H_{\text{HF}}</math>, T</b> $\pm 0.1$	<b>A</b> <b>%</b> $\pm 1$	<b>G,</b> <b>mm/s</b> $\pm 0.01$	<b>assignment</b>
300	$\text{BaFe}_{0.71}\text{Ni}_{0.94}(\text{PO}_4)_2$	N1S1	0.34	-0.09	52.0	30	0.40	$\text{Fe}_2\text{O}_3$
		N1D1	0.38	1.09	-	37	0.31	$\text{Fe}^{3+}$ (1)
		N1D2	0.40	0.76	-	33	0.29	$\text{Fe}^{3+}$ (2)
78	$\text{BaFe}_{0.71}\text{Ni}_{0.94}(\text{PO}_4)_2$	N1S2	0.48	0.21	54.1	21	0.30	$\text{Fe}_2\text{O}_3$ (i-m)
		N1S3	0.51	0.33	54.8	7	0.27	$\text{Fe}_2\text{O}_3$ (ii-m)
		N1D3	0.53	1.09	-	38	0.29	$\text{Fe}^{3+}$ (1)
300	$\text{BaFe}_{0.71}\text{Ni}_{0.94}(\text{PO}_4)_2$	N1D4	0.54	0.76	-	34	0.27	$\text{Fe}^{3+}$ (2)
		N1S1	0.34	-0.09	52.0	30	0.40	$\text{Fe}_2\text{O}_3$
		N1D1	0.38	1.09	-	37	0.31	$\text{Fe}^{3+}$ (1)
78	$\text{BaFe}_{0.71}\text{Ni}_{0.94}(\text{PO}_4)_2$	N1D2	0.40	0.76	-	33	0.29	$\text{Fe}^{3+}$ (2)
		N1S2	0.48	0.21	54.1	21	0.30	$\text{Fe}_2\text{O}_3$ (i-m)
		N1S3	0.51	0.33	54.8	7	0.27	$\text{Fe}_2\text{O}_3$ (ii-m)
300	$\text{BaFe}_{0.37}\text{Ni}_{1.45}(\text{PO}_4)_2$	N1D3	0.53	1.09	-	38	0.29	$\text{Fe}^{3+}$ (1)
		N1D4	0.54	0.76	-	34	0.27	$\text{Fe}^{3+}$ (2)
		N15D1	(0.34)	0.91	-	(33)f	0.46	$SP(\text{Fe}_2\text{O}_3)$
78	$\text{BaFe}_{0.37}\text{Ni}_{1.45}(\text{PO}_4)_2$	N15D2	0.44	1.07	-	35	0.29	$\text{Fe}^{3+}$ (1)
		N15D3	0.45	0.71	-	32	0.29	$\text{Fe}^{3+}$ (2)
		N15D4	(0.47)	0.95	-	(33)f	0.43	$SP(\text{Fe}_2\text{O}_3)$
		N15D5	0.55	1.02	-	33	0.29	$\text{Fe}^{3+}$ (1)
		N15D6	0.55	0.75	-	34	0.29	$\text{Fe}^{3+}$ (2)

The combined TEM/EDX analysis on heated  $y_{\text{Ni}} = 1.45$ , i.e.  $\text{BaFe}_{0.37}\text{Ni}_{1.45}(\text{PO}_4)_2$  shows homogeneous Fe:Ni ratio in the particles core, e.g. 0.46:1.36 in figure II.34. In the external particles we find a diversity of behaviors from the Fe enrichment to the Fe exhaustion. Here, it is probable that the  $\text{Ni}^{2+}$  obstacles can merely rearrange in the structure leading to fragmentation of the crystals for  $\text{Fe}^{2+}$  removal and growth of  $\text{Fe}_2\text{O}_3$  intergrown nano-domains. Once again it leads to super-paramagnetic characteristics due to their size. This result is in good agreement with the Mössbauer spectroscopy.



**Figure II.34.** Coupled TEM images and EDX analysis of a)  $BaFe_{0.37}Ni_{1.45}(PO_4)_2$  and b)  $BaFe_{1.03}Ni_{0.46}(PO_4)_2$ .

#### 4.3.3. Full Fe/M reorganization in depleted phase ; a single crystal study

- $BaFe^{3+}_{0.67}M^{2+}_1(PO_4)_2$  crystal structure:

Single crystal with suitable size for XRD collection have been selected after heating  $BaFe_{0.98}Co_{1.02}(PO_4)_2$  and  $BaFe_{0.63}Ni_{1.04}(PO_4)_2$  12h at 600°C. The crystal structure refinement was carried out for more insights about eventual Fe/Co and Fe/Ni ordering in these samples, in relation with the discussion above. The two compounds show similar precession frames which denote similar structures. As systematically found in all  $BaFe_{2-x}(PO_4)_2$  phases reported so far ( $x = 2/7, 1/2, 2/3$ ) [3, 60] the collected crystal presents three twinning domains related by 120° and 240° around  $c^*$  due to the rhombohedral pseudo-symmetry, as determined with the software CellNow.[52] In this case the imbrication between the spots is particularly tricky, leading for instance to ondulated dot lines in the  $[h\ 0.33\ l]_{\text{Rhomb}}$  precessions images. In fact they correspond to the superposition of three contributions as shown in the figure II.34(b), while the full dataset can be indexed with the three misoriented domains.

In a first approach, we processed a refinement in the sub-cell corresponding to the parent rhombohedral cell of  $BaFe_2(XO_4)_2$ . This preliminary refinement give clues about the metal stoichiometry, as reported for several  $BaFe_{2-x}(PO_4)_2$  polytypes [60]. At this stage there are no means for Fe/Co distinction, leading to the formula  $Ba(Fe,M)_{1.63}(PO_4)_2$  ( $a = 4.8096(14)$  Å,  $c = 23.6634(9)$  Å, space group R-3,  $R_{\text{obs}} = 3.66\%$ ,  $R_{\text{all}} = 3.76\%$ ) after refining the occupancy of the metal site 6c (0,0, $z \sim 1/3$ ) and assuming a mixed Fe/Co composition. We note that the refined formula is very close to  $BaM_{1.66}(PO_4)_2$ , the ideal expected formula being  $BaFe_{0.67}M_1(PO_4)_2$  after Fe-exsolution in  $BaFe_1M_1(PO_4)_2$  following equation 1.

In a second stage, taking into account weaker supercell reflections due to a partial order between metal and vacancies, it was possible to fully index the collected reflections in a triclinic unit ( $a = 8.3313(4)$ ,  $b = 8.3316(4)$ ,  $c = 8.3598(4)$ ,  $\alpha = 70.606(3)^\circ$ ,  $\beta = 99.558(3)^\circ$ ,  $\gamma = 120.013(3)^\circ$ ) cell given by the relation:

$$\begin{matrix} a_{Tricl} \\ a_{Tricl} \\ a_{Tricl} \end{matrix} = \begin{bmatrix} -2 & -1 & 0 \\ 1 & -1 & 0 \\ 1/3 & -1/3 & 1/3 \end{bmatrix} \begin{matrix} a_{Rhomb} \\ b_{Rhomb} \\ c_{Rhomb} \end{matrix}$$

The crystal structure was solved and refined leading to final  $R_{obs} = 5.33\%$ , with the three domains contributions equal to 0.3651, 0.3241 and 0.3108. The occupancies of the three independent metal sites M1, M2 and M3 are refined to 91.2%, 69.0%, 72.5% but have been restrained to 100%, 75% and 75% to match the ideal formula refined in the subcell.

For the Fe/Ni case, single crystal diffraction has been performed as well. In the same way that in the previous case, the crystal structure refinement was carried out in a first approach in the corresponding parent rhombohedral unit cell. This refinement lead to a final stoichiometry of  $Ba(Fe,Ni)_{1.72}(PO_4)_2$  in a R-3 unit cell with parameters  $a = 4.796(28) \text{ \AA}$  and  $c = 23.535(22) \text{ \AA}$ . After refining occupancy of the metal site 6c (0,0, $z \sim 1/3$ ) and assuming a mixed Fe/Ni composition, final refinement leads to a  $R_{obs} = 2.49 / R_{all} = 2.55$  without presence of distorted octahedral metal positions at 9e (1/2, 0, 0).

Precession images of the crystal are compared to that from the Fe/Co, explained previously, in figure II.35.

Very similar patterns are found in both cases, so, to take in account weaker supercell reflections we used the same triclinic unit cell than in  $BaFe_{0.67}Co_1(PO_4)_2$  phase.

The crystal structure was then solved in a triclinic (S.G. P-1) unit cell with  $a = 8.3078(7) \text{ \AA}$ ,  $b = 8.3074(7) \text{ \AA}$ ,  $c = 8.3194(8) \text{ \AA}$ ,  $\alpha = 70.567(4)^\circ$ ,  $\beta = 99.559(39)^\circ$ ,  $\gamma = 120.034(36)^\circ$ . As announced for all the previous pristine structures three twin domains are systematically presents and related by 120 and 240 ° around the  $c^*$  reciprocal axis. After refinement, the different domains contribution are equal to 0.3346, 0.3354 and 0.3300. Contrary to the  $BaFe_{0.67}Co_1(PO_4)_2$  case, in the  $[h0.331]_{Rhomb}$  ondulated dot lines are not so clear, but large distorted dots are in the same place.

Final refinement taking into account weaker supercell reflections leads to a  $R_{obs} = 2.83\% / R_{all} = 5.87\%$ . In this case, we observe again the existence of a metal site with almost 100% occupancy whereas the other two sites are partially occupied. The obtained formula after occupancy refinement corresponds to  $BaFe_{0.63}Ni_{1.04}(PO_4)_2$ .

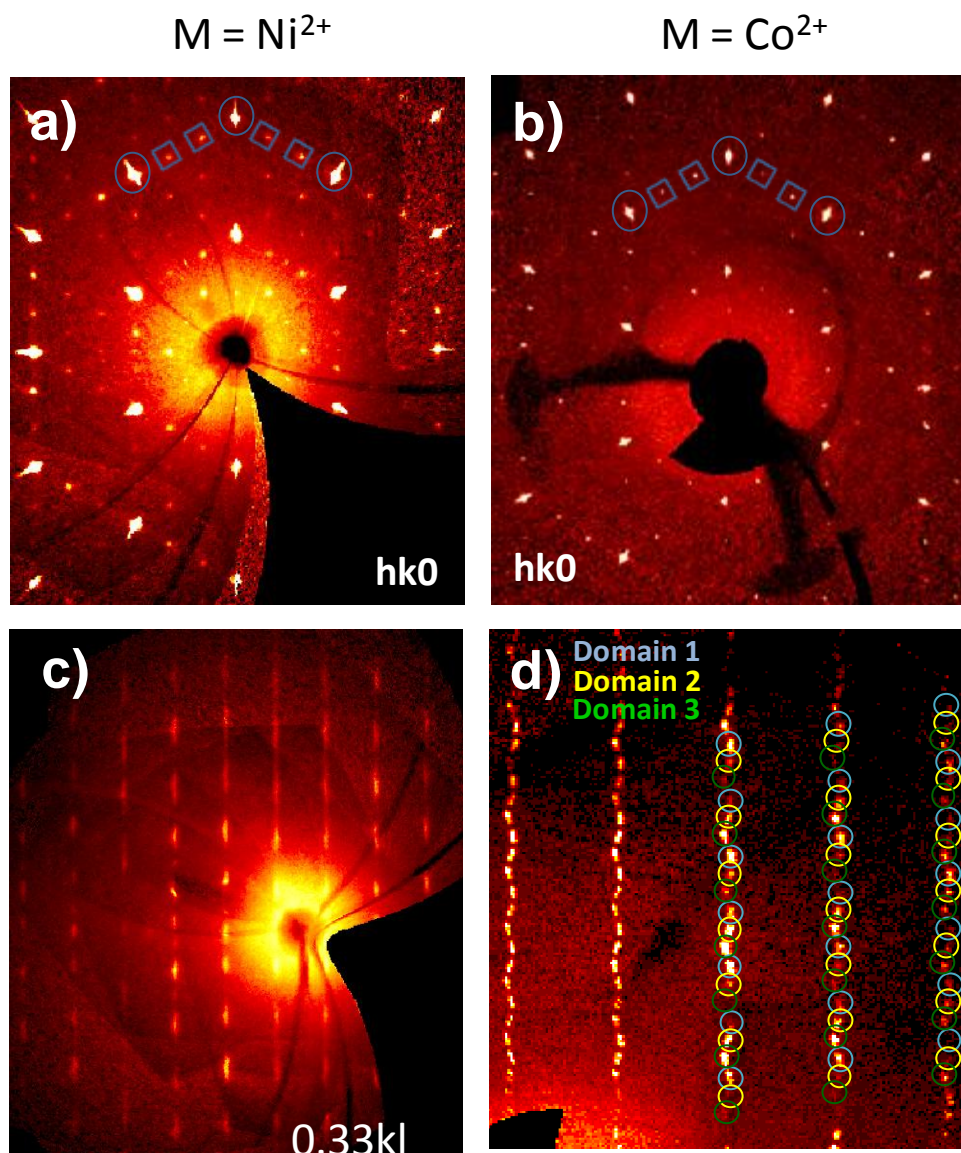


**Figure II.35.** Precession image in the rhombohedral unit cell of the  $[h k 0]$  layer showing supercell spots for  $\text{BaFe}_{0.67}\text{Ni}_{1.04}(\text{PO}_4)_2$  (a) and for  $\text{BaFe}_{0.67}\text{Co}_{1.02}(\text{PO}_4)_2$  (c). Precession image in the rhombohedral unit cell of the  $[h 0.33 l]$  layer with evidence of the three different twinned domains for  $\text{BaFe}_{0.67}\text{Ni}_{1.02}(\text{PO}_4)_2$  (c) and  $\text{BaFe}_{0.67}\text{Co}_{1.02}(\text{PO}_4)_2$  (d) single crystal.

To validate the refined models, we note that the calculated powder XRD diagrams match rather well the experimental powder patterns for the composition  $y_M \approx 1$  after thermal treatment (figure II.36).

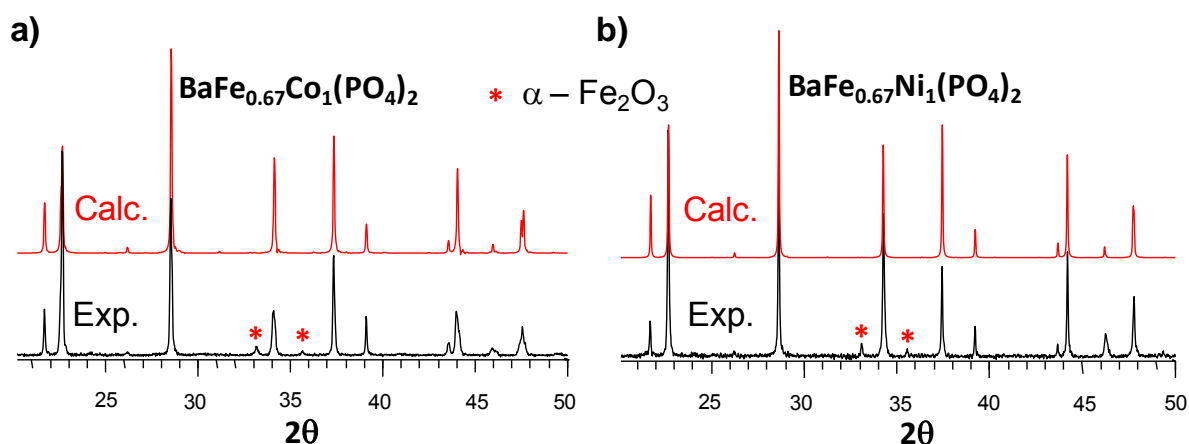


**Figure II.36.** Comparison between experimental powder XRD pattern and calculated one from single crystal of  $\text{BaFe}_{0.67}\text{Co}(\text{PO}_4)_2$  (a) and  $\text{BaFe}_{0.67}\text{Ni}(\text{PO}_4)_2$ .

Dealing with the honeycomb layer, the final structure is almost but not fully ordered. M-O bond distances are listed in the Table II.7. It shows ordering in 1D-columns with a  $3a_{\text{Rhomb}}$  period. These columns are stacked to pave the 2D-layers. It is striking that bond valence sums calculated in the  $\text{Co}^{2+}/\text{Ni}^{2+}$  and  $\text{Fe}^{3+}$  hypotheses indicate chemical and charge segregation. Finally using 100%  $\text{Fe}^{3+}$  in M1 and 75%  $\text{Co}^{2+}/\text{Ni}^{2+}$  in M2 and M3 yields the ideal, charge-balanced formula  $\text{BaFe}_{0.67}\text{M}_1(\text{PO}_4)_2$  and the best BVS agreements. This is in good agreement with the Mössbauer spectroscopy as the  $\text{Fe}^{3+}$  component in the depleted  $\text{BaFe}_{0.67}\text{M}_1(\text{PO}_4)_2$  phase spectra is fitted by a single doublet with narrow line width, indicating a uniform surrounding for all the  $\text{Fe}^{3+}$  cations (Tables II.5, II.6).

In the layers, the  $\text{M}^{2+}$  sites (75% occupied) are arranged in zig zag chains running along the  $\langle 210 \rangle_{\text{rhomb}}$  direction and shown in blue on figure II.37(a). The chains are linked together by the fully occupied  $\text{Fe}^{3+}$  dimers shown in grey. The analogy of this structure with the one refined for  $\text{BaFe}_{1.67}(\text{PO}_4)_2$  prepared after partial Fe exsolution is depicted in the figure II.37(b). In the latter, the fully occupied Fe dimers are replaced by elongated  $\text{Fe}^{2+}\text{O}_6$  octahedra, between  $\text{Fe}^{3+}$  chains. In  $\text{BaFe}_{0.67}\text{M}(\text{PO}_4)_2$  the segregation between  $\text{M}^{2+}$  chains and  $\text{Fe}^{3+}$  sites demonstrates that not only Fe but also Co and Ni ions re-organize themselves in the Fe-depleted layers. Further details about crystal data collection are reported in the annex. Atomic coordinates and anisotropic displacements are shown in the annex as well.

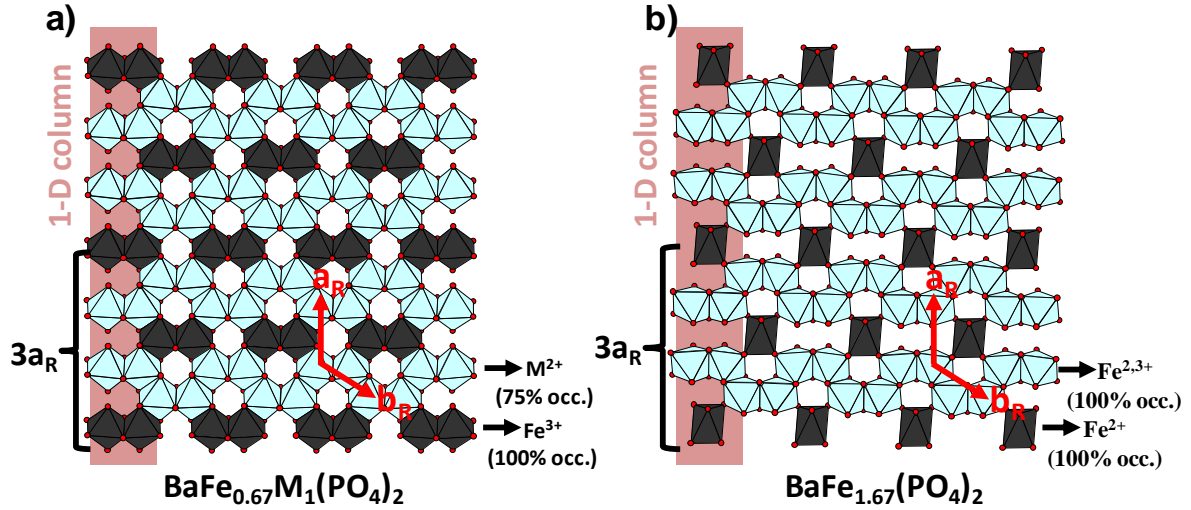


**Figure II.37.** Structural analogies between  $BaFe_{0.67}M_1(PO_4)_2$  (a), and  $BaFe_{1.67}(PO_4)_2$  (b) with evidence of the  $3a_R$  super-period. The red arrows correspond to the parent rhombohedral cell.

**Table II.7.** Atomic distances and associated Bond Valence Sums ( $\Sigma s_{ij}$ ) values, calculated using parameters associated to  $Fe^{3+}$  and  $Co^{2+}$  from reference[53], of  $BaFe_{0.67}Co(PO_4)_2$ .

Distances d (Å)											
$BaFe_{0.67}Co(PO_4)_2$						$BaFe_{0.67}Ni(PO_4)_2$					
<i>M ions</i>											
Co1-O1	2.14(3)	Co2-O1	2.26(3)	Fe1-O4	1.96(2)	Ni1-O2	2.09(7)	Ni2-O1	2.11(1)	Fe1-O1	2.09(0)
Co1-O2	2.02(2)	Co2-O3	2.11(2)	Fe1-O5	2.00(3)	Ni1-O6	2.08(2)	Ni2-O3	2.16(5)	Fe1-O2	2.08(3)
Co1-O2	2.03(3)	Co2-O4	2.08(3)	Fe1-O8	2.15(3)	Ni1-O6	2.14(9)	Ni2-O8	2.12(9)	Fe1-O3	2.06(6)
Co1-O3	2.16(3)	Co2-O5	2.05(2)	Fe1-O8	2.09(2)	Ni1-O7	2.12(9)	Ni2-O8	2.06(0)	Fe1-O5	2.00(5)
Co1-O9	2.09(4)	Co2-O11	2.08(3)	Fe1-O9	2.02(2)	Ni1-O10	1.99(8)	Ni2-O10	2.02(5)	Fe1-O5	2.02(1)
Co1-O10	2.10(2)	Co2-O11	2.05(2)	Fe1-O10	2.10(3)	Ni1-O11	1.98(8)	Ni2-O11	1.99(0)	Fe1-O7	2.05(5)
$\Sigma s_{ij}$	2.09(7)	$\Sigma s_{ij}$	1.99(6)	$\Sigma s_{ij}$	2.79(8)	$\Sigma s_{ij}$	2.04(6)	$\Sigma s_{ij}$	2.00(2)	$\Sigma s_{ij}$	2.68(2)
<i>P ions</i>											
P1-O3	1.53(4)	P2-O1	1.54(4)	P3-O2	1.58(2)	P1-O1	1.53(1)	P2-O5	1.59(4)	P3-O3	1.53(1)
P1-O5	1.62(2)	P2-O4	1.61(2)	P3-O6	1.53(4)	P1-O2	1.55(4)	P2-O6	1.52(4)	P3-O4	1.51(3)
P1-O7	1.53(5)	P2-O9	1.53(3)	P3-O8	1.58(4)	P1-O9	1.52(1)	P2-O8	1.58(5)	P3-O7	1.54(9)
P1-O10	1.49(3)	P2-O12	1.51(8)	P3-O11	1.50(3)	P1-O10	1.58(5)	P2-O12	1.51(3)	P3-O11	1.59(4)
<i>Ba ions</i>											
Ba1-O7	2.78(3)x2	Ba2-O6	2.76(0)	Ba2-O7	2.78(3)	Ba1-O1	3.10(4)	Ba1-O4	2.86(2)	Ba2-O4	2.96(4)x2
Ba1-O12	2.82(4)x2	Ba2-O6	2.59(7)	Ba2-O12	2.79(4)	Ba1-O3	3.03(2)	Ba1-O4	2.75(2)	Ba2-O6	3.05(2)x2

## 5. Synchrotron « in situ » diffraction.

The crystallographic features showed by  $\text{BaFe}_2(\text{PO}_4)_2$  and  $\text{BaFe}_{2-y}\text{M}_y(\text{PO}_4)_2$  after thermal treatments and the difficulties encountered to follow and treat the evolution of the “in-situ” Powder X-Ray diffractogram because of their complexity (high number of peaks with small separation and small intensities when passing from R-3 to the P-1 symmetry), made us think about a synchrotron XRD study “in situ” during a thermal treatment of the phases. For this purpose a proposal to SOLEIL synchrotron was deposited and has been accepted. Taking into account the high intensity of the synchrotron beam, the aim of the project was to follow evolution of the phase transformation during the exsolution reaction “in situ” when increasing the temperature, in order to identify different satellite peaks of very weak intensities, involving the existence of modulation vectors related to the superstructures observed previously (section 3.4).

For this purpose a preliminary study was realized in a Rigaku SmartLab equipped with an Anton Paar DHS 1100 Domed Hot Stage for high temperature measurement under controlled atmospheres. This diffractometer was used to optimize all the parameters involved in the reaction such as the heating rate, the minimal time required to reach the end of the exsolution reaction or the minimal temperature needed to reach the most exsolved (100%  $\text{Fe}^{3+}$ ) phase. In addition, static and dynamic atmospheres were tested. At the beginning we preferred a static atmosphere in order to imitate the furnace conditions; however, the volume of air enclosed in the graphite dome does not contain enough oxygen to allow the whole phase oxidization. Thus, we finally chose dynamic atmosphere conditions, to ensure the full sample oxidation.

The samples studied in this section correspond to the most iron rich  $\text{BaFe}_{1.5}\text{M}_{0.5}(\text{PO}_4)_2$  substituted phases (M= Ni, Co) and to  $\text{BaFe}_2(\text{PO}_4)_2$ . After several tests the chosen protocol to drive the reaction for  $\text{BaFe}_2(\text{PO}_4)_2$  was a heating rate of 5 °C/min from ambient to 600 °C. Finally the sample was kept at 600 °C for two hours to ensure the complete transformation and be sure to obtain the final stable phase. For the Fe/M samples the treatment was similar but with a final temperature of 700 °C, because the M atoms hamper the exsolution and the reaction is not finished after the 2 hours treatment at 600 °C.  $2\theta$  scans were realized between 20-40° with a counting time of 1 second every 0.02° step.

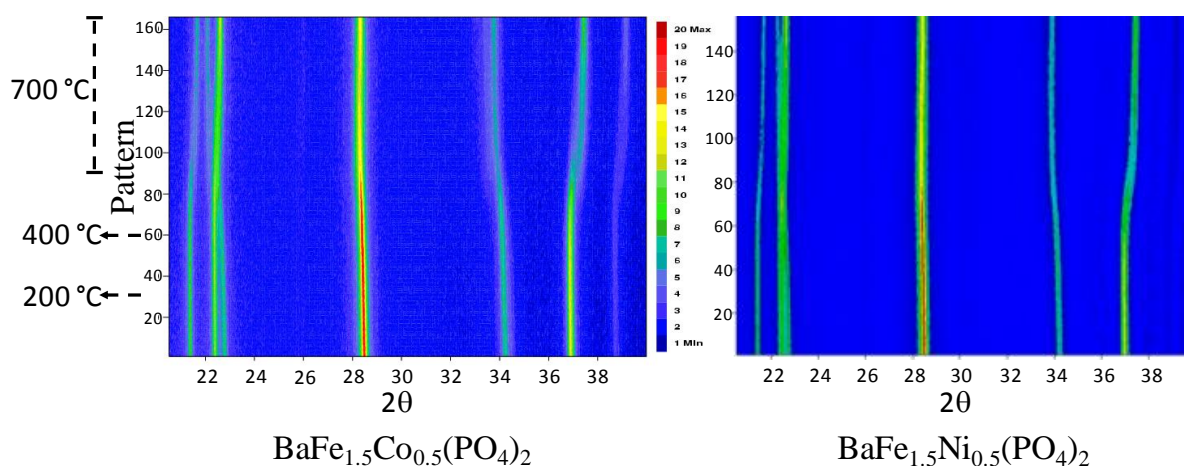


**Figure II.38.** XRD « in situ » patterns evolution for  $BaFe_{1.5}M_{0.5}(PO_4)_2$  ( $M= Co, Ni$ ) recorded on the Rigaku SmartLab.

Figure II.38 shows the diffractograms evolution obtained on the Rigaku SmartLab, for  $BaFe_{1.5-x}Co_{0.5}(PO_4)_2$  and  $BaFe_{1.5-x}Ni_{0.5}(PO_4)_2$  phases during the whole thermal treatment. We can observe the start of the transformation around the pattern number 60 which corresponds to a temperature of 400 °C. The reflections displacements are related to unit cell parameters evolution (see section 4.2.) and are ending around the pattern 150 where  $T= 700$  °C has been kept for an hour. Patterns performed with longer measuring times, at room temperature after thermal treatment, show no extra reflections, keeping, at least in those conditions, the rhombohedral symmetry, even if a partial cationic order has been determined by single crystal diffraction in section 4.3.3.

The experiment was then reproduced with the same optimized conditions on Diffabs beamline; however, its technical specifications didn't allow us to achieve completely our target. The main problem faced was the characteristics of the detector and the beam geometry used. The XPAD 2-D detector presents some advantages but also some important disadvantages for the purpose searched. Its principal advantage is a very short measuring time, because, depending of the distance and the position, it can measure a large portion of the diffraction rings. This property is very interesting with respect to the kinetic aspect of our experiments where the sample evolves continuously in time during the phase transformation. However, the main disadvantage working in parallel beam is the inability to focus the detector on the diffracted zone of the sample surface. The focus would avoid the dome reflections detection. This was the case in the laboratory diffractometer with a Bragg Brentano configuration where we could focus in the sample playing with the slits of the linear detector. Figure II.39 presents a schema of both geometries.

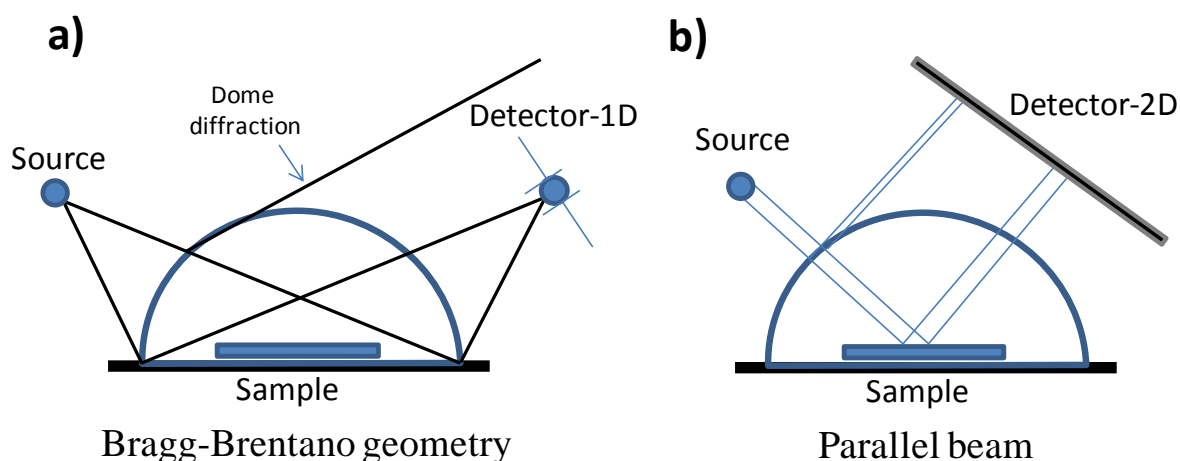


**Figure II.39.** Differences between the geometries and detectors of the experiments realized in the laboratory (a) and in the synchrotron beamline (b).

In our case, the detector-2D presents an important problem associated to the dome, since some very intense reflections of graphite avoid a good visualization of the patterns evolution (see  $2\theta \approx 13^\circ$  in figure II.40), masking the small reflections of the phase. However, even if it is not huge, there is an improvement of the intensities of the diffracted reflections of the sample, compared to the data obtained on the laboratory diffractometer.

For Fe/M samples where, at least with the laboratory diffractometer, the rhombohedral symmetry is kept over all the transformation (no evidence of satellite reflections), the resolution problem becomes still more important. Figure II.40 shows the evolution of XRD patterns of the Fe/Ni sample as example. Apart from the  $\text{Fe}_2\text{O}_3$  reflection which appears around the pattern 85 corresponding to a  $T = 500^\circ\text{C}$ , there is an additional reflection which appears at  $2\theta = 14.3^\circ$ . This reflection could justify a symmetry loss of the compound, however, the poor resolution and the absence of more unidentified reflections make impossible to go further in conclusion.

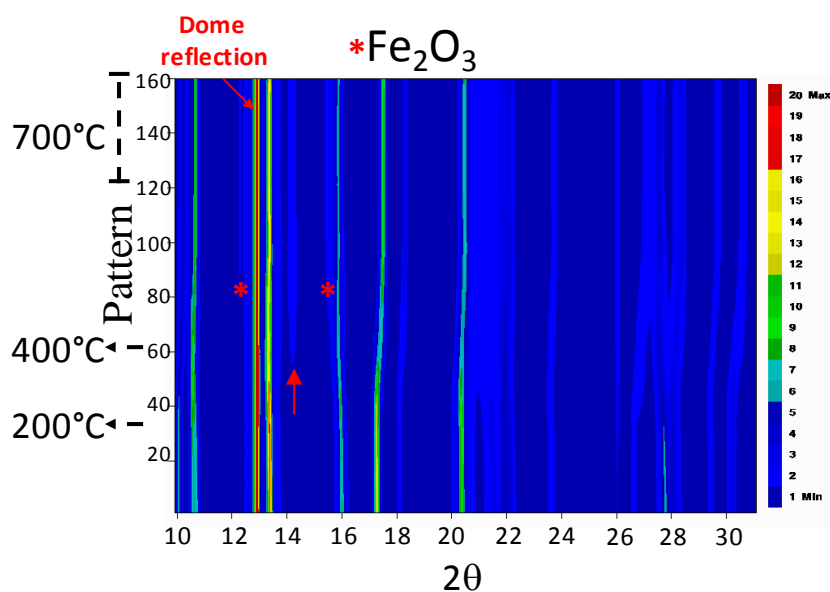


**Figure II.40.** Synchrotron “in situ” XRD patterns for  $BaFe_{1.5-x}Ni_{0.5}(PO_4)_2$ , asterisks show the most intense  $Fe_2O_3$  reflections and red arrow shows the unidentified reflection.

On the other hand, for the  $BaFe_2(PO_4)_2$  sample, showed in figure II.41, we can remark some details on synchrotron patterns. Firstly, around patterns 50-60 ( $T= 300-400^\circ C$ ) we can observe the first reflections displacements. At the beginning they can be associated to the thermal dilatation and the beginning of exsolution process, but these displacements continue while temperature increases and from pattern 80 ( $T= 500^\circ C$ ) several peaks start to split; the phase loses the rhombohedral symmetry to become triclinic (section 3.2). After  $600^\circ C$  (around pattern 120) we don't observe further changes, which means that  $BaFe_{1.33}(PO_4)_2$  is reached.

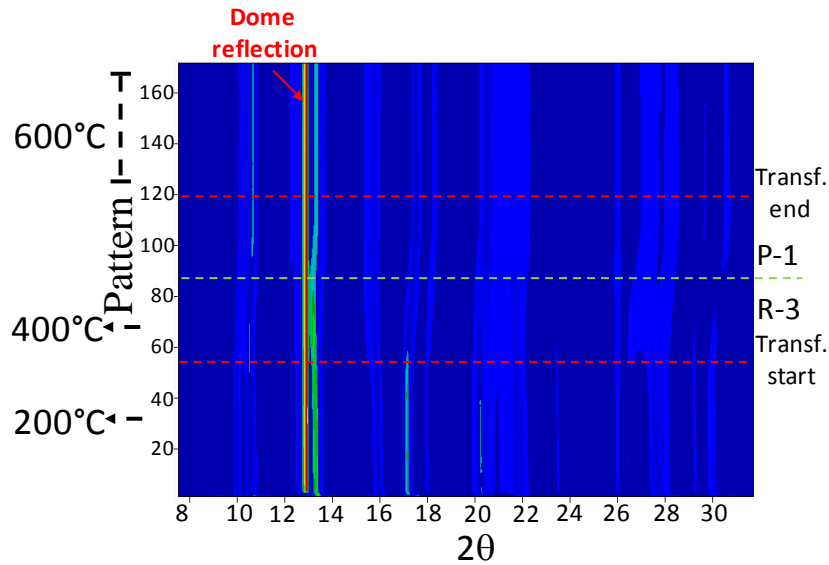


**Figure II.41.** « *in situ* » patterns for  $\text{BaFe}_{2-x}(\text{PO}_4)_2$  on synchrotron beamline ( $\lambda = 0.7293\text{\AA}$ ). Dome reflection mask phase intensities.

Moreover, the bad resolution makes hard the identification of satellite reflections. Figure II.42(a) shows the different resolution of the same pattern ( $\text{BaFe}_{1.33}(\text{PO}_4)_2$ ) measured on the 11-BM (blue) beamline and on DIFFABS (red and green) during the “in situ” measurement (with dome and 3 seconds per image) and at ambient temperature after thermal treatment (without dome and 6 seconds per image). Satellite reflections can be deduced, as shown by the asterisk in figure II.42(a), on the pattern recorded with longer time per image and it is still recognizable with shorter measured times.

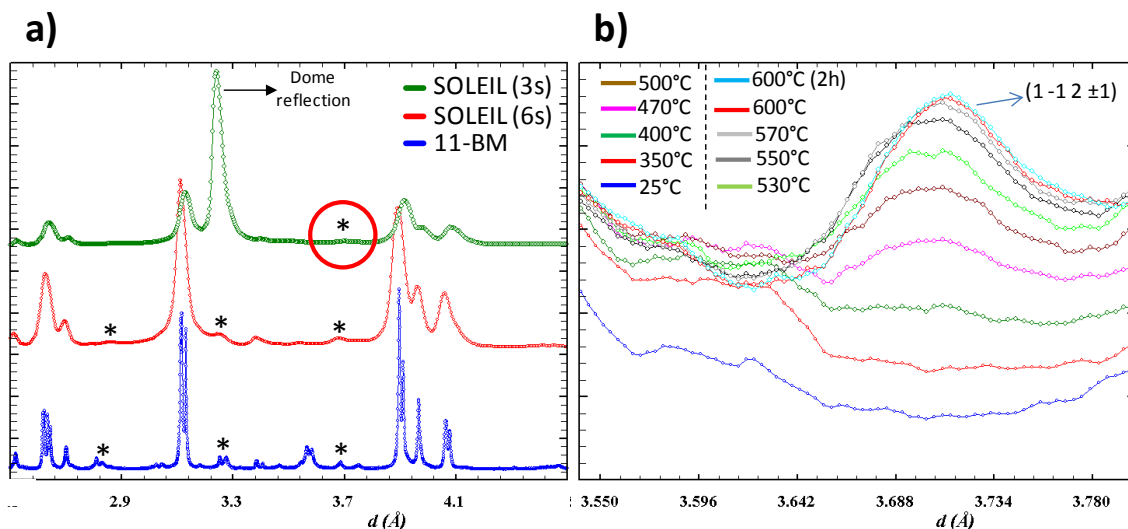


**Figure II.42. a)**  $\text{BaFe}_{1.33}(\text{PO}_4)_2$  sample comparison between patterns recorded on 11-BM beamline (blue) and on DIFFABS (red) at SOLEIL synchrotron facilities. Asterisks show the presence of satellite reflections. **b)** Zoom of satellite reflection (red circle on figure a) evolution within temperatures.

However, if we zoom the zone where the satellite reflection is expected ( $d=3.7\text{\AA}$ ), we can observe its evolution during the thermal treatment as presented in figure II.42(b). It shows that superstructures of  $\text{BaFe}_{2-x}(\text{PO}_4)_2$  are formed at high temperature during the phase transformation and not during the sample cooling. This result it can be explained if we consider that only  $\text{Fe}^{2+}$  is mobile, so when of all the iron atoms are oxidized, this  $\text{Fe}^{3+}$  is already placed (even at moderate temperature) in the most stable position, inducing the superstructure.

However, we have been able to identified and follow the evolution of only one satellite reflections of  $\text{BaFe}_{1.33}(\text{PO}_4)_2$ , and it doesn't allow to establish the presence of the other superstructures ( $\text{BaFe}_{1.71}(\text{PO}_4)_2$ ,  $\text{BaFe}_{1.66}(\text{PO}_4)_2$ ,  $\text{BaFe}_{1.5}(\text{PO}_4)_2\dots$ ) observed by single crystal at high temperature.

## 6. Magnetic characterization.

For magnetic characterization, magnetization cycles at 2 K for  $\text{BaFe}_{1.33}(\text{PO}_4)_2$  and at 2 and 300 K for  $\text{BaFe}_{2-x}\text{M}(\text{PO}_4)_2$  exsolved phases and temperature dependent magnetic susceptibility, were measured on a MPMS Squid (Quantum Design). Typical measurements were performed using the zero field cooling (ZFC) and field cooling (FC) procedures under a 0.1 T field.

### 6.1. $\text{BaFe}_{2-x}(\text{PO}_4)_2$ .

The magnetic susceptibility (approximated as  $M/H$ ) measured at  $\mu_0H = 0.1\text{T}$  for  $\text{BaFe}_{1.33}(\text{PO}_4)_2$  after washing the second phase  $\text{Fe}_2\text{O}_3$ , is shown on the figure II.43(a). It shows a paramagnetic behaviour down to 23K. The Curie-Weiss fit gives  $\mu_{\text{eff}} = 5.96 \mu_{\text{B}}/\text{Fe}$  and  $\theta_{\text{CW}} = -29.4\text{K}$ . It is very close to the spin-only value expected for  $\text{Fe}^{3+}$  ( $S=5/2$ ,  $L=0$ ,  $\mu_{\text{eff}}=5.91 \mu_{\text{B}}$ ) while antiferromagnetic (AFM) interactions are predominant. It was well establish that  $\text{BaFe}_2(\text{PO}_4)_2$  is a 2D- uniaxial ferromagnet ( $T_{\text{C}} = 65.5 \text{K}$ ) with soft magnetization, unsaturated magnetization due to robust domain walls and magnetic moments refined by powder neutron diffraction ( $5.01\mu_{\text{B}}/\text{Fe}$ ) parallel to the c-axis.[1] Our result shows that Fe-depletion and oxidation favour AFM exchanges. In  $\text{BaFe}_2(\text{PO}_4)_2$  the superexchanges (SSE)  $\text{Fe}^{2+}\text{-O-Fe}^{2+}$  strongly predominate on other in-plane Fe-O-O-Fe super super exchanges (SSEs) and are responsible for the ferromagnetic character. All paths are strongly modified in the depleted compounds, as shown in the table II.8, but conserve most of their Fe-O-Fe angles close to  $90^\circ$

for both  $x=1/3$  and  $x=2/3$ . The most decisive change concerns the contribution of at least one  $\text{Fe}^{3+}$  site in all SSE exchanges for  $x=1/3$ , while only  $\text{Fe}^{3+}$  ions are concerned for  $x=2/3$ . Assuming predominant SSE paths, the contribution of trivalent iron systematically lead to AFM exchanges, as discussed in our previous work about Fe-exsolution into mixed valent  $\text{BaFe}^{2/3+}_{2-x}(\text{PO}_4)_2$ . [3] The figure II.43(b) shows the evolution of the magnetization  $M(H)$  at 2K between  $x=0$ ,  $x=0.4$  (multiphased sample with predominant  $x = 1/3$  according to powder synchrotron data) and  $x=2/3$ . It appears clearly that the decrease of the coercitive moment ( $2.25\mu\text{B}$  for  $x=0$  ( $\text{Fe}^{2+}$ ),  $0.12\mu\text{B}$  for  $x=0.4$  ( $\text{Fe}^{2.5+}$ ) and 0 for  $x=2/3$  ( $\text{Fe}^{3+}$ )) on increasing  $x$  ( i.e. Ferro  $\rightarrow$  weak ferro  $\rightarrow$  antiferromagnetic) result from AFM SSEs, as soon as  $\text{Fe}^{3+}$  ions are involved. Although SSE probably has a crucial role, they would also play in favour of AFM. The weak ferrimagnetism for  $x=0.4$  most presumably stem from remaining  $\text{Fe}^{2+}\text{-O-Fe}^{2+}$  contacts in this multi-phase sample. Of course in so complex depleted layers, frustration and non-collinear spins are plausible, but once again stem from AFM SSE's.

**Table II.8.** Geometry of the Fe-O-Fe superexchange paths in the  $\text{BaFe}_{2-x}(\text{PO}_4)_2$  phases.

Fe interaction	$d_{\text{Fe-Fe}}$ (Å)	$\angle\text{Fe-O-Fe}$ (°)	Fe interaction	$d_{\text{Fe-Fe}}$ (Å)	$\angle\text{Fe-O-Fe}$ (°)
<b>x=0</b>			<b>x=1/3</b>		
$\text{Fe}^{2+}\text{-Fe}^{2+}$ Corner-sharing	2.8181(1)	82.974(189)	$\text{Fe}_{1a}^{3+}\text{-Fe}_{3a}^{2+}$ Corner-sharing	3.5429(40)	109.484(962)
<b>x=2/3</b>			$\text{Fe}_{2a}^{3+}\text{-Fe}_{3a}^{2+}$ Corner-sharing	3.5034(40)	107.495(1154)
$\text{Fe}_3^{3+}\text{-Fe}_3^{3+}$ Face-sharing	3.0508(84)	94.994(1117)	$\text{Fe}_{1a}^{3+}\text{-Fe}_{1a}^{3+}$ Face-sharing	3.0475(67)	91.831(821)
$\text{Fe}_4^{3+}\text{-Fe}_4^{3+}$ Face-sharing	3.0494(85)	94.611(1408)	$\text{Fe}_{2a}^{3+}\text{-Fe}_{2a}^{3+}$ Face-sharing	3.0071(78)	90.583(915)
$\text{Fe}_1^{3+}\text{-Fe}_3^{3+}$ Face-sharing	3.0915(73)	89.658(967) 100.207(1141)	$\text{Fe}_{1a}^{3+}\text{-Fe}_{2a}^{3+}$ Face-sharing	2.8960(45)	85.057(845)
$\text{Fe}_2^{3+}\text{-Fe}_4^{3+}$ Face-sharing	3.0956(71)	98.499(1103) 94.586(1040)	$\text{Fe}_{1a}^{3+}\text{-Fe}_{2a}^{3+}$ Face-sharing	2.8960(45)	89.047(907)

For  $\text{BaFe}_{1.33}(\text{PO}_4)_2$ ,  $\chi(T)$  shows two sharp anomalies at 16.2 K and 4.2K. They are fully reproducible on ZFC and FC measurements which denote no net magnetic moment as confirmed by the monotone  $M(H)$  increasing at 2K. It could be ascribed to spin-reorientation or competing ranges of antiferromagnetic correlations, e.g.in plane short-range and 3D long-range. At least the magnetic ordering across  $\sim 8\text{Å}$  interlayers occurs  $T_N = 5.3\text{K}$  for

BaCo<sub>2</sub>(AsO<sub>4</sub>)<sub>2</sub> [36] close to the low temperature anomaly, although dealing with different spin magnitudes Fe<sup>3+</sup>, S=5/2 ions and Co<sup>2+</sup>, S=3/2 ions.

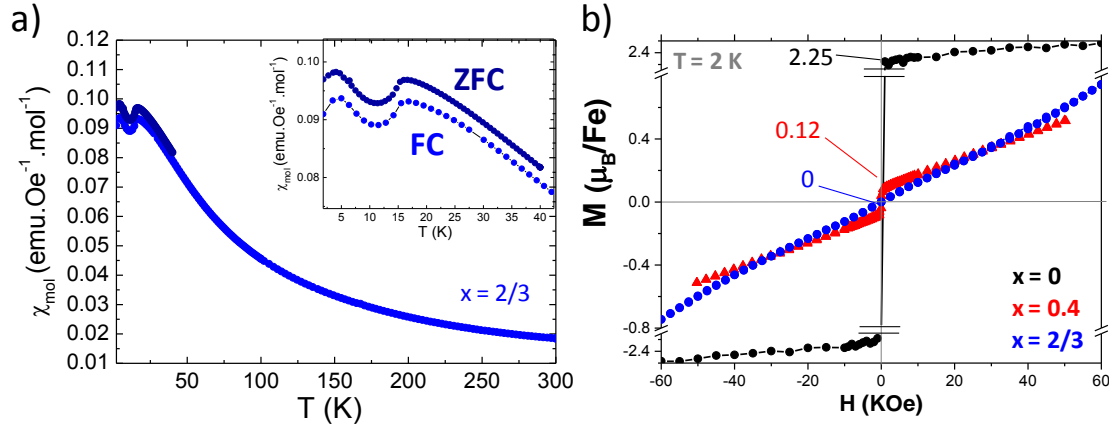


**Figure II.43.** a)  $M/H$  (at  $\mu_0 H = 0.1$  T) of  $BaFe_{1.33}(PO_4)_2$  after removing the  $Fe_2O_3$  phase. b) Comparison between the magnetization of three  $BaFe_{(2-x)}(PO_4)_2$  phases with  $x=0$  (2D ferromagnet),  $x=0.6$  (ferrimagnet) and  $x=2/3$  (antiferromagnetic).

## 6.2. Exsolved $BaFe_{2-x}M_x(PO_4)_2$ ( $M = Co^{2+}, Ni^{2+}$ ).

Before exsolution, the  $BaFe_{2-y}M_y(PO_4)_2$  ( $M = Co, Ni$ ) compounds present potentially very complex mixed cation systems, as solid solutions between  $BaCo_2(PO_4)_2$ , a quasi 2D-XY helimagnet[64],  $BaNi_2(PO_4)_2$ , a quasi 2D XY antiferromagnet with collinear spins and a Kosterlitz Thouless transition[65], and  $BaFe_2(PO_4)_2$  a 2D-ising ferromagnet.[1] The study of the magnetic properties of these solid solutions have not been studied during my PhD work.

After exsolution, negative exchanges can be predicted for  $Fe^{3+}-O-Ni^{2+}$  and  $Fe^{3+}-O-Co^{2+}$  from Kanamori-Goodenough rules. After exsolution, we have considered the ideal formulae given in Table II.4, predicted from the maximal exsolution of  $Fe^{2+}$  giving mixed  $Co^{2+}-Ni^{2+}/Fe^{3+}$  matrices, see eq (1). The samples have been washed from the  $Fe_2O_3$  second phase by sonication, although a small fraction of the nanosized  $Fe_2O_3$  cannot be fully removed.

- **Fe/Ni system:**

The evolution of  $\chi(T)$  for  $Ba(Fe_{2-y}Ni_y)_{2-x}(PO_4)_2$  is shown in figure II.44. Néel-like anomalies are evidenced at  $T_N = 13.7$  K ( $y=0.5$ , sharp), 6.6 K ( $y=1$ , sharp) and 5.1 K ( $y=1.5$ , broad) which shows a progressive shift but remain located between the two peaks evidenced for  $y=0$ . We note that in any case, the transition temperatures are lower than  $T_N = 24$  K reported for  $BaNi_2(PO_4)_2$ [66]. It most plausibly denotes an increasing distribution of short range correlations due to metal vacancies in disordered  $Ni^{2+}/Fe^{3+}$  depleted lattices. The  $M(H)$  magnetization plots confirm antiferromagnetic systems with no remanent moment nor metamagnetic transition between 300 K and 2 K (fig II.44 b, c) even though a smooth upturn

is detected around  $H=3$  KOe for  $y_{\text{Ni}}=0.5$ . In the paramagnetic regime, the values of effective moments were fitted between 5.70 and 7.58  $\mu_{\text{B}}$  which roughly agrees with the values calculated from ideal formulae, see Table II.4. In addition to the spin-orbit coupling expected strong for  $\text{Ni}^{2+}$  ions, shifts from the theoretical values may denote partial removal of  $\text{Fe}_2\text{O}_3$  and/or deviations from the ideals Fe/Ni stoichiometries.

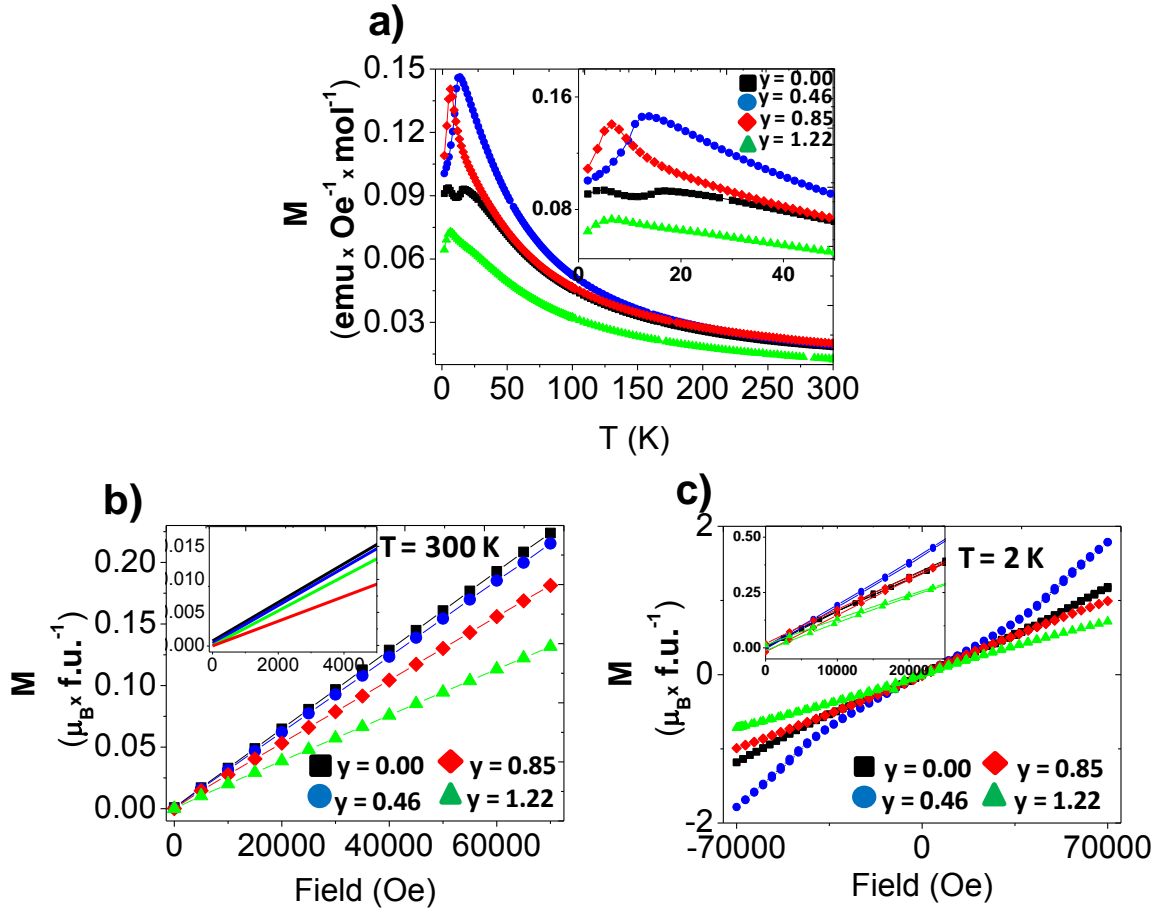


**Figure II.44.** Magnetic characterization of  $\text{BaFe}_{2-y}\text{Ni}_y(\text{PO}_4)_2$  after Fe exsolution:  $\chi(T)$  for the mixed Fe/Ni (a) phase. Magnetization plots at 300K and 2K for Fe/Ni(b, c).

- **Fe/Co system :**

In the case of  $\text{Ba}(\text{Fe}_{2-y}\text{Co}_y)_{1-x}(\text{PO}_4)_2$ , magnetic plots in figure II.45 show that the situation is more complicated. The  $M(H)$  plots at room temperature for  $\text{BaFe}_{0.65}\text{Co}_{1.02}(\text{PO}_4)_2$  and  $\text{BaFe}_{0.45}\text{Co}_{1.32}(\text{PO}_4)_2$  show a weak remanent moment (figure II.45, d). This is most probably related to the intimate coating of nano-textured  $\text{Fe}_2\text{O}_3$  grains at the crystallite surface, leading to superparamagnetism with blocking temperatures above room temperature. For these two compositions the concave shape of  $\chi(T)$  plots have been fitted using  $\chi=C/(T-\theta)+\chi_0$ , using the approximation of a constant superparamagnetic magnetization. This same approximation was successfully applied to  $\text{BaFe}_{2-x}(\text{PO}_4)_2$ [3]. The fits are very good (see figure II.46) giving  $\chi_0 = 0.021$  and  $0.020 \text{ emu} \cdot \text{mol}^{-1} \cdot \text{Oe}^{-1}$  for  $\text{BaFe}_{0.65}\text{Co}_{1.02}(\text{PO}_4)_2$  and  $\text{BaFe}_{0.45}\text{Co}_{1.32}(\text{PO}_4)_2$

respectively and show positive Curie Weiss temperatures which may be due to the super paramagnetic impurity . In these two samples, disordered  $\text{Co}^{2+}$  rich domains are expected, reminiscent of the  $\text{BaCo}_2(\text{XO}_4)_2$  phases ( $\text{X}=\text{P}^{5+}, \text{As}^{5+}$ ) which show in-plane helical magnetic structures, easy spin alignment under magnetic field and magnetization steps at low temperature for the arsenate.[67] Therefore it is not surprising that in  $\text{BaFe}_{0.65}\text{Co}_{1.02}(\text{PO}_4)_2$  and  $\text{BaFe}_{0.45}\text{Co}_{1.32}(\text{PO}_4)_2$  the  $M(H)$  at 2K shows an abrupt step in the low field region below  $\mu_0H = 0.6$  T, above which it recovers the  $M(H)$  slope typical of the Fe-rich compounds. The susceptibility measured for  $\text{BaFe}_{0.45}\text{Co}_{1.32}(\text{PO}_4)_2$  is very large, it reaches  $\sim 2$  emu/mol.Oe which is very similar to values reported for  $\chi_{(a,b)}$  in  $\text{BaCo}_2(\text{PO}_4)_2$ .[67] We conclude that in the two deficient systems the magnetic behaviour is driven by antiferromagnetic  $\text{Fe}^{3+}\text{-O-Fe}^{3+}$ ,  $\text{Fe}^{3+}\text{-O-M}^{2+}$  and  $\text{M}^{2+}\text{-O-M}^{2+}$  through edge-shared octahedra. For Ni-rich compounds, under an applied field the antiferromagnetism (AFM) is much more robust than in Co-rich compounds in good agreement with the parent Ni (AFM with site to site collinear spins) and Co compounds (soft helical AFM with nearly FM chains).

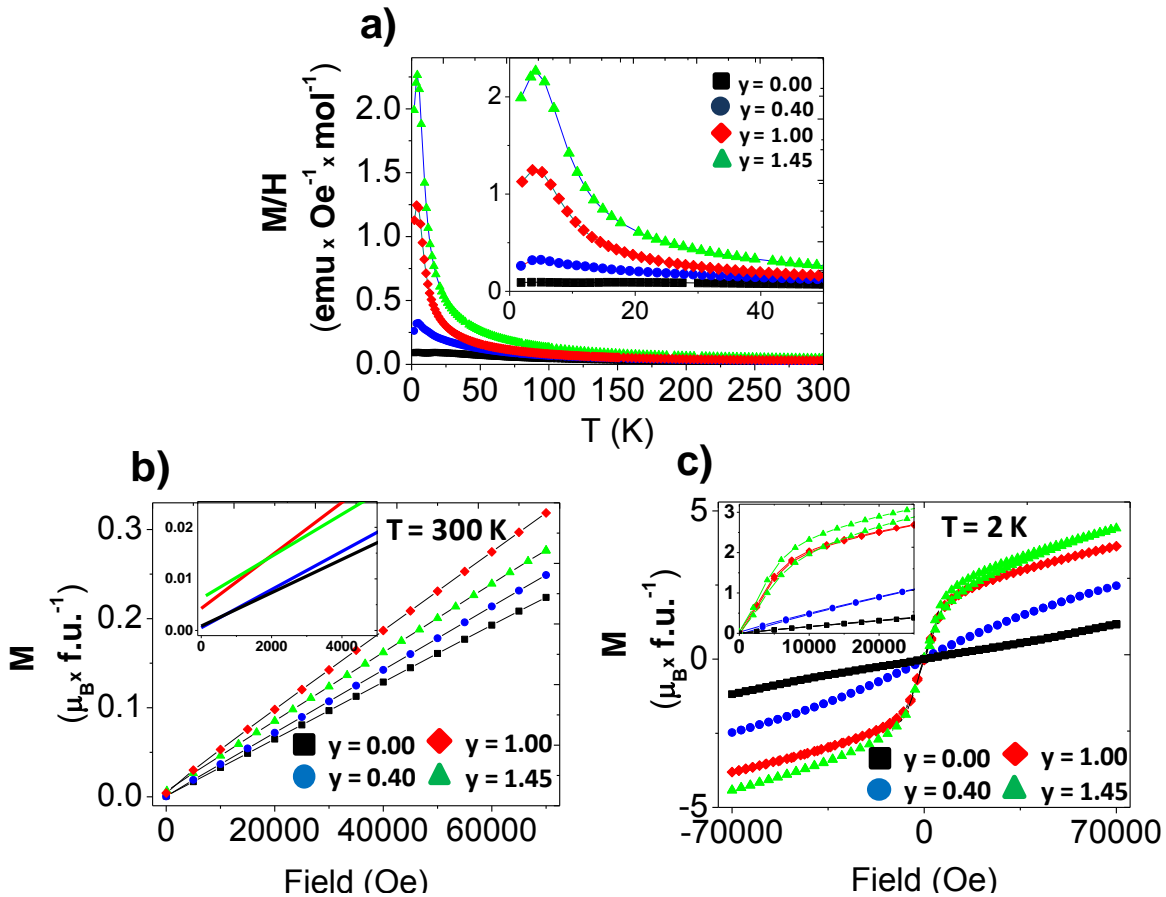


**Figure II.45.** Magnetic characterization of  $\text{BaFe}_{2-y}\text{Co}_y(\text{PO}_4)_2$  after Fe exsolution:  $\chi(T)$  for the mixed Fe/Co (a) phase. Magnetization plots at 300K and 2K for Fe/Co (b, c).

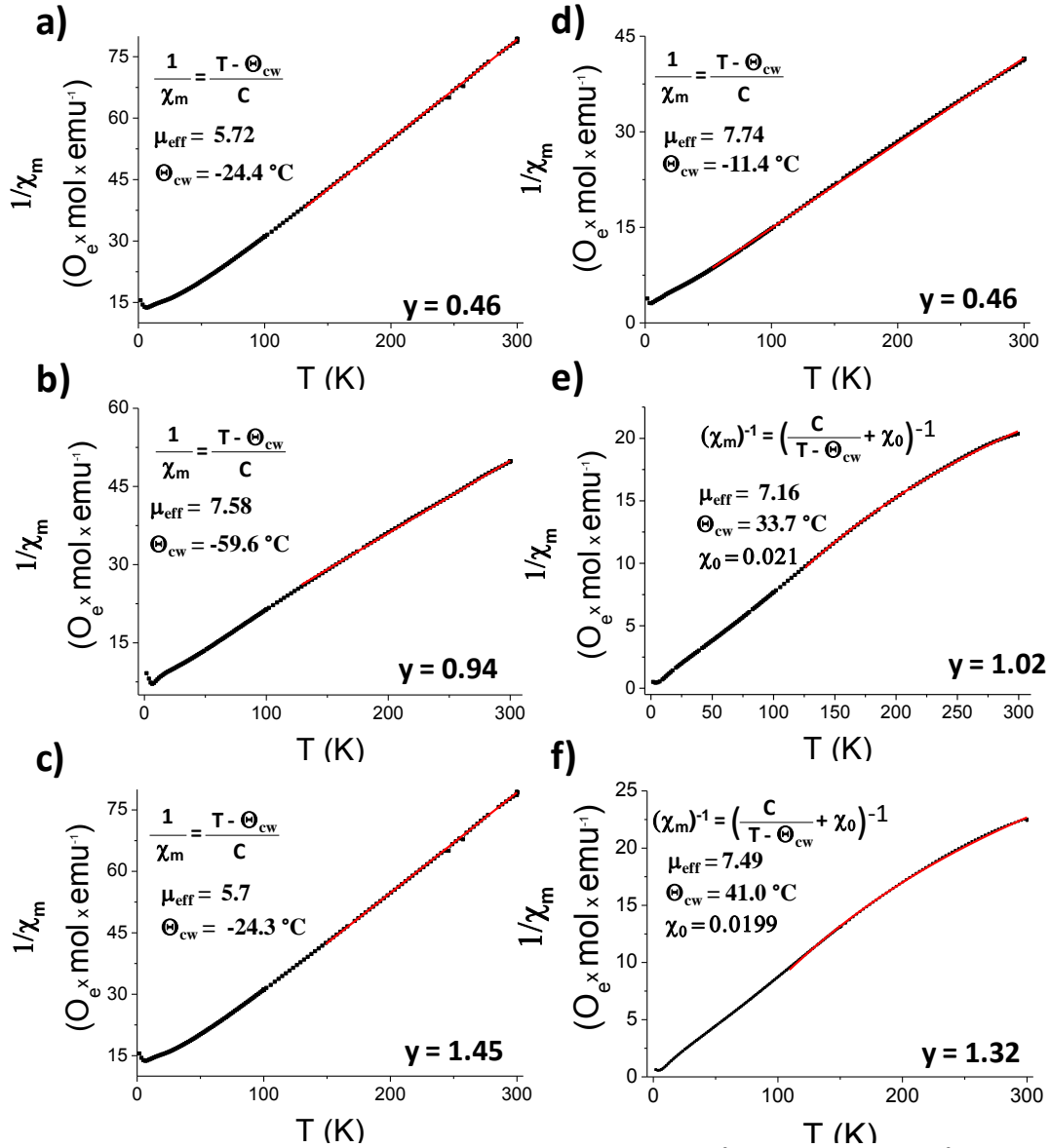


**Figure II.46.** Curie-Weiss fit for  $BaFe_{2-y}M_y(PO_4)_2$  for  $M = Ni^{2+}$  (a, b; c) and  $Co^{2+}$  (d, e, f). For e) and f) the  $\chi_0$  constant results from superparamagnetic contribution of  $\alpha\text{-Fe}_2\text{O}_3$  with blocking temperature above room temperature.

## 7. Conclusion.

$BaFe_2(PO_4)_2$  exsolves and reincorporates up to  $1/3^{\text{rd}}$  of its Fe-content in mild oxidizing/reducing conditions leading to  $\alpha\text{-Fe}_2\text{O}_3$  nanoparticles and a collection of  $BaFe_{2-x}(PO_4)_2$  phases. The identified phases at various  $x$  values systematically show full Fe/ $V_{\text{Fe}}$  orderings within novel layered charge ordered topologies. We show here that the main motifs paving the 2D-layers consist of 1D-chains with periods function of  $x$ . It suggests that full ordering should take place for any  $x$  rational value and form an unprecedentedly rich crystal-chemist playground. The variety of ordered phases in competition as single crystals or

polycrystalline samples highlights easy Fe-diffusion mechanisms, especially taking into account the modest exsolution temperatures. Two possible Fe diffusion paths are viewable through i) Ba/PO<sub>4</sub> interleaves or ii) in-plane across shared edges following octahedral chains. Due to the non-destructive Fe diffusion and easy Fe/V<sub>Fe</sub> re-organization at long range (even at the scale of large single-crystal), this second proposition is the most plausible and is currently under study using ab-initio relaxations. Ni<sup>2+</sup> and Co<sup>2+</sup> isomorphs being stable at high-temperature in air, the driving force is the Fe<sup>2+</sup>/Fe<sup>3+</sup> redox. It is reminiscent of the possible extrusion of 1/3<sup>rd</sup> of Fe ions in the olivine LiFePO<sub>4</sub>[17, 18]. In the Mn<sup>2+</sup> doped olivines, the role of the iron oxidation was clearly evidenced by Mn<sup>2+</sup> ions remaining stable after Fe-exsolution[62]. It is clear that the exsolution of mixed Ba(Fe,M)<sub>2</sub>(PO<sub>4</sub>)<sub>2</sub> phases will bring important insights on the control of the conditions and microstructure of the exsolved Fe<sub>2</sub>O<sub>3</sub> particles, these latter being of potential interest for a new generation of renewable photo-catalysts.

The oxidation of mixed metallic Ba(Fe,M)<sup>2+</sup><sub>2</sub>(PO<sub>4</sub>)<sub>2</sub> (M=Co, Ni) phases after heating in air at 600°C for 12 hours leads to Fe-deficient phases with a full oxidation of Fe<sup>2+</sup> to Fe<sup>3+</sup> ones and preserving divalent M cations. The exsolved iron ions form nanoclusters at the surface of the parent phase, with a strong dependence of the cluster size on the Fe/M ratio. In the oxidation of the parent BaFe<sup>2+</sup><sub>2</sub>(PO<sub>4</sub>)<sub>2</sub> phase, the reorganization of Fe ions and V<sub>Fe</sub> vacancies after exsolution inside the 2D-layers leads to variety of supercell orderings with period related to the Fe-depletion rate. In the mixed metal systems, although M<sup>2+</sup> ions hamper the Fe-diffusion, the distribution of Fe<sup>3+</sup> and M<sup>2+</sup> centres is almost fully ordered which proves that not only Fe ions but also Co<sup>2+</sup>/Ni<sup>2+</sup> ions are mobile in this crystal structure. This easy reorganization proves that the metal diffusion paths are confined within the 2D-layers. It opens broad possibilities to achieve new metal-depleted layered topologies, by tuning the initial Fe/M ratio and also the oxidation conditions for partial iron oxidation. Taking into account our experimental observation for the possible (but low) exsolution of cobalt in cobalt-rich phases, attempts for a significant exsolution of cobalt in the BaCo<sub>2</sub>(PO<sub>4</sub>)<sub>2</sub> and BaNi<sub>2</sub>(PO<sub>4</sub>)<sub>2</sub> under strongly oxidizing conditions, such as high pressure oxygen, are currently under investigation.

## 8. Li insertion in iron deficient phases.

My PhD work dealing with topochemical routes, we have obviously being very attracted in the possibility for alkali insertion in the depleted  $\text{BaFe}_{2-x}(\text{PO}_4)_2$  series. Thus, the last part of this chapter has been dedicated to do a brief evaluation of their potentialities in the domain of energetic storage starting from the most iron exsolved compound presented before :  $\text{BaFe}_{1.33}(\text{PO}_4)_2$ . Experimentally, experiments have been realized using either chemical insertion of  $\text{Li}^+$ , either electrochemical incorporation using  $\text{BaFe}_{1.33}(\text{PO}_4)_2$  as a positive electrode (cathode) in Li batteries.

For this purpose, after checking the feasibility of the  $\text{Li}^+$  incorporation in the Fe-depleted network we have performed some electrochemical experiences at the LRCS laboratory in Amiens, France. Chronopotentiometry at imposed current of the phase (cathode) vs.  $\text{Li}^0$  (anode) was also performed in order to check the reversibility of the electrochemical reaction.

This part of my work should only be considered as an initial “brief evaluation” of potentialities and no further optimization of our compounds, i.e. composition, microstructure, carbon mixing or electrochemical parameters have been achieved for reason of time. Nevertheless, these first experiences have allowed verifying the alkali mobility in the layered framework as well as its stability in the experimental conditions.

I will start this section by a brief description of Li-ion batteries and then with the protocol set for the sample preparation for electrochemical tests. After that, I will describe our chemical and electrochemical results.

### 8.1. Li batteries.

Li battery correspond to several elementary electrochemical cells connected in serie and in parallel in such a way that once electrodes are switched reactions are produced in all of the electrochemical cells, generating an electric current that can be exploited. Every cell is composed of a cathode, an anode and an electrolyte. Figure II.47 shows a schematic description of the swagelock<sup>®</sup>-type cell used during all our experiences.

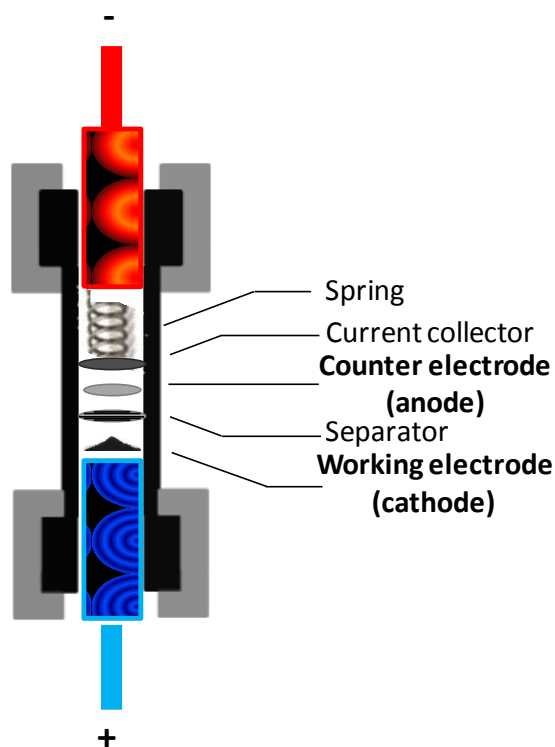


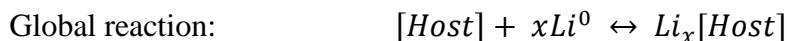
*Figure II.47. Schematic description of a Swagelok<sup>®</sup> cell.*

Historically, the anode is the electrode where the ( $\text{Li}^0 \rightarrow \text{Li}^+ + 1e^-$ ) electrochemical oxidation is produced during the battery discharge. It produces one electron which goes to the external circuit. The cyclability of this kind of anode is bad due to the formation of Li dendrites and battery short breaks. For this reason at a commercial level it is the Li-ion battery which was relevant. Here the anode is in general made of graphite with intercalated  $\text{Li}^+$ , avoiding the presence of  $\text{Li}^0$  during the charge/discharge process. However, we used  $\text{Li}^0$  anode for a easier setup.

On the other hand, the cathode is reduced during discharge cycle; accepted electrons came from the anode through the external circuit. In cathode reaction,  $\text{Li}^+$  cation created in anode, will be inserted as guests in the host network which compose the positive cathode.

The third part of the electrochemical cell is the electrolyte. Optimal electrolyte consists in a good ionic conductor which allows a charge transfer and chemical stability across the internal circuit in order to have an easy displacement of the  $\text{Li}^+$  cations from the anode to the cathode and vice versa (during the charge cycle). The electrolyte we used was a guaranteed high purity (from certificate analysis:  $\text{H}_2\text{O} < 10 \text{ ppm}$  ; acides libres  $< 35 \text{ ppm}$ ) and commercial (Merck, LP30) made by a mixture of ethylene carbonate and dymethyl carbonate 50/50 weight proportion, soaked in a solution of high purity  $\text{LiPF}_6$   $1 \text{ mol/l}^{-1}$ .

The total reactions might be described as:



A discharge cycle consists in the insertion of  $Li^+$  cations coming from oxidation of the anode ( $Li^0$  during the experiences), in the cathode matrix. On the contrary, during the charge cycle these cations go out from the cathode network to come back to the anode and be reduced to  $Li^0$  metal.

There are some characteristics that any compound able to insert  $Li^+$  in its framework must fulfill in order to be a good cathode:

- High density charge, which is obtained by insertion/deintercalation of high amounts of Li in the structure in order to improve the cell capacity.
- The insertion /deintercalation process must be reversible and should not affect solid structure which must stay invariable.
- The cathode compound may be a good electronic and ionic conductor and it must be stable in all the work voltage range.

### 8.1.1. Sample preparation

Electrochemical experiences were carried out for several compositions presented in the previous section. Here we will focus on  $BaFe_{1.33}(PO_4)_2$  where in addition to the electrochemical experiences, chemical Li incorporation was achieved and characterized by solid state NMR spectroscopy and ICP analysis.

Different samples were mechanically grinded with a 16.7% weight of active black carbon for twenty minutes. Active carbon improves the electronic conductivity whereas the grinding process homogenizes crystal size and improves the contact between the particles.

All the electrochemical measures have been performed in a two electrodes laboratory cell, in a Swagelok<sup>®</sup> type. All the cells were assembled in a glove box under an Argon purified atmosphere.

### 8.1.2. Electrochemical measurements.

The tests realized at the laboratory consisted in chronopotentiometry in a galvanostatic mode through an imposed current where the voltage is recorded as a function of time. In some cases, experiences were performed using galvanostatic intermittent titration technique (GITT). This technique establishes open current periods during the measure. It is generally used to measure diffusivity coefficient by measure of the ionic current under applied voltage. In our case, current interruptions it helps to compensate polarization effects due to the poor ionic conductivity of the sample and allows improving insertion/desintercalation efficiency.

In general, for this kind of experiences the nomenclature used to describe the different charge/discharge regimes it is of the type C/n, being C the capacity of the compound and “n” the hours to do a complete charge or discharge cycle. In our case we do not know accurately how many Li<sup>+</sup> could be inserted in the phase, so what we called a “complete” charge (x=0) or discharge cycle (x=1), the insertion/deintercalation of one atom of Li per formula. So, knowing the amount of active material used to prepare the battery we can establish the intensity current imposed to complete one charge or discharge cycle in “n” hours

## 8.2. Li chemical incorporation.

### 8.2.1. Experimental procedure.

Several insertion process have been tried inspired by the bibliography in that field (LiBH<sub>4</sub> in THF<sub>[68]</sub>, molten salts...[69, 70]). However, all those techniques lead to unsuccessful results where the initial BaFe<sub>1.33</sub>(PO<sub>4</sub>)<sub>2</sub> was not modified after XRD examination or sometimes destroyed at the end of the process. The insertion process was only achieved after mixing BaFe<sub>1.33</sub>(PO<sub>4</sub>)<sub>2</sub> with Li<sub>2</sub>CO<sub>3</sub> (Aldrich, 99.00%) heated at 600°C for 24h under H<sub>2</sub>(3%)/Ar atmosphere. 0.25 gr of BaFe<sub>1.33</sub>(PO<sub>4</sub>)<sub>2</sub> were mixed and grinded with twice stoichiometric quantity of Lithium carbonate. Initial powder changed from red dark to black, indicating the change in iron oxide state. From this polycrystalline sample (sample 1) we were able to find a crystal big enough to be collected, crystal 1. In parallel, some BaFe<sub>1.33</sub>(PO<sub>4</sub>)<sub>2</sub> crystals were immerse in alumina crucible with a large excess of lithium carbonate and followed the same thermal treatment leading to a black single crystals platelets. From this sample was collected the crystal 2.

After the thermal treatment, the samples were carefully washed several times in hot water and ethanol to eliminate possible remains of reactants at the surface.

The figure II.48 summarizes the different chemical insertion tests.

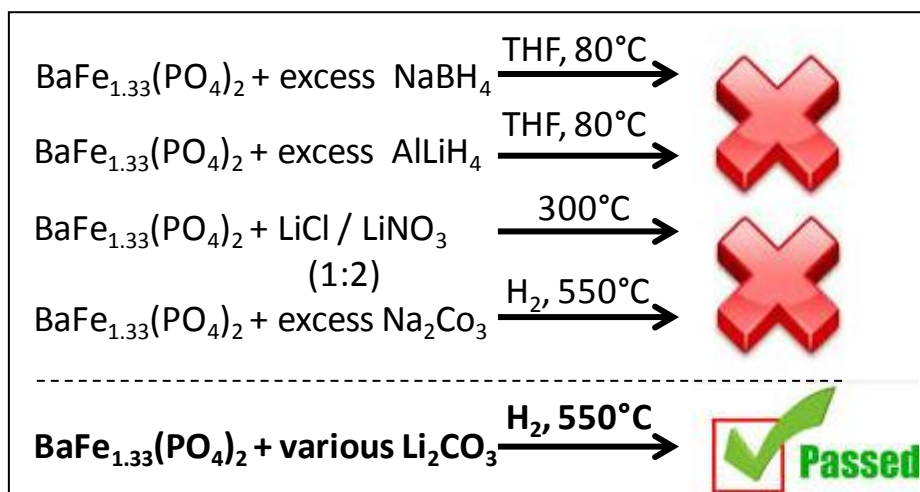


**Figure II.48.** Summary of tested reactions for metal alkaline insertion in  $\text{BaFe}_{1.33}(\text{PO}_4)_2$

### 8.2.2. Characterization of the mixed $\text{Ba}(\text{Fe,Li})_x(\text{PO}_4)_2$ .

Powder and single crystal X-ray diffractions were carried out at the same conditions and with the same instruments described previously.

Solid state  $^7\text{Li}$  nuclear magnetic resonance (NMR) spectra were performed on a 4.7 T Bruker BioSpin spectrometer equipped with an AVANCE-III console and a 1.3 mm double resonance probe spinning at 62.5 kHz. At such magnetic field,  $^7\text{Li}$  Larmor frequency is 77.7 MHz. Chemical shifts were referenced to 1 M  $\text{LiCl}_{(\text{aq})}$ . Hahn echo experiments with one rotor period were recorded. Experiments were conducted in Orléans (France) with Dr. Elodie Salager.

Inductively coupled plasma atomic emission spectroscopy (ICP-AES) was performed in a Varian Vista Pro with a charged coupled device (CCD) detector, covering a spectral range from 167 to 765 nm. A known amount of sample was dissolved in concentrated  $\text{HNO}_3$  to realize the experience. For the reference we used  $\text{LiFe}(\text{PO}_4)$  dissolved in the same conditions.

## 8.3. Lithiated phase characterization.

### 8.3.1. Inductively coupled plasma atomic emission spectroscopy (ICP-AES).

To realize the ICP-AES a known amount of sample 1 was dissolved in a volume of concentrated  $\text{HNO}_3$ . We have carefully washed by sonication the sample to remove the maximal possible second Li-based phase (unreacted). The same treatment was made with

LiFePO<sub>4</sub> which will serve as reference. The results obtained after the measures are presented in table II.9.

**Table II.9.** Atomic proportion from ICP-AES results.

Sample	g / Kg of sample				Exp. Formula
	Ba <sub>exp</sub> /Ba <sub>calc</sub> Corr. Coeff.	Fe <sub>exp</sub> /Fe <sub>calc</sub> Corr. Coeff.	Li <sub>exp</sub> /Li <sub>calc</sub> Corr. Coeff.	P <sub>exp</sub> /P <sub>calc</sub> Corr. Coeff.	
LiFePO <sub>4</sub>	-	365/354 1.03	48/44 1.1	187/196 0.95	Li <sub>1.15</sub> Fe <sub>1.08</sub> PO <sub>4</sub>
Sample 1	243	225	12	126	Ba <sub>0.83</sub> Fe <sub>1.82</sub> Li <sub>0.67</sub> (PO <sub>4</sub> ) <sub>2</sub>

After applying the correction factor found using LiFePO<sub>4</sub> as reference and considering two groups phosphates per formula; the stoichiometry of sample 1 is Ba<sub>0.83</sub>Fe<sub>1.82</sub>Li<sub>0.67</sub>(PO<sub>4</sub>)<sub>2</sub>. This result is relevant although, we cannot decide the incorporation of all the revealed lithium despite washing. Tightly hold Li<sup>+</sup> at surface remains an important source. The iron amount is slight higher than expected, but as DRX pattern of figure X. shows, Fe<sub>2</sub>O<sub>3</sub> also remains at the surface of the grains.

In order to verify the real insertion of the lithium we also performed some solid state NMR experiments.

### 8.3.2. Solid state <sup>7</sup>Li NMR.

Solid-state NMR is a powerful characterization technique that can probe the local environment of the lithium. This method is frequently used to study battery materials.[71] It should be noted that <sup>7</sup>Li NMR spectrum of a diamagnetic compound exhibits usually a sharp signal located around 0 ppm. However, when a paramagnetic specie is introduced into the material, a large shift is observed ascribed to a hyperfine interaction (Fermi-contact shift). In that case, a line-broadening is also noticed attributed to the dipolar coupling between the unpaired electron and the lithium.

<sup>7</sup>Li NMR spectrum of the BaFe<sub>1.33</sub>Li<sub>x</sub>(PO<sub>4</sub>)<sub>2</sub> recorded with a spinning frequency of 62.5 kHz is presented in figure II.49. A very broad lineshape is observed. Another spinning frequency spectrum was recorded (55 kHz, not shown), which allows distinguishing isotropic resonances located from 100 to -300 ppm. A large manifold of spinning sidebands accompanies the isotropic resonances. This line broadening results from the paramagnetic

coupling between the unpaired electron (from the iron) and the nucleus under observation ( $^7\text{Li}$ ).  $^6\text{Li}$  NMR spectra of these materials would allow an easier identification of the isotropic resonance since this isotope is less affected by the paramagnetism coming from the material. Unfortunately, the  $^6\text{Li}$  natural abundance is quite low (7.6%) and  $^6\text{Li}$  NMR experiments require numerous scans. We haven't had enough magnet time to record such experiments.

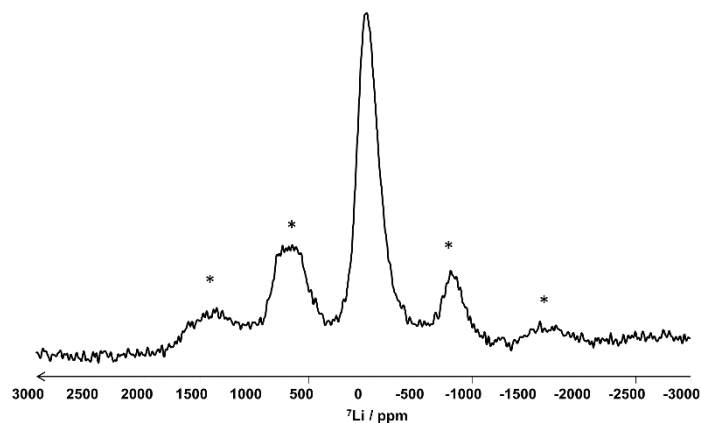


**Figure II.49.**  $^7\text{Li}$  NMR spectrum of  $\text{BaFe}_{1.33}\text{Li}_x(\text{PO}_4)_2$  recorded at  $B_0=4.7$  T with a spinning speed of 62.5 kHz. Peaks with an asterisk correspond to the spinning side bands.

Even if the signal shows a very broad lineshape (from 100 up to -300 ppm) multiple components can be distinguished. A tentative decomposition of this signal with DMfit software[72] is shown in figure II.50 (only the isotropic resonances are presented).

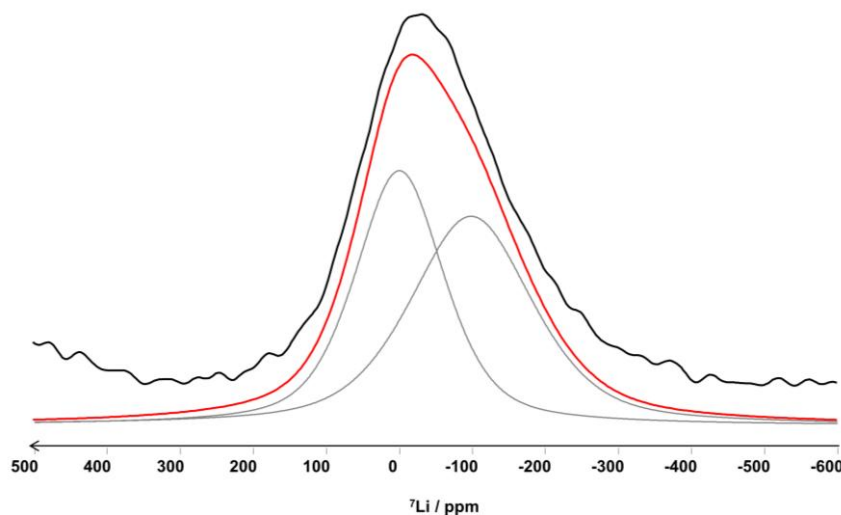


**Figure II.50.** Decomposition of the  $^7\text{Li}$  NMR spectrum of  $\text{BaFe}_{1.33}\text{Li}_x(\text{PO}_4)_2$ . (Only the isotropic resonances are shown). In black the experimental spectrum is shown, the grey and red spectra are the simulated ones.

The deconvolution reveals signals resonating at *ca.* 0 and -100 ppm. This decomposition serves only as an eye-guide to the reader since it is really difficult to simulate such broad signal with overlapping peaks. However, the simulation tends to prove the presence of at least two lithium sites. As stated above, the 0 ppm signal can be ascribed to the presence of diamagnetic species in the materials, and consequently to remaining  $\text{Li}_2\text{CO}_3$ . However, this signal exhibits a surprisingly very broad line-shape for a diamagnetic compound, which tends to prove an overlapping of two lithium sites (see below). The large shift observed for the other signal at -100 ppm is characteristic of a lithium site inside a paramagnetic material.[71] The line-broadening also proves the presence in close proximity of an unpaired electron. Unfortunately, the two signals may have opposite NMR properties in terms of  $T_1$  and  $T_2$  and consequently, it seems difficult to have quantitative results. In order to confirm our assignment for the 0 ppm signal, we mixed the previous materials  $\text{BaFe}_{1.33}\text{Li}_x(\text{PO}_4)_2$  with 50%w of  $\text{Li}_2\text{CO}_3$  and recorded the NMR spectrum within exactly the same condition (figure II.51).

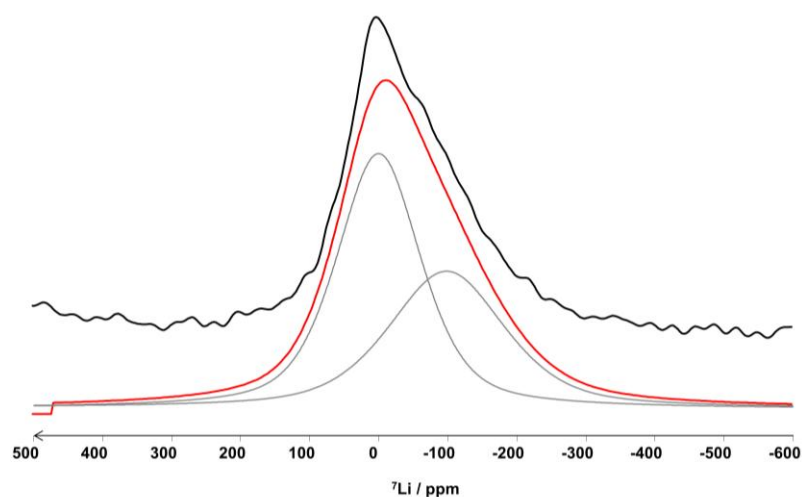


**Figure II.51.** Decomposition of the  $^7\text{Li}$  NMR spectrum of  $\text{BaFe}_{1.33}\text{Li}_x(\text{PO}_4)_2 + \text{Li}_2\text{CO}_3$ . (Only the isotropic resonances are shown). In black the experimental spectrum is represented, the grey and red spectra are the simulated ones.

In that case, the deconvolution reveals that the 0 ppm signal intensity only slightly increases. This result tends to prove that more  $\text{Li}_2\text{CO}_3$  is inserted in the structure (-100 ppm) but there is also some  $\text{Li}_2\text{CO}_3$  at the surface of the particle (0 ppm). The presence of high paramagnetism in the materials implies a large broadening of the signal.

Figures II.50 - II.51 allow a safe conclusion regarding the lithium insertion. Multiple lithium sites are presents in the material. We proved that some lithium is inserted into the

$\text{BaFe}_{1.33}\text{Li}_x(\text{PO}_4)_2$  structure (signal at -100 ppm). The second lithium site is less shifted (0 ppm) but with also a large line-broadening, and may be attributed to a superposition of some  $\text{Li}_2\text{CO}_3$  at the surface of the particles, and another lithium site inserted into the structure.

### 8.3.3. Structure of the lithiated phase.

#### 8.3.3.1. Polycrystalline sample.

Polycrystalline powder and single crystal of the iron phosphate sample have been studied by x-ray diffraction and both of them lead to similar conclusions.

Figure II.52 shows a comparison between the pattern of the  $\text{BaFe}_{1.33}(\text{PO}_4)_2$  phase versus the lithiated phase after the reaction under  $\text{H}_2$  with  $\text{Li}_2\text{CO}_3$ . On the contrary to the triclinic  $\text{BaFe}_{1.33}(\text{PO}_4)_2$  all the intensities record the lithiated pattern can be indexed to a rhombohedral unit cell, but with different parameters that those of  $\text{BaFe}_2(\text{PO}_4)_2$ . However it is possible in reducing conditions that certain amounts of the  $\text{Fe}_2\text{O}_3$  second phase is reincorporated together with  $\text{Li}^+$ . Unit cell refinement of the polycrystalline lithiated phase leads to  $a = 4.814(9) \text{ \AA}$  and  $c = 24.343(4) \text{ \AA}$ . These values are intermediate between the  $\text{BaFe}_2(\text{PO}_4)_2$  and  $\text{BaFe}_{1.33}(\text{PO}_4)_2$  as expected. Single crystal diffraction will help us to go deeper in this parameters evolution.

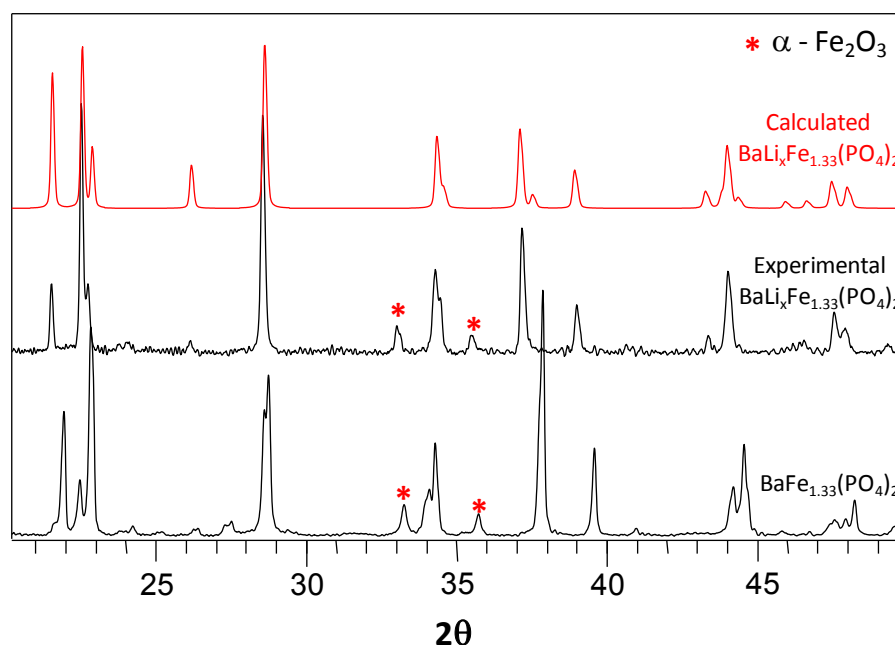


**Figure II.52.** XRD patterns comparison between experimental  $\text{BaFe}_{1.33}(\text{PO}_4)_2$  before and after lithiation treatment and the corresponding calculated pattern from the structure resolution by single crystal XRD.

Some Fe<sub>2</sub>O<sub>3</sub> peaks being present in the XRD pattern of the lithiated phase suggest that in the thermal treatment under H<sub>2</sub> with Li<sub>2</sub>CO<sub>3</sub> is subject to preference for Li insertion compared to the full iron reincorporation. The red XRD pattern corresponds to the theoretical diagram deriving from the single crystal data of crystal 1 (see the 6.3.3.2 section) discussed below. It shows a good accord with the experimental one with just little unit cell parameters differences as shown in table II.10.

### 8.3.3.2. Single Crystal structure.

Two different single crystals were collected. The first one (crystal 1) came from BaFe<sub>1.33</sub>P<sub>2</sub>O<sub>8</sub> reacted with lithium carbonate in excess and leads to a final formula of BaFe<sub>1.62</sub>Li<sub>0.323</sub>(PO<sub>4</sub>)<sub>2</sub>, whereas the second one (crystal 2) was found in the polycrystalline sample reacted with Li<sub>2</sub>CO<sub>3</sub> in stoichiometry according to the reaction:



However, the final product leads to a final formula of BaFe<sub>1.33</sub>Li<sub>0.425</sub>(PO<sub>4</sub>)<sub>2</sub>.

Both of crystals were indexed in the rhomboedral unit cell with parameters slightly changed. As discussed in section 3.4, the Fe occupancy is reliable. The lattice parameters are compared to BaFe<sub>2</sub>(PO<sub>4</sub>)<sub>2</sub> and BaFe<sub>2-x</sub>(PO<sub>4</sub>)<sub>2</sub> phases R-3 subcells. Table II.10 shows these values. Unit cell parameters comparison between the two lithiated crystals and the rhombohedral subcell approaches of the BaFe<sub>2-x</sub>(PO<sub>4</sub>)<sub>2</sub> phases shows clear differences. Both of crystals present values of *a* smaller than expected for iron occupancies refinement and *c* values are not far from the BaFe<sub>2</sub>(PO<sub>4</sub>)<sub>2</sub>

**Table II.10.** Unit cell parameters comparison between the two different lithiated crystals, the reduced BaFe<sub>2</sub>(PO<sub>4</sub>)<sub>2</sub> and the oxidized BaFe<sub>1.33</sub>(PO<sub>4</sub>)<sub>2</sub>.

Parameters (Å)	a	c
BaFe <sup>2+</sup> <sub>2</sub> (PO <sub>4</sub> ) <sub>2</sub>	4.8730(2)	23.368(2)
BaFe <sup>2.34+</sup> <sub>1.71</sub> (PO <sub>4</sub> ) <sub>2</sub>	4.8278(1)	24.084(1)
BaFe <sup>2.4+</sup> <sub>1.67</sub> (PO <sub>4</sub> ) <sub>2</sub>	4.8097(4)	24.079(2)
BaFe <sup>3+</sup> <sub>1.33</sub> (PO <sub>4</sub> ) <sub>2</sub>	4.760(4)	23.793(6)
BaFe <sup>2.27+</sup> <sub>1.62</sub> Li <sub>0.323</sub> (PO <sub>4</sub> ) <sub>2</sub>	4.8444(2)	23.350(1)
BaFe <sup>2.69+</sup> <sub>1.33</sub> Li <sub>0.425</sub> (PO <sub>4</sub> ) <sub>2</sub>	4.8114(4)	23.316(1)

In both of cases the two crystals are twinned by the obverse-reverse rhombohedral twinning as we can see in the precession images showed in figure II.53.

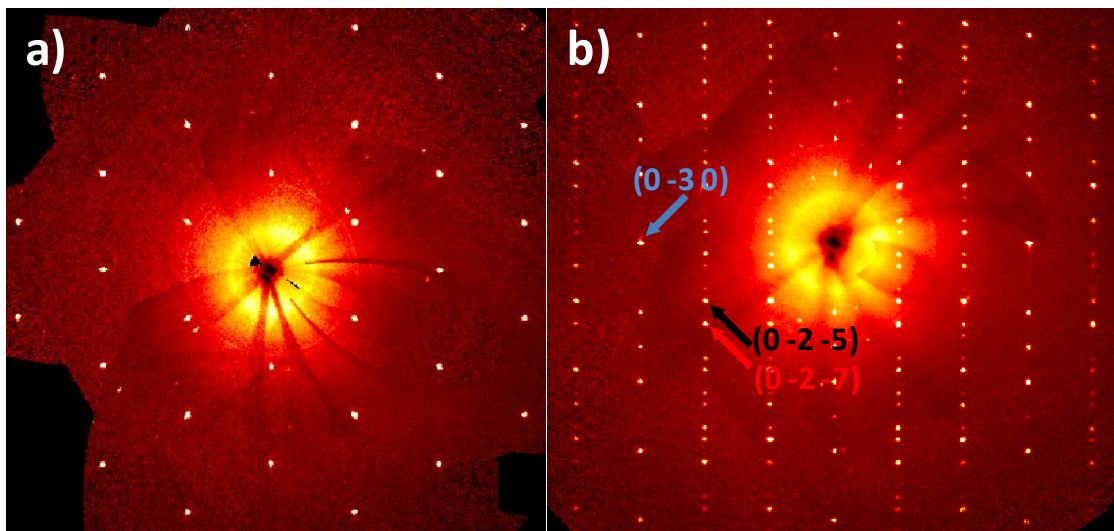


**Figure II.53.** Crystal 2 precession images in the rhombohedral unit cell of the  $[hk0]$  (a) and  $[0kl]$  (b) layers. Red/black arrows in (b) show characteristic reflexions for obverse/reverse unit cell respectively whereas blue arrow points to a common o/r reflexion.

- Crystal 2:  $BaFe_{1.62}Li_{0.323}(PO_4)_2$ :

All reflected intensities match the rhombohedral unit cell, and there are no evidences for additional supercell reflections. The R-3 refinement leads to  $R_{obs} = 1.44\%$  and  $R_{all} = 1.58\%$ ,  $a = 4.8444(2) \text{ \AA}$ ,  $c = 23.350(1) \text{ \AA}$ . The twin ratio was refined 0.231(0) for this phase. We refined the occupancy of a mixed Fe/Li octahedral site. Clearly, as expected, the Li atom doesn't improve the refinement quality and the real Li insertion remains puzzling. However the lattice parameters are different from those of the  $BaFe_{1.67}(PO_4)_2$  subcell, and the BVS calculated for Fe (using  $Fe^{2+}$  data) suggest a mixed  $Fe^{2/3+}$  valence, in good agreement with the  $BaFe_{1.62}^{2.27+}Li_{0.32}(PO_4)_2$ .

- Crystal 1:  $BaFe_{1.33}Li_{0.425}(PO_4)_2$ :

In this case, all the reflexions were indexed in a rhombohedral unit cell R-3 with parameters  $a = 4.8114(4) \text{ \AA}$ ,  $c = 23.316(1) \text{ \AA}$ . The final refinement, leads to a  $R_{obs} = 1.62\%$  and  $R_{all} = 1.74\%$  to the formula mentioned above of  $BaFe_{1.33}Li_{0.425}(PO_4)_2$  and a twin proportion refined to 0.448(9). For this refinement we started, as in the case before, refining the occupancy of the iron site. The refinement led directly to the occupancy 0.6600(2), i.e.  $BaFe_{1.33}(PO_4)_2$  in the final formula. Once more lattice parameters are very different from those of  $BaFe_{1.33}(PO_4)_2$ , see Table II.10. Here, the Fourier difference maps show residual electron density intensity of  $0.28 \text{ e}^-/\text{A}^3$  placed just above the iron position. Contrary to the

first crystal described, here, the Li site it is not exactly the same that the iron one but slightly above, over the empty octahedral created by the iron exsolution as is shown in figure II.54. The refinement of this position gives the final formula  $\text{BaFe}^{2.69+}_{1.33}\text{Li}_{0.425}(\text{PO}_4)_2$ , however in both cases the announced stoichiometry should not be too literally, dealing with light Li scatterer.

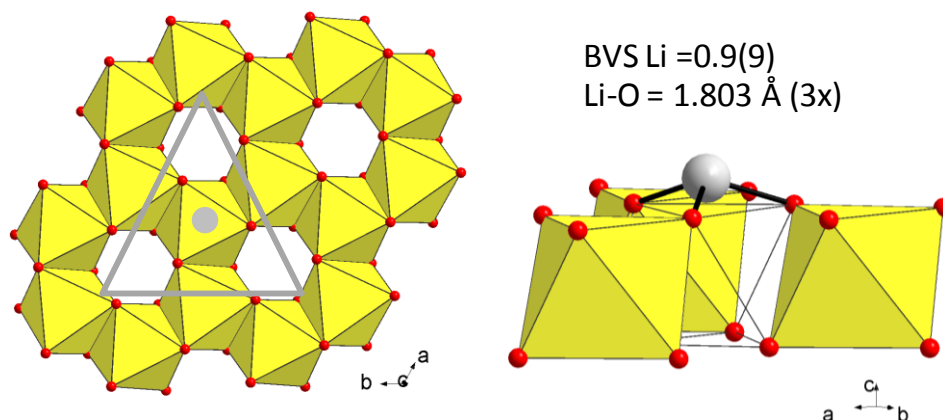


*Figure II.54. Crystallographic site position of Li atom in the structure.*

Atomic coordinates with corresponding atomic displacement, interatomic distances and crystal collection details of both of crystals are presented in annexes.

## 8.4. Electrochemical experiences.

### 8.4.1. $\text{BaFe}_{1.33}(\text{PO}_4)_2$ as cathode in a Li battery.

$\text{BaFe}_{1.33}(\text{PO}_4)_2$  phase was prepared as described here above to be used as a cathode, and different galvanostatic cycles were carried out in a half-cell face to  $\text{Li}^0$  at different conditions.

In a first approach, the battery was prepared to do just one discharge cycle, which means sample reduction by  $\text{Li}^+$  insertion, with a very low current ( $C/200$ ) in order to insert the highest  $\text{Li}^+$  amount in the structure. The experience was realized in a GITT mode.

As shown in figure II.55(a), the battery started with an initial voltage ( $V_0$ ) of 3.17 V. This value matches well with typical  $V_0$  in  $\text{Fe}^{3+}$  compounds. The first discharge cycle (Li insertion) of the prepared sample is completed at the value  $x=0.25$  where  $x$  corresponds to the number of Li inserted per formula leading to  $\text{BaFe}_{1.33}\text{Li}_x(\text{PO}_4)_2$ . The chronopotentiometry shows no plateau at any temperature, this behavior could be indicative of the existence of

solid solutions instead of two different phases during the lithiation process. GITT allows underlining a high polarization effect.

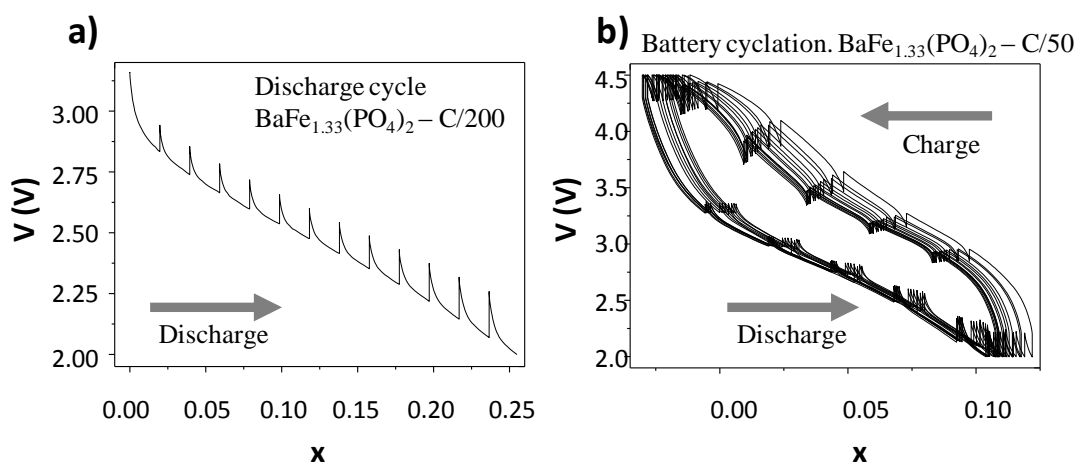


**Figure II.55.** First discharge cycle (Li+insertion) of  $\text{BaFe}_{1.33}(\text{PO}_4)_2$  at C/200 (a), and cyclability test of  $\text{BaFe}_{1.33}(\text{PO}_4)_2$  as cathode versus  $\text{Li}^0$  anode at C/50 (b).

In a second experience we repeated the sample preparation, but in this case we applied a current a bit higher, corresponding to a C/50 and we let the battery working for several charge/discharge cycles with the aim to verify the reversibility of the electrochemical Li insertion. Figure II.55(b) shows the experience result. The first remarkable fact is the important role played by the imposed current; increasing the current leads to a lower Li insertion going from the 0.25 achieved in the first discharge cycle mentioned above (fig. II.55a) to 0.15 in this second case. Nevertheless, this second experience shows a good reversibility even if the amount of Li exchanged is lower. We can observe, however, a slight shift through values  $x < 0$  which would mean that we extract more Li than we have inserted. This shift is more evident during the first cycles and could be related with a partial decomposition at the beginning.

The comparison between the cathode residue before and after battery cyclation at C/50 is presented in figure II.56. We can see clearly that the phase remains in the pattern after cyclation. However, both patterns are not exactly the same. The residue pattern shows weak reflections displacements related with changes in the unit cell parameters; and changes in the intensities of some reflections which could be associated to different atomic compositions. It is also remarkable a small increase in the amount of  $\text{Fe}_2\text{O}_3$ , probably due to a small phase decomposition.

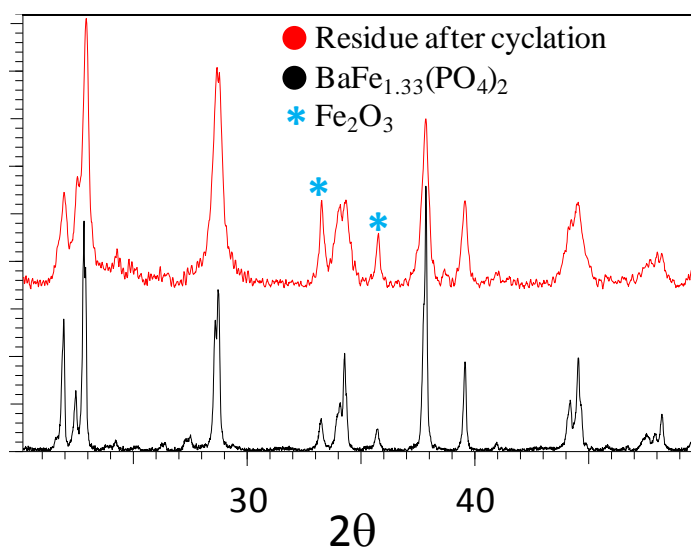


**Figure II.56.** XRD pattern comparison between the sample before and after cyclation process.

Finally, some chronopotentiometric tests were realized in the exsolved solid solutions  $\text{BaFe}^{3+}\text{M}^{2+}_{0.5}(\text{PO}_4)_2$  ( $\text{M} = \text{Co}, \text{Ni}$ ), but no good results were obtained. The charge/discharge cycles were very short and there is no reversibility of the cycles. The small amount of sample used was not enough to allow an XRD phase preparation, but the non reversibility could be indicative of phase decomposition. This result is not completely unexpected since the diffusion hampering by nickel or cobalt in this compound was proposed (Chapter II, 4.3).

#### 8.4.2. Electrochemical oxidation of $\text{BaFe}_{1.33}(\text{PO}_4)_2$ .

In another kind of experience,  $\text{BaFe}_{1.33}(\text{PO}_4)_2$  sample was directly connected in a charge cycle, which means a cathode oxidation. The 3+ oxidation state of iron in  $\text{BaFe}_{1.33}(\text{PO}_4)_2$  allows to imagine a possible  $\text{Fe}^{3+} \rightarrow \text{Fe}^{4+} + \text{e}^-$  oxidation reaction.

For this, another cell was mounted and in this case, a negative current of -0.014 mA was applied. With respect to the sample active weight used to prepare the cathode, this current suppose a rate of C/50, and the program was established to do just one cycle from the initial voltage work (3.20 V) till 4.5V. Figure II.57 shows the cell voltage as a function of x, being x the number of Li inserted/desintercalated per u.f.

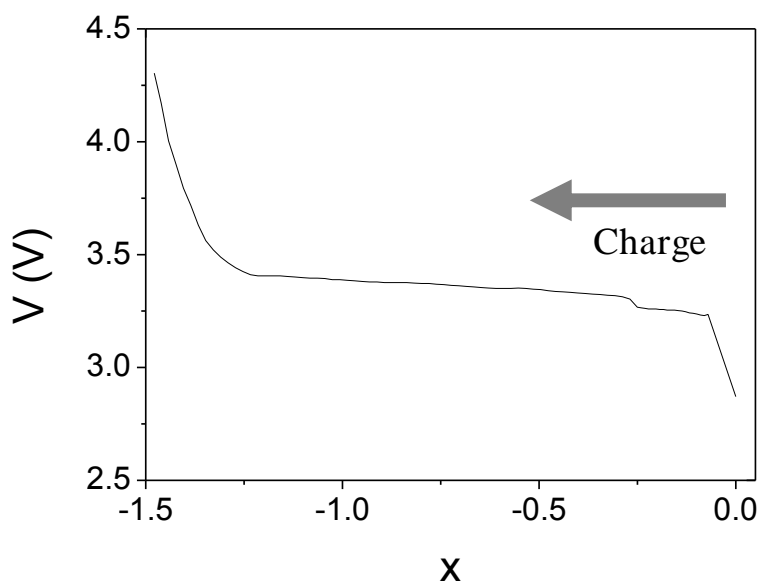
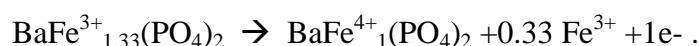


**Figure II.57.** Graphic representation of the voltage as a function of time for one charge cycle using  $BaFe_{1.33}(PO_4)_2$  as a cathode.

In this case, the existence of a plateau at a potential of around 3.4 V vs. Li is observed. It is remarkable that a virtual value of  $x = -1.25$  is reached. This value is very close to the full amount of iron susceptible to be oxidized from +3 to +4, which is of i.e. 1.33. However, this oxidation should not be compatible with Fe exsolution since  $x = -1.25$  (i.e. exchange of 1.25 electron /f.u.) is greater than maximal expected reaction:



Nevertheless, the phase being 2D, the full oxidation of the iron could be driven by an outflow of  $Ba^{2+}$  which could suggest a partial destruction of the phase. At this point, we are not capable of establishing a well reasoned mechanism of what is happening in the material, and more experiences will be required in order to conclude.

#### 8.4.3. $BaFe_{1.33}Li_{0.425}(PO_4)_2$ as cathode in a Li battery.

The last presented electrochemical experience consisted of a chronopotentiometry test on the  $BaFe_{1.33}Li_{0.425}(PO_4)_2$  sample lithiated by chemical route and described above in 8.3.

The battery preparation was made exactly in the same way that in the previous cases. However in this case the battery started in a charge cycle in order to know if we could extract the Li of the compound in a reversible way. To start the charge cycle the applied current is 0.038 mA. Figure II.58 presents the result of the first four charge cycles. The battery starts

with a  $V_0 = 3.10$  V. Unfortunately, the work potential go up very quickly, arriving to the limit of the 4.5 V just after 0.15 Li desintercalated.

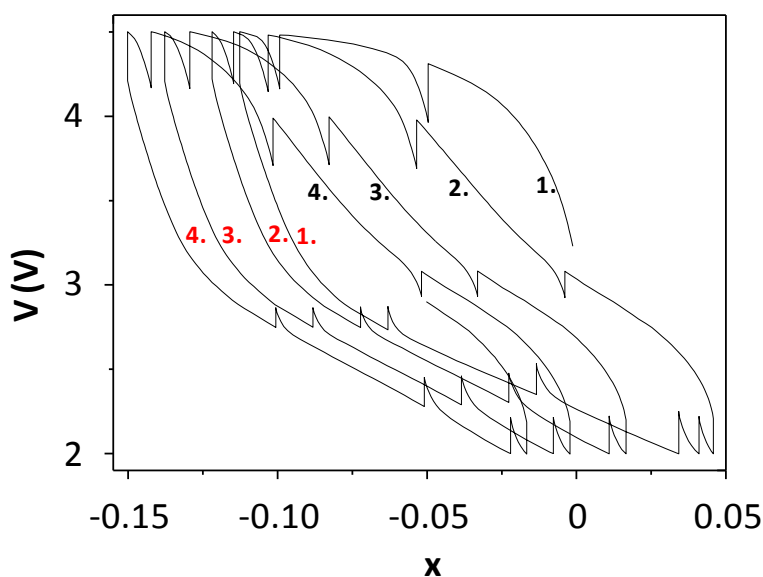


**Figure II.58.** First cycles of the  $\text{BaFe}_{1.33}\text{Li}_{0.425}(\text{PO}_4)_2$  chronopotentiometry, numbers indicate the cycle, being black for the charge and red for discharge.

During the first discharge cycle, we observe a curve shape similar to those observed for the  $\text{BaFe}_{1.33}(\text{PO}_4)_2$ . That means no plateau and high polarization. In this first discharge cycle the cathode reaches the value  $x = +0.05$ , which gives a charge/discharge amplitude of  $\sim 0.2 \text{ Li}^+$ . It is similar to ratio found in the depleted phase  $\text{BaFe}_{1.33}\text{P}_2\text{O}_8$ , i.e.  $\sim 0.15 \text{ Li}^+$ , see 8.4.1.

## 8.5. Conclusion.

Initial experiments have been performed in the different phases studied previously in this chapter. We have initiated work about the cationic mobility by electrochemical methods. The main problem with this studies is that conclusions obtained are not enough clear, and there are still several points that must be clarified.

Despite everything, there are still some interesting points to remark. Even if the efficiency of the insertion and the batteries parameters are far away from the current phases used as cathode materials, we could verify the possibility of reversible reactions by electrochemical pathways, showing a similar behavior to the one found by the classic chemical reactions (exolution reversibility).

One of the main problems with the iron phase it is the difficulty to remove all the  $\text{Fe}_2\text{O}_3$  at the surface of the exsolved compound. This oxide hampers the Li movement, so that it avoids the exchange of a higher Li amount, as expected from a chemical point of view of the compound studied. So, a new line of research could consist in studying possible electrolytes where this iron oxide could be solubilize. In that case, we can forget the Li to concentrate in the iron which will become the atom who will go in and out from the host with the corresponding work potential.

## Bibliography

- [1] H. Kabbour, R. David, A. Pautrat, H.J. Koo, M.H. Whangbo, G. Andre, O. Mentre, *Angewandte Chemie-International Edition* **51** (2012) (47) 11745.
- [2] R. David, A. Pautrat, D. Filimonov, H. Kabbour, H. Vezin, M.H. Whangbo, O. Mentre, *Journal of the American Chemical Society* **135** (2013) (35) 13023.
- [3] R. David, H. Kabbour, D. Filimonov, M. Huve, A. Pautrat, O. Mentre, *Angewandte Chemie-International Edition* **53** (2014) (49) 13365.
- [4] I. Blazquez Alcover, R. David, S. Daviero-Minaud, D. Filimonob, M. Huvé, P. Roussel, H. Kabbour, O. Mentré, *Crystal Growth & Design* **15** (2015) 4237–4247.
- [5] I. Blazquez Alcover, S. Daviero-Minaud, D. Régnal, D. Filimonov, M. Huvé, J.P. Atfield, H. Kabbour, O. Mentré, *Inorganic Chemistry* **54** (2015) 8733–8743.
- [6] M. Leblanc, V. Maisonneuve, A. Tressaud, *Chemical Reviews* **115** (2015) (2) 1191.
- [7] J. Koehler, *Angewandte Chemie-International Edition* **47** (2008) (24) 4470.
- [8] Y. Kobayashi, O.J. Hernandez, T. Sakaguchi, T. Yajima, T. Roisnel, Y. Tsujimoto, M. Morita, Y. Noda, Y. Mogami, A. Kitada, M. Ohkura, S. Hosokawa, Z.F. Li, K. Hayashi, Y. Kusano, J.E. Kim, N. Tsuji, A. Fujiwara, Y. Matsushita, K. Yoshimura, K. Takegoshi, M. Inoue, M. Takano, H. Kageyama, *Nature Materials* **11** (2012) (6) 507.
- [9] M. Giorgetti, S. Mukerjee, S. Passerini, J. McBreen, W.H. Smyrl, *Journal of the Electrochemical Society* **148** (2001) (7) A768.
- [10] M. Morcrette, P. Rozier, L. Dupont, E. Mugnier, L. Sannier, J. Galy, J.M. Tarascon, *Nature Materials* **2** (2003) (11) 755.
- [11] C.H. Bartholomew, *Catalysis Reviews-Science and Engineering* **24** (1982) (1) 67.
- [12] K. Takehira, *Catalysis Surveys from Japan* **6** (2002) (1-2) 19.
- [13] H. Tanaka, *Catalysis Surveys from Asia* **9** (2005) (2) 63.
- [14] J.R. Neilson, T.M. McQueen, *Journal of the American Chemical Society* **134** (2012) (18) 7750.
- [15] J. Bacsá, A.Y. Ganin, Y. Takabayashi, K.E. Christensen, K. Prassides, M.J. Rosseinsky, J.B. Claridge, *Chemical Science* **2** (2011) (6) 1054.
- [16] S. Kondoh, M. Kitamura, N. Morimoto, *American Mineralogist* **70** (1985) (7-8) 737.
- [17] S. Hamelet, P. Gibot, M. Casas-Cabanas, D. Bonnin, C.P. Grey, J. Cabana, J.B. Leriche, J. Rodriguez-Carvajal, M. Courty, S. Levasseur, P. Carlach, M. van Thournout, J.M. Tarascon, C. Masquelier, *Journal of Materials Chemistry* **19** (2009) (23) 3979.
- [18] S. Hamelet, M. Casas-Cabanas, L. Dupont, C. Davoisne, J.M. Tarascon, C. Masquelier, *Chemistry of Materials* **23** (2011) (1) 32.
- [19] P. Fu, Y. Kong, L. Zhang, *Geochimica* (1979) (2) 103.
- [20] M. Kitamura, B. Shen, S. Banno, N. Morimoto, *American Mineralogist* **69** (1984) (1-2) 154.
- [21] B. Shen, O. Tamada, M. Kitamura, N. Morimoto, *American Mineralogist* **71** (1986) (11-12) 1455.
- [22] T. Mikouchi, H. Takeda, M. Miyamoto, K. Ohsumi, G.A. McKay, *American Mineralogist* **80** (1995) (5-6) 585.
- [23] D. Lattard, *American Mineralogist* **80** (1995) (9-10) 968.
- [24] M. Koltypin, D. Aurbach, L. Nazar, B. Ellis, *Electrochemical and Solid State Letters* **10** (2007) (2) A40.
- [25] J.F. Martin, A. Yamada, G. Kobayashi, S.I. Nishimura, R. Kanno, D. Guyomard, N. Dupre, *Electrochemical and Solid State Letters* **11** (2008) (1) A12.
- [26] W. Porcher, P. Moreau, B. Lestriez, S. Jouanneau, D. Guyomard, *Electrochemical and Solid State Letters* **11** (2008) (1) A4.
- [27] Z. Wang, Z. Wang, W. Peng, H. Guo, X. Li, J. Wang, A. Qi, *Ionics* **20** (2014) (11) 1525.
- [28] S.K. Maji, N. Mukherjee, A. Mondal, B. Adhikary, *Polyhedron* **33** (2012) (1) 145.
- [29] J. Chen, L.N. Xu, W.Y. Li, X.L. Gou, *Advanced Materials* **17** (2005) (5) 582.
- [30] M.A. Gondal, A. Hameed, Z.H. Yamani, A. Suwaiyan, *Chemical Physics Letters* **385** (2004) (1-2) 111.

- [31] T. Ohmori, H. Takahashi, H. Mametsuka, E. Suzuki, *Physical Chemistry Chemical Physics* **2** (2000) (15) 3519.
- [32] D.P. Tang, R. Yuan, Y.Q. Chai, *Biotechnology Letters* **28** (2006) (8) 559.
- [33] R. Zboril, M. Mashlan, D. Petridis, *Chemistry of Materials* **14** (2002) (3) 969.
- [34] J. Deng, M. Cai, W. Sun, X. Liao, W. Chu, X.S. Zhao, *Chemsuschem* **6** (2013) (11) 2061.
- [35] R. David, Oxydes et Ferromagnétisme de Basse-Dimensionnalité; Nouvelles Topologies à Propriétés Remarquables, *UCCS* (2014).
- [36] L.P. Regnault, P. Burlet, J. Rossatmignod, *Physica B & C* **86** (1977) (JAN-M) 660.
- [37] N. Rogado, Q. Huang, J.W. Lynn, A.P. Ramirez, D. Huse, R.J. Cava, *Physical Review B* **65** (2002) (14).
- [38] M. Heinrich, H.K. von Nidda, A. Loidl, N. Rogado, R.J. Cava, *Physical Review Letters* **91** (2003) (13).
- [39] J.B. Goodenough, *Magnetism And The Chemical Bond.*, Wiley-Intersciences, New York (1963).
- [40] H. Kabbour, E. Janod, B. Corraze, M. Danot, C. Lee, M.-H. Whangbo, L. Cario, *Journal of the American Chemical Society* **130** (2008) (26) 8261.
- [41] D.D. Dai, M.H. Whangbo, *Inorganic Chemistry* **44** (2005) (12) 4407.
- [42] Y. Zhang, H.J. Xiang, M.H. Whangbo, *Physical Review B* **79** (2009) (5).
- [43] Y. Zhang, E. Kan, H. Xiang, A. Villesuzanne, M.-H. Whangbo, *Inorganic Chemistry* **50** (2011) (5) 1758.
- [44] SAINT+, Bruker Analytical X-ray Systems: Madison, WI, (x2), (2001).
- [45] SADABS, Bruker Analytical X-ray Systems: Madison, WI, (x2), *Bruker/Siemens Area detector absorption and other corrections* (2011).
- [46] L. Palatinus, G. Chapuis, *Journal of Applied Crystallography* **40** (2007) 786.
- [47] M.D. V. Petricek, L. Palatinus, JANA 2000, In: C. Institut of Physics: Praha, Editor (2005).
- [48] P. Stadelmann, JEMS: Java Electron Microscopy Software, Available from: <http://cime.epfl.ch> (1999-2003).
- [49] V.I. Pet'kov, I.A. Shchelokov, M.D. Surazhskaya, K.K. Palkina, A.S. Kanishcheva, A.V. Knyazev, *Russian Journal of Inorganic Chemistry* **55** (2010) (9) 1352.
- [50] F. Bodker, M.F. Hansen, C.B. Koch, K. Lefmann, S. Morup, *Physical Review B* **61** (2000) (10) 6826.
- [51] H.M. Lu, X.K. Meng, *Journal of Physical Chemistry C* **114** (2010) (49) 21291.
- [52] G.M. Sheldrick, CELL NOW, program for unit cell determination, In: G. Göttingen University: Göttingen, Editor, <http://shelx.uni-ac.gwdg.de/SHELX>.
- [53] N.E. Brese, M. Okeeffe, *Acta Crystallographica Section B-Structural Science* **47** (1991) 192.
- [54] J. Darriet, L. Elcoro, A. El Abed, E. Gaudin, J.M. Perez-Mato, *Chemistry of Materials* **14** (2002) (8) 3349.
- [55] J.M. Perez-Mato, M. Zakhour-Nakhl, F. Weill, J. Darriet, *Journal of Materials Chemistry* **9** (1999) (11) 2795.
- [56] S. Eymond, C. Martin, A. Durif, *Materials Research Bulletin* **4** (1969) (8) 595.
- [57] R. David, H. Kabbour, A. Pautrat, O. Mentre, *Inorganic Chemistry* **52** (2013) (15) 8732.
- [58] J. Rodriguez-Carvajal, Fullprof, <http://www.ill.eu/sites/fullprof/> (2001).
- [59] R.D. Shannon, *Acta Crystallographica Section A* **32** (1976) (SEP1) 751.
- [60] I. Blazquez Alcover, R. David, S. Daviero-Minaud, D. Filimonob, M. Huvé, P. Roussel, H. Kabbour, O. Mentre, *Submitted* (2015).
- [61] T. Muraliganth, A. Manthiram, *Journal of Physical Chemistry C* **114** (2010) (36) 15530.
- [62] R. Amissé, S. Hamelet, D. Hanzel, M. Courty, R. Dominko, C. Masquelier, *Journal of the Electrochemical Society* **160** (2013) (9) A1446.
- [63] K.C. Hebbar, S.M. Dharmaprakash, P.M. Rao, *Bulletin of Materials Science* **14** (1991) (5) 1219.
- [64] J.R.-M. L. Regnault, J. Villain, A. De Combarie, SPECIFIC HEAT OF THE QUASI 2D-XY HELIMAGNETS BaCo<sub>2</sub>(AsO<sub>4</sub>)<sub>2</sub> AND BaCo<sub>2</sub>(PO<sub>4</sub>)<sub>2</sub>, *Journal de Physique Colloques* (1978), p.759-761.

- [65] L.P. Regnault, J. Rossatmignod, J.Y. Henry, L.J. Dejongh, *Journal of Magnetism and Magnetic Materials* **31-4** (1983) (FEB) 1205.
- [66] L.P. Regnault, J.Y. Henry, J. Rossatmignod, A. Decombarieu, *Journal of Magnetism and Magnetic Materials* **15-8** (1980) (JAN-) 1021.
- [67] L.J.D. Jongh, *Magnetic Properties of Layered Transition Metal Compounds*, Kluwer Academic Publishers (1990).
- [68] S.J. Hibble, P.G. Dickens, J.C. Evison, *Journal of the Chemical Society-Chemical Communications* (1985) (24) 1809.
- [69] W. Xiao, W. Liu, X. Mao, H. Zhu, D. Wang, *Electrochimica Acta* **88** (2013) 756.
- [70] Y. Tian, D. Chen, X. Jiao, Y. Duan, *Chemical Communications* (2007) (20) 2072.
- [71] C.P. Grey, N. Dupre, *Chemical Reviews* **104** (2004) (10) 4493.
- [72] D. Massiot, F. Fayon, M. Capron, I. King, S. Le Calve, B. Alonso, J.O. Durand, B. Bujoli, Z.H. Gan, G. Hoatson, *Magnetic Resonance in Chemistry* **40** (2002) (1) 70.

## **Chapter III.**

New Fe phases with remarkable topotactic transformations.

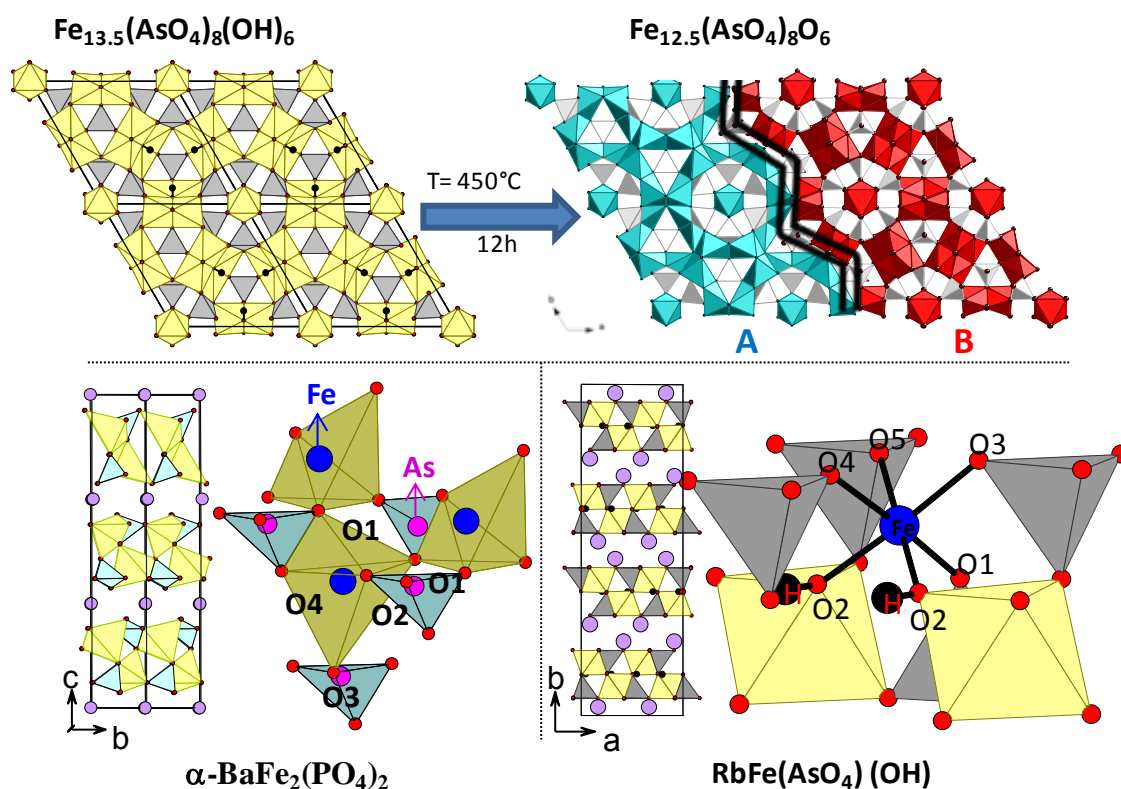
**Abstract.**

During our search for new compounds inspired from the Ba-Fe-P-O system, several new phases have been discovered. In this last chapter, we have compiled three of them, with their preliminary characterizations.

The first phase synthesized is  $\text{Fe}_{13.5}(\text{AsO}_4)_8(\text{OH})_6$ . This compound belonging to a family of the open framework phases,  $\text{M}_{11}\square_1(\text{HPO}_3)_8(\text{OH})_6$  ( $\text{M} = \text{Zn}^{2+}, \text{Co}^{2+}, \text{Ni}^{2+}$ )[1], contains mixed valent  $\text{Fe}^{2+}/\text{Fe}^{3+}$  cations. It shows a very unique kind of iron exsolution, associated to the  $\text{Fe}^{2+} \rightarrow \text{Fe}^{3+}$  oxidation and dehydroxylation process. It leads to a composite phase, made of an imbrication of two oppositely charged lattices, and finally, to an amorphization when the thermal treatment duration or temperature are increased.

The second phase was obtained during the research of new synthesis methods to attempt to prepare the rhomboedral  $\text{BaFe}_2(\text{PO}_4)_2$  (chapter II 2.) by solid state route. A new trigonal polytype of  $\text{BaFe}_2(\text{PO}_4)_2$ , isostructural with  $\alpha\text{-BaCo}_2(\text{PO}_4)_2$ , a polymorph solved during the study of the  $\text{BaCo}_2(\text{PO}_4)_2$  phase diagram[2] has been isolated. Its structure has been solved by synchrotron X-ray diffraction and first magnetic measures were performed.

To finish, we present a new compound whose formula is  $\text{RbFeAsO}_4(\text{OH})$  was isolated by hydrothermal synthesis and its structure was determined by single crystal XRD.



## **1. $\text{Fe}_{13.5}(\text{AsO}_4)_8(\text{OH})_6$ and its imbricated charged structures after thermal treatment.**

Following the discovery of the astonishing  $\text{Fe}^{2+}$  network behavior at moderate temperatures in the previous  $\text{Ba}(\text{Fe},\text{M})(\text{PO}_4)_2$  cases, we have continued our study focusing on the research of new adequate lattices for Fe-exsolution. In this context, a new and very interesting phase was prepared by hydrothermal synthesis. This phase shows important structural similarity with already reported open frameworks phases based on phosphites or selenites oxy-anions. This crystallo-chemistry aspects will be presented hereafter, in complement to the structural characterization task. The concerned new compound presents an interesting topochemical structural transformation after heating, due to a partial  $\text{Fe}^{2+}$  exsolution together with dehydroxilation. To our knowledge the resulting compound is unique in nature from the crystallographic viewpoint, due to the intimate mixing between two charged crystal structures that are created in equal amount for charge balance.

### **1.1. Synthesis and characterization techniques.**

Crystalline powders were synthesized under hydrothermal conditions from a mixture of metal iron (7 mmol),  $\text{As}_2\text{O}_5$  (3.5 mmol) and KCl (7 mmol) with a 1/1/1 Ratio. Precursors were placed in a 50ml Teflon lined stainless steel autoclave, with addition of 15 ml of deionized water. The reactor was heated in oven, from ambient temperature to  $200^\circ\text{C}$  for 20 hours under autogenous pressure. It was maintained 24 hours at  $200^\circ\text{C}$ , followed by a slow cooling to room temperature in 72 hours. The initial pH was  $\sim 2-3$ . These low values of pH are justified by the reaction:  $\text{As}_2\text{O}_5 + 3\text{H}_2\text{O} \rightarrow \text{H}_3\text{AsO}_4$ .

After reaction the pH of the solution goes up to 7-8. The solid product was filtered off, rinsed with water and left to dry in air at ambient temperature.

The obtained powder is not a single phase, but mainly contains brown-green long thin crystalline needles  $\sim 5-10$  micron long, corresponding to the interesting compound. It is mixed with small black octahedral crystals present in small quantities and identified as an isostructural phase of the wihelmkleinite[3] mineral of formula  $\text{Fe}^{\text{II}}\text{Fe}^{\text{III}}_2(\text{AsO}_4)_2(\text{OH})_2$  (from single crystal tests, lattice parameters :  $a=6.6585 \text{ \AA}$ ,  $b=7.6266 \text{ \AA}$  and  $c=7.4187 \text{ \AA}$ ,  $P2_1/n$  space group). A small amount of unreacted metal iron remains in the final products, which is a real problem for further magnetic measurements.

It is noteworthy that KCl must be present in the initial reacting solution to obtain the phase and may act as mineralizer. If absent, we obtain the formation of the iron pyro-arsenate,  $\text{Fe}^{\text{II}}_2(\text{As}_2\text{O}_7)(\text{H}_2\text{O})_2$  [4].

The Powder XRD pattern in figure III.1 shows the major phase  $\text{Fe}_{13.5}(\text{AsO}_4)_8(\text{OH})_6$  in presence of minor impurities. Concerning  $\text{Fe}_{13.5}(\text{AsO}_4)_8(\text{OH})_6$  the experimental XRD pattern shows a good agreement with the calculated pattern using the established structural data, see below. As mentioned above, we have also identified a weak amount of unreacted metal-iron, although extra XRD-lines have not been clearly identified but may overlap with the pattern of the minor amount of wihelmkleinite.

Single crystal X-ray diffraction, transmission electron microscopy and  $^{57}\text{Fe}$  Mössbauer spectroscopy were carried under same conditions as described in the other chapters.

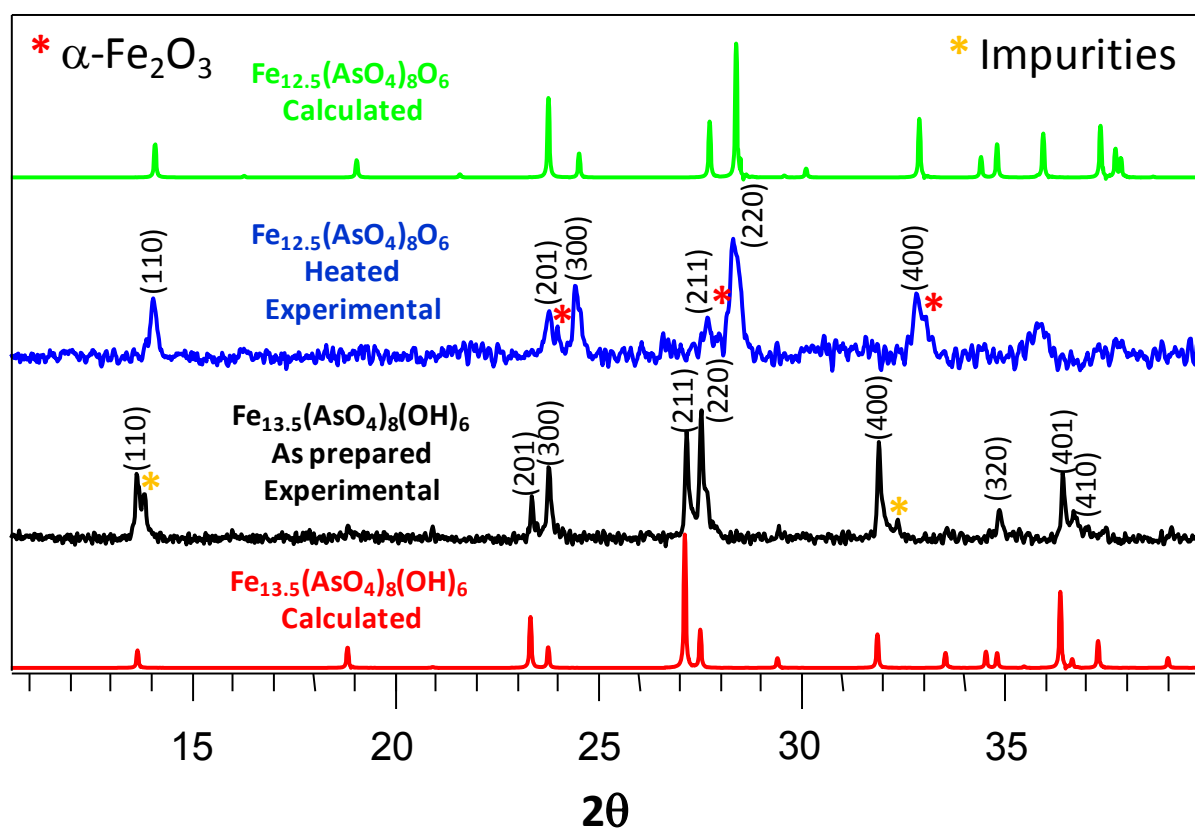


**Figure III.1.** Experimental and calculated (from single crystal structure resolution) Powder X-ray diffraction for as-prepared  $\text{Fe}_{13.5}(\text{AsO}_4)_8(\text{OH})_6$  and heated  $\text{Fe}_{12.5}(\text{AsO}_4)_8\text{O}_6$ .

## 1.2. Structural characterization.

A single crystal was collected and after data integration and corrections we refined the hexagonal lattice parameters  $a = 12.908(4) \text{ \AA}$  and  $c = 5.160(6) \text{ \AA}$  from the full dataset. The crystal structure was solved using the charge Flipping method (SuperFlip) and refined in the  $P6_3mc$  non centrosymmetric space group (NCS) using Jana 2006. There is no structural ambiguity concerning the main framework which consists of one independent iron site Fe1 (12d), two arsenic As1 and As2 (2a) sites and six surrounding oxygen positions. These atoms form the typical hexagonal framework already reported in a number of related phosphites and selenites phases, e.g.  $M_{11}\square_1(\text{HPO}_3)_8(\text{OH})_6$  (see the recent ref [5] for an overview) and  $M_{12}(\text{X})_2(\text{SeO}_3)_8(\text{OH})_6$ , ( $M = \text{Co}^{2+}, \text{Ni}^{2+}$ ;  $\text{X} = \text{OH}^-, \text{F}^-$ ).[6] Contrarily to what systematically found in the  $M_{11}\square_1$  phases, the refinement of the Fe1 occupancy leads to fulfilled positions. The hydrogen atom connected to the atom O2 of the hydroxyl group was located in Fourier difference maps and was fixed ( $\text{O2-H} = 1.02 \text{ \AA}$ ). Note that these hydroxides ions are common to all related compounds. The isotropic thermal parameters for H was restrained equal to  $1.5 \times U_{\text{iso}}(\text{O2})$  and the OH bond leads to very consistent bond valence sum calculation for O2, i.e.  $\text{BVS} = 1.72 \text{ v.u.}$

A second iron site was located in the center of the hexagonal channels. In the phosphite or selenite phases, these sites are either empty either occupied by  $\text{OH}^-$  or halide ions, i.e see the formula of the related compounds mentioned above. The coordination of the Fe hosts is performed by oxygen corners of the arsenates pointing in the tunnels, while for  $\text{HPO}_3^{2-}$  or  $\text{SeO}_3^{2-}$  oxy-anions, the tunnels are empty due to covalent P-H units or electron lone pairs of  $\text{Se}^{4+}$  ions in the tunnels. The site occupancy was refined to 74.9(2) % and significantly lowers agreement factors by *ca.* 2%. Finally the refined crystal formulation corresponds to  $\text{Fe}_{13.5}(\text{AsO}_4)_8(\text{OH})_6$  and the crystal structure is presented in figure III.2 as well as the two other examples mentioned.

### 1.2.1. Crystal structure and Fe valence of $\text{Fe}_{13.5}(\text{AsO}_4)_8(\text{OH})_6$ .

The crystal structure shows a complex tridimensional framework which contains two types of tunnel along the  $c$  axis, a small trigonal one and large hexagonal one. The iron-based framework is built of dimmers of face sharing  $\text{FeO}_6$  octahedra into  $\text{Fe}_2\text{O}_9$  units, linked together along the “ $c$ ” axis by edge sharing and linked in the (a,b) plane by corner sharing. The cohesion is performed by bridging  $\text{AsO}_4$  groups. The trigonal tunnels contain apical As-O units. All  $\text{AsO}_4$  groups are oriented “up” with respect to the NCS symmetry. It forms a polar

crystal structure. It is a similar situation as found for the cooperative “up” orientation between all  $\text{HPO}_3$  and  $\text{ESeO}_3$  (where  $E$  denote the stereoactive  $\text{Se}^{3+}$  lone pair) in  $\text{Ni}_{11}\square_1(\text{HPO}_3)_8(\text{OH})_6$ [5] and  $\text{M}_{12}(\text{X})_2(\text{SeO}_3)_8(\text{OH})_6$  ( $\text{M} = \text{Co}^{2+}, \text{Ni}^{2+}$ ;  $\text{X} = \text{OH}^-, \text{F}^-$ ).[6] A representation of these structures as well as the new  $\text{Fe}_{13.5}(\text{AsO}_4)_8(\text{OH})_6$  is presented in the figure III.2. However in these two structural types, the hexagonal tunnels are empty, bordered by H atoms or  $E$  lone pairs of electrons. In our compound, the  $\text{AsO}_4$  decorating the channels create face-sharing octahedral cavities,  $3/4^{\text{th}}$  filled by Fe2 atoms. This feature give to this phase an original character since, to the best of our knowledge, such Fe-based chains have never been identified isolated in oxide. On the opposite, dealing with bigger anions such as  $\text{Cl}^-$  or  $\text{Br}^-$  halides, similar chains of face-sharing  $\text{Fe}^{2+}\text{X}_6$  octahedra can be found, e.g. in the hexagonal 2H-polytypes  $\text{CsFeCl}_3$ .[7] The bond valence calculations leads to 2.1(4)/2.2(5) and 2.1(2)/2.2(4) for Fe1 and Fe2 respectively using data from ref [8] for  $\text{Fe}^{2+}$  and  $\text{Fe}^{3+}$  octahedral ions respectively. Pertinent distances are listed in the Table III.1 and show regular octahedra  $\text{FeO}_6$  ( $3 \times 2.10 + 3 \times 2.13$ ) for Fe2 very similar for  $\text{Fe}^{2+}\text{O}_6$  octahedra in  $\text{BaFe}_2(\text{PO}_4)_2$  ( $3 \times 2.11 + 3 \times 2.14$ ). Their valence state was ascribed to  $\text{Fe}^{2+}$ .

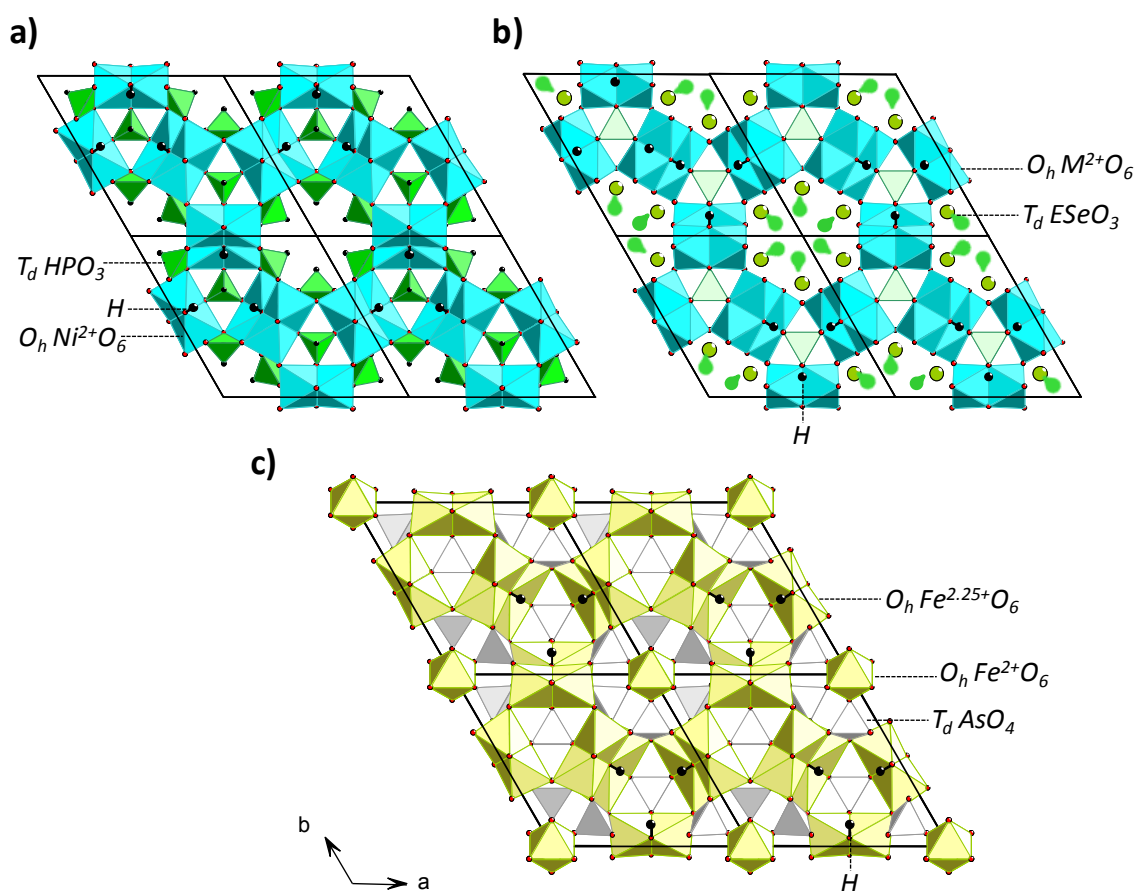


**Figure III.2.** (a,b) projection of the crystal structures of  $\text{Ni}_{11}\square_1(\text{HPO}_3)_8(\text{OH})_6$  (a),  $\text{M}_{12}(\text{X})_2(\text{SeO}_3)_8(\text{OH})_6$  (b) and the new compound  $\text{Fe}_{13.5}(\text{AsO}_4)_8(\text{OH})_6$  (c).

Face sharing octahedral chains exist for small  $M^{4+}$  ions ( $Mn^{4+}$ ,  $Co^{4+}$ ,  $Ni^{4+}$ ) in  $BaMO_3$  hexagonal perovskites 2H-polytypes, leading to M-M distances of *ca.* 2.4 Å. In our compound even dealing with larger  $Fe^{2+}$  ions,  $r = 0.61\text{Å}$  in the LS state, (the LS low spin configuration is preferred in face-sharing topologies, see ref [9]) strong constraints are driven by experimentally observed elongated  $FeO_6$  octahedra along the c-axis and long Fe-Fe distances of 2.58 Å. Most presumably the  $1/4^{\text{th}}$  of empty octahedral relax the octahedral stacking along the chains axis.

Dealing with the hexagonal framework, i.e. the Fe1 atom, taking into account the relatively distorted  $Fe1O_4(OH)_2$  sites (see Table 1), mixed valence states can be suggested as further comforted by Mössbauer spectroscopy. The ideal distribution charge for Fe1  $3/4^{\text{th}}$   $Fe^{2+}$  and  $1/4^{\text{th}}$   $Fe^{3+}$  yields the neutral formula  $Fe^{+2.25}_{12} Fe^{2+}_{1.5} (OH)_6(AsO_4)_8$ .

**Table III.1.** Interatomic distances and corresponding iron Bond Valence Sum ( $\Sigma s_{ij}$ ) values, calculated using parameters associated to  $Fe^{+2}$  from reference[8], for  $Fe_{13.5}(AsO_4)_8(OH)_6$ .

Distances d (Å)					
$Fe_{13.5}(AsO_4)_8(OH)_6$					
Fe ions			As ions		
Fe1-O1	2.07(0)	Fe2-O5	2.10(4) x2	As1-O1	1.69(9) x2
Fe1-O1	2.06(3)	Fe2-O5	2.12(6) x2	As1-O5	1.65(6)
Fe1-O2H	2.19(0)	Fe1-Fe1	2.08(1)	As1-O3	1.71(0)
Fe1-O2H	2.27(6)	Fe2-Fe2	2.58(0)	As2-O4	1.69(9) x3
Fe1-O3	2.07(7)	$\Sigma s_{ij}(Fe^{2+}/Fe^{3+})$	2.1(2)/2.2(4)	As2-O6	1.63(0)
Fe1-O4	2.05(4)				
$\Sigma s_{ij}(Fe^{2+}/Fe^{3+})$	2.1(4)/2.2(5)				

$^{57}Fe$  Mössbauer spectroscopy analysis was performed on the “as-prepared” sample using lorentzian profiles for the different contributions. Results of the hyperfine parameters are given in the Table III.2. In this table we have reported the atomic contribution of the two main  $Fe^{2+}$  and  $Fe^{3+}$  components before and after deduction of the Fe-metal contributions. The figure III.3 presents the Mössbauer spectra of the  $Fe_{13.5}(AsO_4)_8(OH)_6$ .

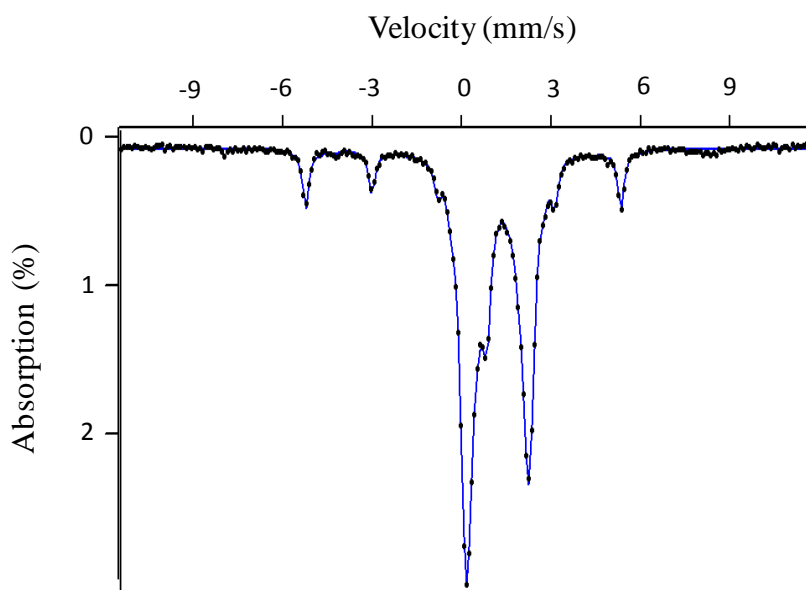


Figure III.3.  $^{57}\text{Fe}$  Mössbauer spectra at 298 K of  $\text{Fe}_{13.5}(\text{AsO}_4)_8(\text{OH})_6$ .

Table III.2.  $^{57}\text{Fe}$  Mössbauer hyperfine parameters of  $\text{Fe}_{13.5}(\text{AsO}_4)_8(\text{OH})_6$  at 293K. The second % column corresponds to the main phase without the Fe-second phase.

<b>Lorentzian refinement</b>										
DIS	$\delta$ (mm/s)	$\Gamma$ (mm/s)	$\epsilon$ (mm/s)	$\Delta$ (mm/s)	H (T)	% exp.		% calc. site		ox. state.
H1	0.005	0.21	-0.002	-	33.0	10	-	-	-	$\text{Fe}^0$
D2	1.17	0.57	-	2.00	-	70	78	78	$^{67}\text{Fe}_1$	$\text{Fe}^{2+}$
D1	0.41	0.39	-	0.71	-	20	22	22	$^{12}\text{Fe}_2$ $^{22}\text{Fe}_1$	$\text{Fe}^{3+}$
<b>Distribution refinement</b>										
DIS	$\delta$ (mm/s)	$\Gamma$ (mm/s)	$\epsilon$ (mm/s)	$\Delta$ (mm/s)	H (T)	%exp.		%calc. site		ox. state.
H1	0.00001	0.20	0.0001	-	32	8	0	-	-	$\text{Fe}^0$
D2	1.16	0.30	-	1.96	-	70	76	78	$^{67}\text{Fe}_1$ $^{11}\text{Fe}_2$	$\text{Fe}^{2+}$
D1	0.40	0.25	-	0.87	-	22	24	22	$^{22}\text{Fe}_1$	$\text{Fe}^{3+}$

After deconvolution of the spectra using lorentzian components, the magnetically ordered  $\text{Fe}^0$  sextuplet is refined to 10%. Excluding this contribution in our analysis, the two observed paramagnetic contributions D1( $\text{Fe}^{3+}$ ) and D2( $\text{Fe}^{2+}$ ) were refined to 22% and 78% respectively. They are associated to rather large  $\Gamma$  linewidths, especially concerning D2 ( $\Gamma =$

0.57 mm/sec) which suggests the participation of several crystallographic sites and comfort  $\text{Fe}^{2+}$  ions in both Fe1 and Fe2 sites. For D1 we find  $\Gamma = 0.39$  mm/sec which match well  $\text{Fe}^{3+}$  statistically distributed in a mixed valent site. The agreement between the theoretical and experimental  $\text{Fe}^{2+}/\text{Fe}^{3+}$  ratio of 3.83 and 3.16 respectively is not bad. We have also performed calculations of distribution after fixing  $\Gamma$  values accordingly to the spectrometer experimental resolution. The results give similar spectroscopic characteristics and same H1 (8%), D1 (22%), D2 (70%) distribution. It confirms a very large distribution of quadrupolar splittings  $\Delta$  and the probable  $\text{Fe}^{2+}$  distribution over two crystallographic positions ( $\Delta_{\text{D2}} = 2.65$  mm/sec).

### 1.2.2. Topotactic Transformation.

After heating in air at 450°C for 12 hours, this phase undergoes a very complex topotactic transformation, which is unique to the best of our knowledge in terms of the resulting product. In few words the obtained material consists of the intimate imbrication of two related phases negatively and positively charged respectively. Here we do not deal with positive and negative subunits associated in a composite crystal structure, but really to charged 3D crystal structure that coexist in fragments. This section is dedicated to the characterization of this phenomenon.

The Figure III.1 shows the XRD patterns before and after heating the compound at 450°C for 12 hours. After this treatment needle-shaped crystals are conserved but darkened compared to the original brown-green color of the  $\text{Fe}_{13.5}(\text{AsO}_4)_8(\text{OH})_6$  phase. The Powder XRD pattern shows that the original metal iron impurity is oxidized into  $\alpha\text{-Fe}_2\text{O}_3$ .

Compared to the original hexagonal unit cell, an important cell contraction occurs, especially pronounced in the (a,b) basal plane; i.e. initial  $a = 12.940(2)$  Å,  $c = 5.18(12)$  Å  $\rightarrow$  final  $a = 12.54(4)$  Å,  $c = 5.14(19)$  Å. At first sight, it is reminiscent of the oxidation of  $\text{Fe}^{2+}$  ions into smaller  $\text{Fe}^{3+}$  ones. The broadening of all reflexions after heating indicates a lowering of the crystallinity. At this stage, taking into account the initial structure hold along the  $c$  axis by infinite chains of  $\text{AsO}_4$  tetrahedra and chains of face sharing  $\text{Fe}^{2+}\text{O}_6$  octahedra, the slight change of the  $c$  parameter suggests that these templating units should be preserved along  $c$  direction, after heating. This assumption is one key-argument in the discussion below, while establishing the structural model and most plausible charge distribution

The sample oxidation was confirmed by Mössbauer spectroscopy and the spectra performed it is presented, figure III.4.

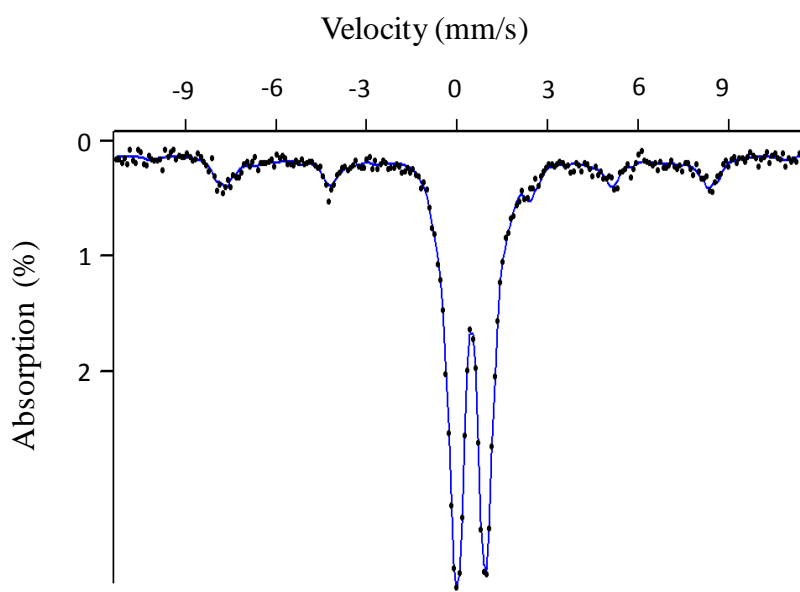


**Figure III.4.**  $^{57}\text{Fe}$  Mössbauer spectra at 298 K of  $\text{Fe}_{12.5}(\text{AsO}_4)_8\text{O}_6$ .

The refinement of the distributions was performed by fixing the line widths  $\Gamma$  to the experimental resolution for standard  $\text{Fe}^{2+}$  and  $\text{Fe}^{3+}$  reference samples. After deconvolution, we can assign the refined components as follows:

- The H1 sextuplet contribution corresponds to  $\alpha\text{-Fe}_2\text{O}_3$ , including 8% arising (from the initial metal iron second phase) and another extra 4% (from the partial Fe exsolution). The large  $\Delta$  values match rather well the distribution of sites deduced from single crystal XRD, see model below and Table III.3.

- After deduction of the 8% of  $\text{Fe}_2\text{O}_3$  from the initial iron oxidation, the three contributions D1 ( $\text{Fe}^{3+}$ ), D2 ( $\text{Fe}^{2+}$ ) and  $\text{Fe}_2\text{O}_3$  represent 88%, 7.6% and 4.4% respectively.

If one considers the plausible preservation of the 75% filled face-sharing  $\text{Fe}^{2+}\text{O}_6$  chains (original Fe2 site) proposed above, one immediately remarks the good matching between the Mössbauer analysis and the mechanism proposed below. In the following equation, the reaction involves the concomitant dehydroxilation and  $\text{Fe}_2\text{O}_3$  exsolution, starting from the initial  $\text{Fe}^{2.25+}_{12}\text{Fe}^{2+}_{1.5}(\text{OH})_6(\text{AsO}_4)_8$  phase :



The relative contribution for D1, D2 and  $\text{Fe}_2\text{O}_3$  are given in the Table III.3. Although this assessment is numerically exact, we will see later that the reaction is in fact more complex leading not to one but to the mixture of two phases.

**Table III.3.**  $^{57}\text{Fe}$  Mössbauer hyperfine parameters of  $\text{Fe}_{12.5}(\text{AsO}_4)_8(\text{OH})_6$  at 293K.

DIS	$\delta$ (mm/s)	$\Gamma$ (mm/s)	$\varepsilon$ (mm/s)	$\Delta$ (mm/s)	H (T)	%exp.	%calc. site		Site	
H1	0.35	0.40	-0.07	-	47.9	12	4	7	-	$\text{Fe}^{3+}_2\text{O}_3$
D2	1.05	0.35	-	2.65	-	7	8	11	$\frac{5.5_{\text{Fe2A}}}{5.5_{\text{Fe2B}}}$	$\text{Fe}^{2+}$
D1	0.42	0.25	-	1.05	-	81	88	82	$\frac{45_{\text{Fe1A}}}{37_{\text{Fe1B}}}$	$\text{Fe}^{3+}$

### 1.3. Evidence for two imbricated charged sublattices.

#### 1.3.1. Transmission electron microscopy characterization.

First, one notes that the TEM images of the transformed product shows the conservation of the needle like crystallites more or less damaged. The figure III.5 represents the heterogeneity of the different crystals. Figure III.5 (a) illustrates the example of well preserved rod crystals (majority of them) whereas figure III.5 (b) shows full fragmentation in tiny domains. The corresponding electron diffraction patterns are similar whatever the degree of collapsing. The medium resolution image of damaged crystal (figure III.5 (c)) shows that the periodicity along c direction is well preserved.

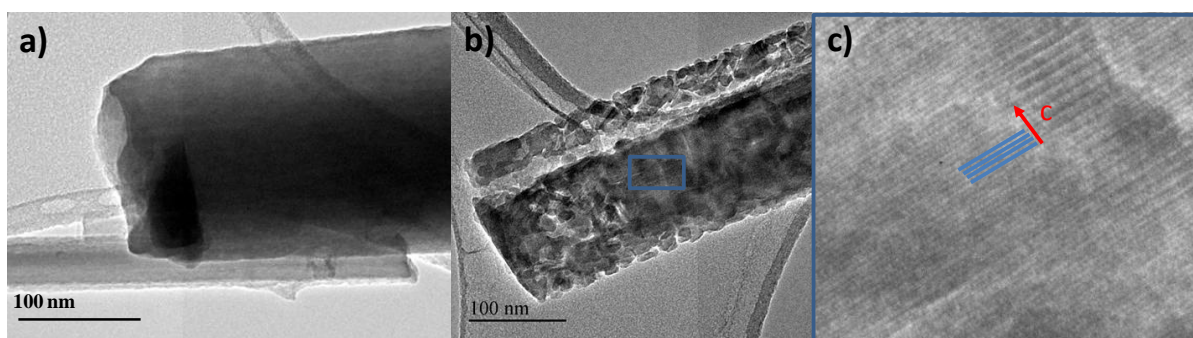


**Figure III.5.** TEM images of  $\text{Fe}_{13.5}(\text{AsO}_4)_8(\text{OH})_6$  after heating with more or less deteriorated needle-shape crystals (a, b). Conservation of the c-period in the image mode (c).

Area selected electron diffraction shows a clear deterioration of the diffraction pattern, after heating the phase, see figure III.6. In the ED patterns, the d-spacing along c is conserved but perpendicular axes are damaged by strong erratic spots or diffuse lines, see figure III.6 (b). After heating the (hk0) layer is well preserved, see figure III.6 (c), similarly to what

observe in single crystals, see figure III.8 (b). On the opposite the next (hk1) layer can be reached by tilting the sample and shows diffuse diffraction instead the expected hexagonal lattice, figure III.6 (d).

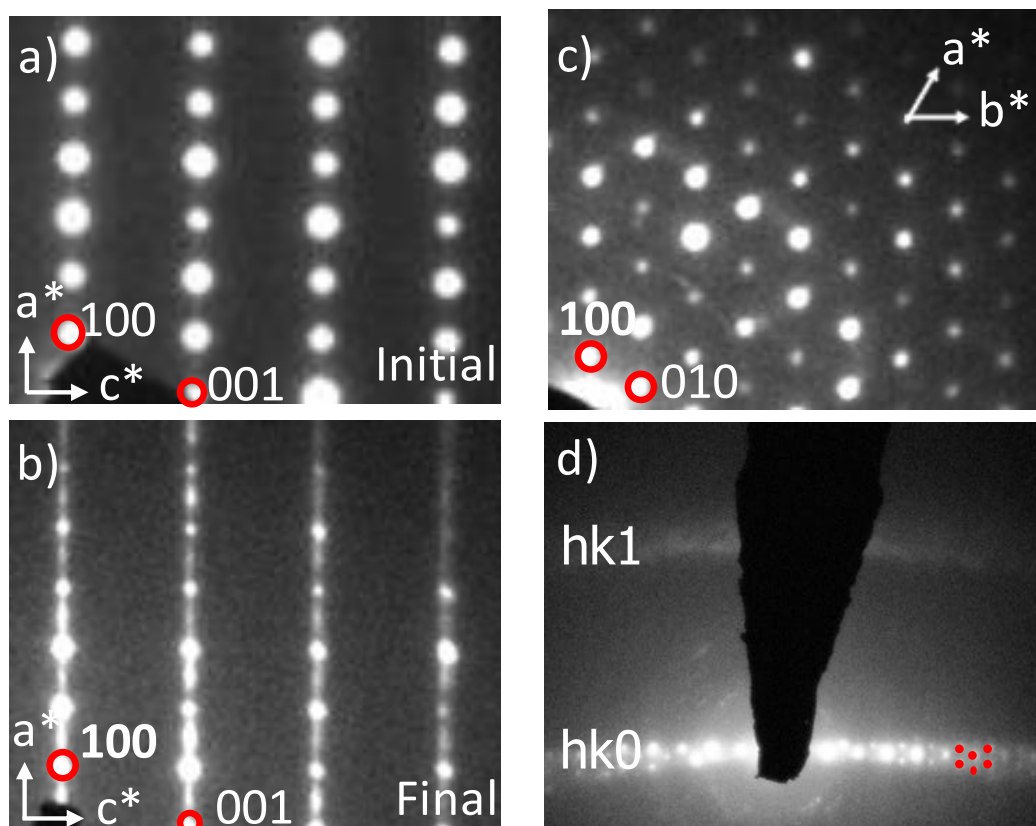


**Figure III.6.** ED patterns of different zones from the iron  $Fe_{13.5}(AsO_4)_8(OH)_6$  as prepared ( $h0l$ ) (a), and after heat ( $h0l$ ) (b), ( $hk0$ ) (c). Tilted view of the hexagonal ( $hk0$ ) plane (d).

The Figure III.7 (a) presents the a-c projections by high resolution imaging for the ED pattern of figure III.6 (b). We can remark the good periodicity along the c-axis. On the opposite, bands with different contrast alternate along the a-axis. This changing contrast can be assigned to the presence of different very small domains in good agreement with the ED pattern of figure III.5 (b).

In addition, the figure III.7 (b) shows a-b plane of the phase. We can clearly observe a hexagonal motif with two different contrasts. Assuming the co-existence of two different domains, we can confirm that they are randomly mixed in the a-b plane but each domain is preserved well-ordered along the c direction.

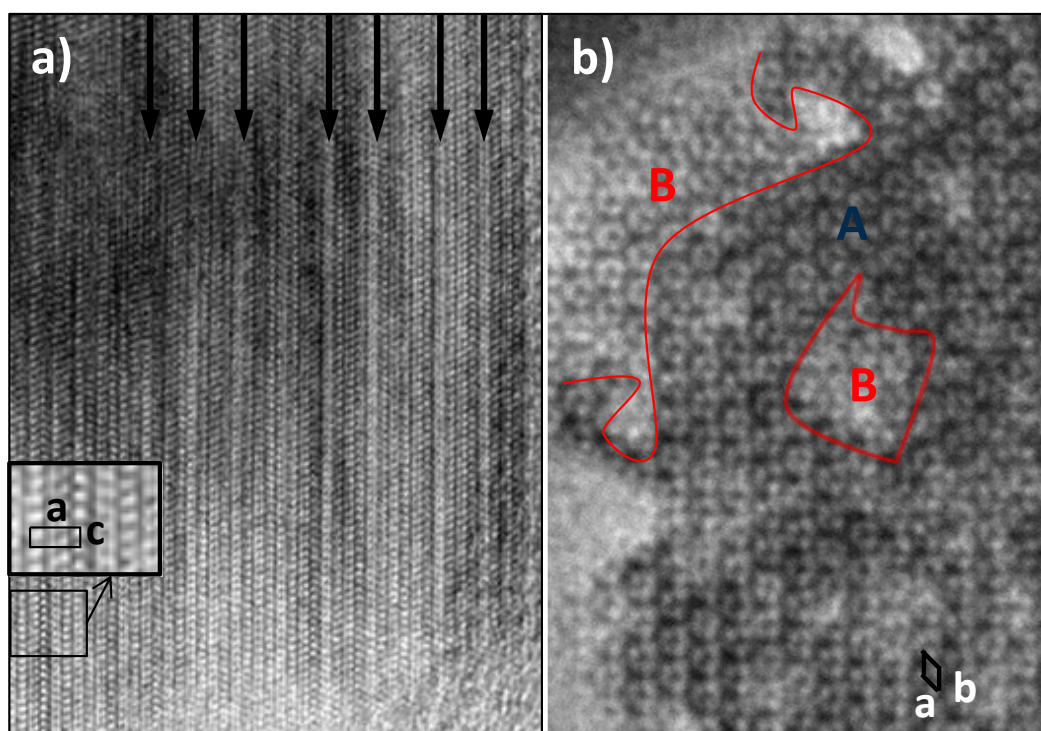


**Figure III.7.** HREM Image of the  $(a,c)$  plane (a) and of the hexagonal  $(a,b)$  plane (b) planes.

### 1.3.2. Single crystal analysis.

Similar diffraction characteristics can be deduced after examination of the precession frames reconstructed after data collection of heated needle-shape crystal. The  $hk0$  layer can be fully indexed in a hexagonal cell with  $a = 12.558(2) \text{ \AA}$ ,  $c = 5.087(7) \text{ \AA}$ , values very close to those refined from the powder XRD pattern. Particular layers, such as the  $h0l$  one presented figure III.8 (b), show a number of more or less defined extra spots in erratic positions, but preserving the  $c$ -periodicity. In fact, as evidenced on the reconstructed  $hk1$  layer which consists of main spots within a 2D-diffuse lattice see figure III.8 (d), these “spots” correspond to the intersection of axes with the diffuse scattering lattice. This lattice respects the hexagonal symmetry but proves important disorder in the phases.

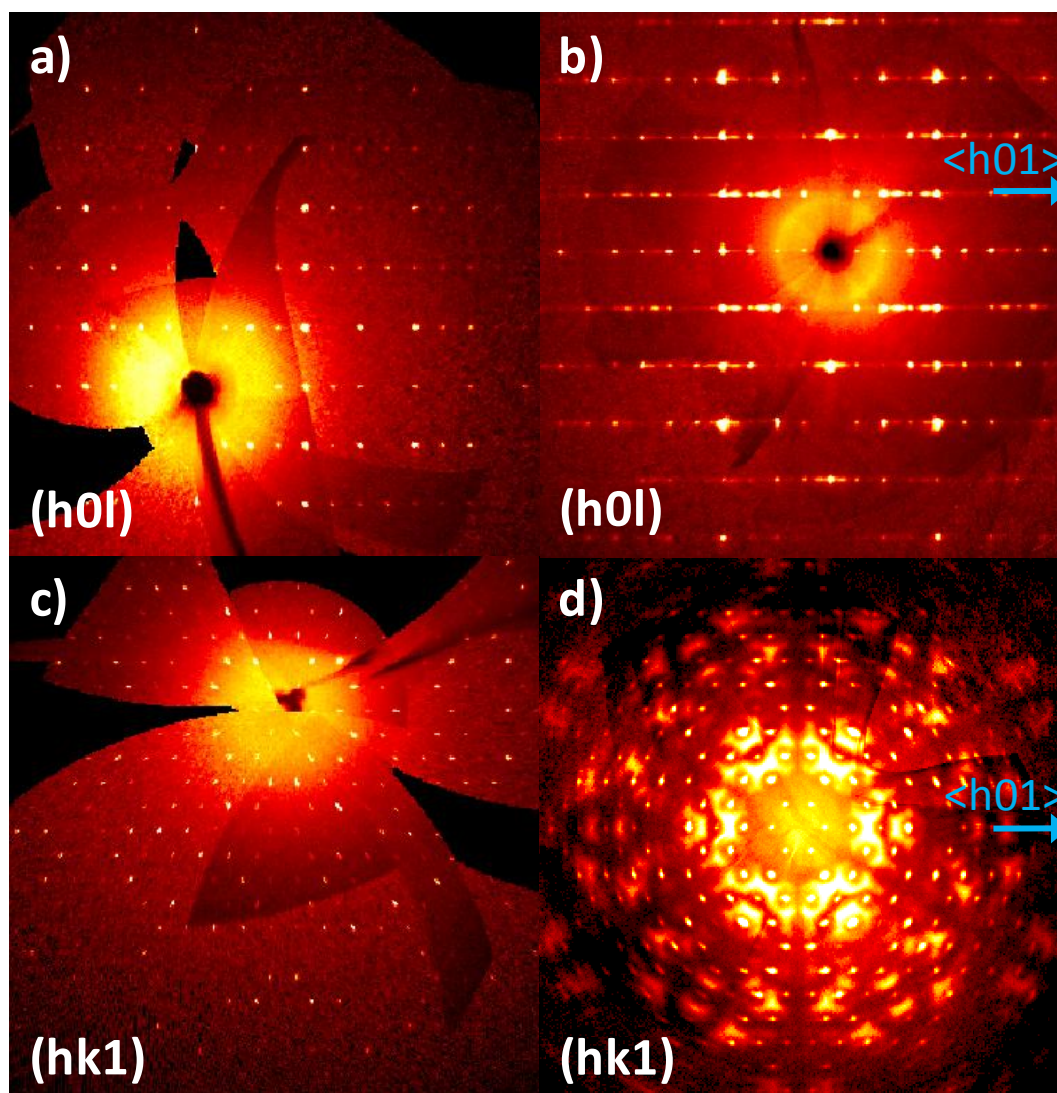


**Figure III.8.** Precession images of the  $[h\ 0\ l]$  and  $[h\ k\ l]$  for  $Fe_{13.5}(AsO_4)_8(OH)_6$  as prepared (a, c) and after thermal treatment (b, d).

After integration of the full recorded data set, the merging factor  $R_{\text{int}} = 9.74\%$ , in the 6mm point group validates an hexagonal or related symmetry. The structural resolution and refinement were particularly tricky and have been tested in the initial  $P6_3mc$  and compatible subgroups  $Cmc2_1$  and  $Cc$  space group, using several models and defect types (twins, mixture of two phases with or without rigid bodies for  $AsO_4$  groups). It essentially leads to similar results, although the successive lowering of symmetry complicates the refinements of more and more independent atomic parameters. Finally, our best model consists of an intimate mixture of two structures (at the atomic scale) in the original  $P6_3mc$  space group. The most important obstacle concerns the doubling of almost each cationic position. In detail, comparatively to the initial structure, the As and Fe atoms are systematic found within atomic pairs  $Fe_A-Fe_B$  and  $As_A-As_B$  separated by  $\sim 2\text{\AA}$  along  $c$ , see figure III.9.

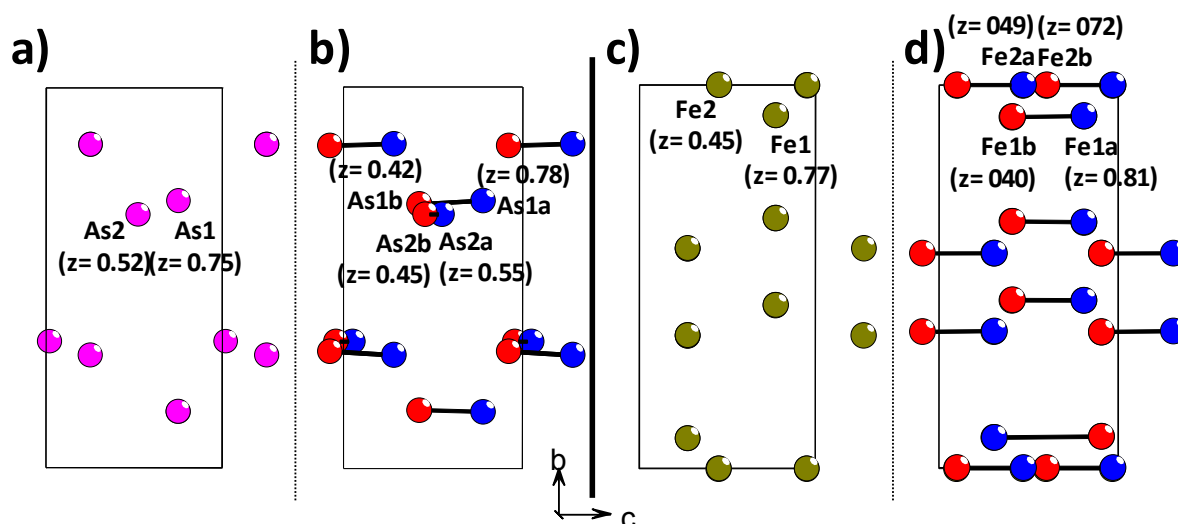


**Figure III.9.** As (a and b) and Fe (c and d) positions in the unit cell representation of  $Fe_{13.5}(AsO_4)_8(OH)_6$  and  $Fe_{12.5}(AsO_4)_8O_6$ , with creation of pairs after heating.

Most oxygen atoms have been carefully located at correct distances (1.6-1.7 Å) of the arsenic cations on Fourier difference maps. They have been refined or not depending on their stability of the refinement process. In the last stage to avoid  $AsO_4$  excessive distortions, restraints on As-O, O-O and Ba-O distances have been introduced, which *in fine* lower the reliability factors. Finally we obtain a very complex “*composite-like*” structure built on two intergrown frameworks called A and B, both crystallizing in the  $P6_3mc$  space group. The selection of the atoms belonging to the A or B components was achieved with respect to consistent interatomic distances. Finally it leads to two consistent individual crystal structures.

It is fundamental to clarify, that i) none of the tested twinning laws (for instance a mirror plane perpendicular to  $c$  suppressed the “atomic-pair” problem. ii) the composite approach which involve a mixture of two phases in the same crystal did not converge ( $R \sim 20\%$ ). In this approach, the collected intensities are the sum of intensities diffracted by each phase ( $I_{diff} = I_A + I_B = F_A^2 + F_B^2$ ) approach intensity. It implies that an intimate mixing between small domains at the unit-cell scale ( $I_{diff} = I_{A+B} = (F_A + F_B)^2$ ). The refinement of the occupancies of each component leads to a  $\sim 50\%$  for each A and B contributions. This point will be explained later by the opposite charge of the two structures.

Dealing with the two distinct crystal structures A and B, another important aspect concerns the occupancy of Fe1A (refined to 1.0(7) and fixed to 1.00) compared to that of Fe1B (refined to 0.7(2) and fixed to 10/12) which differentiate the stoichiometry of the two structures. We found similar results also in  $C2/c$  and  $Cc$  subgroups, i.e. even when each FeA and FeB atoms were split in satellite positions. The interatomic distances of both of phases

are listed in the table III.4. Most typical differences between the pristine crystal structure and those of its A and B modifications are shown on the figure III.10 (a,b,c). In all phases the face-sharing octahedral  $\text{Fe}^{2+}$  chains are preserved as also depicted. The triangular channels that contain  $\text{AsO}_4$  groups are also conserved. The *as-refined* imbrication between the  $\text{AsO}_4\text{A}$  and  $\text{AsO}_4\text{B}$  of are shown in the figure III.10 (d).

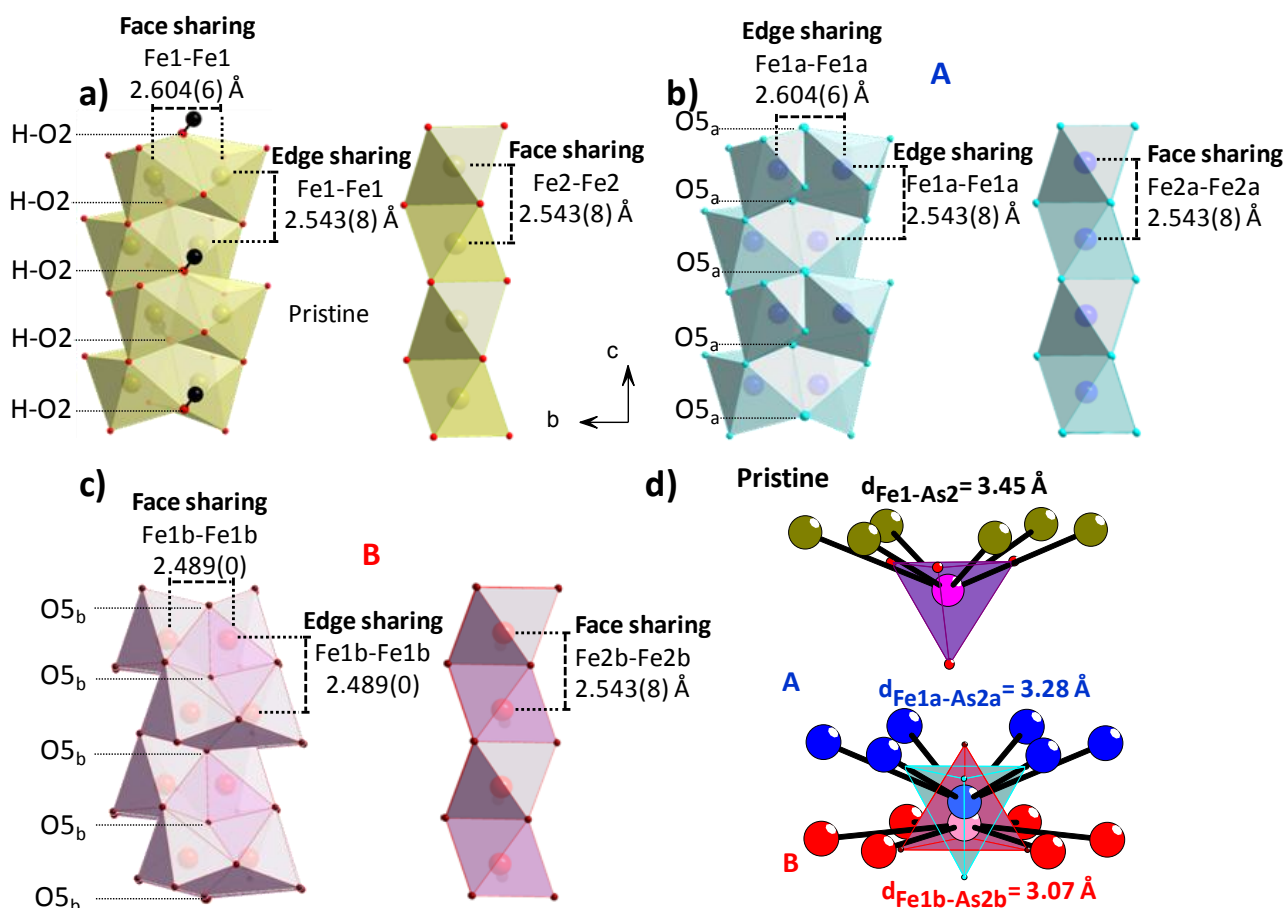


**Figure III.10.** Interatomic iron distances for  $\text{Fe}_{13.5}(\text{AsO}_4)_8(\text{OH})_6$  as prepared (a) and for the A (b) and B (c) structures, as well as  $\text{Fe1-As2}$  distances for all of them (d).

After the dehydroxilation, the modified hydroxyl groups ( $\text{O2-H} \rightarrow \text{O5A/O5B}$ ) changes considerably their direct environment leading to different Fe-O distance and angles as shown figure III.11.

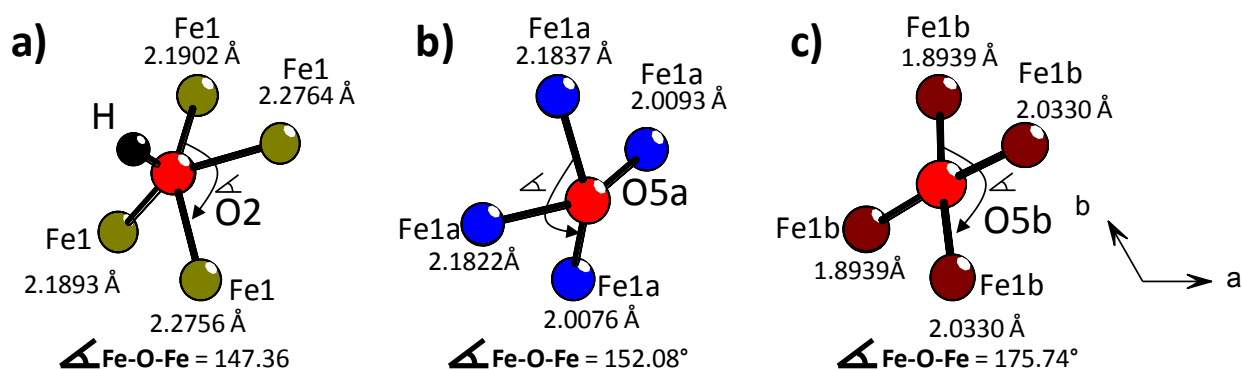
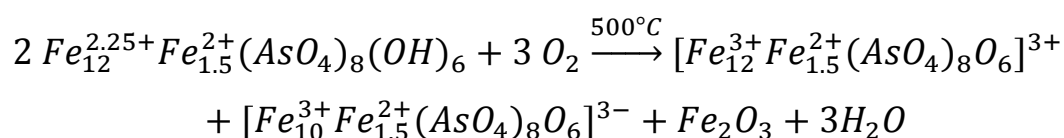


**Figure III.11.** Environment changes for the oxygen O2 in  $Fe_{13.5}(AsO_4)_8O_6$  (a), becoming O5 a and b after heating in  $[Fe_{13.5}(AsO_4)_8O_6]^{3+}$  (b) and  $[Fe_{11.5}(AsO_4)_8O_6]^{3-}$  (c) respectively.

To explain the unjustified 50% weight of each A and B component, the most plausible reason stem from their concomitant creation due to positive and negative charges respectively according to the equation:  $2 \text{pristine} \rightarrow A^{n+} + B^{n-}$ .

This result is in good agreement with the Fe1A and Fe1B occupancies discussed above and with our Mossbauer analysis also discussed here before, see table III.3.

Finally the final reaction can be written:



The partial charge on each fragment justifies the 50% weight of each of them for electroneutrality. Figure III.12 (a, b, c) shows the unit cell of  $Fe_{13.5}(AsO_4)_8(OH)_6$  as prepared and of the two imbricated phases after heat. Additionally, a projection of the two imbricated structures in the (a, b) plane is presented figure III.12 (d).

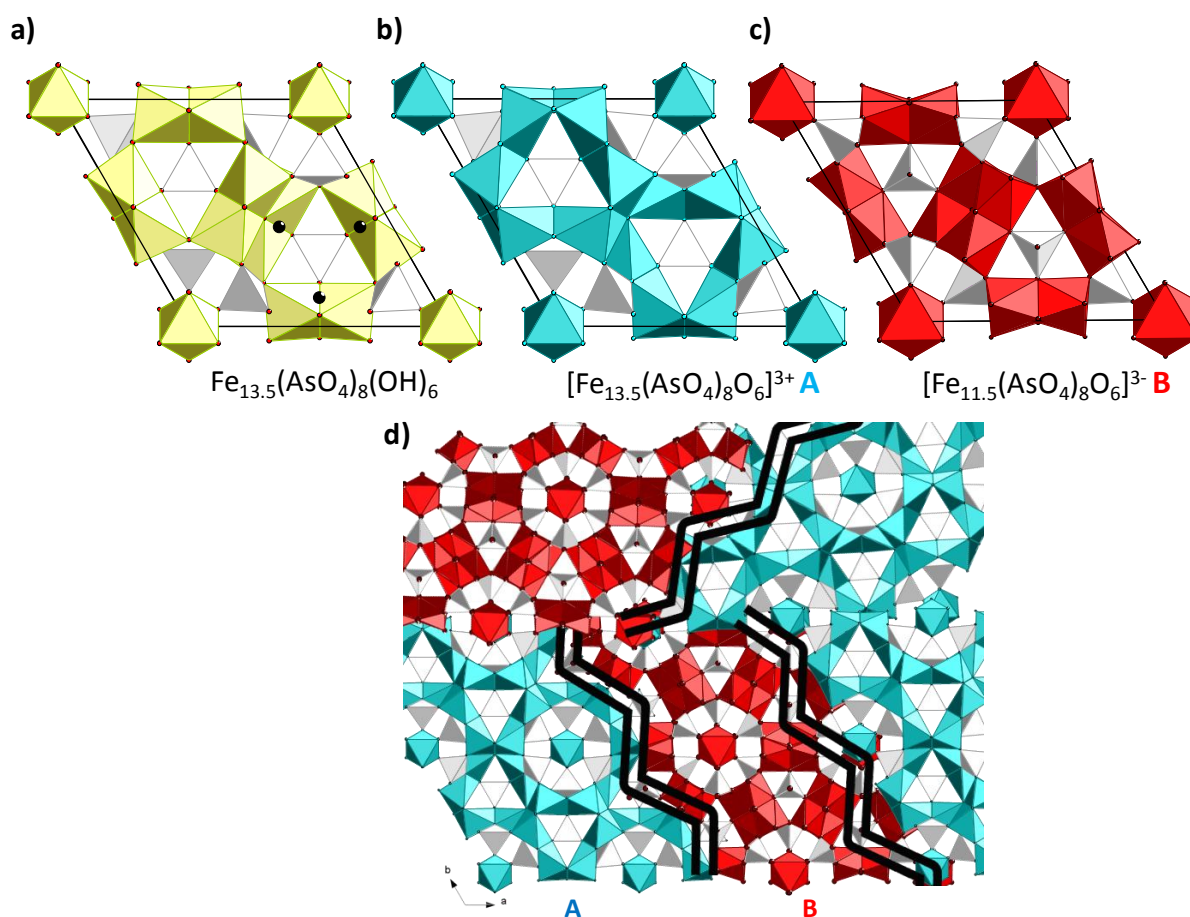


**Figure III.12.** Representation of the unit cell in the a-b plane of  $\text{Fe}_{13.5}(\text{AsO}_4)_8(\text{OH})_6$  (a),  $[\text{Fe}_{13.5}(\text{AsO}_4)_8\text{O}_6]^{+3}$  (b) and  $[\text{Fe}_{11.5}(\text{AsO}_4)_8\text{O}_6]^{-3}$  (c). Structural imbrications of  $[\text{Fe}_{13.5}(\text{AsO}_4)_8\text{O}_6]^{+3}$  and  $[\text{Fe}_{11.5}(\text{AsO}_4)_8\text{O}_6]^{-3}$  (d).

- **Phase A:** The structure of A corresponds to the  $[\text{Fe}_{13.5}(\text{AsO}_4)_8\text{O}_6]^{3+}$  formula. Hydroxides groups of the parent framework are replaced by bridging oxygen with shorter Fe-O5A, as presented in figure III.10 (b) and figure III.11.

The iron octahedral dimers share an edge rather than the face sharing topology in the original structure, leading to highly distorted  $\text{FeO}_6$  octahedra as highlighted in the table III.4. This new conformation in the A-phase changes the structure,  $\text{Fe}_2\text{O}_9$  dimers are not sharing the corners anymore but a common edge. This new structure gives rise to crown of  $\text{FeO}_6$  octahedra in the hexagonal tunnels. The trigonal tunnels containing the  $\text{AsO}_4$  units keep the “up” orientation, but the two associated structure (A vs. B) refined in the same unit cell have inversed orientations.

- **Phase B:** On the other hand, the structure B has the formula  $[\text{Fe}_{11.5}(\text{AsO}_4)_8\text{O}_6]^{3-}$  and is very similar to that of the pristine, although the dehydroxilation leads to very distorted  $\text{Fe}^{3+}\text{O}_6$  octahedra in place of regular  $\text{Fe}^{2+}\text{O}_5(\text{OH})$  ones. In this case face

shared dimers are conserved although very distorted. The main difference with respect to the pristine phase is the change of orientation of the trigonal tunnel, where  $AsO_4$  groups are oriented in a “down” orientation as we can see figure III.12 (c). In addition, Fe1b occupancy is refined to 10/12. It matches well the systematic metal-deficient character announced in similar framework, e.g [1, 10, 11] where the occupancy of M is 11/12<sup>th</sup>.

Interatomic distances of the two new structures show important differences with respect to the pristine compound and between them as well. Bond valence calculations on iron sites should be examined with precaution because we do not deal with exact lattice parameter in this disordered intergrowth. Fe-O interatomic distances as well as BVS for iron are presented in table III.4.

**Table III.4.** Fe-O distances and corresponding Bond Valence Sum ( $\Sigma s_{ij}$ ) values, calculated using parameters associated to  $Fe^{+2}$  from reference[8], for  $[Fe_{12}^{3+}Fe_{1.5}^{2+}(AsO_4)_8O_6]^{3+}$  and  $[Fe_{10}^{3+}Fe_{1.5}^{2+}(AsO_4)_8O_6]^{3-}$ .

Distance Fe-O (Å)				
$[Fe_{12}^{3+}Fe_{1.5}^{2+}(AsO_4)_8O_6]^{3+}$		$[Fe_{10}^{3+}Fe_{1.5}^{2+}(AsO_4)_8O_6]^{3-}$		
Fe1a-O1a	2.1141	Fe1b-O1b	2.0700	
Fe1a-O3a	2.0544	Fe1b-O3b	2.1246	
Fe1a-O4a	2.0949	Fe1b-O4b	1.7683	
Fe1a-O4a	2.0394	Fe1b-O4b	2.3966	
Fe1a-O5a	2.2017	Fe1b-O5b	1.8247	
Fe1a-O5a	2.0137	Fe1b-O5b	2.2431	
$\Sigma s_{ij}$	<b>2.35</b>	$\Sigma s_{ij}$	<b>2.86</b>	
Fe2a-O2a	1.8705 x 3	Fe2b-O2b	2.0689 x 3	
Fe2a-O2a	2.5575 x 3	Fe2b-O2b	2.0820 x 3	
$\Sigma s_{ij}$	<b>2.38</b>	$\Sigma s_{ij}$	<b>2.39</b>	

## 1.4. Conclusion.

Here, we have presented the structure of a new “open framework” phase, related to previous phosphites or selenites structures, but with considerable differences due to the substitution of  $HPO_3^{2-}$  or  $SeO_3^{2-}$  by  $AsO_4^{3-}$ . It leads to  $Fe^{2+}$  occupied channels rather than empty ones in the phosphite case, and the obtained face-sharing of  $FeO_6$  octahedra is original, to the best of our knowledge.

This phase, containing mainly  $Fe^{2+}$  ions (11.5  $Fe^{2+}$  vs. 2  $Fe^{3+}$  per unit cell), presents a structural transformation never reported before. The pristine structure transforms a composite network made by two different charged phases  $A^{n+}$  and  $B^{n-}$  imbricated at the atomic scale. It is

striking that the crystal refinement using a mixture of two phases did not converge. The periodicity of each A and B sub-phases is preserved along c, due to strong cation-ion interactions but alternate in the (a,b) plane, which suggest the  $\text{AsO}_4$  groups form the anti-phase boundaries. The transformation involves the dehydroxilation of the parent compounds, and a partial Fe-exsolution. It results in an oxidation process where only  $\text{Fe}^{2+}$  columns are preserved as templating units in both sub-phases. To our knowledge this observation is unique since it involves charged lattices that balance their charge by an intimate mixing. *In fine* we show here the existence of charged crystal structures, for the first time. Once more, we recall that we are not dealing here with standard composite between large domains but rather a very disordered mixture in the (a,b) plane between thin bands. However the c-lattice being preserved one should admit that both structural domains A and B extend at long range along the hexagonal axis.

### 2. Solid Synthesis of $\alpha\text{-BaFe}_2(\text{PO}_4)_2$ .

In the chapter II 2.3, I mentioned the synthesis of a new  $\text{BaFe}_2(\text{PO}_4)_2$  polytype and the solid state reaction was discussed because it seems a possible step to rhombohedral  $\text{BaFe}_2(\text{PO}_4)_2$  without solvothermal treatment. In this section I will present the preliminary structural and magnetic characterization of this trigonal phase.

#### 2.1. Powder synthesis.

The chemical route used to obtain this new phase has already been used to synthesize similar compounds as  $\text{SrFe}_2(\text{PO}_4)_2$ . [12] To perform such a reaction  $\text{Fe}(\text{PO}_4)_3$  and  $\text{Ba}_3(\text{PO}_4)_2$  precursors were synthesized using stoichiometric mixtures of  $\text{BaCO}_3$  (Aldrich, 99.00%),  $\text{NH}_4\text{H}_2\text{PO}_4$  (Alfa Caesar, 98.00%), and  $\text{Fe}_2\text{O}_3$  (Aldrich, 99.00%) in a solid state reaction at 1273 K for 100 h with intermediate grindings.

Then, stoichiometric amounts of Fe,  $\text{Fe}(\text{PO}_4)$  and  $\text{Ba}_3(\text{PO}_4)_2$  were weighted according to the reaction:  $2\text{Fe}^0 + 4\text{Fe}^{3+}(\text{PO}_4) + \text{Ba}_3(\text{PO}_4)_2 \rightarrow 3\text{BaFe}^{2+}_2(\text{PO}_4)_2$ , grinded and heated at  $910^\circ\text{C}$  for 10 days under argon atmosphere, in order to stabilize and avoid the oxidation of  $\text{Fe}^{2+}$  created during the redox reaction between  $\text{Fe}^0$  and  $\text{Fe}^{3+}$ . In a last stage, an annealing under vacuum at  $910^\circ\text{C}$  improved the preparation of a single phased material.

#### 2.2. Structural characterization.

Product obtained before the last vacuum annealing was characterized by powder XRD and suggests a nearly monophasic pattern. It allows us to determine the unit cell and to propose the symmetry of the phase. In order to resolve the structure we took the opportunity to send a sample to 11-BM synchrotron facilities.

High quality data were obtained from 11-BM synchrotron. However, this data showed a non negligible amount of additional phases, well crystalline but in weak amount. It corresponds to undetermined phases, not clearly observed using the laboratory XRD patterns. These impurities, showed on figure III.13, overlap with the main reflections intensities which lead to difficulties during the Rietveld refinement. As mentioned above, impurities could be removed after reheat a prepared pellet of the sample in a sealed tube at 910 °C for another 72h, as used for magnetic measurements.

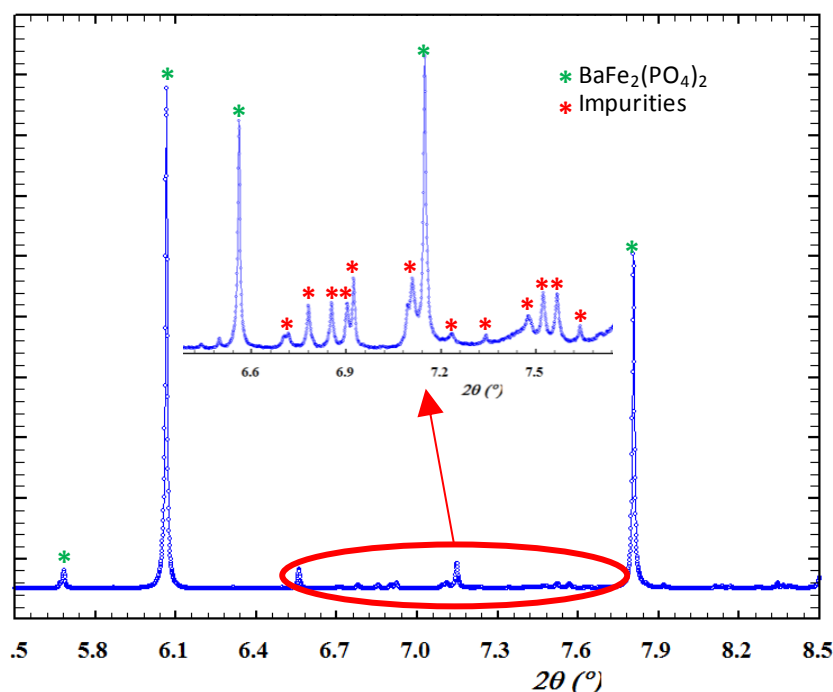


**Figure III.13.** Impurities observed on the synchrotron-XRD pattern.

The experimental pattern is rather similar to one of the known  $\alpha$ -BaCo<sub>2</sub>(PO<sub>4</sub>)<sub>2</sub> polymorphs (monoclinic, P21/a,  $a = 9.211(3)$  Å,  $b = 5.004(2)$  Å,  $c = 8.085(3)$ ,  $\beta = 92.737(1)^\circ$ ).<sup>[2]</sup> However in the  $\alpha$ -BaFe<sub>2</sub>(PO<sub>4</sub>)<sub>2</sub> case, all the diffracted intensities could be indexed in a trigonal unit cell with parameters  $a = 5.110(8)$  Å,  $c = 25.108(9)$  Å. In fact the two phases are very similar but the iron form is even more distorted and contains three layers by unit cell instead of one for the cobalt phase. This aspect will be detailed below. Observed and calculated diffractometers after Rietveld refinement are presented figure III.14.

After simulating the profile using the “Le Bail” method a structural model, based on the cobalt polytype was proposed. The Rietveld refinement of the structural model led to  $\chi^2 = 13.6$ ,  $R_{\text{exp}} = 5.87$  and  $R_w = 21.6$ . These values are much higher than expected for a correct solution; unfortunately, the impurities make much harder a correct resolution. In order to minimize their effect, the main impurities peaks between  $2\theta = 6.5-9$  were pointed as background points. Even though, the solution proposed match well with the hypothesis realized, and we can consider as correct the structured designed.

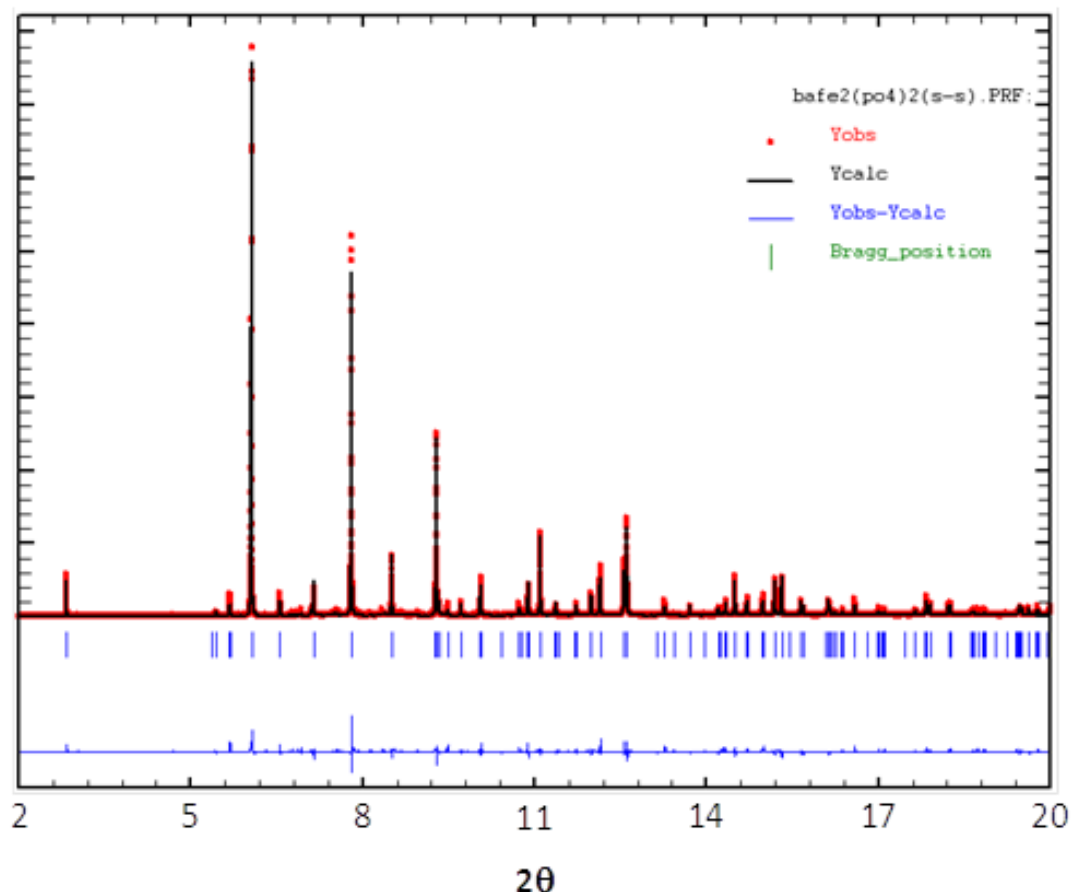


**Figure III.14.** Rietveld refinement of  $\text{BaFe}_2(\text{PO}_4)_2$ .

The structure, which is shown in figure III.15, can be defined as infinite  $\text{FePO}_4$  layers with  $\text{Ba}^{2+}$  placed between them. The shortest distance between two Fe from adjacent layers is of 6.32 Å. The layers are made by zigzag chains of distorted iron triangular bipyramids connected between them by a corner. The shared corner corresponds to oxygen (O1) which is part of an equatorial bipyramid and of the apical apex of the next one. The chains of  $[\text{FeO}_5]$  and  $[\text{PO}_4]$  are interconnected in a complex manner. Every iron bipyramid share an edge (O1 and O4) with a phosphate group; two others oxygens (O2 and O3) with another two different

phosphates group and the last oxygen is shared by a phosphate and another iron bipyramid, every O1 is attached to two iron bipyramid and one phosphate group..

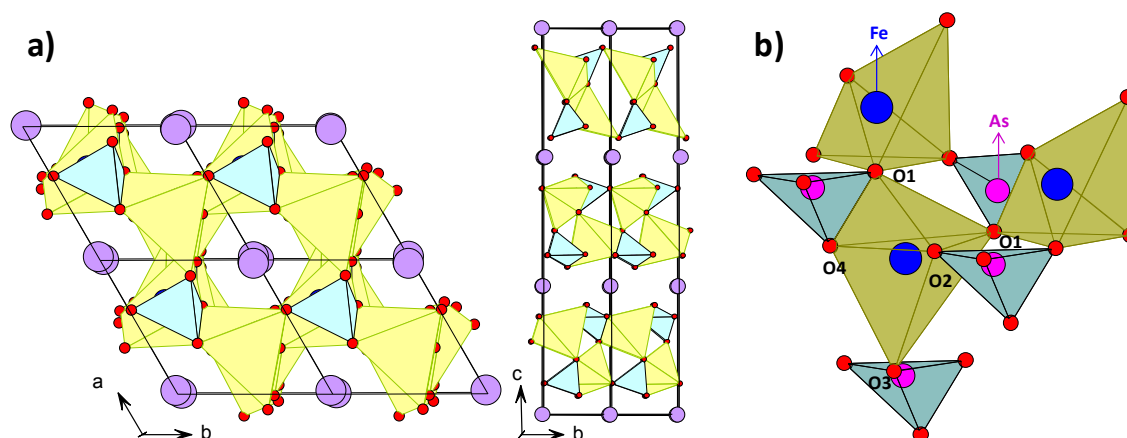


**Figure III.15.** *c-b and a-b projections of  $BaFe_2(PO_4)_2$  unit cell (a), interatomic connection of iron bipyramid (b).*

Table III. 5 presents the different interatomic distances Fe – O and As – O, It shows different irregularities in the coordinate polyhedrons. Atomic coordinates and displacements are presented in the annex.

**Table III.5.** *Interatomic distances Fe-O and As-O for trigonal  $BaFe_2(PO_4)_2$ .*

Interatomic distances (Å)							
BaFe <sub>2</sub> (PO <sub>4</sub> ) <sub>2</sub>							
Fe ions				P ions			
Fe-O1	2.039(2)	Fe-O2	2.566(9)	P-O1	1.550(9)	P-O3	1.551(9)
Fe-O1	2.524(4)	Fe-O3	2.016(8)	P-O2	1.547(5)	P-O4	1.553(5)
	Fe-O2	1.819(8)					

### 2.3. Magnetic characterization.

The magnetic properties have been measured on a sample obtained after annealing under vacuum the powder. From XRD this compound appears as a single phase. However, the susceptibility and magnetization plots suggest important contamination, a major problem dealing with high temperature Fe-based phases. The figure III.16 shows preliminary  $\chi(T)$ ,  $\chi^{-1}(T)$  and  $M(H)$ . It shows an AFM compound with appearing of a net magnetic moment at

15K. The remanent moment is around  $0.15 \mu_B/\text{FU}$  at 5K. At least this is probably characteristic of the main phase. However, looking at the paramagnetic regime it reveals a very erratic behavior with two different behaviors above and below 250K. None of them give the expected effective moment for  $\text{Fe}^{2+}$ , i.e.  $4.89 \mu_B/\text{Fe}^{2+}$ , which suggest contamination. For reason of time we have not been able to pursue this study further.

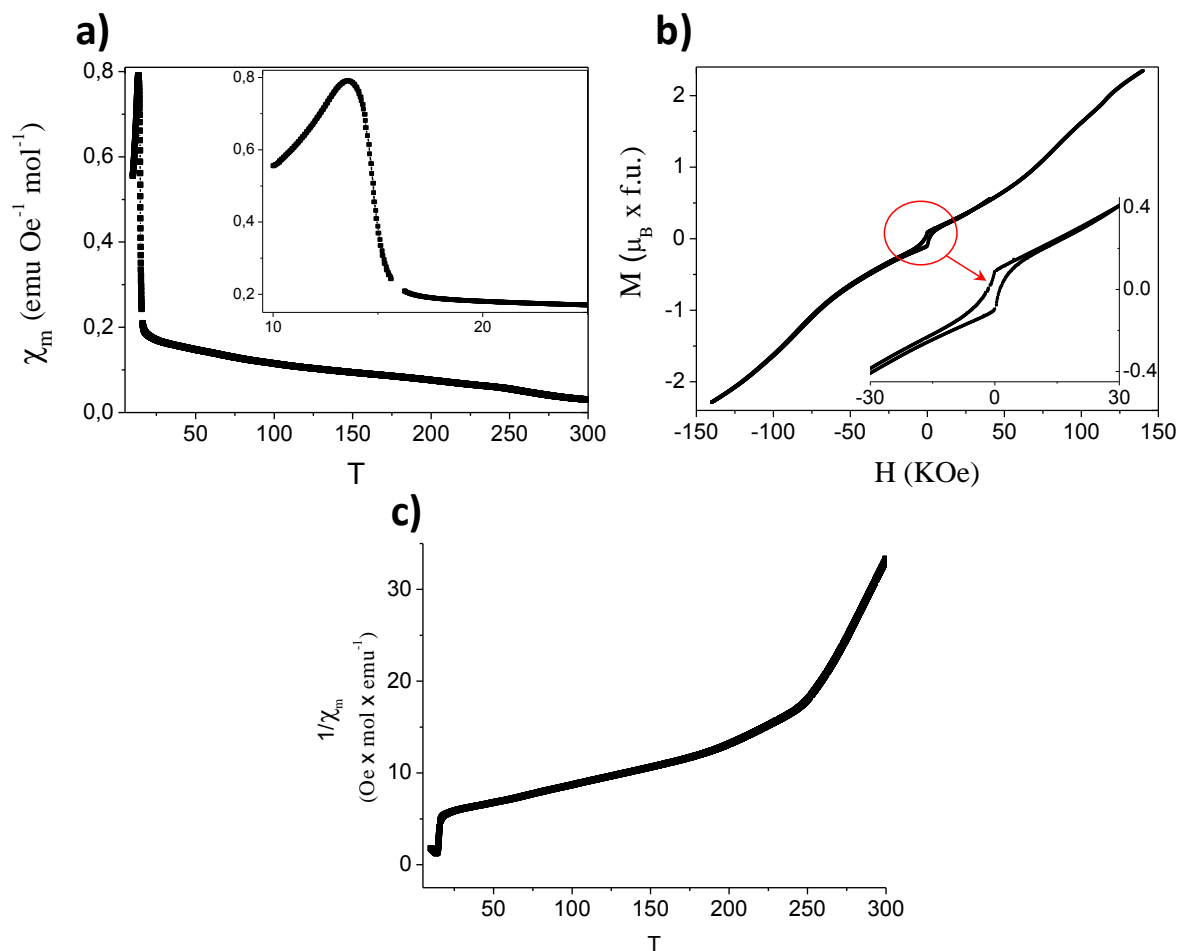


**Figure III.16.** Magnetic measurements of  $a\text{-BaFe}_2(\text{PO}_4)_2$

### 3. $\text{RbFe}(\text{AsO}_4)(\text{OH})$ .

To conclude this last chapter, I present here below the structure of the new compound  $\text{RbFeAsO}_4(\text{OH})$ . This compound was prepared in the frame of our search for new layered phases inspired by those obtained using a large counter cation such as  $\text{Ba}^{2+}$  ( $r=1.35 \text{ \AA}$ ) which likely template low-D magnetic topologies. Here we have tested several preparations dealing with  $\text{Rb}^+$  alkali ions ( $r=1.67 \text{ \AA}$ ). Although very far from the topochemical routes highlighted

during my work, this short section is dedicated to the preliminary work (synthesis and the single crystal X-ray diffraction) of this new compound with an original crystal structure. The hydrogen atom was located on Fourier difference maps and refined. The refined O2-H bond length is 0.83Å.

### 3.1. Synthesis

Stoichiometric amount of  $\text{As}_2\text{O}_5$ ,  $\text{Rb}_2\text{CO}_3$  and metal iron were mixed in 6 ml of water and introduced in a 25 ml Teflon autoclave vessel. The mixture was placed in an oven and heated following the thermal treatment described in figure III.17.

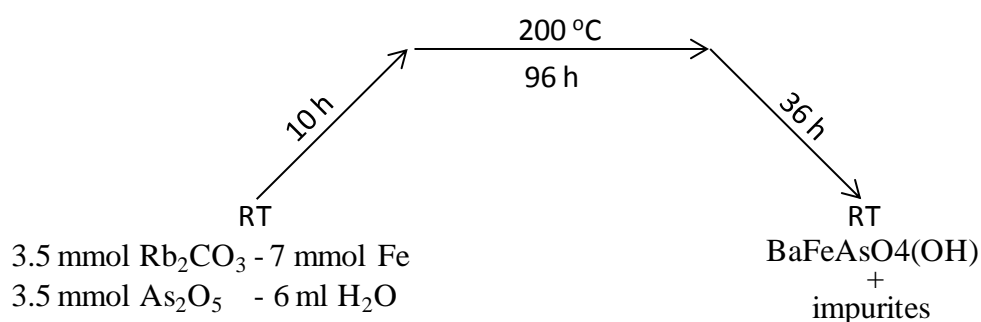


**Figure III.17.** Thermal treatment followed for  $\text{RbFeAsO}_4(\text{OH})$  synthesis.

After reaction, the obtained product was filtered and washed several times in deionized water and ethanol.  $\text{RbFeAsO}_4(\text{OH})$  crystals was found as the main phase with some others impurities such as metal iron.

$\text{RbFeAsO}_4(\text{OH})$  crystals are hexagonal transparent platelets with hexagonal-like faces. One single crystal was separated and mounted on a glass fiber to be collected.

### 3.2. Structure determination.

Crystal data collection together with atomic coordinates and displacements are presented in the annex. Diffraction data led to an orthorhombic (space group  $\text{Fdd2}$ ) unit cell with parameters of  $a = 9.804(5)\text{ \AA}$ ,  $b = 32.07(4)\text{ \AA}$ ,  $c = 5.659(9)\text{ \AA}$  and with a final  $R_{\text{obs}}/R_{\text{all}}$  5.11/8.31 %. We note here the necessity to use a twinning low related to 3-fold axis between adjacent domains in the (a,c) plane due to the geometrical relation  $\sqrt{3} \cdot c \sim a$ .

The structure of this new compound is presented in figure III.18 and the different Fe-O and As-O interatomic distances are presented in table III.6.

**Table III.6.** Interatomic distances in  $RbFeAsO_4(OH)$ .

Interatomic distances (Å)							
RbFe(AsO <sub>4</sub> )(OH)							
Fe ions				As ions			
Fe-O1	1.934(7)	Fe-O3	2.059(6)	As-O1	1.673(5)	As-O4	1.664(0)
Fe-O2H	2.012(5)	Fe-O4	2.083(7)	As-O3	1.715(8)	As-O5	1.698(2)
Fe-O2H	2.000(5)	Fe-O5	2.048(1)				

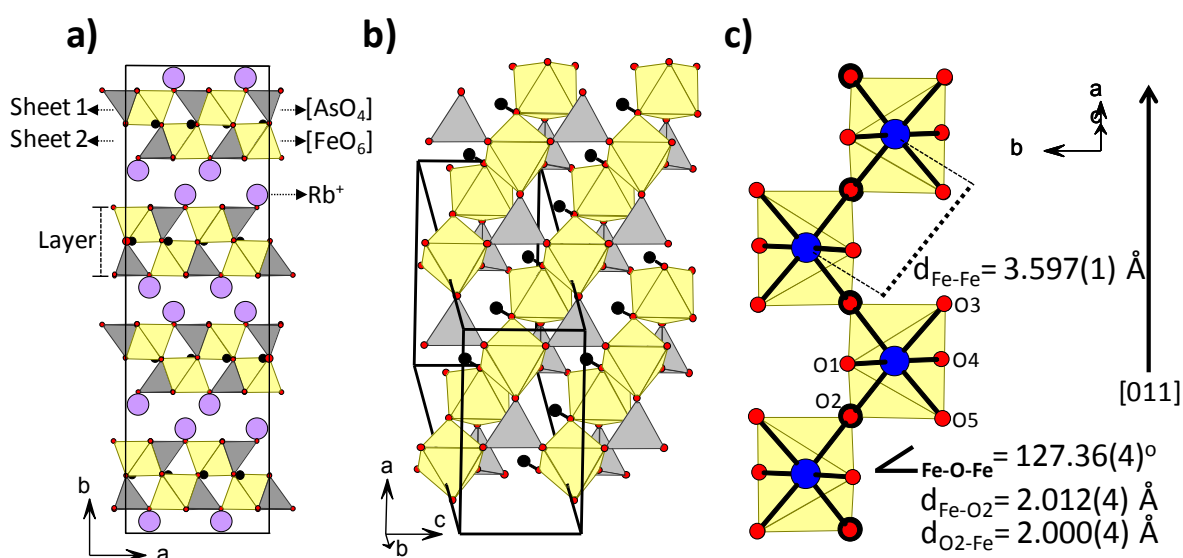


**Figure III.18.** *b-a* and projections of the  $RbFeAsO_4(OH)$  unit cell (a),  $[AsO_4]$  tetrahedrons (grey) connect the iron  $[FeO_6]$  chains (b) and  $[FeO_6]$  octahedrons chains along  $[011]$  (c).

$RbFeAsO_4(OH)$  is made of the stacking of  $[Fe(AsO_4)(OH)]^-$  layers with a double layer of  $Rb^+$  cations placed between them. The  $[Fe(AsO_4)(OH)]^-$  layers are made by double sheets of  $[FeO_6]$  octahedron and  $[AsO_4]$  tetrahedron connected by corners. Both octahedra and tetrahedra share all their corners.

Arsenates tetrahedra have an  $O_3$  basis forming the edge of the double-layers while the fourth As-O bonds are pointing inside the sheets through  $[010]$  direction. A schematic representation of  $[AsO_4]$  connections is presented in figure III.19 (a).

The iron octahedra form infinite zigzag chains, with a “double sheet” thickness, growing along  $[011]$  direction (figure III.18 c). The common corner O2 is the hydroxide

group, leading to a BVS on the OH of 2.0, when considering two Fe and one H in its coordination sphere.

These chains are connected between them by the arsenate tetrahedrons. As shown in figure III.19 (b), every  $\text{FeO}_4(\text{OH})_2$  octahedron share four oxygens with four  $[\text{AsO}_4]$  tetrahedra, and two OH groups with two octahedral of the chains.

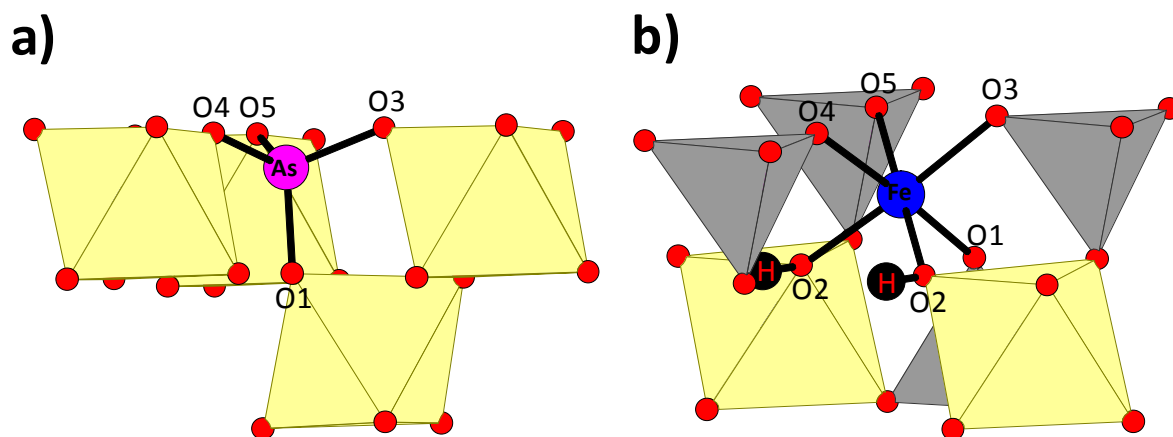


**Figure III.19.** Arsenate tetrahedron (a) and iron octahedron (b) connectivity.

Oxygen BVS calculations are presented in table III.7. Before adding the proton in the structure O2 BVS showed an unusual valence value of  $\approx 1$ . This proton was placed in a residual intensity peak next to the O2 with  $d_{\text{O-H}} = 0.82(0)$  Å.

**Table III.7.** Bond Valence Sum ( $\sum s_{ij}$ ) values, calculated using parameters associated to,  $\text{Rb}^+$ ,  $\text{Fe}^{2+}$ ,  $\text{As}^{5+}$  and  $\text{O}^{2-}$  from reference[8], for  $\text{RbFeAsO}_4(\text{OH})$ .

BVS					
<b>Rb</b>	1.1(9)	<b>O1</b>	2.3(8)	<b>O4</b>	2.1(7)
<b>Fe</b>	3.0(1)	<b>O2</b>	2.0(0)	<b>H</b>	0.8(7)
<b>As</b>	5.0(5)	<b>O3</b>	2.0(2)		

According to our research this structure topology is inedited so far. Efforts are now furnished to obtain this compound in large and single-phase amount.

### Bibliography.

- [1] M.D. Marcos, P. Amoros, A. Beltranporter, R. Martinezmanez, J.P. Attfield, *Chemistry of Materials* **5** (1993) (1) 121.
- [2] R. David, H. Kabbour, A. Pautrat, O. Mentre, *Inorganic Chemistry* **52** (2013) (15) 8732.

- [3] G. Adiwidjaja, K. Friese, K.H. Klaska, P.B. Moore, J. Schluter, *Zeitschrift Fur Kristallographie* **215** (2000) (2) 96.
- [4] S.B. Wiggin, R.W. Hughes, D.J. Price, M.T. Weller, *Dalton Transactions* (2007) (27) 2935.
- [5] M. Poiénar, A. Maignan, P. Sfirloaga, S. Malo, R. Vlazan, A. Guesdon, F. Laine, J. Rouquette, C. Martin, *Solid State Sciences* **39** (2015) 92.
- [6] P. Amoros, M.D. Marcos, M. Roca, A. BeltranPorter, D. BeltranPorter, *Journal of Solid State Chemistry* **126** (1996) (2) 169.
- [7] J.A.J. Basten, Q.A.G. Vanvlimmeren, W.J.M. Dejonge, *Physical Review B* **18** (1978) (5) 2179.
- [8] N.E. Brese, M. Okeeffe, *Acta Crystallographica Section B-Structural Science* **47** (1991) 192.
- [9] R. David, H. Kabbour, P. Bordet, D. Pelloquin, O. Leynaud, M. Trentesaux, O. Mentre, *Journal of Materials Chemistry C* **2** (2014) (44) 9457.
- [10] M.P. Attfield, R.E. Morris, A.K. Cheetham, *Acta Crystallographica Section C-Crystal Structure Communications* **50** (1994) 981.
- [11] M.D. Marcos, P. Amoros, A. Lebail, *Journal of Solid State Chemistry* **107** (1993) (1) 250.
- [12] A.A. Belik, M. Azuma, M. Takano, B.I. Lazoryak, *Chemistry of Materials* **16** (2004) (22) 4311.

General conclusion.

## General conclusion.

---

Throughout my PhD, I carried out expansive research concerning several examples of topotactic transformations, with the aim to implement and understand the mechanisms by which these structural modifications are produced, using either crystallography either characterization of nano-objects. This work, especially dealing with the exfoliation and exsolution tasks, was the first of this kind in the solid state chemistry group, which may be the reason while in some cases the study remain at their preliminary stages. At least, it is clear that our understanding of topochemical reactions opens doors to the creation or texturation of new materials synthesized by rational design. One major idea is that these kinds of transformations, performed generally by “soft” chemistry methods or at moderate temperature, lead to metastable phases which cannot be synthesized by classic high temperature routes.

During these three years I have developed my research around three main lines of thought. The first is devoted to the exfoliation of a new family of positive oxide 2D nanoflakes. The second focuses on cationic mobility and exsolution in crystalline compounds with interesting magnetic or electrochemical properties. Finally as a standard in my research group, I also spend time trying to elaborate new crystalline phases, an important mission, although not directly related to the topochemical context.

This work has enabled me to enter more deeply into the knowledge of scientific domains as crystallography, spectroscopic techniques or into different physical properties as electrochemical or magnetic behaviors.

With respect to the first research subject, the exfoliation of oxides, presented in the first chapter of this manuscript, we can consider this work mainly as a success.

The bromo-cobaltites targeted for exsolution are built on covalent blocks, with strong disorder in the  $[\text{Ba}_2\text{O}_2\text{Br}]$  interlayer. It suggests a facile separation between the elementary blocks through the chemical removal of this layer in a first approach. The anionic exchange in these layers has been demonstrated and these compounds thus became good candidates for exfoliation and creation of bidimensional elementary oxides blocks. They could potentially be used for the achievement of new structures by recombination. We have been able to structurally characterize the so-obtained 2D nanoparticles (width $\gg$ thickness) from the initial  $15\text{H-Ba}_7\text{Co}_6\text{BrO}_{17}$ . These particles show a width/thickness ratio  $>10$ , and a slight positive charge on their surface. This makes these, the first positive nanoblocks obtained by exfoliation process which do not belong to double-hydroxide or earth-rare hydroxide families, the only compounds allowing the formation of positive oxide nanosheets so far.

## General conclusion.

---

However, it was not possible to obtain single “oxide sub-units blocks”. As AFM measurements showed, in the best cases, the thickness of the “flakes” corresponded to the assembly of 5-6 elementary cobaltite blocks. This problem might be due to i) the strongest than expected bonding between the blocks and the interleaves ii) the elementary block structure itself, which is composed of columnar trimers or tetramers of face-sharing  $[\text{Co}^{3+}\text{O}_6]$  octahedrons only linked by terminal  $[\text{Co}^{4+}\text{O}_4]$  tetrahedral and  $\text{Ba}^{2+}$  counter ions. These blocks are much less compact than double hydroxide layered blocks and the small number of connections between the columns makes them more fragile. At a critical size, the created constraints could mechanically collapse the phase, preventing a complete exfoliation. Several interlayers may be required in order to be mechanically rigidified and stabilized. The second problem was related with the heterogeneity of the sample. An improvement in the centrifugation process of the suspension would be required to be able to select same sized particles and thus be able to evaluate more precisely the size effect on the physical properties evolution. Despite these two problems, exfoliated particles with a thickness of 10 nm and a width of 100-200 nm are obtained, and the full preservation of the structure was studied and proved by “in plane” XRD and DANES experiments. This dramatic reduction in particle size, compared to polycrystalline samples, will certainly affect their physical properties.

The magnetic characterization of these “nanoflakes” is in progress, but the complexity of their manipulation in colloids makes it difficult to obtain accurate measurements.

The use of the restacked 2D oxides is also envisaged as catalyst in total oxidation reaction. Recombination of mixed oxide nanosheets are also in progress and the first experiences of oxide recombination by flocculation between our exfoliated positives nanocobaltites and negative  $[\text{Ca}_2\text{Nb}_3\text{O}_{10}]^-$  nanosheets has been performed. However, the main problem encountered during the recombination process was the miscibility between the suspensions containing the different types of nanoparticles, the cobalt nanosheets was in butanol, while negative sheet are generally in aqueous solution. These results open the door to synthesis of new hierarchical materials made of different brick assembly.

The second main line of research conducted during this doctorat, as described in chapter II and part of chapter III, concerns cationic mobility in bidimensional iron barium phosphate phases,  $\text{BaFe}_2(\text{PO}_4)_2$ , where  $\text{Fe}^{2+}$  was proven to be a mobile species at moderate temperatures, by an iron exsolution and oxidation process. This mobility

## General conclusion.

---

creates different iron/vacancy combinations in the layers and the formation of  $\alpha$ -Fe<sub>2</sub>O<sub>3</sub> nanoparticles on the crystals surface. For this investigation, an in-depth study on the comprehension of the Fe<sup>2+</sup> migration in BaFe<sub>2</sub>(PO<sub>4</sub>)<sub>2</sub> was conducted. A careful crystallographic examination of different intermediate phases BaFe<sub>2-x</sub>(PO<sub>4</sub>)<sub>2</sub> (x= 2/7, 1/3, 1/2) was performed and a logic of the exsolution pathways was established and detailed, including information on forbidden situations and the prediction of other possible ordered structures. This logic sets a strong correlation between the different ordered structures and the iron content in the layers.

The exsolution reaction vanishes when all the Fe<sup>2+</sup> ions of the structure are oxidized into Fe<sup>3+</sup>. Here, I present the new compound BaFe<sup>3+</sup><sub>1.33</sub>(PO<sub>4</sub>)<sub>2</sub>, containing only Fe<sup>3+</sup> and never obtained before by classical syntheses. This compound presents a strongly depleted network, which makes it a good candidate for further cationic intercalation carried out by chemical or electrochemical methods. Furthermore, preliminary studies were carried out in order to insert lithium ions in the structure.

The Li<sup>+</sup> insertion was achieved in BaFe<sub>1.33</sub>(PO<sub>4</sub>)<sub>2</sub> by solid state reaction with lithium carbonate at 550 °C and under a reductive atmosphere (Ar/H<sub>2</sub>(3%)). The same compound, also used as a cathode in a Li battery, presents a cyclability of about 0.15 Li<sup>+</sup>/formula.

The heterogeneous composition of the chemical preparation and the low performance of the charge/discharge cycle versus Li were the main problems found during these experiments. Both can be justified by the difficulties encountered during the limited removal of the coating Fe<sub>2</sub>O<sub>3</sub> nanoparticles. Long time sonication seems insufficient to eliminate all the nanoparticles exsolved because of their small size and their high interaction with the crystal surface. This residue hampers the cationic mobility and limits the intercalation reaction.

Nevertheless, the reversibility of the iron exsolution observed under reductive conditions is greatly interesting and further research is envisaged with the objective to create a new generation of energy storing batteries with mobile Fe-ions.

Solid solutions of BaFe<sub>2-y</sub>M<sub>y</sub>(PO<sub>4</sub>)<sub>2</sub> with Co<sup>2+</sup> and Ni<sup>2+</sup> have also been studied. In these compounds, selective iron exsolution has been demonstrated as well as how the substitution ratio of iron for the cobalt or nickel influences the Fe<sub>2</sub>O<sub>3</sub> nanoparticles' size by hampering the iron exsolution. Finally, in the last chapter, I have summarized some of the new interesting Fe<sup>2/3+</sup> structures of compounds synthesized during my work. Brief

## General conclusion.

---

structure determination of  $\text{RbFe}(\text{AsO}_4)(\text{OH})$ ,  $\text{Fe}_{13.5}(\text{AsO}_4)_8(\text{OH})_6$  or of the new  $\alpha$ - $\text{BaFe}_2(\text{PO}_4)_2$  polytype is described.

Special attention is paid to the surprising crystallographic features showed by the  $\text{Fe}_{13.5}(\text{AsO}_4)_8(\text{OH})_6$  after heating. In an unprecedented way, this new “open network” phase with a mixed  $\text{Fe}^{2/3+}$  valence suffers a structure transformation which leads to a composite network of two different charged structures,  $\text{A}^{n+}$  and  $\text{B}^{n-}$  (similar symmetry and cell lattice), imbricated at the atomic scale. To my knowledge, this comportment has never been seen before. At this point, the crystallography implies the refinement of two structures in one unique cells, due to the imbrication of nanosized domains at the atomic scale.

In conclusion, this manuscript presents a review of different topochemical reactions, where, by structural transformations I have obtained new metastable materials with unique properties. They can also act as a step within more complex transformations conducted by hierarchical process, leading to the achievement of new materials with pre-established properties.

# **ANNEXES.**

# ANNEX 1.

## Characterization techniques.

The aim of this work is to find and understand different structural transformations of the studied compounds, to establish relations between these changes and the modifications of physical properties such as magnetism. To carry on this research, I have used several characterization techniques.

In this annex I will do a brief review of the techniques I have used and which I consider to be the most important for my research work.

For all compounds presented in this manuscript, powder x-ray diffraction has been performed as routine, to follow the different structural changes during the transformation processes, but also as a powerful technique to determine compound's structure with the synchrotron radiation. In the same way, single crystal x-ray diffraction has been used to solve most of the new structures presented in this manuscript.

A special mention is also required for the x-ray absorption techniques that we have used during two visits to the SOLEIL synchrotron facilities and which have been very useful in this work. They helped us to go beyond in our phases's characterization, giving information hard to obtain otherwise.

The third technique developed in this annex is the scanning electron microscopy (SEM), for which I have been formed as operator. It was used as routine technique after every chemical process performed, to observe morphological changes in our samples. In addition, the SEM apparatus is provided with an energy dispersive x-ray detector, allowing to perform energy dispersive x-ray analysis for chemical determination. It will also briefly described.

### 1. X-ray diffraction (XRD).

#### 1.1. Fundamental principles of XRD.

X-ray diffraction principles are based on the interaction of a monochromatic x-ray beam with a wavelength  $\lambda$ , and crystalline matter. Max von Laue, in 1912, discovered

that crystalline substances act as three-dimensional diffraction gratings for X-ray wavelengths, similar to the spacing of planes in a crystal lattice. The result consists of constructive interference of monochromatic X-rays,[1] leading to coherent scattering radiations of same wavelength in defined space directions, characteristic of the crystallographic structure of the compound.

The X-rays are collimated and directed onto the sample. When the geometry of the incident X-rays impinging the sample satisfies the Bragg Equation ( $n\lambda=2d\sin\theta$ ), constructive interference occurs. A detector collects and processes this X-ray signal and converts it to a count rate which is then output to a device such as a printer or computer monitor.

There are two different diffraction techniques, depending of the kind of sample used:

- *Single crystal diffraction*: This technique provides very accurate measures of the diffracted intensities during the data collection by experimental control of the crystal orientation. The excellent spatial resolution of the reflections makes of this technique the most used for determination of crystal structure of new compounds.
- *Powder diffraction*: This technique is mainly used for crystalline phase's identification, even if it can be an alternative to do structural refinements in absence of single crystals. The main drawback of this technique is the mono dimensional representation of the three-dimensional reciprocal space. This approach supposes information lost with respect to the previous technique. The consequence of this information missing will be a considerable overlapping of reflections in low symmetry or big unit cell cases; which make much harder or even impossible to extract the intensity factors needed to solve the structure.

### **1.2. Single crystal XRD.**

Single crystal diffraction measurements for all the samples of this manuscript were performed using an APEX DUO (Brüker-AXS) single crystal diffractometer (figure 1). It combines molybdenum and copper X-ray sources with a highly accurate 4-axis KAPPA goniometer and is equipped with a bi-dimensional CCD-4K detector.

## Annexes.

---

These circles refer to the four angles ( $2\theta$ ,  $\chi$ ,  $\varphi$ , and  $\Omega$ ) that define the geometrical relationship between the crystal lattice, the incident ray and the detector positions.

In my case, intensities were collected using the molybdenum source ( $\lambda = 0.71073\text{\AA}$ ) which is the most used wavelength in single crystal diffraction. The molybdenum  $K_{\alpha}$  radiation was isolated thanks to a graphite monochromator.

The most suitable crystal is selected from the sample using a needle and washed from powder and small crystals stuck on the surface using special grease. The crystal is stuck on the extremity of a thin glass fiber and fixed on the goniometer head in order to know the orientation crystal in all the space directions and also to allow the crystal to be focused under the x-ray beam during the entire collection.

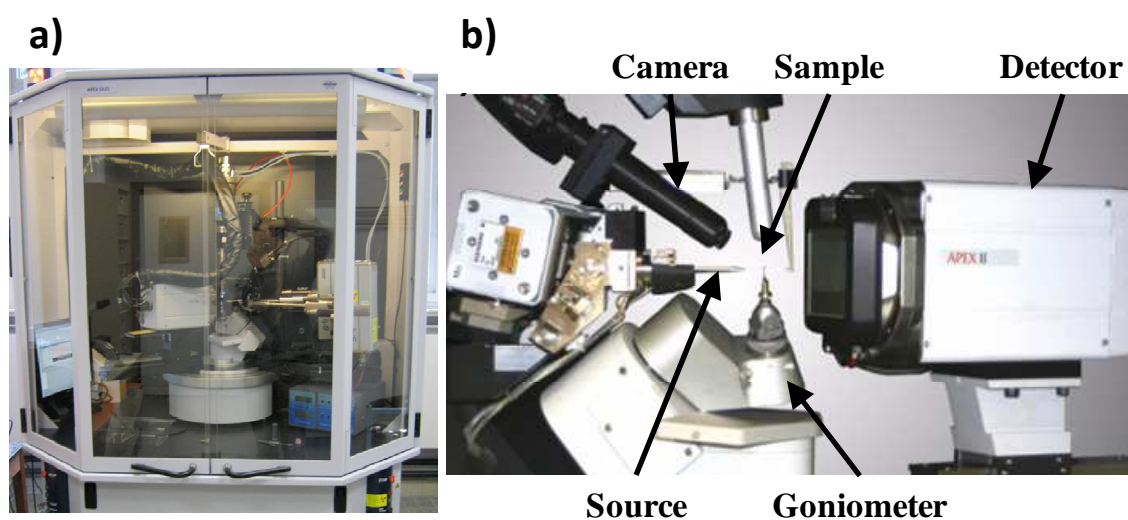


**Figure 1.:** a) Picture of an APEX DUO (Bruker-AXS) single crystal diffractometer and b) Zoom from the inside of the chamber.

On a first step, a quick test is performed with a collection of 30 diffraction images, by scanning along  $\Omega$  angle (rotation along an axis perpendicular to the beam), with a time counting of 20 s per image. This test allows finding unit cell parameters and its corresponding symmetry (Laue group). This information will be used to determine the strategy of data collection, taking in account different parameters (distance detector, time per image, redundancy...). The collected intensities obtained correspond to a scanning of the reciprocal sphere in order to harvest all the reflections with an intensity  $I \geq 3\sigma(I)$  needed to resolve the structure.

## Annexes.

---

The structural determination of the single crystal consists of attributing the electron density distribution to the atoms positions in the unit cell from the collected data.

Intensities diffracted by the different atomic planes are measured for all the lattice family planes (written with Miller indices h, k, l) of the Ewald sphere depending on the symmetry of the crystal. Bragg's law is respected for each lattice plane (hkl) in diffraction position.

$$n\lambda_{Mo} = 2 d_{hkl} \sin(\theta)$$

Here,  $n$  is an integer number,  $\lambda$  corresponds to the wavelength of the Mo source,  $d_{hkl}$  to the space between the diffracted planes and  $\theta$  to the incident angle.

Once all intensities of the corresponding unit cell have been collected we can start with the structural determination.

The diffracted beam is characterized by its amplitude which is a vectorial size:  $\vec{F}_{hkl}$ . The relation between the  $F_{hkl}$  module, called structure factor, and the atomic positions is given by the following equation:

$$F_{hkl} = \sum_{j=1}^N f_j \exp(2\pi i(hx_j + ky_j + lz_j))$$

Where  $N$  represents the number of atoms in a unit cell,  $f_j$  corresponds to the atomic form factor of the atom "j", and  $x_j, y_j, z_j$  are the atomic coordinates of the atom "j".

The electron density at each point (x,y,z) is proportional to the Fourier transform of the structure factor. It is defined in terms of a Fourier series:

$$\rho(xyz) = \frac{1}{v_0} \sum_k \sum_l F(kl) \exp[-2\pi i(x + yl + zl) - \Phi(kl)]$$

Where  $v_0$  is the volume of unit cell.

The density of electrons allows finding the atom positions: the atomic positions correspond to the maxima of electronic density. The experimental measurements give access to the intensities of the diffracted beams which are proportional to the square of the structure factor.

$$I_{hkl} \approx k |F_{hkl}|^2$$

## Annexes.

---

These collected intensities are extracted and corrected from Lorentz-polarization factor, linked to the experimental conditions, with the software SaintPlus 7.12 from Brüker.[2] In addition, absorption corrections linked to the geometry of the crystal, and therefore to the structural model, are done with the software SADABS.[3]

At this point, space group is determined by the symmetry extinction rules and will be confirmed by the structural resolution.

For this structural elucidation, we used the “charge flipping” method.[4] This ab initio method was implemented in the software “Superflip”.[5] The aim of this method consists to find the good value of the phase ( $\Phi$ ). For that, the algorithm used makes an iteration process comparing successive Fourier coefficients structures factors (measured) with reconstructed electronic density functions from randomly phase values. It does an interpretation of calculated electronic density just from the magnitudes of the observed structure factors. Different parameters as the R factor, the total charge or the phase changes are used to reach the convergence. Once it converges, and density maps are reconstructed atoms can be placed and symmetry is deduced by analysis of these density maps.

After this, helped by the software Jana2006[6], we use the least squares method and try to get the best accord between the calculated and the observed model to include the lighter atom positions and the anisotropic atomic displacement parameters for heavy atoms. Finally, depending on the cases, additional parameters as isotropic extinction or site occupancy factor (SOF) can also be refined.

The refinement advancement is controlled by several parameters, especially by the reliability coefficient (R) which represents the average of relative error on structure factors.

$$R = \frac{\sum(|F_{calc}| - |F_{obs}|)}{\sum|F_{obs}|}$$

This parameters among others (GOF, wR,...) allow to judge the quality of the refinement, they should be as lower as possible.

### 1.3. Powder XRD.

During this work, laboratory XRD patterns have been used to carry out unit cell parameters refinement and phase identification, from the study of position and profile of the measured reflections.

For structural determination, powder samples data were collected on the Synchrotron 11-BM beamline at the Advanced Photon Source (APS, Argonne National Laboratory) with a wavelength of  $\lambda=0.4137\text{\AA}$ . This shorter wavelength of the synchrotron X-ray beam, compared to  $\text{CuK}_{\alpha 1}$  ( $\lambda_1=1.54056\text{\AA}$ ) of our diffractometer, provides greater structural information by enabling more observations over a wider Q-range (especially for smaller d-spacing, Q being the scattering vector), which is essential for correct pattern indexing. It also strongly reduces or eliminates fluorescence problems encountered for most of our samples which contain iron or cobalt atoms, this latest fluorescing when interact with the copper wavelength. Moreover, the higher energy radiation source reduces the sample absorption, which allows using the transmission geometry, even for compounds containing heavy elements, to avoid the preferential orientation problems frequent on reflection geometry instruments. All the characteristics and advantages of the Argonne Synchrotron diffractometer are resumed on the website page <http://11bm.xray.aps.anl.gov/faq.html>.

With respect to the X-ray laboratory instrumentation, the D8 Passeur from Bruker-AXS was used for room temperature measurements (figure 2). This device is equipped with a rapid linear Lynxeye detector and an auto sampler with 90 positions working in transmission as well as in reflection geometry, using  $\text{CuK}_{\alpha 1}$  ( $\lambda_1=1.54056\text{\AA}$ ) and  $\text{CuK}_{\alpha 2}$  ( $\lambda_2=1.54439\text{\AA}$ ) radiation with intensities  $I_{\lambda 1}/I_{\lambda 2} = 0.5$ . It enables a quick switch between the para-focusing Bragg-Brentano geometry to parallel beam geometry without realignment system. In the  $\theta/\theta$  configuration the sample holder is fixed whereas the X-ray tube and the detector turn around the sample with an angle  $\theta$ .

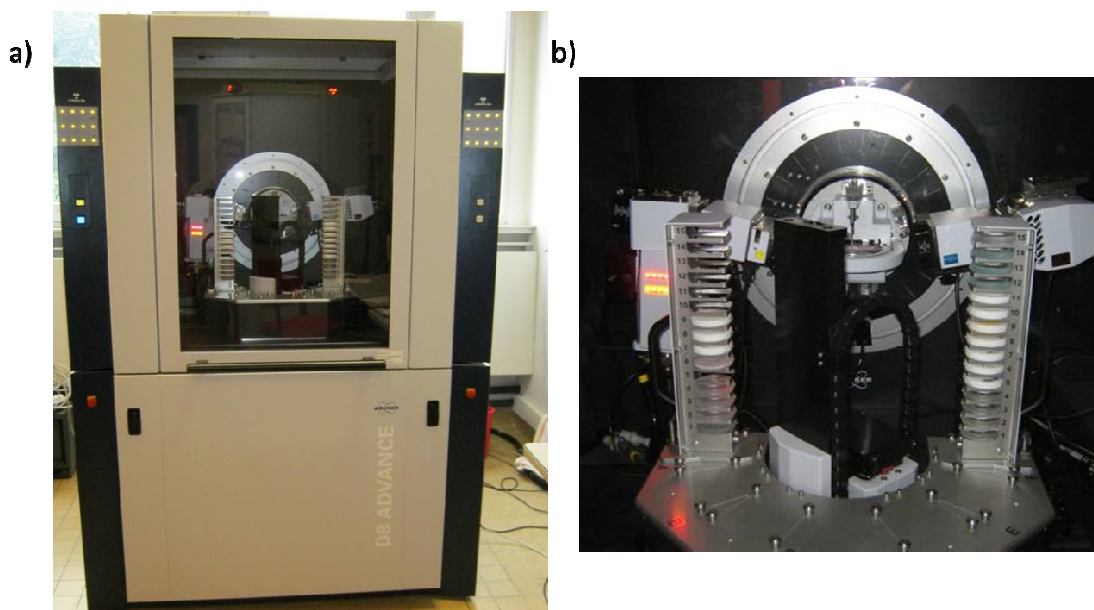


**Figure 2.** a) Picture of a D8 Passeur (Bruker-AXS) diffractometer and b) Zoom from the inside of the chamber.

Some samples were also investigated by high temperature X – ray diffraction in order to observe *in situ* the structural transformations produced at such temperatures. Measurements were performed on a D8 Advance diffractometer (Bruker AXS) equipped with a reactor chamber. XRK-900, a heating chamber specially designed for x-ray diffraction. It allows experiments from room temperature up to 900 °C and also allows working under controlled atmosphere (N<sub>2</sub>, O<sub>2</sub>, H<sub>2</sub> (3%)...) including oxidative/reductive atmosphere. The main technical characteristic consists in a Vantec 2-D detector which allows obtaining good patterns with short time-acquisition and a  $\theta$ - $\theta$  Bragg-Bratano geommetry.

To finish, some diffraction experiments were carried out in a Rigaku “SmartLab” diffractometer in order to optimize the conditional conditions of our synchrotrons experiences (chapter II, section 4.4). This diffractometer is equipped with high power 9 kW Cu rotating anode generator specifically optimized for the optics and geometry. The sample is manipulated with 3- circles ( $\omega$ ,  $\chi$ ,  $\varphi$ ) and the detector is moved with 2-circles ( $2\theta$  and  $2\theta\chi$ ), two additional circles can be obtained with a special sample holder (R<sub>x</sub>, R<sub>y</sub>). In addition it was also equipped with an Anton Paar DHS 1100 Domed Hot Stage prepared to work in controlled atmospheres (air, inert gas, vacuum of 10<sup>-1</sup> mbar) until 1100°C.

## Annexes.

---

- *Powder structural refinement. Rietveld method.*

When the growing of single crystal with an adequate size for single crystal diffraction measurement is difficult, this method is a good alternative to find out a structural model of the material. Rietveld analysis gives access to information like cell parameters of the unit cell, space group, atomic positions, site occupations and atomic displacements (isotropic or anisotropic). This technique relies on a comparison of intensities and the profile of an observed diagram with a calculated one; this latest is based on the hypothesis of a correct structural model. These types of refinement were carried out with Fullprof software.[7]

The first step of the refinement is a “profile matching” also called “Le Bail method” [8] consisting on the refinement of profile parameters without the knowledge of the crystalline structure. Before this, the approximate cell parameters should be known or can be found by doing an indexing with software as DicVol.[9] The aim of this fundamental step is to determine the best profile function which corresponding to the experimental diffraction pattern.

During my thesis it was done following this order:

The background points were peaked manually from the input diffractogram file with WinPloter program (included in Fullprof Suite).[10] Typically the background was composed of 40-50 points. Then the  $2\theta$  zero point and the cell parameters were refined to adjust the position of the calculated peaks whereas the background is kept fix. After that, the parameters  $W$ ,  $V$  and  $U$  of the Caglioti formula ( $H^2 = U \tan^2\theta + V \tan\theta + W$  where  $H$  represents the  $F_{WHM}$ ) were refined, in order to adjust the peak profile.[11] The peak profile is described as a mixture of Gaussian and Lorentzian behavior. In the cases of this thesis, the Pseudo-Voigt profile ( $Vp(2\theta) = \eta L(2\theta,H) + (1 - \eta) G(2\theta,H)$ ) fits the best. Then the  $\eta$  parameter (proportion between Gaussian and Lorentzian behavior) must be also refined. At the end, if necessary, the asymmetrical parameters were finally refined at low  $2\theta$  angles. To match the experimental and theoretical profiles, the least-squares method is used. It gives an output factor  $\chi^2$  which shows the agreement between experimental and simulated profile (the  $\chi^2$  parameter has to tend as close as possible to 1 in order to consider a refinement as “good”).

---

## Annexes.

---

For the second step (structural refinement), a high quality diffractogram measured over a wide  $2\theta$  range is required to allow a good refinement. The Rietveld method is based on a least-squares approach to characterize measured data points of a diffraction pattern,  $y_{obs,i}$ , with an analytic function,  $y_{calc,i}$ , taking into account unit cell parameters, atomic positions, anisotropic and/or isotropic temperature vibrations and site occupancies. The refinement process minimizes the following function:

$$M = \sum_i w_i (y_{obs,i} - y_{calc,i})^2$$

where  $w_i = 1/\sigma_i$  is the weighting factor and  $\sigma_i$  is the standard deviation of  $y_{obs,i}$

Different reliability factors enable to judge of the quality of the refinement:

The weighted profile R-factor:

$$R_{wp} = \sqrt{\frac{\sum_i w_i (y_{obs,i} - y_{calc,i})^2}{\sum_i w_i (y_{obs,i})^2}}$$

The unweighted profile R-factor:

$$R_p = \frac{\sum_i |y_{obs,i} - y_{calc,i}|}{\sum_i y_{obs,i}^2}$$

The expected R-factor:

$$R_{exp} = \sqrt{\frac{N - P + C}{\sum_i w_i (y_{obs,i})^2}}$$

where N, P and C are respectively the number of independent observations, the number of refined parameters and the number of constraints between these two parameters.

The goodness of fit (GOF) is given by:

$$\chi^2 = \left(\frac{R_{wp}}{R_{exp}}\right)$$

However, profile R-factors measure GOF for structure + peak shape +background, then it might happen that with very good counting statistics and minor profile problems one gets high  $R_{wp}$  &  $\chi^2$  values. Whereas with poor counting statistics and high backgrounds, the  $R_{wp}$  and  $\chi^2$  values will be low and these good output data come from fitting background. Finally, it is also very important to judge quality of refinement from the plot of the fit.

### 2. X-ray absorption (XAS).

#### 2.1. SOLEIL synchrotron: DiffAbs beamline.

SOLEIL is a third generation (2.75GeV) synchrotron facility located on Plateau de Saclay near Paris, France. It consists on a circular particles accelerator where the particles, electrons in this case, move in packets around a fix rayon circle.

Most of experiences performed using synchrotron radiation in this work where carry on the DiffAbs beamline after acceptation of two different proposals, one about the exfoliation of the halogeno-cobaltite  $\text{Ba}_7\text{Co}_6\text{BrO}_{17}$  (chapter I) and the second one about the iron exsolution in  $\text{BaFe}_2(\text{PO}_4)_2$  and its solid solutions of Co and Ni (chapter II).

The DiffAbs beamline allows the study of a huge variety of materials thanks to a combination of different characterization techniques available, based on X-ray diffraction and X-ray absorption. This beamline can work in two modes with a standard beam mode and a micro beam mode. In the standard mode receiving a light with energies from 3 to 23 KeV, the beam size (H x V) is of  $300 \times 300 \mu\text{m}^2$  and a photons flow of  $10^{12}$ - $10^{13}$  ph./sec and from 3 to 20 KeV. In the micro beam mode the beam size is of  $14 \times 11 \mu\text{m}^2$  and the photons flow of  $10^{10}$ - $10^{11}$  ph./sec, being possible to reduce de beam size with a reduction of the photons flow. These characteristics allow to use techniques working in a hard X-Ray domain.

The combination of different techniques as diffraction or absorption spectroscopy, performed on the same zone of the sample and under the same experimental conditions will give to us a coherent set of data which will allow us to establish correlations needed for a good characterization of the sample. During our experiments we have combined powder X-Ray Diffraction (P-XRD), X-Ray absorption near-edge spectroscopy (XANES) and diffraction anomalous near edge structure (DANES)

The DiffAbs beamline extract a monochromatic beam from the incoming white beam thanks to two Si (111) monochromator. The first Si crystal is plan and obtains a monochromatic beam as the result of the diffraction principles. The second one is curved and is used to restore parallelism and focus the beam in the horizontal plane. A

## Annexes.

---

secondary focusing system with Kirkpatrick-Baez geometry, consisting in two cross and curved mirrors, allows to obtain an X-Rays micrometric beam on the sample.

The experimental station (see figure 3) consists in a 6/8 circles diffractometer with 4 circles for the sample orientation, 2 more circles of the detectors and another 2 from the analyzer. Two different detectors were used during the analysis, depending of the technique. A XPAD S-140 small 2-D detector was used for the powder X-Ray diffraction experiments ( $2\theta_{\lambda=0.7392\text{nm}} = 7^\circ$  /image) and a second detector, a 4-element Silicon drift detector for X-Ray fluorescence, was used to collect the XANES signal. For DANES experiments the detector, an Avalanche Photo Diode (APD), was placed on opposition of the beam source with the sample orientated on a Bragg position over the entire experiment. Thus, the detector collects the fluorescent x-ray belonging exclusively to the absorber atoms of the chosen reflection.

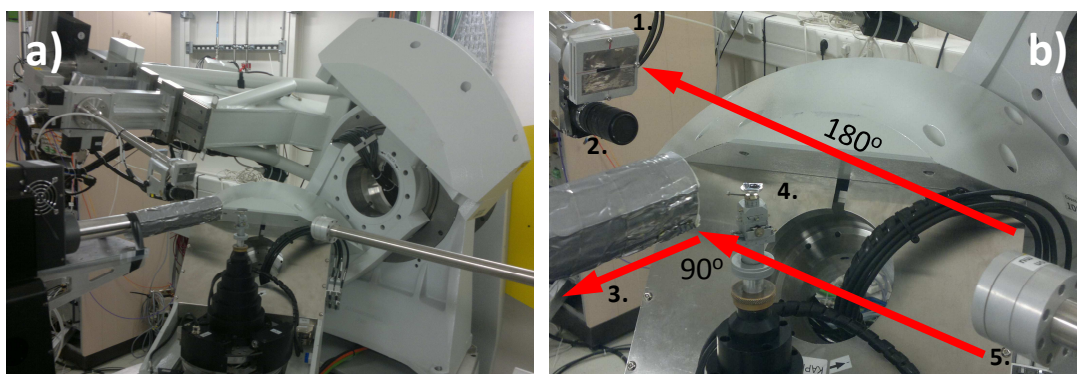


**Figure 3.** a) General view of the experimental station. b) 1. XPAD 2-D detector. 2. Camera, 3. Si diodes detector, 4. sample, 5. Source.

### 2.2. X-ray absorption spectroscopy (XAS).

X-ray absorption spectroscopy (XAS) is an analytical technique to obtain information about the local environment and the oxidation state of the absorber atoms in a sample. This technique can be used for gas liquid or solid state matter, and doesn't need a long range order, contrary to x-ray diffraction.

When an x-ray photons beam reaches a sample, several elastic and inelastic diffusion processes appear. In this section we will focus our attention on the process where the sample absorbs a part of the incident beam. The phenomenon of XAS is related with the photoelectric effect where an electron can be extracted from its energetic level to the continuum by a photon with a concrete energy  $h\nu$ . XAS analysis

## Annexes.

---

consists to study the variation of the absorption coefficient  $\mu$  as a function of the incident photon's energy.

When an “x” thickness sample is put under an x-ray photons beam with an intensity of  $I_0$ , it will absorb a part of that intensity. The unabsorbed intensity  $I$  evolution follows the Lambert-Beer Law:

$$I = I_0 e^{(-\mu(E)x)}$$

Absorption coefficient presents discontinuities due to the different absorption thresholds. These thresholds are related with the energetic level of the ejected electron. They are noted by a letter corresponding to the first quantum number  $n$  associated to the energetic level where the electron is placed. So, It is used K, L, M... for  $n = 1, 2, 3...$  The energetic level of the electron will also depend of the second quantum number  $l$ . In addition, when  $l \neq 0$  spin-orbit coupling produces a supplementary split characterized by the quantum number  $j$ . The different thresholds are indicated by a subscript, then,  $L_I$  corresponds to  $n = 2, m = 0$ , so excited electron comes from 2s orbital,  $L_{II}$  corresponds to  $n = 2, m = 1, j = 1/2$ , so  $2p_{1/2}$  and  $L_{III}$  corresponds to  $n = 2, m = 1, j = 3/2$ , so  $2p_{3/2}$ . Figure 4 shows the different L thresholds of Cs as example.[12] During the XAS experiences described in this work Fe, Co, Ni and Br K edges were studied.

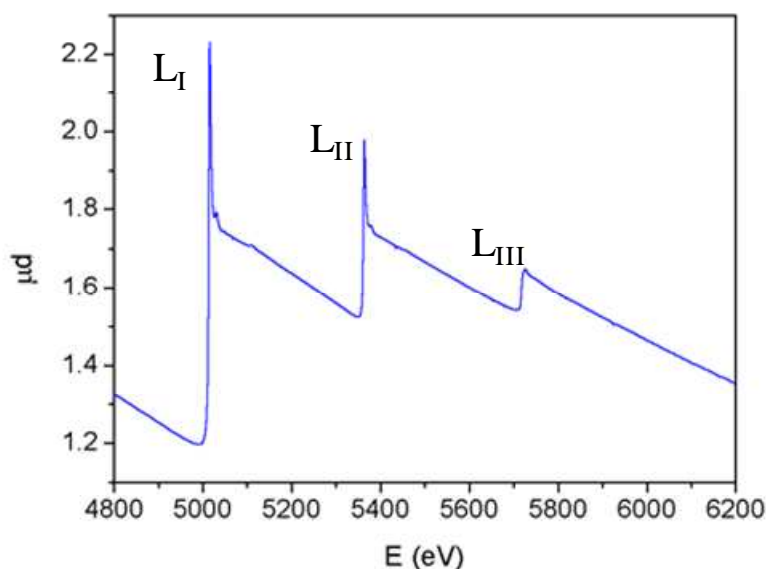


**Figure 4.** The L-edge spectrum of Cs.

Threshold energy is an inherent feature of the atomic element studied.

## Annexes.

---

If we consider  $E_0$  as the ionization energy of the core electrons of the element studied, we can remark several different regions in the absorption spectra which are presented in the example of the K-edge of Fe in the figure 5. Traditionally, the absorption spectra are divided in two different regions: the Near Edge spectra (XANES) and the Extended x-ray Absorption Fine Structure (EXAFS). Both of processes have the same physical origin, but the spectra interpretation gives different information. XANES region is situated proximate to the threshold, typically within 60 eV around the main absorption edge. This technique is strongly sensitive to coordination chemistry (e.g., octahedral, tetrahedral coordination) and to formal coordination state of the absorbing atom, while the EXAFS is used to determinate coordination number and distances of the neighbors of the absorbing atom. In our case we have only consider the XANES part.

At the beginning the photons beam have an  $E < E_0$ , the absorption it is almost zero because electrons have not enough energy to jump from its elemental state. When we increase the energy there is a first remarkable point, near  $E_0$  the pre-edge. This region of the spectra depend of the first available energetic levels before the final state of the absorbing atom, which will depend of different parameters as the coordination sphere and its small distortions. These empty levels have a low energy and it doesn't allow the photoelectron to propagate.

When the incident x-ray has an energy equal to that of the binding energy of a core-level electron, a sharp rise in absorption is observed, known as absorption edge, corresponding to the transition of the electron from the core level to the continuum. After this point two different mechanisms are involved for the decay of the excited atomic state after the x-ray absorption. The first mechanism is the x-ray fluorescence where a higher energy electron core-level electron fills the deeper core hole, ejecting an x-ray photon-electron of well-defined energy. The fluorescence energies emitted in this way are the characteristic signature of the atom. The second process for de-excitation of the core hole is the Auger effect, in which an electron drops from a higher electron level and a second electron is emitted into the continuum. In the hard x-ray domain, in which we worked, the fluorescence mechanism prevails over the Auger effect.

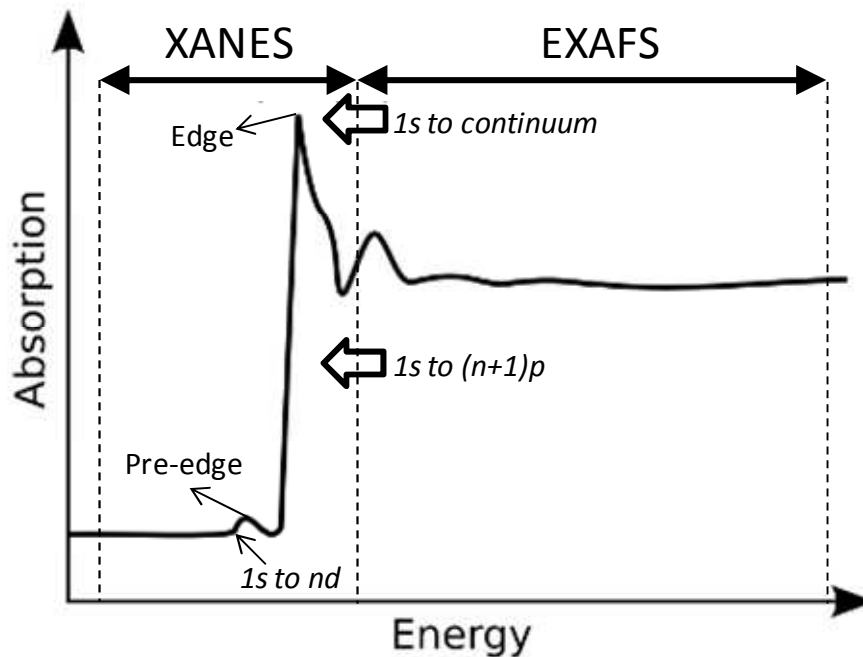


**Figure 5.** presentation of a K-edge absorption spectra, with the different remarkable regions.

XAFS spectra can be measured in transmission or fluorescence geometry. In our case the data collection was made in fluorescence mode where the energy dependence of the absorption coefficient  $\mu(E)$  evolves as  $\mu(E) \propto I_f/I_0$  where  $I_f$  is the intensity of the fluorescence signal correlated to the absorption process. The energy discrimination in the full fluorescence signal is made electronically thanks to the solid Si-detector.

- *Diffraction anomalous near edge structure (DANES).*

This technique measures the elastic Bragg reflection intensities versus photon energy. It allows to provide information from the specific subset of atoms selected by the diffraction condition. To carry on measurements by DANES technique, the sample is placed in a Bragg position. In our case, for the halide-cobaltite, we chose the (002) reflection, because it was the most intense of the diagram, and the (110) when it was intense enough. This Bragg position was calculated for all the wavelength range scanned and the sample rotates to keep the Bragg position during all the experiment. In this position, the detector receives the signal from the absorber atoms of the planes family corresponding to the chosen (hkl).

### 3. Scanning electron microscopy.

Scanning electron microscopy is a complementary technique in the study and characterization of the samples in solid chemistry. SEM is a type of electron microscope that gives images of a sample by scanning the surface with high-energy beam of electrons in a raster scan pattern. When the electron beam arrives on the sample surface, several interactions are produced as absorption or emission of electrons, electronic diffusion or diffraction, emission of secondary electrons, Auger electrons or photons, etc. Figure X presents some examples of the electronic interactions which can occur in the sample. All of these interactions can be used to reveal information about the sample including external morphology (texture), chemical composition, and crystalline structure and orientation of materials making up the sample.

During SEM experiences the secondary electrons coupled with the backscattered ones are mainly analyzed. The secondary electrons give information concerning sample topography whereas backscattered electrons contribute to information about composition homogeneity. The microscope I have used had also an X-ray detector which allows knowing sample composition by energy dispersive X-ray spectroscopy (EDS).

The scanning electron microscope used in the work presented in this manuscript is Hitachi S4700 equipped with an EDS micro-analyzer and with field emission guns (FEG) (Figure, (b)).

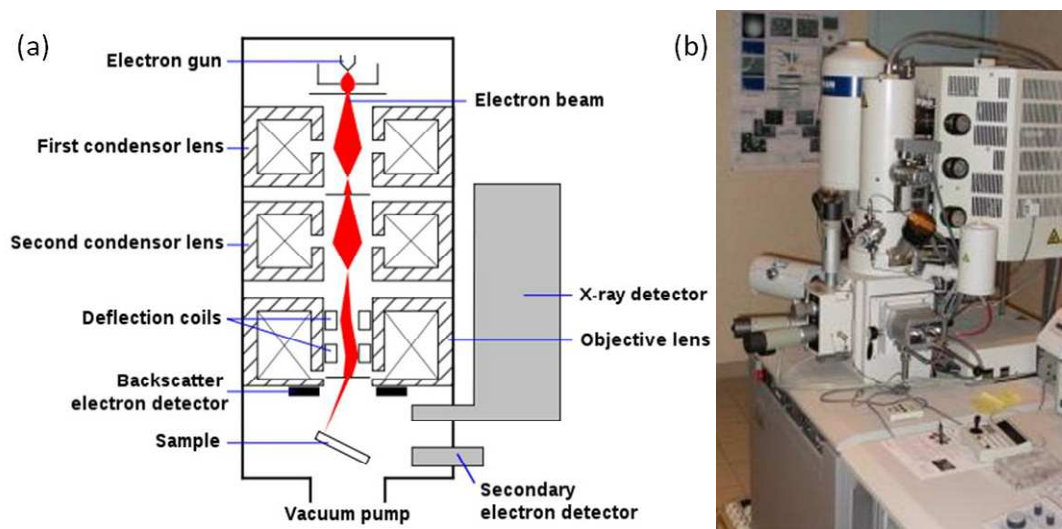


*Figure 6. (a) Schema for SEM machine and (b) Hitachi S4700.*

---

## Annexes.

---

The electron beam is emitted from an electron gun fitted with a tungsten filament cathode (schema form Figure 6, (a)). Tungsten is normally used in thermionic electron guns because it has the highest melting point and lowest vapor pressure of all metals. Thereby it can be heated for electron emission. It is also of low cost.

The electron beam, which typically has an energy between 0.5 keV to 40 keV, is focused by one or two condenser lenses to a spot about 0.4 nm to 5 nm in diameter. The beam passes through pairs of scanning coils or pairs of deflector plates in the electron column, typically in the final lens, which deflect the beam in the x and y axes so that it scans over a rectangular area of the sample surface.

When the primary electron beam interacts with the sample, the electrons lose energy by repeated random scattering and absorption within a teardrop-shaped volume, known as volume of primary excitation, which extends from less than 0.1  $\mu\text{m}$  to around 5  $\mu\text{m}$  into the surface.

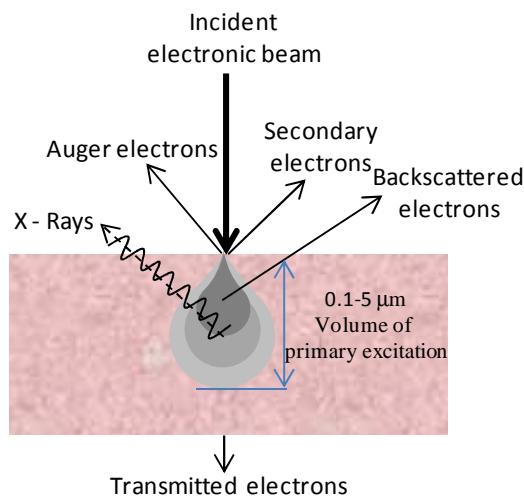


**Figure 7.** Several possible radiations occurred after beam-sample interaction.

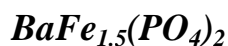
Secondary electrons, backscattered electrons and characteristic x-ray radiation are detected by the different detectors. Electrons detection transforms the electrons in light when they arrive, sending a signal which finishes becoming an image. X-ray detector receives the different x-ray photons which wavelengths are characteristic of the different elements. Those signatures allow a semi-quantitative analysis to determine the elemental composition of the sample.

### Bibliography.

- [1] A. Putnis, *An introduction to mineral sciences.*, Cambridge University Press, Cambridge, UK (1992).
- [2] SAINT+, Bruker Analytical X-ray Systems: Madison, WI, (x2), (2001).
- [3] SADABS, Bruker Analytical X-ray Systems: Madison, WI, (x2), *Bruker/Siemens Area detector absorption and other corrections* (2011).
- [4] G. Oszlanyi, A. Suto, *Acta Crystallographica Section A* **64** (2008) 123.
- [5] L. Palatinus, G. Chapuis, *Journal of Applied Crystallography* **40** (2007) 786.
- [6] M.D. V. Petricek, L. Palatinus, JANA 2000, In: C. Institut of Physics: Praha, Editor (2005).
- [7] J. Rodriguez-Carvajal, Fullprof, <http://www.ill.eu/sites/fullprof/> (2001).
- [8] A. Le Bail, H. Duroy, J.L. Fourquet, *Materials Research Bulletin* **23** (1988) (3) 447.
- [9] A. Boulton, D. Louer, *Journal of Applied Crystallography* **24** (1991) 987.
- [10] T. Roisnel, J. Rodriguez-Carvajal, *Epdic 7: European Powder Diffraction, Pts 1 and 2* **378-3** (2001) 118.
- [11] G. Caglioti, A. Paoletti, F.P. Ricci, *Nuclear Instruments & Methods* **3** (1958) (4) 223.
- [12] J.P. Gomilsek, A. Kodre, I. Arcon, M. Hribar, *Physical Review A* **68** (2003) (4).

# ANNEX 2.

## Single crystal data collection tables.



Crystal Data (T= 293 K)	
Formula	BaFe <sub>1.5</sub> (PO <sub>4</sub> ) <sub>2</sub>
Molar weight (g/mol)	411.1
Symmetry	Triclinic
Space group	P-1 (N° 2)
Unit cell (Å) and angle (°)	a = 19.101(6) Å    α=99.559(13)°
	b= 8.272(3) Å    β= 89.718(12)°
	c= 8.525(3) Å    γ= 149.942(7)°
Volume	638.5(4) Å <sup>3</sup>
Z	4
Data Collection	
Equipment	Bruker DUO
λ (Mo Kα (graphite monochromator); Å)	0.71073
Density calc. (g/cm <sup>3</sup> )	4.276
Crystal dimensions (μm)	8x4x1
Color	Black
Scan mode	ω, φ
θ (min-max) (°)	2.22-32.4
μ (mm <sup>-1</sup> ; for λ Kα = 0.7107 Å)	10.001
T <sub>min</sub> /T <sub>max</sub>	0.75
R(int) (%)	5.8
Recording reciprocal space	-24≤h≤28, -11≤k≤7, -11≤l≤12
Number of measured reflections	6055
Number of independent reflections/(I > 3σ(I)), total	3146/1819
Refinement	
Number of refined parameters	106
Refinement method	Least squares on F
Twin fraction hkl/(120° around c*)	0.378(7)/0.306(10)
Weighting scheme	Unit
R1(F) [ I > 3σ(I) ] / R1(F <sup>2</sup> ) [all data], %	13.79/18.49
wR <sup>2</sup> (F <sup>2</sup> ) [ I > 3σ(I) ] / wR2(F <sup>2</sup> ) [all data], %	14.89/16.86
GOF(obs)/ GOF(all)	2.54/2.96
Max/Min residual electronic density (e <sup>-</sup> Å <sup>3</sup> )	12.88/-9.90

**BaFe<sub>1.33</sub>(PO<sub>4</sub>)<sub>2</sub>**

Crystal Data (T= 293 K )		
Formula	BaFe <sub>1.33</sub> (PO <sub>4</sub> ) <sub>2</sub>	
Molar weight (g/mol)	401.7	
Symmetry	Triclinic	
Space group	P-1	
Unit cell (Å) and angle (°)	a = 8.241(2)	α=78.197(11)
	b= 9.6426(10)	β= 77.508(12)
	c= 12.700(3)	γ= 73.469(10)
Volume	933.5(3) Å <sup>3</sup>	
Z	6	
Data Collection		
Equipment	Bruker DUO	
λ (Mo Kα (graphite monochromator); Å)	0.71073	
Density calc. (g/cm <sup>3</sup> )	4.2875	
Crystal dimensions (μm)	30*15*5	
Color	Dark red	
Scan mode	ω, φ	
θ (min-max) (°)	1.66-33.34	
μ (mm <sup>-1</sup> ; for λ Kα = 0.7107 Å)	9.887	
T <sub>min</sub> /T <sub>max</sub>	0.84	
R(int) (%)	5.8	
Recording reciprocal space	-12≤h≤12, -14≤k≤13, -17≤l≤19	
Number of measured reflections	15355	
Number of independent reflections/(I > 3σ(I)), total	5304/1537	
Refinement		
Number of refined parameters	169	
Refinement method	Least squares on F	
Twin fraction hkl/(120° around c*)	0.531(18)/ 0.163(19)	
Weighting scheme	Unit	
R1(F) [ I > 3σ(I) ] / R1(F <sup>2</sup> ) [all data], %	5.96/20.38	
wR <sup>2</sup> (F <sup>2</sup> ) [ I > 3σ(I) ] / wR2(F <sup>2</sup> ) [all data], %	6.06/14.80	
GOF(obs)/GOF(all)	1.39/1.81	
Max/Min residual electronic density (e <sup>-</sup> / Å <sup>3</sup> )	8.01/-6.00	

<b>BaFe<sub>0.67</sub>Co(PO<sub>4</sub>)<sub>2</sub></b>		
<b>Crystal Data (T= 293 K )</b>		
Formula	BaFe <sub>0.67</sub> Co(PO <sub>4</sub> ) <sub>2</sub>	
Molar weight (g/mol)	423.5	
Symmetry	Triclinic	
Space group	P-1 (N° 2)	
Unit cell (Å) and angle (°)	a = 8.3313(4)	$\alpha = 70.606(3)$
	b = 8.3316(4)	$\beta = 99.558(3)$
	c = 8.3598(4)	$\gamma = 120.013(3)$
Volume	473.96(4) Å <sup>3</sup>	
Z	3	
<b>Data Collection</b>		
Equipment	Bruker DUO	
$\lambda$ (Mo K $\alpha$ (graphite monochromator); Å)	0.71073	
Density calc. (g/cm <sup>3</sup> )	4.4509	
Crystal dimensions ( $\mu\text{m}$ )	100x40x10	
Color	Reddish	
Scan mode	$\omega, \varphi$	
$\theta$ (min-max) (°)	3.31-34.69	
$\mu$ (mm <sup>-1</sup> ; for $\lambda$ K $\alpha = 0.7107$ Å)	10.803	
$T_{\text{min}}/T_{\text{max}}$	0.6019/0.7459	
R(int) (%)	1.94	
Recording reciprocal space	$-12 \leq h \leq 12, -12 \leq k \leq 12, -11 \leq l \leq 13$	
Number of measured reflections	7624	
Number of independent reflections ( $I > 3\sigma(I)$ ), total	1676/1185	
<b>Refinement</b>		
Number of refined parameters	93	
Refinement method	Least squares on F	
Twin fraction hkl/(120° around c*)	0.365(11)/ 0.311(7)	
Weighting scheme	Unit	
R1(F) [ $I > 3\sigma(I)$ ]/R1(F <sup>2</sup> ) [all data], %	5.76/8.32	
wR <sup>2</sup> (F <sup>2</sup> ) [ $I > 3\sigma(I)$ ]/wR2(F <sup>2</sup> ) [all data], %	5.05/6.26	
GOF(obs)/ GOF(all)	3.93/3.82	
Max/Min residual electronic density (e <sup>-</sup> / Å <sup>3</sup> )	2.37/-2.52	

<b>BaFe<sub>0.625</sub>Ni<sub>1.037</sub>(PO<sub>4</sub>)<sub>2</sub></b>		
<b>Crystal Data (T= 293 K)</b>		
Formula	BaFe <sub>0.625</sub> Ni <sub>1.037</sub> (PO <sub>4</sub> ) <sub>2</sub>	
Molar weight (g/mol)	423	
Symmetry	Triclinic	
Space group	P-1 (N° 2)	
Unit cell (Å) and angle (°)	a = 8.3078(7)	α = 70.567(3)
	b = 8.3074(7)	β = 99.558(39)
	c = 8.3194(8)	γ = 120.034(36)
Volume	468.75(9) Å <sup>3</sup>	
Z	3	
<b>Data Collection</b>		
Equipment	Bruker DUO	
λ (Mo Kα (graphite monochromator); Å)	0.71073	
Density calc. (g/cm <sup>3</sup> )	4.4958	
Crystal dimensions (μm)	200x100x100	
Color	Dark red	
Scan mode	ω, φ	
θ (min-max) (°)	2.83-35.92	
μ (mm <sup>-1</sup> ; for λ Kα = 0.7107 Å)	11.296	
T <sub>min</sub> /T <sub>max</sub>	0.5932/0.7470	
R(int) (%)	2.21/2.28	
Recording reciprocal space	-12≤h≤13, -10≤k≤13, -11≤l≤13	
Number of measured reflections	10644	
Number of independent reflections/(I > 3σ(I)), total	3941/2106	
<b>Refinement</b>		
Number of refined parameters	121	
Refinement method	Least squares on F	
Twin fraction hkl/(120° around c*)	0.336(3)/ 0.331(3)	
Weighting scheme	Sigma	
R1(F)[ I > 3σ(I)]/R1(F <sup>2</sup> ) [all data], %	2.64/5.12	
wR <sup>2</sup> (F <sup>2</sup> ) [ I > 3σ(I)]/wR2(F <sup>2</sup> ) [all data], %	3.60/4.03	
GOF(obs)/ GOF(all)	1.79/1.45	
Max/Min residual electronic density (e <sup>-</sup> / Å <sup>3</sup> )	1.13/-1.50	

***BaFe<sub>1.62</sub>Li<sub>0.322</sub>(PO<sub>4</sub>)<sub>2</sub>***

<b>Crystal Data (T= 293 K )</b>		
Formula	BaFe <sub>1.62</sub> Li <sub>0.322</sub> (PO <sub>4</sub> ) <sub>2</sub>	
Molar weight (g/mol)	420.2	
Symmetry	Rhombohedral	
Space group	R-3	
Unit cell (Å) and angle (°)	a = 8.8444(2)	α= 90
	b= 8.8444(2)	β= 90
	c= 23.3501(1)	γ= 120
Volume	474.569(3) Å <sup>3</sup>	
Z	3	
<b>Data Collection</b>		
Equipment	Bruker DUO	
λ (Mo Kα (graphite monochromator); Å)	0.71073	
Density calc. (g/cm <sup>3</sup> )	4.4105	
Crystal dimensions (μm)	20*10*5	
Color	Black	
Scan mode	ω, φ	
θ (min-max) (°)	2.62-27.45	
μ (mm <sup>-1</sup> ; for λ Kα = 0.7107 Å)	10.364	
T <sub>min</sub> /T <sub>max</sub>	0.6234/ 0.8421	
R(int) (%)	7.2	
Recording reciprocal space	-6≤h≤6, -6≤k≤6, -30≤l≤28	
Number of measured reflections	5308	
Number of independent reflections/(I > 3σ(I)), total	411/389	
<b>Refinement</b>		
Number of refined parameters	17	
Refinement method	Least squares on F	
Twin fraction hkl/(120° around c*)	0.2310(8)	
Weighting scheme	Sigma	
R1(F)[ I > 3σ(I)]/R1(F <sup>2</sup> ) [all data], %	1.44/4.58	
wR <sup>2</sup> (F <sup>2</sup> ) [ I > 3σ(I)]/wR2(F <sup>2</sup> ) [all data], %	1.89/1.90	
GOF(obs)/GOF(all)	1.28/1.25	
Max/Min residual electronic density (e <sup>-</sup> / Å <sup>3</sup> )	0.41/-0.43	

***BaFe<sub>1.33</sub>Li<sub>0.425</sub>(PO<sub>4</sub>)<sub>2</sub>***

<b>Crystal Data (T= 293 K )</b>	
Formula	BaFe <sub>1.33</sub> Li <sub>0.425</sub> (PO <sub>4</sub> ) <sub>2</sub>
Molar weight (g/mol)	403.9
Symmetry	Thombohedric
Space group	R-3
Unit cell (Å) and angle (°)	a = 4.8114(1)     α= 90
	b= 4.8114 (1)     β= 90
	c= 23.3161(3)     γ= 90
Volume	467.4438( ) Å <sup>3</sup>
Z	3
<b>Data Collection</b>	
Equipment	Bruker DUO
λ (Mo Kα (graphite monochromator); Å)	0.71073
Density calc. (g/cm <sup>3</sup> )	4.3049
Crystal dimensions (μm)	10*10*5
Color	Black
Scan mode	ω, φ
θ (min-max) (°)	2.62-36.17
μ (mm <sup>-1</sup> ; for λ Kα = 0.7107 Å)	9.844
T <sub>min</sub> /T <sub>max</sub>	0.6459/0.7985
R(int) (%)	5.8
Recording reciprocal space	-6≤h≤7, -7≤k≤7, -37≤l≤35
Number of measured reflections	4101
Number of independent reflections/(I > 3σ(I)), total	303/294
<b>Refinement</b>	
Number of refined parameters	303
Refinement method	Least squares on F
Twin fraction hkl/(120° around c*)	0.3215(6)
Weighting scheme	Sigma
R1(F) [ I > 3σ(I) ] / R1(F <sup>2</sup> ) [all data], %	1.62/1.74
wR <sup>2</sup> (F <sup>2</sup> ) [ I > 3σ(I) ] / wR2(F <sup>2</sup> ) [all data], %	1.90/1.95
GOF(obs)/GOF(all)	1.25/1.26
Max/Min residual electronic density (e <sup>-</sup> / Å <sup>3</sup> )	035/-0.52

## Annexes.

<b>Fe<sub>13.5</sub>(AsO<sub>4</sub>)<sub>8</sub>(OH)<sub>6</sub></b>		
<b>Crystal Data (T= 293 K)</b>		
Formula	Fe <sub>13.5</sub> (AsO <sub>4</sub> ) <sub>8</sub> (OH) <sub>6</sub>	
Molar weight (g/mol)	1967.3	
Symmetry	Hexagonal	
Space group	P 6 <sub>3</sub> mc (N°186)	
Unit cell (Å) and angle (°)	a = 12.9084(14)	α = 90
	b = 12.9084(14)	β = 90
	c = 5.1606(5)	γ = 120
Volume	744.69(14) Å <sup>3</sup>	
Z	1	
<b>Data Collection</b>		
Equipment	Bruker DUO	
λ (Mo Kα (graphite monochromator); Å)	0.71073	
Density calc. (g/cm <sup>3</sup> )	4.3868	
Crystal dimensions (μm)	10x10x200	
Color	Transparent	
Scan mode	ω, φ	
θ (min-max) (°)	1.82-30.09	
μ (mm <sup>-1</sup> ; for λ Kα = 0.7107 Å)	15.324	
T <sub>min</sub> /T <sub>max</sub>	0.7284/0.7458	
R(int) (%)	3.3	
Recording reciprocal space	-18 ≤ h ≤ 17, -13 ≤ k ≤ 18, -7 ≤ l ≤ 5	
Number of measured reflections	5122	
Number of independent reflections/(I > 3σ(I)), total	770/517	
<b>Refinement</b>		
Number of refined parameters	60	
Refinement method	Least squares on F	
Twin fraction	0.0452(2)	
Weighting scheme	Sigma	
R1(F) [ I > 3σ(I) ] / R1(F <sup>2</sup> ) [all data], %	3.31/6.42	
wR <sup>2</sup> (F <sup>2</sup> ) [ I > 3σ(I) ] / wR2(F <sup>2</sup> ) [all data], %	3.96/3.27	
GOF(obs) / GOF(all)	1.10/0.98	
Max/Min residual electronic density (e <sup>-</sup> / Å <sup>3</sup> )	0.82/-0.92	

## Annexes.

<b>Fe<sub>12.5</sub>(AsO<sub>4</sub>)<sub>8</sub>(OH)<sub>6</sub></b>		
<b>Crystal Data (T= 293 K)</b>		
Formula	Fe <sub>12.5</sub> (AsO <sub>4</sub> ) <sub>8</sub> (OH) <sub>6</sub>	
Molar weight (g/mol)	1905.4	
Symmetry	Hexagonal	
Space group	P 6 <sub>3</sub> mc (N°186)	
Unit cell (Å) and angle (°)	a = 12.5582(18)	α = 70.606(3)
	b = 12.5582(18)	β = 99.558(3)
	c = 5.0877(9)	γ = 120.013(3)
Volume	694.88(19) Å <sup>3</sup>	
Z	2	
<b>Data Collection</b>		
Equipment	Bruker DUO	
λ (Mo Kα (graphite monochromator); Å)	0.71073	
Density calc. (g/cm <sup>3</sup> )	9.1068	
Crystal dimensions (μm)	10x10x200	
Color	Black	
Scan mode	ω, φ	
θ (min-max) (°)	1.87-23.93	
μ (mm <sup>-1</sup> ; for λ Kα = 0.7107 Å)	31.839	
T <sub>min</sub> /T <sub>max</sub>	0.5362/0.7449	
R(int) (%)	9.74/9.75	
Recording reciprocal space	-14≤h≤14, -14≤k≤14, -5≤l≤5	
Number of measured reflections	27565	
Number of independent reflections/(I > 3σ(I)), total	422/421	
<b>Refinement</b>		
Number of refined parameters	69	
Refinement method	Least squares on F	
Twin fraction hkl/(120° around c*)	0.23(18)	
Weighting scheme	Unit	
R1(F)[ I > 3σ(I)]/R1(F <sup>2</sup> ) [all data], %	10.88/10.88	
wR <sup>2</sup> (F <sup>2</sup> ) [ I > 3σ(I)]/wR2(F <sup>2</sup> ) [all data], %	11.11/11.11	
GOF(obs)/ GOF(all)	2.49/2.50	
Max/Min residual electronic density (e <sup>-</sup> / Å <sup>3</sup> )	4.42/-4.48	

***RbFeAsO<sub>4</sub>(OH)*****Crystal Data (T= 293 K )**

Formula	RbFeAsO <sub>4</sub> (OH)	
Molar weight (g/mol)	297.2	
Symmetry	Orthorhombic	
Space group	F d d 2 (N° 43)	
Unit cell (Å) and angle (°)	a = 9.804(4) Å	α= 90°
	b= 32.074 (1) Å	β= 90°
	c= 5.659(2) Å	γ= 90°
Volume	1779.9(5) Å <sup>3</sup>	
Z	16	
<b>Data Collection</b>		
Equipment	Bruker DUO	
λ (Mo Kα (graphite monochromator); Å)	0.71073	
Density calc. (g/cm <sup>3</sup> )	4.4368	
Crystal dimensions (μm)	50x5x5	
Color	Pale yellow	
Scan mode	ω, φ	
θ (min-max) (°)	3.18-31.4	
μ (mm <sup>-1</sup> ; for λ Kα = 0.7107 Å)	21.549	
T <sub>min</sub> /T <sub>max</sub>	0.75	
R(int) (%)	5.8	
Recording reciprocal space	-24≤h≤28, -11≤k≤7, -11≤l≤12	
Number of measured reflections	6258	
Number of independent reflections/(I > 3σ(I)), total	3021/1829	
<b>Refinement</b>		
Number of refined parameters	148	
Refinement method	Least squares on F	
Twin fraction	0.213(9)/0.217(7)	
Weighting scheme	Sigma	
R1(F)[ I > 3σ(I)]/R1(F <sup>2</sup> ) [all data], %	5.11/8.31	
wR <sup>2</sup> (F <sup>2</sup> ) [ I > 3σ(I)]/wR2(F <sup>2</sup> ) [all data], %	8.35/9.52	
GOF(obs)/ GOF(all)	1.28/1.21	
Max/Min residual electronic density (e <sup>-</sup> / Å <sup>3</sup> )	3.45/-1.58	

# ANNEX 3.

## Atomic coordinates and displacement tables.

### BaFe<sub>1.5</sub>(PO<sub>4</sub>)<sub>2</sub>

Atome	Wyck.	X	y	z	U <sub>eq./iso</sub> (Å <sup>2</sup> )
Ba1	1b	0	0	0.5	0.014(3)
Ba2	1f	0.5	0	0.5	0.014(3)
Ba3	2i	0.2432(2)	-0.0080(6)	0.4774(3)	0.012(3)
Fe1	2i	-0.1401(6)	-0.3756(14)	0.9988(6)	0.0124(10)
Fe2	2i	0.3688(6)	0.3334(15)	0.0166(6)	0.0132(10)
Fe3	1d	0.5	0	0	0.0215(18)
Fe4	1c	0	-0.5	0	0.033(2)
P1	2i	0.3165(11)	-0.135(3)	0.7714(11)	0.0116(16)
P2	2i	0.0753(13)	-0.123(3)	0.7900(12)	0.0186(19)
P3	2i	0.4369(11)	0.169(3)	0.2147(11)	0.0133(17)
P4	2i	0.1826(12)	0.173(3)	0.2279(12)	0.0164(18)
O1	2i	0.227(4)	0.321(9)	0.411(4)	0.021(6)
O2	2i	-0.081(3)	-0.099(7)	0.859(3)	0.007(4)
O3	2i	0.829(3)	0.058(8)	0.123(4)	0.019(6)
O4	2i	0.491(4)	0.299(9)	0.400(4)	0.023(6)
O5	2i	0.277(3)	-0.220(7)	0.582(3)	0.012(5)
O6	2i	-0.333(3)	-0.785(7)	0.865(3)	0.009(5)
O7	2i	0.159(3)	0.213(8)	0.848(4)	0.018(6)
O8	2i	0.416(3)	0.226(7)	0.864(3)	0.010(3)
O9	2i	0.348(3)	0.145(7)	0.167(3)	0.010(3)
O10	2i	0.094(3)	-0.169(9)	0.197(4)	0.022(6)
O11	2i	-0.074(4)	-0.427(9)	0.855(4)	0.023(6)
O12	2i	-0.178(3)	-0.576(8)	1.158(3)	0.013(5)

## Annexes.

O13	2i	0.325(3)	0.434(7)	0.170(3)	0.010(3)		
O14	2i	0.034(4)	-0.263(9)	0.605(3)	0.021(6)		
O15	2i	0.573(3)	0.420(8)	0.137(3)	0.011(5)		
O16	2i	0.405(3)	-0.114(7)	0.798(3)	0.014(5)		
Atome		$U_{11}$	$U_{22}$	$U_{33}$	$U_{12}$	$U_{13}$	$U_{23}$
Ba1		0.0109(9)	0.0143(12)	0.0255(10)	0.0116(10)	0.0082(9)	0.0142(11)
Ba2		0.0109(9)	0.0143(12)	0.0255(10)	0.0116(10)	0.0082(9)	0.0142(11)
Ba3		0.0084(8)	0.0090(11)	0.0192(10)	0.0075(9)	0.0041(8)	0.0069(9)

## $BaFe_{1.33}(PO_4)_2$

Atome	Wyck.	x	y	z	$U_{eq./iso} (\text{\AA}^2)$
Ba1	1a	0	0	0	0.0152(9)
Ba2	1h	-0.5	-0.5	0.5	0.0152(10)
Ba3	2i	-0.4885(3)	-0.1557(3)	0.16626(18)	0.0155(7)
Ba4	2i	0.0212(3)	-0.3482(2)	0.32239(19)	0.0133(7)
Fe1	2i	-0.6486(7)	0.1795(6)	0.3250(4)	0.0138(10)
Fe2	2i	-0.1473(7)	0.3258(5)	0.1797(4)	0.0104(9)
Fe3	2i	-0.1860(7)	0.0232(6)	0.4874(4)	0.0130(10)
Fe4	2i	0.3153(7)	-0.5117(6)	0.0169(4)	0.0131(10)
P1	2i	-0.4254(12)	-0.1479(9)	0.4242(7)	0.0072(13)
P2	2i	-0.0813(13)	-0.3567(10)	0.0744(8)	0.0126(15)
P3	2i	-0.5570(10)	-0.5180(8)	0.2355(6)	0.0044(13)
P4	2i	0.0812(12)	0.0185(10)	0.2664(8)	0.0107(15)
P5	2i	-0.4124(11)	0.1905(9)	0.0908(7)	0.0065(13)
P6	2i	-0.0588(13)	0.3116(10)	0.4093(8)	0.0133(16)
O1	2i	0.150(4)	-0.122(3)	0.208(2)	0.016(5)

## Annexes.

O2	2i	-0.597(3)	-0.392(3)	0.295(2)	0.014(5)	
O3	2i	-0.402(4)	0.167(3)	0.508(2)	0.014(5)	
O5	2i	0.301(4)	-0.495(4)	0.167(3)	0.025(6)	
O6	2i	-0.582(3)	0.173(3)	0.164(2)	0.011(5)	
O7	2i	0.209(3)	0.021(3)	0.332(2)	0.012(5)	
O8	2i	-0.039(3)	0.152(3)	0.4814(19)	0.008(4)	
O9	2i	-0.543(3)	0.339(3)	0.3122(19)	0.008(4)	
O10	2i	0.054(4)	0.162(3)	0.179(2)	0.014(5)	
O12	2i	-0.883(3)	0.323(3)	0.344(2)	0.010(4)	
O13	2i	0.096(3)	-0.365(3)	-0.009(2)	0.012(5)	
O14	2i	-0.454(4)	0.345(3)	0.018(2)	0.018(5)	
O15	2i	-0.694(3)	0.134(3)	0.4928(19)	0.008(4)	
O16	2i	-0.358(3)	0.069(2)	0.0233(17)	0.004(3)	
O17	2i	0.135(3)	-0.424(3)	0.5173(19)	0.010(4)	
O18	2i	-0.332(3)	-0.276(3)	0.370(2)	0.010(4)	
O19	2i	-0.188(3)	0.321(2)	0.3336(18)	0.006(4)	
O20	2i	-0.089(3)	-0.007(3)	0.341(2)	0.009(4)	
O21	2i	-0.379(3)	0.475(3)	0.156(2)	0.009(4)	
O22	2i	-0.268(3)	0.179(2)	0.1470(19)	0.007(4)	
O23	2i	-0.118(4)	-0.225(3)	0.132(2)	0.016(5)	
O24	2i	-0.060(4)	-0.495(3)	0.163(2)	0.021(6)	
O25	2i	-0.220(3)	-0.341(3)	0.013(2)	0.010(4)	
O26	2i	-0.453(4)	-0.007(3)	0.338(2)	0.015(5)	
<b>Atome</b>	<b>U<sub>11</sub></b>	<b>U<sub>22</sub></b>	<b>U<sub>33</sub></b>	<b>U<sub>12</sub></b>	<b>U<sub>13</sub></b>	<b>U<sub>23</sub></b>
Ba1	0.0111(14)	0.0155(14)	0.0150(14)	-0.0036(11)	0.0008(11)	0.0040(10)
Ba2	0.0201(16)	0.0152(13)	0.0097(13)	-0.0110(12)	-0.0062(11)	0.0123(10)
Ba3	0.0143(11)	0.0165(10)	0.0122(10)	-0.0091(8)	-0.0009(8)	0.0118(7)
Ba4	0.0105(10)	0.0156(10)	0.0097(9)	-0.0046(8)	0.0019(7)	0.0051(7)

## Annexes.

### BaFe<sub>0.67</sub>Co(PO<sub>4</sub>)<sub>2</sub>

Atome	Wyck.	x	y	z	U <sub>eq./iso</sub> (Å <sup>2</sup> )	
Ba1	1e	0.5	0.5	0	0.014(3)	
Ba2	2i	0.8340(3);	1.1639(3)	0.00576(19)	0.014(3)	
Co1	2i	0.4953(13)	-0.3349(14)	0.4943(5)	0.012(3)	
Co2	2i	0.1475(11);	0.0028(13)	0.4893(6)	0.0124(10)	
Fe1	2i	0.8198(9);	0.3270(11)	0.4912(4)	0.0132(10)	
P1	2i	0.1678(13)	0.4123(18)	0.2792(7)	0.0215(18)	
P2	2i	0.4980(15)	0.074(2)	0.2784(9)	0.033(2)	
P3	2i	0.1674(12)	-0.7391(18)	0.7205(7)	0.0116(16)	
O1	2i	0.605(4);-	-0.042(4)	0.337(4)	0.0186(19)	
O2	2i	0.370(3);-	-0.611(3)	0.645(3)	0.0133(17)	
O3	2i	0.271(3);	0.294(4)	0.335(3)	0.0164(18)	
O4	2i	0.294(3);-	-0.059(3)	0.361(3)	0.021(6)	
O5	2i	0.039(3);	0.279(3)	0.359(3)	0.007(4)	
O6	2i	0.142(4);-	-0.818(5)	0.914(2)	0.019(6)	
O7	2i	0.189(3);	0.495(3)	0.0857(17)	0.023(6)	
O8	2i	0.060(3);-	-0.618(4)	0.652(3)	0.012(5)	
O9	2i	0.593(3);	0.253(3)	0.341(3)	0.009(5)	
O10	2i	0.260(3);	0.589(3)	0.338(3)	0.018(6)	
O11	2i	0.075(3);	-0.923(3)	0.670(3)	0.010(3)	
O12	2i	0.515(4);	0.151(5)	0.087(2)	0.010(3)	
Atome	U <sub>11</sub>	U <sub>22</sub>	U <sub>33</sub>	U <sub>12</sub>	U <sub>13</sub>	U <sub>23</sub>
Ba1	0.0112(19)	0.012(2)	0.0678(14)	-0.0003(17)	0.0072(18)	-0.022(2)
Ba2	0.0165(18)	0.0097(17)	0.0324(6)	0.0052(15)	-0.0078(14)	-0.0092(16)
Co/Fe	0.026(3)	0.0107(19)	0.0164(8)	-0.001(2)	-0.0057(18)	0.002(2)

## Annexes.

### **BaFe<sub>0.625</sub>Ni<sub>1.037</sub>(PO<sub>4</sub>)<sub>2</sub>**

Atome	Wyck.	x	y	z	U <sub>eq./iso</sub> (Å <sup>2</sup> )	
Ba1	1e	0.66698(4)	0.83643(5)	0.49328(4)	0.0141(3)	
Ba2	2i	1	1.5	0.5	0.0168(3)	
Fe1	2i	1.3323(2)	1.3296(3)	0.99301(7)	0.0067(4)	
Ni1	2i	1.0095(3)	0.6701(3)	0.99308(10)	0.0143(6)	
Ni2	2i	0.6691(3)	1.0066(4)	0.99469(10)	0.0190(7)	
P1	2i	0.9995(4)	1.0735(5)	0.77990(12)	0.0068(8)	
P2	2i	0.3355(4)	0.7399(5)	0.77970(13)	0.0067(8)	
P3	2i	0.6681(4)	0.4126(4)	0.77996(13)	0.0063(8)	
O1	2i	0.7958(7)	0.9494(8)	0.8361(8)	0.0119(10)	
O2	2i	1.0930(7)	1.2564(8)	0.8438(11)	0.0104(11)	
O3	2i	0.4638(7)	0.2860(8)	0.8342(8)	0.0107(9)	
O4	2i	0.6506(7)	0.4717(11)	0.5878(3)	0.0076(7)	
O5	2i	0.4371(6)	0.6115(6)	0.8602(6)	0.0036(7)	
O6	2i	0.1315(7)	0.6161(8)	0.8321(8)	0.0109(10)	
O7	2i	0.7611(7)	0.5933(8)	0.8459(10)	0.0102(11)	
O8	2i	0.4266(7)	0.9225(9)	0.8399(11)	0.0128(12)	
O9	2i	0.9798(7)	1.1349(12)	0.5870(3)	0.0079(7)	
O10	2i	1.1033(7)	0.9481(7)	0.8548(6)	0.0092(9)	
O11	2i	0.7697(6)	0.2835(7)	0.8553(6)	0.0080(8)	
O12	2i	0.3194(8)	0.7969(12)	0.5874(4)	0.0120(7)	
Atome	U <sub>11</sub>	U <sub>22</sub>	U <sub>33</sub>	U <sub>12</sub>	U <sub>13</sub>	U <sub>23</sub>
Ba1	0.0065(3)	0.0129(4)	0.02399(13)	0.0050(3)	0.0017(3)	-0.0053(3)
Ba2	0.0062(3)	0.0135(4)	0.0323(2)	0.0048(4)	0.0024(3)	-0.0073(4)
Fe1	0.0061(5)	0.0106(6)	0.0017(3)	0.0031(5)	-0.0009(4)	-0.0019(5)

## Annexes.

Ni1	0.0100(5)	0.0293(8)	0.0098(4)	0.0155(6)	0.0002(5)	-0.0028(6)
Ni2	0.0287(8)	0.0242(9)	0.0123(4)	0.0199(8)	-0.0019(6)	-0.0042(7)
P1	0.0053(9)	0.0089(10)	0.0073(5)	0.0044(9)	-0.0007(7)	-0.0022(8)
P2	0.0070(9)	0.0102(10)	0.0065(4)	0.0067(9)	0.0001(7)	-0.0025(8)
P3	0.0080(9)	0.0079(11)	0.0054(5)	0.0056(9)	-0.0004(7)	-0.0019(8)

### BaFe<sub>1.62</sub>Li<sub>0.322</sub>(PO<sub>4</sub>)<sub>2</sub>

Atome	Wyck.	x	y	z	U <sub>eq./iso</sub> (Å <sup>2</sup> )
Ba	3b	0.16667	0.33333	0.66667	0.0101(8)
Fe/Li	6c	0	1	0.3301(6)	0.0087(4)
P	6c	0	1	0.0747(8)	0.0067(9)
O1	18f	-0.3682(7)	0.6413(0)	0.3268(9)	0.0108(8)
O2	6c	0	1	0.0736(8)	0.0073(5)

Atome	U <sub>11</sub>	U <sub>22</sub>	U <sub>33</sub>	U <sub>12</sub>	U <sub>13</sub>	U <sub>23</sub>
Ba	0.0101(8)	0.0101(8)	0.01596	0.00509	0	0
Fe	0.00870	0.00870	0.00910	0.00437	0	0
P	0.00680	0.00680	0.00820	0.00340	0	0

## Annexes.

### **BaFe<sub>1.33</sub>Li<sub>0.425</sub>(PO<sub>4</sub>)<sub>2</sub>**

Atome	Wyck.	x	y	z	U <sub>eq./iso</sub> (Å <sup>2</sup> )
Ba	3b	0.33333	0.66667	0.16667	0.0101(6)
Fe	6c	0.66667	1.33333	0.0030(6)	0.0087(0)
Li	6c	0.66667	1.33333	0.0757(1)	0.0841(7)
P	6c	0	1	0.0736(8)	0.0073(5)
O1	6c	0.33333	0	1	0.0129(8)
O2	18f	1	0.2990(6)	1.33333	0.0120(4)

Atome	U <sub>11</sub>	U <sub>22</sub>	U <sub>33</sub>	U <sub>12</sub>	U <sub>13</sub>	U <sub>23</sub>
Ba	0.0101(8)	0.0101(8)	0.01596	0.00509	0	0
Fe	0.00870	0.00870	0.00910	0.00437	0	0
P	0.00680	0.00680	0.00820	0.00340	0	0

### **Fe<sub>13.5</sub> (AsO<sub>4</sub>)<sub>8</sub>(OH)<sub>6</sub>**

Atome	Wyck.	x	y	z	U <sub>eq./iso</sub> (Å <sup>2</sup> )
Fe1	12d	0.57397(9)	0.92094(9)	0.7735(3)	0.0111(4)
Fe2	12d	1	1	0.4509(7)	0.0192(13)
As1	2a	0.85173(4)	0.70347(9)	0.7511(3)	0.0097(3)
As2	2a	0.3333	0.6667	0.5200(4)	0.0129(5)
O1	6c	1.0645(4)	0.7254(5)	0.4268(10)	0.014(2)
O2	6c	0.4754(4)	0.9507(7)	1.0822(14)	0.013(3)
O3	2b	0.8103(4)	0.6205(8)	0.4726(14)	0.020(3)
O4	2b	0.4045(4)	0.8090(8)	0.6355(18)	0.030(3)

## Annexes.

O5	6c	0.9250(4)	0.8501(8)	0.7045(19)	0.038(4)	
O6	6c	0.3333	0.6667	0.204(4)	0.120(13)	
Ho2	6c	0.4367	0.8735	1.1858	0.052229	
Atome	U <sub>11</sub>	U <sub>22</sub>	U <sub>33</sub>	U <sub>12</sub>	U <sub>13</sub>	U <sub>23</sub>
Fe1	0.0093(5)	0.0113(5)	0.0115(5)	0.0042(4)	-0.0002(6)	0.0010(6)
Fe2	0.0088(11)	0.0088(11)	0.040(3)	0.0044(5)	0	0
As1	0.0082(3)	0.0112(5)	0.0108(5)	0.0056(2)	0.0002(3)	0.0004(6)
As2	0.0105(6)	0.0105(6)	0.0177(10)	0.0053(3)	0	0
O1	0.009(3)	0.012(3)	0.013(3)	-0.001(2)	0.001(2)	0.002(2)
O2	0.015(3)	0.009(4)	0.011(4)	0.005(2)	0.0035(14)	0.007(3)
O3	0.018(3)	0.033(5)	0.015(4)	0.016(3)	-0.0051(18)	-0.010(4)
O4	0.013(3)	0.011(4)	0.066(7)	0.005(2)	-0.0077(19)	-0.015(4)
O5	0.037(4)	0.028(5)	0.046(7)	0.014(3)	0.004(3)	0.008(5)
O6	0.156(17)	0.156(17)	0.05(2)	0.078(9)	0	0

### Fe<sub>12.5</sub> (AsO<sub>4</sub>)<sub>8</sub>O<sub>6</sub>

Atome	Wyck.	x	y	z	U <sub>eq./iso</sub> (Å <sup>2</sup> )
Fe1a	12d	0.5619(6)	0.9163(6)	0.8054(19)	0.029(3)
Fe1b	12d	0.5611(10)	0.9240(11)	0.400(3)	0.051(5)
Fe2a	2a	1	1	0.488(6)	0.027(9)
Fe2b	2a	1	1	-0.280(8)	0.070(15)
As1a	6c	0.8510(2)	0.7019(4)	0.7800(16)	0.0038(16)
As1b	6c	0.8463(9)	0.6926(18)	0.423(3)	0.096(9)
As2a	2b	0.3333	0.6667	0.550(5)	0.050(8)
As2b	2b	0.3333	0.6667	0.456(5)	0.050(8)

## Annexes.

O1a	6c	0.2641(10)	0.7359(10)	0.683(6)	0.013(4)
O1b	6c	0.5951(12)	1.190(2)	0.866(13)	0.122(16)
O2a	6c	0.9257(14)	0.851(3)	0.727(8)	0.013(4)
O2b	6c	0.917(2)	0.834(4)	0.513(18)	0.122(16)
O3a	6c	0.802(2)	0.605(4)	0.518(7)	0.013(4)
O3b	6c	0.803(4)	0.606(8)	0.707(13)	0.122(16)
O4a	12d	0.668(3)	0.945(2)	0.456(6)	0.013(4)
O4b	12d	0.722(5)	1.075(6)	0.253(13)	0.122(16)
O5a	6c	0.5216(18)	1.043(4)	0.593(10)	0.013(4)
O5b	6c	0.496(6)	0.992(11)	0.64(2)	0.122(16)
O6a	2b	0.3333	0.6667	0.232(5)	0.013(4)
O6b	2b	0.3333	0.6667	0.792(10)	0.122(16)

Atome	U <sub>11</sub>	U <sub>22</sub>	U <sub>33</sub>	U <sub>12</sub>	U <sub>13</sub>	U <sub>23</sub>
Fe1a	0.022(4)	0.026(4)	0.022(4)	0.000(3)	-0.007(4)	-0.006(3)
Fe1b	0.032(5)	0.065(8)	0.062(7)	0.029(5)	-0.003(5)	0.003(6)
Fe2a	-0.002(6)	-0.002(6)	0.08(3)	-0.001(3)	0	0
Fe2b	0.070(18)	0.070(18)	0.07(3)	0.035(9)	0	0
As1a	0.0058(1)	0.001(2)	0.003(2)	0.0004(12)	0.0002(13)	0.000(3)
As1b	0.057(5)	0.165(17)	0.103(11)	0.083(8)	-0.023(6)	-0.046(11)
As2a	0.061(4)	0.061(4)	0.03(2)	0.0305(19)	0	0
As2b	0.061(4)	0.061(4)	0.03(2)	0.0305(19)	0	0

### $\alpha$ -BaFe<sub>2</sub>(PO<sub>4</sub>)<sub>2</sub>

Atome	Wyck.	x	y	z	U <sub>eq./iso</sub> (Å <sup>2</sup> )
Ba1	3a	0.02436	0	1/3	0.03794
Fe1	6c	0.69479	0.26502	0.21644	0.02444
P1	6c	0.66200	0.32575	0.08979	0.0415

## Annexes.

O1	6c	0.65667	0.48610	0.14357	0.0329	
O2	6c	0.88427	0.52204	0.04983	0.0329	
O3	6c	0.62895	0.01398	0.08101	0.0329	
O4	6c	0.37935	0.31772	0.07916	0.0329	
<b>Atome</b>	<b>U<sub>11</sub></b>	<b>U<sub>22</sub></b>	<b>U<sub>33</sub></b>	<b>U<sub>12</sub></b>	<b>U<sub>13</sub></b>	<b>U<sub>23</sub></b>
Ba1	0.03794	0.03072	0.00951	-0.00783	0.01536	-0.01564
Fe1	0.02444	-0.00048	0.01851	-0.02618	0.01630	-0.02278

*Table8. Atomic coordinates, isotropic and anisotropic displacements parameters from XRD single crystals for BaFe<sub>2</sub>(PO<sub>4</sub>)<sub>2</sub>.*

### RbFe(AsO<sub>4</sub>)(OH)

<b>Atome</b>	<b>Wyck.</b>	<b>x</b>	<b>y</b>	<b>z</b>	<b>U<sub>eq./iso</sub> (Å<sup>2</sup>)</b>	
Rb1	16b	0.41547	0.22418	0.55802	0.01240	
Fe1	16b	0.58281	0.15961	0.05872	0.00445	
As1	16b	0.25120	0.17926	0.05312	0.00444	
O1	16b	0.25118	0.12713	0.04001	0.0061	
O2	16b	0.50352	0.12518	-0.20205	0.0120	
O3	16b	0.17137	0.19822	-0.19431	0.0061	
O4	16b	0.17130	0.19592	0.29472	0.0064	
O5	16b	0.41399	0.19720	0.06540	0.0089	
H2	16b	0.54532	0.12525	-0.32753	0.0144	
<b>Atome</b>	<b>U<sub>11</sub></b>	<b>U<sub>22</sub></b>	<b>U<sub>33</sub></b>	<b>U<sub>12</sub></b>	<b>U<sub>13</sub></b>	<b>U<sub>23</sub></b>
Rb1	0.01240	0.02033	0.01247	-0.00161	-0.00024	0.00001
Fe1	0.00445	0.00834	0.00547	0.00384	-0.00214	0.00015
As1	0.00444	0.01063	0.00540	-0.00269	-0.00015	-0.00076

